

Unravelling the Secrets of Ageing in Dye-Sensitised Solar Cells

By

Sunita Gautam Adhikari

Master of Physics

Thesis

Submitted to Flinders University

for the degree of

Doctor of Philosophy

College of Science and Engineering

Aug 2024



Karma Yog: The Yog of Action

न कर्मणामनारम्भान्नैष्कर्म्यं पुरुषोऽक्षनुते ।
न च संन्यसनादेव सिद्धिं समधिगच्छति ॥

No man can attain freedom from activity by refraining from action; nor can he reach perfection by merely refusing to act.

**Śrīmad Bhagavad Gītā, Chapter 3, Verse 4*

“Progress is made by trial and failure; the failures are generally a hundred times more numerous than the successes; yet they are usually left unchronicled.”

-WILLIAM RAMSAY, 1852 – 1916

TABLE OF CONTENTS

TABLE OF CONTENTS	II
ABSTRACT.....	VI
DECLARATION	IX
ACKNOWLEDGEMENTS	X
CONTEXTUAL STATEMENT.....	XII
LIST OF PUBLICATIONS	XIII
LIST OF FIGURES	XV
LIST OF TABLES	XXV
ABBREVIATIONS.....	XXVIII
CHAPTER 1 DYE SENSITISED SOLAR CELLS- AN OVERVIEW	1
1.1 Introduction	1
1.2. Operation of DSSCs	1
1.2.1. Photon absorption and excitation.....	3
1.2.2. Interfacial charge transfer	4
1.2.3. Electron transport.....	4
1.2.4. Electrolyte-to-dye electron transfer or Dye Regeneration	5
1.2.5. Electron loss	5
1.3. DSSC Components.....	6
1.3.1. Photoanodes	6
1.1.1.1 Morphology.....	8
1.1.1.2 Electronic Structure and Trap State	9
1.3.2. Sensitiser	9
1.3.3. Electrolytes.....	13
1.3.4. Counter Electrodes	17
1.4. Dye Anchoring Modes	19
1.4.1. UV Vis	20
1.4.2. XPS	22
1.4.3. Fourier Transform Infrared (FTIR).....	22
1.4.4. Raman	23
1.5. Ageing and Degradation in DSSCs	25
1.6. Commercial and Future Perspective of DSSCs.....	29
1.7. Appendix	31

1.8. References	32
CHAPTER 2 RESEARCH PROJECT	43
2.1. Aims and scope	43
2.2. Research Project	43
2.2.1. Anchoring modes of Ru-based N719 dye onto TiO ₂ substrate	43
2.2.2. Exploring Alteration in Electrochemical Interface of Dye Sensitised Solar Cells-An Experimental Set-up for Ageing Investigation.....	44
2.2.3. Unveiling the Ageing Effect at the Interface of N719 Dye Sensitised Solar Cells.....	44
2.2.4. Conclusion and Outlook.....	45
CHAPTER 3 EXPERIMENTAL METHODS	46
3.1. Analysis Techniques.....	46
3.1.1. JV Characterisation	47
3.1.2. Photoelectron Spectroscopy (PES)	51
3.1.2.1.1. Angle-resolved X-ray Photoelectron Spectroscopy (ARXPS)	56
3.1.3. Ultra-violet Photoelectron Spectroscopy (UPS)	59
3.1.4. Meta-stable Induced Electron Spectroscopy (MIES).....	62
3.1.5. Neutral Impact Collision Ion Scattering Spectroscopy (NICISS)	64
3.1.6. Fourier Transform Infrared Spectroscopy (FTIR)	67
3.1.7. Electrochemical Impedance Spectroscopy (EIS)	70
3.2. Materials.....	73
3.3. Cell Preparation Procedure.....	75
3.4. References	76
CHAPTER 4 ANCHORING MODES OF RU-BASED N719 DYE ONTO TITANIA SUBSTRATE	79
Abstract	79
4.1. Introduction	79
4.2. Experimental	83
4.2.1. Materials	83
4.2.3. Spectroscopic Measures	85
4.3. Results and Discussion.....	85
4.3.1. FTIR.....	85
4.3.2. ARXPS	93
4.3.3. XPS analysis for the re-sensitising test for analysing the TBA ⁺ adsorption	97
4.4. Conclusion.....	100
4.5. Acknowledgements	100
4.6. Appendix	100
4.7. References:	102

CHAPTER 5 EXPLORING ALTERATION IN ELECTROCHEMICAL INTERFACE OF DYE SENSITISED SOLAR CELLS-AN EXPERIMENTAL SET-UP FOR AGEING INVESTIGATION.....	105
Abstract	105
5.1. Introduction	105
5.2. Experimental	107
5.2.1. Materials	107
5.2.2. Sample Preparation	107
5.2.3. Analysis Measures	108
5.3. Result and Discussion	110
5.3.1. Electrolyte Extraction method via ethanol rinsing	110
XPS.....	110
UPS/MIES	114
5.3.2. Ageing Investigation of DSSCs.....	115
A. Effect of ageing on adsorbed dye layer	116
B. Effect of Ageing on Electrolyte and Redox Cycle	117
C. Drop-cast Samples	119
5.3.3. UPS	120
5.3.4. NICISS implementation in ageing investigation	121
5.4. Conclusion.....	123
5.5. Acknowledgements	123
5.6. Appendix	124
5.7. References	125
CHAPTER 6 UNVEILING THE AGEING EFFECT OF N719 DYE-SENSITISED SOLAR CELLS.....	127
Abstract	127
6.1. Introduction	127
6.2. Experimental	129
6.2.1. Materials	129
6.2.2. Sample Preparation.....	129
6.2.3. Analysis Measures.....	129
6.3. Results and Discussion.....	133
6.3.1. Device Level Analysis.....	133
6.3.2. Surface Analysis	136
6.3.3. FT-IR analysis	148
6.3.4. UV-Vis DRS.....	151
6.4. Conclusion.....	155
6.5. Acknowledgements	156

6.6. Appendix	156
6.7. References	157
CHAPTER 7 CONCLUSION AND OUTLOOK	160
7.1. Summary	160
7.2. Outlook.....	162
7.2. References	165
CHAPTER 8 APPENDICES.....	166
8.1 Chapter 1: Dye Sensitised Solar Cells-An Overview.....	166
8.1.1. References	180
8.2 Chapter 4: Anchoring Modes of Ru-based N719 dye onto Titania Substrate.....	182
SEM analysis for the thickness of mesoporous TiO ₂ :	182
XPS defect analysis:	182
FTIR Phenyl isothiocyanate:	184
TBA-adsorption	186
RF-sputtered TiO ₂ and Mesoporous TiO ₂ from XRD:	187
ARXPS	188
XPS analysis for the re-sensitizing test for analysing the TBA ⁺ adsorption	190
8.2.1. References	195
8.3 Chapter 5. Exploring Alteration in Electrochemical Interface of Dye Sensitised Solar Cells- An Experimental Set-up for Ageing Investigation.....	196
XPS analysis for the blank TiO ₂ substrate before and after ethanol rinsing	196
Device level analysis of DSSCs	197
XPS analysis	199
UPS analysis for reference samples.....	202
8.4 Chapter 6. Unveiling the Ageing Effect at the Interface of N719 Dye Sensitised Solar Cells	203
JV characterisation curve for high-performing cells in both dark and light-aged samples	203
Nyquist plot for high performing samples cells aged in dark and light.....	204
The XPS intensity variation in the elemental ratio of the photoanode for the sample cells aged in dark and light.....	205
NICISS characterisation of Ru and I in aged samples.....	206
FTIR spectral analysis of N719 dye, electrolyte and electrolyte solvent adsorbed onto TiO ₂ substrate	207
UV-Vis DRS spectral analysis of N719 dye and electrolyte onto TiO ₂ substrate.....	209
FTIR spectral analysis of various functional group in aged samples	210
DFT calculation and modelling	211

ABSTRACT

With the tremendous increase in the global population, the inflation of energy consumption is inevitable, which will lead to a dark era with no energy resources. Therefore, to avoid the situation of energy crisis, it is important to select an energy source which we can rely on for a long time and is cheaper and eco-friendly, the answer is **Solar and Photovoltaic**.

PV technology is a renewable power source with the capacity to fulfil the energy needs of the world population with the least impact on the environment. Among the third generation of PV, the Dye sensitised solar cells have succeeded in gaining attention due to their easy fabrication process, low production cost, and use of eco-friendly materials. The DSSCs are so far the most economical and eco-friendly with an efficiency of 15%. Though the efficiency is low, unlike other PVs, it holds the capacity to operate under low light conditions, i.e., indoors. Supplementarily, the performance of DSSC is divided among its components, therefore, medium to low-purity materials can achieve reasonable efficiency which makes them competent in the solar market. Contrastingly, the performance of Si-based solar cells relies on the purity of Si used, hence Si-based solar cells are expensive and consume more energy during the manufacturing process.

Due to the flexibility of DSSCs, they are used in wearable solar panels like backpacks and bags. In addition, large modules of DSSCs are built-in tents for military purposes with 1 kW of energy enough to operate a few lights and communication devices. However, the commercial success of DSSCs demands better efficiency with a better understanding of ageing and the cause of degradation under different stress factors with time which is the focus of the research.

The first stage of my work aims to understand the dye anchoring modes of the dyes of my interest N719, on the TiO₂ substrate using Angle-Resolved XPS and FTIR. FTIR being a chemically sensitive technique helps in identifying the dye conformation and anchoring modes. Further, the application of ARXPS which is a surface-sensitive technique provides insights into the concentration profile of the dye-TiO₂ configuration. A better clarification of available and possible anchoring modes of dye will unveil a better understanding of the interfacial properties N719-TiO₂ configuration of interest. The application of the procedure to understand anchoring can be applied to a wide range of absorbent and absorbate.

The second stage of this work targets to establish a technique that can be applied to understand ageing in DSSCs better. The study aims to investigate the application of different surface analytical techniques to observe the change introduced in the dye-TiO₂ interface and dye-TiO₂-

electrolyte interface with ageing. Initially, an effective approach to accessing the cell interface was developed. A procedure for opening the cell and rinsing off the electrolyte layer to excess of the dye layer was used. Further, the impact of the procedure on the dye layer was investigated. The rinsed-off solution was tested by drop-casting the rinsed-off solution onto the blank TiO_2 substrate. The alterations induced into the photoanodes by the methods were quantified using surface-sensitive techniques such as XPS, MIES, and UPS. The results conclude that the ethanol rinsing procedure has negligible impact on the photoanodes. Thus, a systematic methodology for investigating changes made at the cell interface over time is also devised, which will aid in correlating the decline in cell performance with interfacial deterioration. The study focussed on the application of various techniques to understand different aspects of ageing. The techniques include JV characterisation to track the changes in the PV performance overtime followed by XPS, UPS, MIES, and NICISS to observe the changes in dye/ TiO_2 interface. Thus, after establishing an effective ageing technique, an ageing investigation was performed on sample cells under two stress factors: dark and light. The main target of the study is to identify the main causative for the decrease in cell performance under different stress factors and to understand the impact on the cell interface. The device-level performance was traced down by the application of JV characterisation. Additionally, the change in the interfacial impedance was tracked by the application of EIS. The changes in the elemental and chemical composition of the aged sample were investigated using XPS. Furthermore, via the application of UPS, the changes in the DOS of the aged photoanode were explored. Followed by the implementation of NICISS to examine the changes in the concentration of electrolyte and dye elements overtime. Likewise, the change in the dye functional group was determined by the application of FTIR and the impact on dye absorption was observed using UV-Vis DRS.

Overall, the main reason for cell degradation was identified as the penetration of I species into the dye-layer. The I function at regenerating the dye and itself during the cell operation. Over time especially under light irradiation, the iodine species penetrates and gets stuck into the dye layer resulting in some irreversible reaction which impedes the photo generation by the dye molecule and thus, results in efficiency loss of the cell.

Keywords: *Dye Sensitised Solar Cells, Dye anchoring, Ageing, Stability, Degradation, XPS, UPS, MIES, FT-IR, NCISS, EIS, UV-Vis DRS, Interface, Impedance, Resistance, Iodine, N719, Formic Acid, Phenyl isothiocyanate, TBA-Br, Adsorption.*

DECLARATION

I certify that this thesis does not incorporate without acknowledgement any material previously submitted for a degree or diploma in any university; and that to the best of my knowledge and belief, it does not contain any material previously published or written by another person except where due reference is made in the text.

Signed.....

Date. 20/08/2024

ACKNOWLEDGEMENTS

The past four years have been a fantastic time in my life, during which I have seen myself change from a curious student to a self-reliant scientist. My doctoral journey was filled with moving encounters and intriguing science all around me. As this unique and fascinating PhD adventure concludes, I would like to take this chance to acknowledge and thank everyone who, has supported me, whether it was in helping me finish this dissertation or making my time in Australia an unforgettable experience.

First and foremost, I would like to extend my profound gratitude to my supervisor, Prof. Gunther Andersson, for his guidance and moral support throughout my PhD. Without him, I would not have been able to finish my work. As a master's student, I joined Gunther's group, and ever since, he has served as a continual source of encouragement and inspiration for me. I truly appreciate him for believing in me and providing me with the appropriate opportunity. While working in his group, I have grown to appreciate the chance to learn from such a committed professional and to collaborate closely with a decent person.

You are the most pedagogical person I have ever met, so thank you, Gunther.

Thank you, Prof. David Lewis, my co-supervisor, for assisting with several useful talks and for always being accommodating when it came to setting up meetings to further my PhD. To Dr. Jason Gascooke, Cheers, for the valuable discussion throughout. I appreciate you being one of the co- authors of two of my publications. My sincere gratitude goes out to Lars Kloo, Professor of Chemistry at the Royal Institute of Technology (KTH), for his valuable supervision and collaborative research support and guidance.

I owe my deepest gratitude to Andersson's group members, who have become my second family, for their leadership and support throughout my project. To all my past and present colleagues, THANK YOU for giving me the chance to carry out my studies in a supportive environment, especially throughout my pregnancy and for listening to all my vexing experiences and providing me with excellent advice. I am grateful to Dr. Liam Howard-Fabretto and Dr. Benjamin Chambers for technical assistance with the instrument and general guidance. I owe you one, team FMMA.

Much obliged to all my friends for your unceasing support. It has meant a great deal.

Additionally, I want to thank the mechanical and electronics workshops, and CSE Engineering Services Team for their prompt assistance and friendliness throughout.

I would like to express my gratitude to the funding sources that made my PhD work possible. I am beyond grateful for receiving the Flinders University Research Scholarship for three and a half years of my doctoral studies, as well as a full tuition waiver from the Faculty of Science and Engineering.

To my entire family, I want to thank you for helping me with my studies in numerous ways by giving me the love and support I needed throughout the journey. From the bottom of my heart, I want to thank my mother, whose supplication was the key to my achievement, and my father, who loved me from the day I was born and has never stopped encouraging and believing in me. I also appreciate my mother- and father-in-law's encouragement and support throughout the process.

To my little angels, Ojaswee and Ojal, thank you for being my emotional support. Thank you, Ojaswee, for being my strength and for all your support during late-night studies. You are the best sister ever. To Ojal, your birth during the study brought joy and pleasure to our lives. Thank you for everything. I love you a lot.

Dear beloved husband, thank you for your love, support, and patience while you cared for the kids and me throughout the tiring PhD years. I love you.

I want to express my gratitude to the Almighty for providing me with his very best blessings, including amazing mentors, coworkers, parents, siblings, friends, and relatives, as well as all the favourable possibilities that came my way. Finally, sincere thanks to all my teachers, my “gurus”. It's all because of you that I am who I am today, “गुरुर्ब्रह्मा गुरुर्विष्णुः गुरुर्देवो महेश्वरः। गुरुः साक्षात् परं ब्रह्म तस्मै श्री गुरुवे नमः” (Guru is Brahma, Vishnu, and Maheshwara. Guru is the absolute Brahman. Salutations to the Guru.)

I apologise if I forgot to mention some of you; my memory is not the best.

Sunita Gautam Adhikari

Flinders University

Aug 2024

CONTEXTUAL STATEMENT

This thesis presents the investigation of the anchoring mode of N719 dye and interfacial degradation of Dye-Sensitised Solar Cells which was performed as the author's PhD work.

The introduction chapter offers a basic introduction to DSSCs as well as an overview of the current research on anchoring and the ageing of DSSCs, which is directly related to the project. The experimental chapter, on the other hand, comprises the experimental details, methodology, and a review of the methodologies employed in the study. Most of the data provided in the thesis were obtained from experimental measurements at Prof. Gunther Andersson's lab and the solar cell laboratory at Flinders University in Australia. Except for the UV-Vis DRS measurement, which was performed at the University of Adelaide.

Chapters 4-6 are reformatted versions of manuscripts with the same title that are either under review or have been submitted to journals for review.

Most of the experimental work and data analysis was completed by the author exceptions include Dr. Jason Gascooke who was involved in FTIR and UV-Vis data interpretation and Dr. Abdulrahman Alotabi who conducted XRD measurement for RF-sputtered TiO₂. The contribution of the respective co-authors is acknowledged in the final interpretation of the results.

The author of the thesis contributed to the experimental work for two additional publications of which the author is a co-author. These are mentioned in the publication list, but the data from these measurements are not presented in this thesis. The content of the measurements served to support the work of collaborating researchers, and it was not directly related to the content of the thesis. The author of this thesis also contributed to revisions for the published versions of these manuscripts.

LIST OF PUBLICATIONS

The enlisted publications are the basis of this thesis which are referred to below by their Roman Numerals:

- I. Adhikari, S. G., Gascooke, J. R., Alotabi, A. S., & Andersson, G. G. (2024). Anchoring Modes of Ru-Based N719 Dye onto Titania Substrates. The Journal of Physical Chemistry C.
- II. Adhikari SG, Andersson GG. Exploring Alteration in Electrochemical Interface of Dye Sensitised Solar Cells-An Experimental Set-up for Ageing Investigation (in preparation)
- III. Adhikari SG, Gascooke J, Kloo L, Andersson GG. Unveiling the Ageing Effect at the Interface of N719 Dye Sensitised Solar Cells (in preparation)

Co-authored paper not included in the thesis:

- I. Shamsaldeen AA, Kloo L, Yin Y, Gibson C, Adhikari SG, Andersson GG. Influence of TiO₂ surface defects on the adsorption of N719 dye molecules. Physical Chemistry Chemical Physics. 2021;23(38):22160-73.
- II. Duong T, Nguyen T, Huang K, Pham H, Adhikari SG, Khan MR, Duan L, Liang W, Fong KC, Shen H, Bui AD. Bulk Incorporation with 4-Methylphenethylammonium Chloride for Efficient and Stable Methylammonium-Free Perovskite and Perovskite-Silicon Tandem Solar Cells. Advanced Energy Materials.:2203607.
- III. Abd Rahim I H, Lee X Y, Alotabi A S, Osborn D J, Adhikari S G, Andersson G G, Metha G F & Adnan R H. Photocatalytic H₂O₂ Production Over Photocatalysts Prepared By Phosphine-protected Au₁₀₁Nanoparticles on WO₃. Catalysis Science & Technology. (2024).

Presentations, Seminar, and Conference during the candidature:

[Poster] Adhikari S.G., Andersson G.G., Ageing in Dye Sensitised Solar Cell: An Interfacial Study, Molecular Science and Technology HDR Student Conference Nov 2021, Flinders University, Bedford Park, South Australia.

[Poster] Adhikari S.G., Andersson G.G., Interfacial study of aged dye sensitised solar cells to investigate the degradation phenomena introduced under different stress factors, 10th Australian colloid and interface symposium Feb 2021, University of South Australia, Mawson Lake, South Australia.

[Virtual Conference] 7th NANO Boston Conference (NWC Boston-2021) Oct 18-20, 2021.

[Poster and pitch my poster in 1 min] Adhikari S.G., Gascooke J.R., Andersson G.G. Anchoring Modes of N719 Dye onto Titania Substrate, 11th Annual Conference of Flinders Institute for Nanoscale Science and Technology June 2022, Flinders University, Tonsley, South Australia.

[Oral Presentation] Adhikari S.G., Gascooke J.R., Andersson G.G. Dye Anchoring Modes of Ru-based N719 dye investigated using FTIR and ARXPS, High-Resolution Depth Profiling 10 Conference 2022, Flinders University, Tonsley, South Australia.

[Oral Presentation] Adhikari S.G., Gascooke J.R., Abdulrahman Alotabi, Andersson G.G. Investigation of Anchoring Modes of N719 Dye onto Titania Substrate using ARXPS and FT-IR, Molecular Science and Technology HDR Student Conference 2022, Flinders University, Bedford, South Australia.

[Oral Presentation] Adhikari S.G., Gascooke J.R., Abdulrahman Alotabi, Andersson G.G. Investigation of Anchoring Modes of N719 Dye onto Titania Substrate using ARXPS and FT-IR, 34th Australian Colloid and Surface Science Student Conference 2023, Melbourne CBD, Melbourne, Victoria.

[Poster Presentation] Adhikari S.G., Andersson G.G. Unravelling the Secrets of Ageing in Dye Sensitised Solar Cells, 12th Annual Conference of The Flinders Institute for Nanoscale Science & Technology 2023, Flinders University, Tonsley, South Australia.

Workshops:

[Virtual] Australian Synchrotron Microscopy Workshop 2022, 31 Aug- 1 Sep 2022, 10th International Workshop on High-Resolution Depth Profiling 7th-10th Nov 2022, Flinders University, Tonsley, South Australia.

[Pre-conference Workshop] 34th Australian Colloid and Surface Science Student Conference 2023, Melbourne CBD, Melbourne, Victoria.

LIST OF FIGURES

Figure 1.1: Charge transfer kinetics in a typical DSSC during operation. The efficient electron pathways and the electron loss pathways are represented by solid and dashed arrows respectively ⁸⁻⁹ . Modified and reprinted with permission from the American Chemical Society.....	2
Figure 1.2: Diagrammatic representation of charge transfer process in DSSC (I) Photoinduced excitation, (II) electron transfer from photoexcited dye towards the semiconductor film, (III) electron transfer through the semiconductor towards the conducting electrode (IV) reduction of electrolyte redox species (V) dye regeneration by the oxidised electrolyte species (VI) radiative or non-radiative decay of photoexcited dye (VII) reduction of photoexcited dye by electrons from conduction band (E _{cb}) of the semiconductor (VIII) reduction of electrolyte species by electrons from the conduction band (E _{cb}) of the semiconductor (IX) reduction of electrolyte species from the photoexcited dye ¹⁰ . Modified and reprinted with permission from the Royal Society of Chemistry.....	3
Figure 1.3: A typical device structure of DSSCs.....	6
Figure 1.4: The unit cell of TiO ₂ crystallites (a) anatase, (b) rutile and (c) brookite ³⁶	7
Figure 1.5: The TiO ₂ -dye interface before TiCl ₄ treatment (A) and after treatment (B) ⁴¹ . Reprinted with permission from AIP Publishing.....	8
Figure 1.6: Diagrammatic illustration of complete monolayer dye coverage (A), complete multilayer dye coverage (B) and partial coverage with island formation (C).	13
Figure 1.7: The effect of cation on the open circuit voltage with a 10:1 ratio of alkali iodide and iodine in the electrolyte system ¹²² . Reprinted with permission from Elsevier.	16
Figure 1.8: Available modes for the carboxylate anchoring group to bind to metal oxide substrate ¹⁵¹	20
Figure 1.9: The illustration of H- and J-aggregates on the absorption of π -conjugated dye molecule ¹⁵⁷ . Reprinted with permission from the Royal Society of Chemistry.	21
Figure 1.10: FTIR spectra of N719 powder as well as N719 dye adsorbed on oxalic acid treated TiO ₂ (OA-TiO ₂) and without (WO-TiO ₂) in the frequency range (a) 1200-2000 cm ⁻¹ (b) 900-600 cm ⁻¹ ¹⁵⁶ . Reprinted with permission from the American Chemical Society.	23
Figure 1.11: The performance comparison of different PV technologies on (a) Sunny day and (b) Cloudy day ¹⁸⁶ . Reprinted with permission from the Royal Society of Chemistry.	30
Figure 1.12: The schematic illustration of Dye-sensitised photocatalysts for hydrogen production ¹⁸⁸	31
Figure 3.1: Typical JV characterisation curve ³ . Reprinted with permission from Elsevier.....	48
Figure 3.2: Schematic JV curve illustrating the influence of R _s	49
Figure 3.3: Schematic JV curve illustrating the influence of R _{sh}	50
Figure 3.4: The traditional circuit model for the solar cell.	50
Figure 3.5: The Schematic Diagram of the photoemission Process (A) XPS and (B) UPS (modified from ⁷).	52
Figure 3.6: Schematic diagram illustrating the working of XPS ⁹ . Reprinted with permission from Springer.....	54

Figure 3.7: Schematic illustration of the basic working principle of ARXPS and dependence of take-off angle (α) or emission angle (θ) on the information depth probe of the sample ²⁴⁻²⁵ . Reprinted with permission from the American Chemical Society.	58
Figure 3.8: The IMFP (λ) for solid as a function of applied energy for XPS and UPS photon sources ³⁰ . Reprinted with permission from John Wiley and Sons.....	61
Figure 3.9: An illustration for calculating the work function of the sample from the UP spectrum.	62
Figure 3.10: The schematic illustration of energy transfer processes in MIES 1 and 2 indicating RI and AN* occurring in solids with low work function respectively and 3.....	64
Figure 3.11: The diagrammatic representation of the NICISS experimental set-up ⁴¹ . Reprinted with permission from the American Institute of Physics	65
Figure 3.12: The schematic presentation of the NICISS principle.	66
Figure 3.13: NICIS spectra of TQ1 with the onset representing the elements present in the target system.....	67
Figure 3.14: The schema of FTIR instrumentation and operating principle (Reformatted from ⁴³)..	68
Figure 3.15: The sinusoidal current response (I) for the sinusoidal potential (E) applied in EIS.....	71
Figure 3.16: Typical Nyquist plot of DSSC with different interfacial resistance labelled, namely R1-charge transfer resistance at the CE and electrolyte interface, R2-charge transfer resistance at photoanode and R3-Nernst diffusion of I_3^- in the electrolyte.	72
Figure 3.17: The equivalent circuit diagram of the electrochemical system of DSSC.....	73
Figure 3.18: The molecular structure of N719 dye.....	74
Figure 3.19: Detailed information about the DSSC preparation applied in the study.	75
Figure 3.20: The diagrammatic representation of the cell assembly and the cell sealing used in the study.....	75
Figure 4.1: The possible anchoring modes of Ru-based dye molecule on the TiO_2 substrate via COOH acid group and NCS.	82
Figure 4.2: The FTIR spectra of formic acid (black) and formic acid adsorbed on TiO_2 (orange), the formic acid adsorbed spectrum has had the TiO_2 contribution removed. The secondary axis represents the absorbance for the formic acid adsorbed.	87
Figure 4.3: The adsorption model for adsorbate formic acid and adsorbent TiO_2	88
Figure 4.4: The ATR-FTIR spectra of phenyl isothiocyanate (PITC) liquid and PITC adsorbed on TiO_2 substrate from region $500-2500\text{ cm}^{-1}$ and from region $2500-3500\text{ cm}^{-1}$. The adsorbed PITC spectrum has the TiO_2 background subtracted.....	90
Figure 4.5: FTIR spectra of N719 powder (orange) and N719 solution adsorbed on TiO_2 substrate subtracted from blank TiO_2 (green).	91
Figure 4.6: FTIR spectrum of N719 powder (orange) and dye adsorbed onto TiO_2 (green) in high wavenumber region $2700-3200\text{ cm}^{-1}$	92
Figure 4.7: The dye anchoring model illustrating the individual anchoring modes of N719 onto the TiO_2 substrate based on the results observed from FTIR.	93
Figure 4.8: High-resolution XP spectra of N719 adsorbed onto RF-sputtered TiO_2 measured at 0° emission angle, fitted with Shirley background, representing the relative intensity of (A). C1s/Ru3d, (B). O1s, (C). Ti2p, (D). F1s, (E). S2p, and (F). N1s for dye adsorbed onto RF- sputtered TiO_2 measured at 0° emission angle.	94

- Figure 4.9: The variation in the XPS intensity of different components, namely TiO_2 (includes Ti at BE 459 eV and O1s at BE 530 eV and O-COOH at BE 533 eV), COO^-/COOH (includes C-COOH at BE 289 eV), NCS (includes NCS at BE, S-1 at BE and S-2 at BE), and rest of the dye molecule (includes a combination of Ru, CC, CN, CO, Npyd, and TBA), (solid lines) and the fitted intensity ratio (dashed lines) with the emission angles.....95
- Figure 4.10: ARXPS concentration depth profile models for N719 drop-cast on RF-sputtered TiO_2 . The left profile illustrates COO^-/COOH group is binding to the TiO_2 , and the right profile demonstrates the NCS group binding to the TiO_2 substrate. (Note: In the right profile the thickness of the NCS layer is significantly thicker than COO^-/COOH).97
- Figure 4.11: The colour comparison of freshly prepared dye and the dye after 20 consequent re-sensitising.....98
- Figure 4.12: The XPS relative intensity ratio of Ru and TBA^+ adsorbed onto the TiO_2 substrate on multiple sensitisations and the ratio of Ru/TBA^+ . The procedure for determining the relative intensities from XPS data is described in the experimental section.99
- Figure 5.1: High-resolution XP spectra of the core dye elements in 0 hrs photoanode, fitted with a Shirley background, representing the relative intensity of (A.) C1s/Ru3d, (B.) O1s, (C.) Ti2p, (D.) F1s, (E.) S2p, and (F.) N1s. Here, 0 hrs aged sample refers to the cell with electrolyte injected and stored in the dark for 24 hrs.111
- Figure 5.2: The UP (left) and MIE (right) spectra of the photoanode before and after ethanol rinsing.115
- Figure 5.3: The column chart comparing the changes in the atomic intensity of respective dye elements at 0 hrs and 600 hrs. Here, the 0 hrs sample represents the cell which was stored in the dark for 24 hrs.117
- Figure 5.4: The high-resolution XP spectra of the I element in 0 hrs photoanode fitted with Shirley background. I1 represents I, I2 represent I_3^- and I3 represents higher oxidised I species. Here, the 0 hrs sample represents the cell which was stored in the dark for 24 hrs.118
- Figure 5.5: Changes in the XPS relative intensity of the electrolyte components for 0 hrs and 600 hrs aged cells. Here, the 0 hrs sample represents the cell which was stored in the dark for 24 hrs.....119
- Figure 5.6: The UP spectra for the 0 hrs and 600 hrs aged samples and their spectral difference. The spectra difference refers to the difference of 0 hrs from 600 hrs aged photoanode.....120
- Figure 5.7: The NICISS spectra representing dye adsorbed TiO_2 (A), and aged photoanode with dye and electrolyte (B). Here, He^+ is used as the projectile.121
- Figure 5.8: NICISS spectrum of aged cell showing I and Ru peaks shaded, yellow and red respectively. Here, Ne^+ is used as the projectile.122
- Figure 6.1: The simplified equivalent circuits models for DSSCs: commonly used model (A.) and model (B.) used for 792 hr and 1008 hr light aged DSSCs.130
- Figure 6.2: The variation in the fundamental PV parameter, J_{sc} , V_{oc} , FF and efficiency, averaged for 10 samples with the error bars, for dark and light-aged samples. The yellow and black line represents the light and dark-aged samples respectively. The primary horizontal axis (black) and secondary horizontal axis (yellow) represents the ageing time for dark and light samples respectively.134
- Figure 6.3: The variation of the interfacial resistances as a function of ageing time for DSSCs, R1-charge transfer resistance at the CE, electrolyte interface R2-charge transfer resistance at the photoanode interface and R3-Nernst diffusion in the electrolyte, under dark (black) and light (yellow) ageing with the error bars.....136
- Figure 6.4: The high-resolution XP spectra of the core dye elements in 0 hrs photoanode, fitted with Shirley background, representing the relative intensity of (A.) C1s-Ru3d, (B.) O1s, (C.) Ti2p,

(D.) S2p, and (E.) N1s and (F.) I3d. Here, 0 hrs aged sample refers to the cell with electrolyte injected and stored in the dark for 24 hrs.	138
Figure 6.5: The variation in the XPS relative intensity of O1s (top) and Ti (bottom) as a function of ageing time for DSSCs under dark and light conditions.....	139
Figure 6.6: The variation in XPS relative intensity of Ru, in the photoanodes of the cells, as a function of ageing time for DSSCs under dark and light.	140
Figure 6.7: The variation in XPS relative intensity of (A.) Npyd, (B.) SCN^- and (C.) TBA^+ in the photoanodes of the cells, as a function of ageing time for DSSCs under dark and light.....	141
Figure 6.8: The variation in XPS relative intensity of Sulphur species, (A.) S1-from SCN^- , (B.) S2-oxidised S and (C.) S3-TiOS and (D.) sum of S, in the photoanodes of the cells, as a function of ageing time for DSSCs under dark and light.	142
Figure 6.9: The variation in XPS relative intensity of I species, (A.) I1-I $^-$, (B.) I2-I $^-$, (C.) higher oxidised I-species, and (D.) sum of I in the photoanodes of the cells, as a function of ageing time for DSSCs under dark and light.....	143
Figure 6.10: The Ru peak in NICIS spectra for the dark (A.) and light (B.) aged DSSCs.	144
Figure 6.11: The I peak in NICIS spectra for the dark (A.) and light (B.) aged DSSCs.	145
Figure 6.12: The UP spectra obtained after taking the spectral difference of the average of three samples in each 0 hr and 1008 hr ageing period for the dark-aged cells with the reference spectra of dye and electrolyte adsorbed on TiO_2	146
Figure 6.13: The UP spectra obtained after taking the spectral difference of the average of three samples in each 0 hr and 1008 hr ageing period for the light-aged cells with the reference spectra of dye and electrolyte adsorbed on TiO_2	147
Figure 6.14: The IR spectra for the NCS and C=O on dye adsorbed sample and dye adsorbed sample after electrolyte injection.	148
Figure 6.15: The IR spectra for the variation in the SCN^- group for dark (A.) and light-aged (B.) DSSCs.	150
Figure 6.16: The IR spectra for NCS functional group for electrolyte-free dye adsorbed onto TiO_2 , and 1008 hrs light and dark-aged sample.....	151
Figure 6.17: The UV-Vis DRS reflectance spectra of the 0 hrs aged sample and 1008 hrs aged sample under light irradiation (A.) and the wavelength at the inflection point in reflectance spectra obtained by smoothing and taking derivative of reflectance spectra (B.).	152
Figure 6.18: The variation in the inflection point in the wavelength of reflectance spectra of different sample aged in dark and light, with their respective fitting line.	153
Figure 6.19: The variation in the NCS peak position in IR spectrum and wavelength inflection point in UV-Vis DRS for light-aged sample cells with their respective fitting line (A.) and the variation in the J_{sc} for light-aged sample cells with their respective fitting line.	155
Figure 8.1 The molecular structure of high performing dyes	179
Figure 8.2: SEM image of the cross-section of 4 layered TiO_2 deposited on FTO (left) and the thickness of TiO_2 in μm as y-axis and number of layers deposited as x-axis (right).....	182
Figure 8.3: The XPS relative intensity of different elements on the dye adsorbed TiO_2 sample. The sample was successively measured with continuously X-ray exposure for 2 hrs.....	183
Figure 8.4: FTIR spectra of phenyl isothiocyanate adsorbed on TiO_2 (A.) without rinsing measured in N_2 purged environment (B.) in a vacuum without rinsing, and (C.) in N_2 purged environment with rinsing. The spectra have had the spectrum of blank TiO_2 subtracted.....	184

Figure 8.5: The IR spectrum of TBA-Br powder (blue) and 1 M TBA-Br adsorbed onto TiO ₂ substrate measured under vacuum (A.) in region 1400-1550 cm ⁻¹ and (B.) in region 2500-3200 cm ⁻¹	186
Figure 8.6: The XRD spectra of the mesoporous TiO ₂ and RF-sputtered TiO ₂ compared with the reference of Si wafer.	187
Figure 8.7: Illustration of the variation in the intensities of the elements on N719 adsorbed RF-sputtered TiO ₂ substrate to the emission angles in ARXPS. The secondary axis represents the relative atomic intensity of Ru and S.	188
Figure 8.8: The relative intensity of three Nitrogen components, Npyd, NCS, and TBA ⁺ , for the emission angle in ARXPS. The intensity of TBA ⁺ is extremely low, hence, for better data visualization TBA ⁺ is plotted against the secondary axis.	189
Figure 8.9: The XPS intensity ratio of individual dye elements with the substrate on multiple sensitised samples mentioned in the x-axis, respectively. The sample number on the x-axis indicates the number in the sequence of samples dipping into the dye solution.	192
Figure 8.10: The intensity ratio of Ru/TBA ⁺ of the dye solution drop cast onto the TiO ₂ substrate for the fresh dye (before sensitisation) and re-sensitised dye (after multiple sensitisations).	194
Figure 8.11: The CPS ⁺ sun-test equipment used for accelerated ageing in DSSCs (left) and sample loaded on the loading compartment (right).	197
Figure 8.12: The fundamental PV parameters, namely, J _{sc} , V _{oc} , FF, and efficiency for the sample cells aged in light for the mentioned time in hrs. The parameters are an average of 10 samples.	198
Figure 8.13: The UP spectra for the dye adsorbed onto TiO ₂ (blue) and electrolyte adsorbed onto TiO ₂ (orange).	202
Figure 8.14: The JV characteristics of the best-performing sample cells aged in dark (A.) and under light (B.) conditions.	203
Figure 8.15: The Nyquist plot of the samples aged in dark (top) and light (bottom) with respective aged time. The bottom right represents the Nyquist plot for two samples, 792 hr and 1008 hr, and the rest are included in the bottom right.	204
Figure 8.16: NICIS spectra for the presence of Ru on the dark (left), and light (right) aged sample through the ageing period.	206
Figure 8.17: NICIS spectra for the presence of I on the dark (left), and light (right) aged sample through the ageing period.	207
Figure 8.18: FTIR spectra of N719 solution adsorbed on TiO ₂ substrate subtracted from blank TiO ₂	207
Figure 8.19: IR spectra for different functional groups representing the adsorbed dye molecule onto TiO ₂ substrate for dye adsorbed sample and dye-electrolyte sample.	208
Figure 8.20: IR spectra for reference N719 adsorbed onto TiO ₂ and N719 adsorbed onto TiO ₂ further adsorbed into AN and AN:VN solvents. The figure on the left represents the IR for the SCN ⁻ group and the right represents the C=O at 1725 cm ⁻¹	208
Figure 8.21: The UV-Vis DRS reflectance spectra of the dye adsorbed on TiO ₂ with and without electrolyte (A) and of the first derivative to determine the inflection point of the reflectance spectra (B).	209
Figure 8.22: IR spectra for respective functional groups for dark (left) and light (right) aged samples.	210
Figure 8.23: Geometrically optimised structure of molecule (A.), referenced as N719, and molecule (B.), denoting N719 with the substitution of the SCN ⁻ ligand by I in AN.	211

Figure 8.24: The simulated UV-Vis spectrum of molecule (A.) referenced as N719, and molecule (B.), denoting N719 with the substitution of the SCN ⁻ ligand by I ⁻ in AN solvent.	212
Figure 1.1: Charge transfer kinetics in a typical DSSC during operation. The efficient electron pathways and the electron loss pathways are represented by solid and dashed arrows respectively ⁸⁻⁹ . Modified and reprinted with permission from the American Chemical Society.....	2
Figure 1.2: Diagrammatic representation of charge transfer process in DSSC (I) Photoinduced excitation, (II) electron transfer from photoexcited dye towards the semiconductor film, (III) electron transfer through the semiconductor towards the conducting electrode (IV) reduction of electrolyte redox species (V) dye regeneration by the oxidised electrolyte species (VI) radiative or non-radiative decay of photoexcited dye (VII) reduction of photoexcited dye by electrons from conduction band (E _{cb}) of the semiconductor (VIII) reduction of electrolyte species by electrons from the conduction band (E _{cb}) of the semiconductor (IX) reduction of electrolyte species from the photoexcited dye ¹⁰ . Modified and reprinted with permission from the Royal Society of Chemistry.....	3
Figure 1.3: A typical device structure of DSSCs.	6
Figure 1.4: The unit cell of TiO ₂ crystallites (a) anatase, (b) rutile and (c) brookite ³⁶	7
Figure 1.5: The TiO ₂ -dye interface before TiCl ₄ treatment (A) and after treatment (B) ⁴¹ . Reprinted with permission from AIP Publishing.....	8
Figure 1.6: Diagrammatic illustration of complete monolayer dye coverage (A), complete multilayer dye coverage (B) and partial coverage with island formation (C).	13
Figure 1.7: The effect of cation on the open circuit voltage with a 10:1 ratio of alkali iodide and iodine in the electrolyte system ¹²² . Reprinted with permission from Elsevier.	16
Figure 1.8: Available modes for the carboxylate anchoring group to bind to metal oxide substrate ¹⁵¹	20
Figure 1.9: The illustration of H- and J-aggregates on the absorption of π -conjugated dye molecule ¹⁵⁷ . Reprinted with permission from the Royal Society of Chemistry.	21
Figure 1.10: FTIR spectra of N719 powder as well as N719 dye adsorbed on oxalic acid treated TiO ₂ (OA-TiO ₂) and without (WO-TiO ₂) in the frequency range (a) 1200-2000 cm ⁻¹ (b) 900-600 cm ⁻¹ ¹⁵⁶ . Reprinted with permission from the American Chemical Society.	23
Figure 1.11: The performance comparison of different PV technologies on (a) Sunny day and (b) Cloudy day ¹⁸⁶ . Reprinted with permission from the Royal Society of Chemistry.	30
Figure 1.12: The schematic illustration of Dye-sensitised photocatalysts for hydrogen production ¹⁸⁸	31
Figure 3.1: Typical JV characterisation curve ³ . Reprinted with permission from Elsevier.....	48
Figure 3.2: Schematic JV curve illustrating the influence of R _s	49
Figure 3.3: Schematic JV curve illustrating the influence of R _{sh}	50
Figure 3.4: The traditional circuit model for the solar cell.	50
Figure 3.5: The Schematic Diagram of the photoemission Process (A) XPS and (B) UPS (modified from ⁷).	52
Figure 3.6: Schematic diagram illustrating the working of XPS ⁹ . Reprinted with permission from Springer.....	54
Figure 3.7: Schematic illustration of the basic working principle of ARXPS and dependence of take-off angle (α) or emission angle (θ) on the information depth probe of the sample ²⁴⁻²⁵ . Reprinted with permission from the American Chemical Society.	58

Figure 3.8: The IMFP (λ) for solid as a function of applied energy for XPS and UPS photon sources ³⁰ . Reprinted with permission from John Wiley and Sons.....	61
Figure 3.9: An illustration for calculating the work function of the sample from the UP spectrum.	62
Figure 3.10: The schematic illustration of energy transfer processes in MIES 1 and 2 indicating RI and AN* occurring in solids with low work function respectively and 3.....	64
Figure 3.11: The diagrammatic representation of the NICISS experimental set-up ⁴¹ . Reprinted with permission from the American Institute of Physics	65
Figure 3.12: The schematic presentation of the NICISS principle.	66
Figure 3.13: NICIS spectra of TQ1 with the onset representing the elements present in the target system.....	67
Figure 3.14: The schema of FTIR instrumentation and operating principle (Reformatted from ⁴³)..	68
Figure 3.15: The sinusoidal current response (I) for the sinusoidal potential (E) applied in EIS.....	71
Figure 3.16: Typical Nyquist plot of DSSC with different interfacial resistance labelled, namely R1-charge transfer resistance at the CE and electrolyte interface, R2-charge transfer resistance at photoanode and R3-Nernst diffusion of I_3^- in the electrolyte.	72
Figure 3.17: The equivalent circuit diagram of the electrochemical system of DSSC.....	73
Figure 3.18: The molecular structure of N719 dye.....	74
Figure 3.19: Detailed information about the DSSC preparation applied in the study.	75
Figure 3.20: The diagrammatic representation of the cell assembly and the cell sealing used in the study.....	75
Figure 4.1: The possible anchoring modes of Ru-based dye molecule on the TiO_2 substrate via COOH acid group and NCS.	82
Figure 4.2: The FTIR spectra of formic acid (black) and formic acid adsorbed on TiO_2 (orange), the formic acid adsorbed spectrum has had the TiO_2 contribution removed. The secondary axis represents the absorbance for the formic acid adsorbed.	87
Figure 4.3: The adsorption model for adsorbate formic acid and adsorbent TiO_2	88
Figure 4.4: The ATR-FTIR spectra of phenyl isothiocyanate (PITC) liquid and PITC adsorbed on TiO_2 substrate from region $500-2500\text{ cm}^{-1}$ and from region $2500-3500\text{ cm}^{-1}$. The adsorbed PITC spectrum has the TiO_2 background subtracted.....	90
Figure 4.5: FTIR spectra of N719 powder (orange) and N719 solution adsorbed on TiO_2 substrate subtracted from blank TiO_2 (green).	91
Figure 4.6: FTIR spectrum of N719 powder (orange) and dye adsorbed onto TiO_2 (green) in high wavenumber region $2700-3200\text{ cm}^{-1}$	92
Figure 4.7: The dye anchoring model illustrating the individual anchoring modes of N719 onto the TiO_2 substrate based on the results observed from FTIR.	93
Figure 4.8: High-resolution XP spectra of N719 adsorbed onto RF-sputtered TiO_2 measured at 0° emission angle, fitted with Shirley background, representing the relative intensity of (A). C1s/Ru3d, (B). O1s, (C). Ti2p, (D). F1s, (E). S2p, and (F). N1s for dye adsorbed onto RF- sputtered TiO_2 measured at 0° emission angle.....	94
Figure 4.9: The variation in the XPS intensity of different components, namely TiO_2 (includes Ti at BE 459 eV and O1s at BE 530 eV and O-COOH at BE 533 eV), COO-/COOH (includes C-COOH at BE 289 eV), NCS (includes NCS at BE, S-1 at BE and S-2 at BE), and rest of the dye molecule	

(includes a combination of Ru, CC, CN, CO, Npyd, and TBA), (solid lines) and the fitted intensity ratio (dashed lines) with the emission angles.....	95
Figure 4.10: ARXPS concentration depth profile models for N719 drop-cast on RF-sputtered TiO ₂ . The left profile illustrates COO ⁻ /COOH group is binding to the TiO ₂ , and the right profile demonstrates the NCS group binding to the TiO ₂ substrate. (Note: In the right profile the thickness of the NCS layer is significantly thicker than COO ⁻ /COOH).	97
Figure 4.11: The colour comparison of freshly prepared dye and the dye after 20 consequent re-sensitising.....	98
Figure 4.12: The XPS relative intensity ratio of Ru and TBA ⁺ adsorbed onto the TiO ₂ substrate on multiple sensitisations and the ratio of Ru/TBA ⁺ . The procedure for determining the relative intensities from XPS data is described in the experimental section.	99
Figure 5.1: High-resolution XP spectra of the core dye elements in 0 hrs photoanode, fitted with a Shirley background, representing the relative intensity of (A.) C1s/Ru3d, (B.) O1s, (C.) Ti2p, (D.) F1s, (E.) S2p, and (F.) N1s. Here, 0 hrs aged sample refers to the cell with electrolyte injected and stored in the dark for 24 hrs.	111
Figure 5.2: The UP (left) and MIE (right) spectra of the photoanode before and after ethanol rinsing.	115
Figure 5.3: The column chart comparing the changes in the atomic intensity of respective dye elements at 0 hrs and 600 hrs. Here, the 0 hrs sample represents the cell which was stored in the dark for 24 hrs.	117
Figure 5.4: The high-resolution XP spectra of the I element in 0 hrs photoanode fitted with Shirley background. I1 represents I, I2 represent I ₃ ⁻ and I3 represents higher oxidised I species. Here, the 0 hrs sample represents the cell which was stored in the dark for 24 hrs.	118
Figure 5.5: Changes in the XPS relative intensity of the electrolyte components for 0 hrs and 600 hrs aged cells. Here, the 0 hrs sample represents the cell which was stored in the dark for 24 hrs.....	119
Figure 5.6: The UP spectra for the 0 hrs and 600 hrs aged samples and their spectral difference. The spectra difference refers to the difference of 0 hrs from 600 hrs aged photoanode.....	120
Figure 5.7: The NICISS spectra representing dye adsorbed TiO ₂ (A), and aged photoanode with dye and electrolyte (B). Here, He ⁺ is used as the projectile.	121
Figure 5.8: NICISS spectrum of aged cell showing I and Ru peaks shaded, yellow and red respectively. Here, Ne ⁺ is used as the projectile.	122
Figure 6.1: The simplified equivalent circuits models for DSSCs: commonly used model (A.) and model (B.) used for 792 hr and 1008 hr light aged DSSCs.	130
Figure 6.2: The variation in the fundamental PV parameter, J _{sc} , V _{oc} , FF and efficiency, averaged for 10 samples with the error bars, for dark and light-aged samples. The yellow and black line represents the light and dark-aged samples respectively. The primary horizontal axis (black) and secondary horizontal axis (yellow) represents the ageing time for dark and light samples respectively.	134
Figure 6.3: The variation of the interfacial resistances as a function of ageing time for DSSCs, R1-charge transfer resistance at the CE, electrolyte interface R2-charge transfer resistance at the photoanode interface and R3-Nernst diffusion in the electrolyte, under dark (black) and light (yellow) ageing with the error bars.....	136
Figure 6.4: The high-resolution XP spectra of the core dye elements in 0 hrs photoanode, fitted with Shirley background, representing the relative intensity of (A.) C1s-Ru3d, (B.) O1s, (C.) Ti2p, (D.) S2p, and (E.) N1s and (F.) I3d. Here, 0 hrs aged sample refers to the cell with electrolyte injected and stored in the dark for 24 hrs.	138

Figure 6.5: The variation in the XPS relative intensity of O1s (top) and Ti (bottom) as a function of ageing time for DSSCs under dark and light conditions.....	139
Figure 6.6: The variation in XPS relative intensity of Ru, in the photoanodes of the cells, as a function of ageing time for DSSCs under dark and light.	140
Figure 6.7: The variation in XPS relative intensity of (A.) Npyd, (B.) SCN ⁻ and (C.) TBA ⁺ in the photoanodes of the cells, as a function of ageing time for DSSCs under dark and light.	141
Figure 6.8: The variation in XPS relative intensity of Sulphur species, (A.) S1-from SCN ⁻ , (B.) S2-oxidised S and (C.) S3-TiOS and (D.) sum of S, in the photoanodes of the cells, as a function of ageing time for DSSCs under dark and light.	142
Figure 6.9: The variation in XPS relative intensity of I species, (A.) I1-I ⁻ , (B.) I2-I ₃ ⁻ , (C.) higher oxidised I-species, and (D.) sum of I in the photoanodes of the cells, as a function of ageing time for DSSCs under dark and light.....	143
Figure 6.10: The Ru peak in NICIS spectra for the dark (A.) and light (B.) aged DSSCs.	144
Figure 6.11: The I peak in NICIS spectra for the dark (A.) and light (B.) aged DSSCs.	145
Figure 6.12: The UP spectra obtained after taking the spectral difference of the average of three samples in each 0 hr and 1008 hr ageing period for the dark-aged cells with the reference spectra of dye and electrolyte adsorbed on TiO ₂	146
Figure 6.13: The UP spectra obtained after taking the spectral difference of the average of three samples in each 0 hr and 1008 hr ageing period for the light-aged cells with the reference spectra of dye and electrolyte adsorbed on TiO ₂	147
Figure 6.14: The IR spectra for the NCS and C=O on dye adsorbed sample and dye adsorbed sample after electrolyte injection.	148
Figure 6.15: The IR spectra for the variation in the SCN ⁻ group for dark (A.) and light-aged (B.) DSSCs.	150
Figure 6.16: The IR spectra for NCS functional group for electrolyte-free dye adsorbed onto TiO ₂ , and 1008 hrs light and dark-aged sample.....	151
Figure 6.17: The UV-Vis DRS reflectance spectra of the 0 hrs aged sample and 1008 hrs aged sample under light irradiation (A.) and the wavelength at the inflection point in reflectance spectra obtained by smoothing and taking derivative of reflectance spectra (B.).	152
Figure 6.18: The variation in the inflection point in the wavelength of reflectance spectra of different sample aged in dark and light, with their respective fitting line.	153
Figure 6.19: The variation in the NCS peak position in IR spectrum and wavelength inflection point in UV-Vis DRS for light-aged sample cells with their respective fitting line (A.) and the variation in the J _{sc} for light-aged sample cells with their respective fitting line.....	155
Figure 8.1 The molecular structure of high performing dyes	179
Figure 8.2: SEM image of the cross-section of 4 layered TiO ₂ deposited on FTO (left) and the thickness of TiO ₂ in μm as y-axis and number of layers deposited as x-axis (right).....	182
Figure 8.3: The XPS relative intensity of different elements on the dye adsorbed TiO ₂ sample. The sample was successively measured with continuously X-ray exposure for 2 hrs.....	183
Figure 8.4: FTIR spectra of phenyl isothiocyanate adsorbed on TiO ₂ (A.) without rinsing measured in N ₂ purged environment (B.) in a vacuum without rinsing, and (C.) in N ₂ purged environment with rinsing. The spectra have had the spectrum of blank TiO ₂ subtracted.....	184
Figure 8.5: The IR spectrum of TBA-Br powder (blue) and 1 M TBA-Br adsorbed onto TiO ₂ substrate measured under vacuum (A.) in region 1400-1550 cm ⁻¹ and (B.) in region 2500-3200 cm ⁻¹	186

Figure 8.6: The XRD spectra of the mesoporous TiO ₂ and RF-sputtered TiO ₂ compared with the reference of Si wafer.	187
Figure 8.7: Illustration of the variation in the intensities of the elements on N719 adsorbed RF-sputtered TiO ₂ substrate to the emission angles in ARXPS. The secondary axis represents the relative atomic intensity of Ru and S.	188
Figure 8.8: The relative intensity of three Nitrogen components, Npyd, NCS, and TBA ⁺ , for the emission angle in ARXPS. The intensity of TBA ⁺ is extremely low, hence, for better data visualization TBA ⁺ is plotted against the secondary axis.	189
Figure 8.9: The XPS intensity ratio of individual dye elements with the substrate on multiple sensitised samples mentioned in the x-axis, respectively. The sample number on the x-axis indicates the number in the sequence of samples dipping into the dye solution.	192
Figure 8.10: The intensity ratio of Ru/TBA ⁺ of the dye solution drop cast onto the TiO ₂ substrate for the fresh dye (before sensitisation) and re-sensitised dye (after multiple sensitisations).	194
Figure 8.11: The CPS ⁺ sun-test equipment used for accelerated ageing in DSSCs (left) and sample loaded on the loading compartment (right).	197
Figure 8.12: The fundamental PV parameters, namely, J _{sc} , V _{oc} , FF, and efficiency for the sample cells aged in light for the mentioned time in hrs. The parameters are an average of 10 samples.	198
Figure 8.13: The UP spectra for the dye adsorbed onto TiO ₂ (blue) and electrolyte adsorbed onto TiO ₂ (orange).	202
Figure 8.14: The JV characteristics of the best-performing sample cells aged in dark (A.) and under light (B.) conditions.	203
Figure 8.15: The Nyquist plot of the samples aged in dark (top) and light (bottom) with respective aged time. The bottom right represents the Nyquist plot for two samples, 792 hr and 1008 hr, and the rest are included in the bottom right.	204
Figure 8.16: NICIS spectra for the presence of Ru on the dark (left), and light (right) aged sample through the ageing period.	206
Figure 8.17: NICIS spectra for the presence of I on the dark (left), and light (right) aged sample through the ageing period.	207
Figure 8.18: FTIR spectra of N719 solution adsorbed on TiO ₂ substrate subtracted from blank TiO ₂	207
Figure 8.19: IR spectra for different functional groups representing the adsorbed dye molecule onto TiO ₂ substrate for dye adsorbed sample and dye-electrolyte sample.	208
Figure 8.20: IR spectra for reference N719 adsorbed onto TiO ₂ and N719 adsorbed onto TiO ₂ further adsorbed into AN and AN:VN solvents. The figure on the left represents the IR for the SCN ⁻ group and the right represents the C=O at 1725 cm ⁻¹	208
Figure 8.21: The UV-Vis DRS reflectance spectra of the dye adsorbed on TiO ₂ with and without electrolyte (A) and of the first derivative to determine the inflection point of the reflectance spectra (B).	209
Figure 8.22: IR spectra for respective functional groups for dark (left) and light (right) aged samples.	210
Figure 8.23: Geometrically optimised structure of molecule (A.), referenced as N719, and molecule (B.), denoting N719 with the substitution of the SCN ⁻ ligand by I ⁻ in AN.	211
Figure 8.24: The simulated UV-Vis spectrum of molecule (A.) referenced as N719, and molecule (B.), denoting N719 with the substitution of the SCN ⁻ ligand by I ⁻ in AN solvent.	212

LIST OF TABLES

Table 1.1: The PV parameter of dyes with different cations present in the molecule adapted from ⁷² . Reprinted with permission from John Wiley and Sons.....	11
Table 1.2: The PV parameter of C-based graphene and conducting polymer PANI and their composite ¹³⁷ . Reprinted with permission from Elsevier.	18
Table 1.3: The PV parameter of CoPt alloy with performance parameter high compared to standard Pt-based electrode ¹⁴² . Reprinted with permission from the American Chemical Society.	19
Table 1.5: The list of equipment used in investigating dye anchoring modes with their criteria of measurement ¹⁶¹	24
Table 3.1: Enlisting different techniques applied in the study with their probing depth, the information extracted and the resolution.	46
Table 3.2: The ASF of different elements investigated in the study using an X-ray source at an angle of 54.7° relative to the analyser ¹⁶ . Reprinted with permission from John Wiley and Sons.....	56
Table 4.1: Vibrational mode assignments of adsorbed species for formic acid observed in the adsorption onto the TiO ₂ substrate using ATR-FTIR.	87
Table 4.2: The IR modes of N719 powder and the adsorbed dye on TiO ₂ substrate with the peak assignment.....	91
Table 5.1: The elemental peak positions of the elements in the adsorbed dye on the TiO ₂ substrate before and after ethanol rinsing. The peak position is an average of the four samples investigated and the error is the instrumental error.	112
Table 5.2: The elemental ratios (atomic percentage) of elements representing adsorbed dye on TiO ₂ substrate before and after ethanol rinsing. The elemental ratio is an average of four samples.	112
Table 5.3: The elemental ratios of the elements after XPS analysis of rinsed-off solution drop cast onto PPT-5 layered TiO ₂ substrate. Here, N1 represents a combination of Npyd from the dye molecule and N atoms from molecularly adsorbed N-species; N-2 represents NCS and substitutional N in the oxide lattice of TiO ₂	113
Table 6.1: The IR modes of N719 adsorbed on TiO ₂ substrate with the peak assignment.....	148
Table 8.1: The record-keeping cell configuration with the components. The section for photoanode is non-included because TiO ₂ is the substrate used for dye-adsorption in the listed configuration.	166
Table 8.2: The IR spectrum assignments for liquid phenyl isothiocyanate and the adsorbed phenyl isothiocyanate on a TiO ₂ substrate.....	185
Table 8.3: The elemental ratios of the elements of the 1 st , 5 th , 10 th , 15 th , and 20 th samples respectively re-sensitised in order.....	190
Table 8.4: The elemental peak positions of the 1st, 5th, 10th, 15th, and 20th samples respectively re-sensitised in order.	191
Table 8.5: The elemental ratios of fresh dye and the re-sensitised dye solutions drop-cast on TiO ₂ substrate and analysed with XPS.	193
Table 8.6: The change in the elemental composition of the dye-titania substrate measured before and after ethanol rinsing. The reading displays an average of four photoanodes with the standard error calculated.....	196

Table 8.7: The change in the elemental composition of the TiO ₂ substrate measured before and after ethanol rinsing. The reading displays an average of three photoanodes with the standard error calculated.	197
Table 8.8: The summary of PV performance of the cell aged under light. Average values and standard deviations of 10 cells along with the parameters of the best cells are highlighted in bold.	198
Table 8.9: The change in the elemental composition of the dye-TiO ₂ -electrolyte interface measured for 0 hrs and 600 hrs aged photoanode in light. The reading displays an average of three photoanodes with the standard error calculated.	199
Table 8.10: The peak position in eV for different elemental species of the dye-TiO ₂ -electrolyte interface measured for 0 hrs and 600 hrs aged photoanodes in light. The reading displays an average of three photoanodes with uncertainty of ± 0.2	200
Table 8.11: The elemental ratio obtained from XPS analysis of drop-cast substrates after rinsing off the aged cells. The drop-cast samples were prepared by drop-casting the rinsed-off solution onto a blank TiO ₂ substrate.	201
Table 8.12: The change in the elemental composition of the dye-TiO ₂ -electrolyte interface measured for different aged photoanode samples in the dark. The reading displays an average of three photoanodes with the standard error calculated.	205
Table 8.13: The change in the elemental composition of the dye-TiO ₂ -electrolyte interface measured for different aged photoanode samples in light. The reading displays an average of three photoanodes with the standard error calculated.	206
Table 1.1: The PV parameter of dyes with different cations present in the molecule adapted from ⁷² . Reprinted with permission from John Wiley and Sons.	11
Table 1.2: The PV parameter of C-based graphene and conducting polymer PANI and their composite ¹³⁷ . Reprinted with permission from Elsevier.	18
Table 1.3: The PV parameter of CoPt alloy with performance parameter high compared to standard Pt-based electrode ¹⁴² . Reprinted with permission from the American Chemical Society.	19
Table 1.5: The list of equipment used in investigating dye anchoring modes with their criteria of measurement ¹⁶¹	24
Table 3.1: Enlisting different techniques applied in the study with their probing depth, the information extracted and the resolution.	46
Table 3.2: The ASF of different elements investigated in the study using an X-ray source at an angle of 54.7° relative to the analyser ¹⁶ . Reprinted with permission from John Wiley and Sons.	56
Table 4.1: Vibrational mode assignments of adsorbed species for formic acid observed in the adsorption onto the TiO ₂ substrate using ATR-FTIR.	87
Table 4.2: The IR modes of N719 powder and the adsorbed dye on TiO ₂ substrate with the peak assignment.	91
Table 5.1: The elemental peak positions of the elements in the adsorbed dye on the TiO ₂ substrate before and after ethanol rinsing. The peak position is an average of the four samples investigated and the error is the instrumental error.	112
Table 5.2: The elemental ratios (atomic percentage) of elements representing adsorbed dye on TiO ₂ substrate before and after ethanol rinsing. The elemental ratio is an average of four samples.	112
Table 5.3: The elemental ratios of the elements after XPS analysis of rinsed-off solution drop cast onto PPT-5 layered TiO ₂ substrate. Here, N1 represents a combination of Npyd from the dye	

molecule and N atoms from molecularly adsorbed N-species; N-2 represents NCS and substitutional N in the oxide lattice of TiO ₂ .	113
Table 6.1: The IR modes of N719 adsorbed on TiO ₂ substrate with the peak assignment.	148
Table 8.1: The record-keeping cell configuration with the components. The section for photoanode is non-included because TiO ₂ is the substrate used for dye-adsorption in the listed configuration.	166
Table 8.2: The IR spectrum assignments for liquid phenyl isothiocyanate and the adsorbed phenyl isothiocyanate on a TiO ₂ substrate.	185
Table 8.3: The elemental ratios of the elements of the 1 st , 5 th , 10 th , 15 th , and 20 th samples respectively re-sensitised in order.	190
Table 8.4: The elemental peak positions of the 1st, 5th, 10th, 15th, and 20th samples respectively re-sensitised in order.	191
Table 8.5: The elemental ratios of fresh dye and the re-sensitised dye solutions drop-cast on TiO ₂ substrate and analysed with XPS.	193
Table 8.6: The change in the elemental composition of the dye-titania substrate measured before and after ethanol rinsing. The reading displays an average of four photoanodes with the standard error calculated.	196
Table 8.7: The change in the elemental composition of the TiO ₂ substrate measured before and after ethanol rinsing. The reading displays an average of three photoanodes with the standard error calculated.	197
Table 8.8: The summary of PV performance of the cell aged under light. Average values and standard deviations of 10 cells along with the parameters of the best cells are highlighted in bold.	198
Table 8.9: The change in the elemental composition of the dye-TiO ₂ -electrolyte interface measured for 0 hrs and 600 hrs aged photoanode in light. The reading displays an average of three photoanodes with the standard error calculated.	199
Table 8.10: The peak position in eV for different elemental species of the dye-TiO ₂ -electrolyte interface measured for 0 hrs and 600 hrs aged photoanodes in light. The reading displays an average of three photoanodes with uncertainty of ± 0.2 .	200
Table 8.11: The elemental ratio obtained from XPS analysis of drop-cast substrates after rinsing off the aged cells. The drop-cast samples were prepared by drop-casting the rinsed-off solution onto a blank TiO ₂ substrate.	201
Table 8.12: The change in the elemental composition of the dye-TiO ₂ -electrolyte interface measured for different aged photoanode samples in the dark. The reading displays an average of three photoanodes with the standard error calculated.	205
Table 8.13: The change in the elemental composition of the dye-TiO ₂ -electrolyte interface measured for different aged photoanode samples in light. The reading displays an average of three photoanodes with the standard error calculated.	206

ABBREVIATIONS

Acronym	What (it) Stands For
A	
AD	Auger De-excitation
AMU	Atomic mass unit
AN	Acetonitrile
AN*	Auger Neutralization
ARXPS	Angle-resolved X-ray Photoelectron Spectroscopy
ASF	Atomic Sensitivity Factor
ATR-FTIR	Attenuated Total Reflectance- Fourier Transform Infrared
B	
BE	Binding Energy
C	
CB	Conduction Band
CE	Counter Electrode
CNT	Carbon Nanotube
D	
DFT	Density Functional Theory
DOS	Density of states
DRS	Diffuse Reflectance Spectroscopy
DSSC	Dye Sensitised Solar Cells
E	
EIS	Electrochemical Impedance Spectroscopy
ESCA	Electron Spectroscopy for Chemical Analysis
EXAFS	Extended X-ray Absorption Fine Structure Spectroscopy

F

FF	Fill factor
FTIR	Fourier Transform Infrared
FTO	Fluorine doped tin-oxide

G

GuNCS	Guanidinium thiocyanate
-------	-------------------------

H

HOMO	Highest Occupied Molecular Orbital
------	------------------------------------

I

IEC	International Electrotechnical Commission
IMFP	Inelastic mean-free path
IoT	Internet-of-things
IR	Infrared Region
ITO	Indium doped tin-oxide

J

Jsc	Short circuit current
-----	-----------------------

K

KE	Kinetic Energy
----	----------------

L

LUMO	Least Unoccupied Molecular Orbital
------	------------------------------------

M

MIES	Metastable Induced Electron Spectroscopy
MLCT	Metal ligand charge transfer

N

NICISS	Neutral Impact Collision Ion Scattering Spectroscopy
NIR	Near Infrared Region
NMBI	N-methylbenzimidazole

N3	Cis-bis(isothiocyanato) bis(2,2'-bipyridyl-4,4'-dicarboxylato) ruthenium (II)
N719	Di-tetrabutylammonium cis-bis(isothiocyanato) bis((2,2'-bipyridyl-4,4'-dicarboxylato) ruthenium (II)
O	
OPD	Optical Path Difference
P	
PANI	Polyaniline
PES	Photoelectron Spectroscopy
Pin	Incident Power
PITC	Phenyl isothiocyanate
PPT	Pre and post-treated
PV	Photovoltaic
R	
RF	Radio frequency
RI	Resonance Ionisation
RRS	Raman Resonance Spectroscopy
Rs	Series Resistance
Rsh	Shunt Resistance
S	
SEM	Scanning Electron Microscopy
STC	Standard Test Conditions
T	
TBA	Tetrabutylammonium
TBA-Br	Tetrabutylammonium Bromide
TBP	4-tert Butylpyridine
TCO	Transparent conductive oxide
TD-DFT	Time-dependent density functional theory
TOF	Time of flight
TRRS	Time-resolved Raman Spectroscopy

U

UHV	Ultra-high vacuum
UPS	Ultraviolet Photoelectron Spectroscopy
UV	Ultraviolet

V

Voc	Open circuit voltage
VN	Valeronitrile

X

XAS	X-ray Absorption Spectrometry
XPS	X-ray Photoelectron Spectroscopy
XRD	X-ray Diffraction

Z

Z907	Cis-bis(isothiocyanato) (2,2'-bipyridyl-4,4'-dicarboxylato) (4,4'-di-nonyl-2'-bipyridyl) ruthenium (II)
------	---

CHAPTER 1 DYE SENSITISED SOLAR CELLS- AN OVERVIEW

1.1 Introduction

Dye-sensitised solar cells (DSSCs) are featured as a cost-effective, flexible, stable, eco-friendly substitute for traditional silicon cells and have indeed attracted a lot of scientific and technological interest since the breakthrough in 1991¹. After intensive research for more than two decades, the highest efficiency recorded is 14.3%² which was broken recently achieving 15.2%³. Unlike other photovoltaic (PV) cells, the performance of DSSCs is not limited to one component but divided among the components, a porous wide-gap semiconductor photoanode, a sensitising dye, and a redox electrolyte. Hence, the use of medium to low purity of materials can still achieve reasonable efficiency⁴. In addition, the DSSCs have shown promising outcomes on repeated electric erasure and re-sensitisation of cell components with 90.98% efficiency even after being recycled six times, thus minimising the cost and waste promoting reuse and reduction⁵. DSSCs, with the capability to use high energy photons and to operate under low light conditions, meet the two essential requirements of the multijunction solar cell. Unlike, other solar technologies, the energy region in DSSCs can be easily tuned using varied chromophore designs with molecular-level control⁶. Further, the DSSCs components can be tuned to obtain desirable absorption width, varied thickness of the active layer and chromophore adsorption, to calibrate output photocurrents for minimal thermal loss. This state-of-the-art can be combined with any other technology that uses lower energy photons to develop a high-performing multijunction system⁶. Due to their ability to operate indoors, under low light conditions, these cells are successful candidates in wearables like caps, bags, bag packs, military tents, and other internet-of-things (IoTs). To compete in the existing solar market these cells need to excel in efficiency and stability. DSSCs are vulnerable to many degradations introduced in different components used in their configuration under various stress factors. Heat and/or light have always harmed the cell's performance with time.

1.2. Operation of DSSCs

The basic operation of DSSC is based on photoexcitation of the sensitizer molecule which injects electrons into the semiconductor film and leads towards the external circuit⁷. The operation of the DSSC significantly depends on the relative kinetics of different charge transfer processes occurring in the cell. Thus, it is very crucial to understand the electronic processes

taking place at the photoanodes together with the dynamics of charge transport and charge separation at the interface. The charge transfer phenomena occur from the excited dye to the semiconductor layer of TiO_2 nanoparticles, from the electrolyte to the dye layer and from TiO_2 to the charge collectors, Figure 1.1.

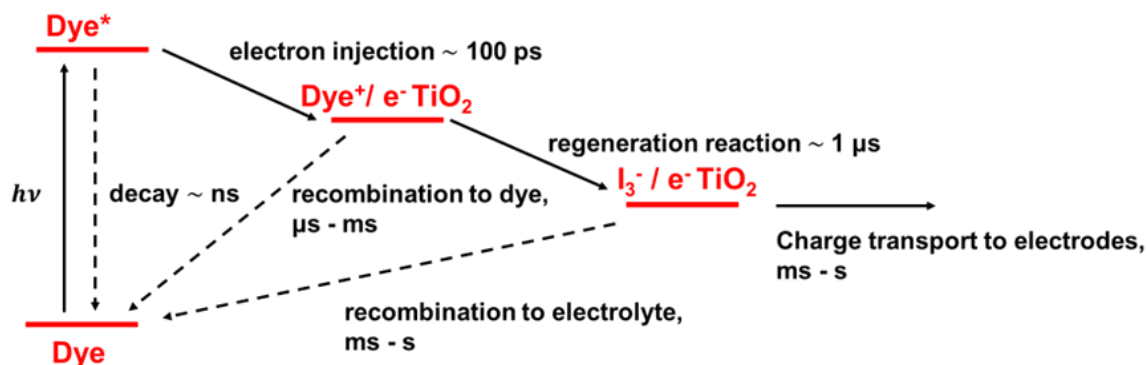


Figure 1.1: Charge transfer kinetics in a typical DSSC during operation. The efficient electron pathways and the electron loss pathways are represented by solid and dashed arrows respectively ⁸⁻⁹. Modified and reprinted with permission from the American Chemical Society.

The charge transfer kinetics of DSSCs, diagrammatical illustrated in Figure 1.2 can be distinguished into the following processes:

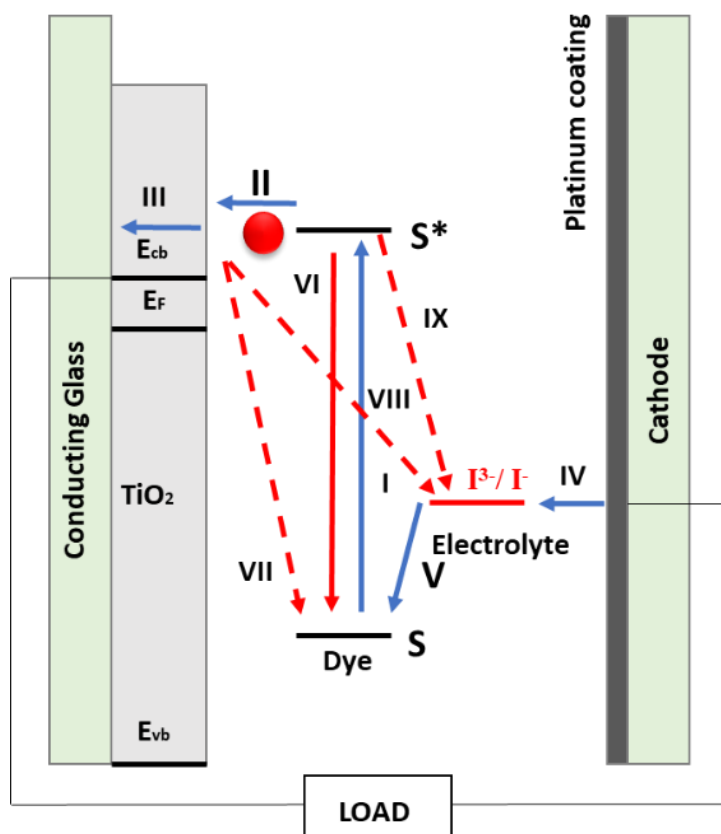


Figure 1.2: Diagrammatic representation of charge transfer process in DSSC (I) Photoinduced excitation, (II) electron transfer from photoexcited dye towards the semiconductor film, (III) electron transfer through the semiconductor towards the conducting electrode (IV) reduction of electrolyte redox species (V) dye regeneration by the oxidised electrolyte species (VI) radiative or non-radiative decay of photoexcited dye (VII) reduction of photoexcited dye by electrons from conduction band (E_{cb}) of the semiconductor (VIII) reduction of electrolyte species by electrons from the conduction band (E_{cb}) of the semiconductor (IX) reduction of electrolyte species from the photoexcited dye ¹⁰. Modified and reprinted with permission from the Royal Society of Chemistry.

1.2.1. Photon absorption and excitation

The dye molecule adsorbed on the semiconductor substrate on photon absorption gets excited from the highest occupied molecular (HOMO) level (S) to an excited (S^*), least unoccupied molecular orbital (LUMO) level, refer to Figure 1.2 (I) for the charge transfer and Equation 1.1 for the reaction.



Equation 1.1

The dye or chromophore acts as a light harvester and upon photo exposure, the dye molecule excites from its ground state which further decomposes into a dye cation and an electron. The phenomenon of electron injection from the excited dye molecule to the mesoporous TiO₂ depends on many factors. One of the factors is the magnitude of electron injection relative to the decay rate of the excited dye molecule to the ground state. High stability in the oxidised state and long-lived excited state is advantageous and increases the rate of electron injection¹¹⁻¹². The typical rate of decay of dye molecules can range from picoseconds to nanoseconds (see Figure 1.1).

1.2.2. Interfacial charge transfer

The electron is ejected from the excited dye molecule into the conduction band (CB) of the semiconductor see Figure 1.2 (II) for the charge transfer and Equation 1.2 for the respective reaction.



The electron injection is further influenced by electron coupling between the LUMO orbital of the dye molecule and energetically accessible band states in the mesoporous TiO₂ and the number density of these states near the dye molecule. The electron injection rate for typical dye is reported as less than $1 \times 10^{12} \text{ s}^{-1}$ ¹³. Furthermore, the electron injection depends upon the energy of TiO₂ CB relative to the oxidation potential of the excited dye molecule which is further dependent on the concentration of excessive ions that determines the potential of the electrolyte⁸.

1.2.3. Electron transport

The electron is then transferred through the semiconductor by a series of trapping and de-trapping shown in Figure 1.2 (III). Meanwhile, some of the electrons are lost to lower energy states by radiative or non-radiative processes like photon relaxation illustrated in Figure 1.2 (VI) and Equation 1.3.



Effective charge collection demands a faster time constant for electron transport to the collection electrode than the charge recombination on the injected electrons with the redox. The electron transport through the mesoporous TiO₂ occurs via a series of trapping and de-trapping in localised sub-bandgap states, which is dependent on the position of the Fermi level of the TiO₂ layer. The charge separation and charge collection kinetics are highly affected by the

energy losses involved during the cell functionalisation which significantly decreases the V_{oc} ¹⁴.

1.2.4. Electrolyte-to-dye electron transfer or Dye Regeneration

Electrons from the redox mediator continuously reduce the oxidised dye molecule. The iodide ions are oxidised to give elementary iodine and an electron (see Equation 1.4).



The oxidised dye molecule accepts the electron to regenerate the dye at the ground state shown in Figure 1.2 (V) and Equation 1.5.



At that instance, the redox mediator diffuses towards the counter electrode (CE) where it gets reduced as shown in Figure 1.2 (IV) and Equation 1.6.

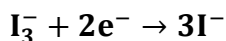


As the phenomenon of electron loss, the electrolyte species gets reduced by the photoexcited dye see Figure 1.2 (IX).

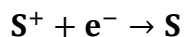
Systematic dye regeneration demands the rate of re-reduction of dye cation by redox to be higher than the charge recombination of the injected electrons with these dye cations. Here, the rate recombination reaction depends on the electron density in the semiconductor layer, which is further affected by the spatial separation of the dye cation (HOMO) orbital from the semiconductor layer. The regeneration reaction is directly influenced by the dye-electrolyte system, like the concentration of iodine, the viscosity of the electrolyte and the dye structure. The rate of regeneration for N719 and I^-/I_3^- electrolyte system in AN solvent is determined as equivalent to $1 \mu s$ ¹⁴, which is fast enough to compete for the recombination reaction ensuring the effective regeneration to happen.

1.2.5. Electron loss

The electron in the CB of the semiconductor may either get back transferred and captured by oxidised species of electrolyte or dye molecule as shown in Figure 1.2 (VIII) (see Equation 1.7) and Figure 1.2 (VII) (see Equation 1.8) respectively.



Equation 1.7



Equation 1.8

1.3. DSSC Components

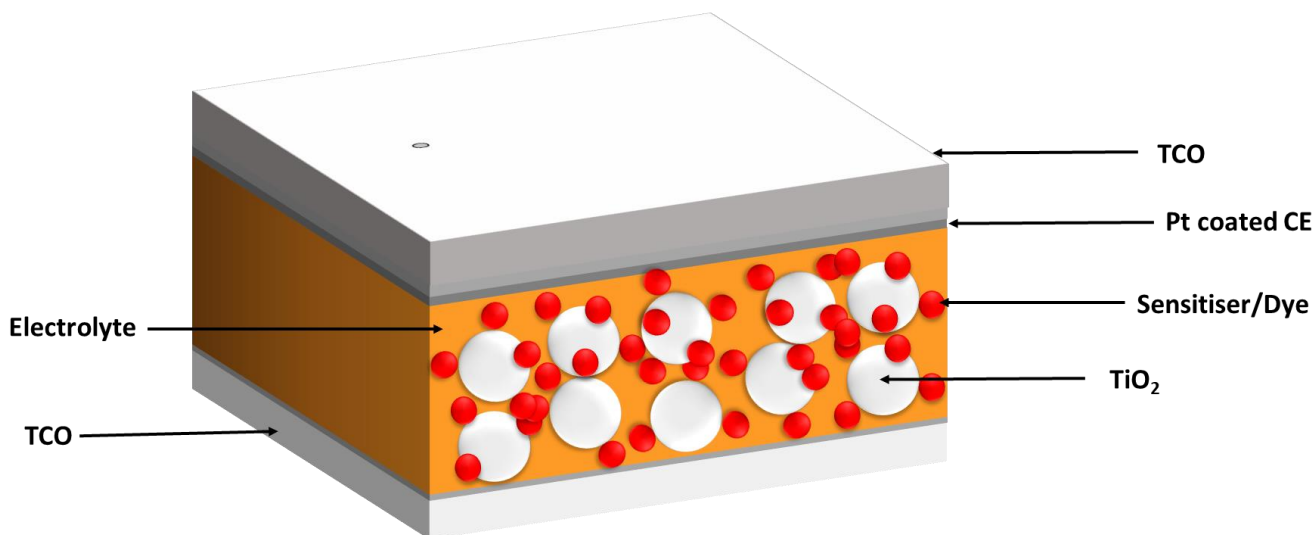


Figure 1.3: A typical device structure of DSSCs.

The dye solar cell comprises five main components: namely, a transparent conductive substrate, a semiconductor film, a sensitizer, a redox electrolyte, and a CE. The schematic diagram of a typical DSSC is shown in Figure 1.3. There is a lot of research done to enhance cell performance and improve cell stability either by introducing an entirely new component or altering the physical or chemical properties of the used components. Some of the techniques applied are listed below:

1.3.1. Photoanodes

The transparent conductive oxide glass is taken as electrodes, especially the indium-tin oxide (ITO) and fluorine-tin oxide (FTO) are the short-listed candidate. The nature of transparent conducting oxide (TCO) glass and the resistivity offered also influences the cell performance. When investigated with similar cell conditions the use of FTO was favoured due to smaller losses as the thermal treatment soared the resistivity in the ITO whereas for the FTO it remained almost unchanged¹⁵⁻¹⁶. Many plastic substrates are gaining attention with the outlook of rendering features like flexibility, light weight, and mass production but still need further improvements especially due to their low melting point¹⁷.

Metal oxides deposited on the transparent oxide-coated glass substrate are the photoanodes for the DSSCs. The photoanode plays a dual role; as a substrate for dye and electrolyte and, as a

charge-transferring medium by accepting and transporting electrons from the adsorbed dye molecule¹. The charge transfer in the TiO₂ mainly occurs through the process of electron trapping de-trapping and diffusion¹⁸. With the development of DSSCs, different materials have been tested as a replacement for TiO₂ photoanode. Metal oxides like ZnO¹⁹⁻²⁰, Nb₂O₅²¹⁻²², Al₂O₃²³⁻²⁴, SnO²⁵⁻²⁶, Fe₂O₃²⁷⁻²⁸, ZrO₂²⁹⁻³⁰ or ternary compounds SrTiO₃³¹, Zn₂SnO₄³²⁻³³ or doped TiO₂³⁴ are tested as photoanodes for DSSCs. The use of semiconducting metal oxide is not limited to DSSCs. They are also a popular candidate as photo-electrode in photoelectrochemical cells for water splitting, n-based and p-based semiconductors as photoanode and photocathode respectively³⁵.

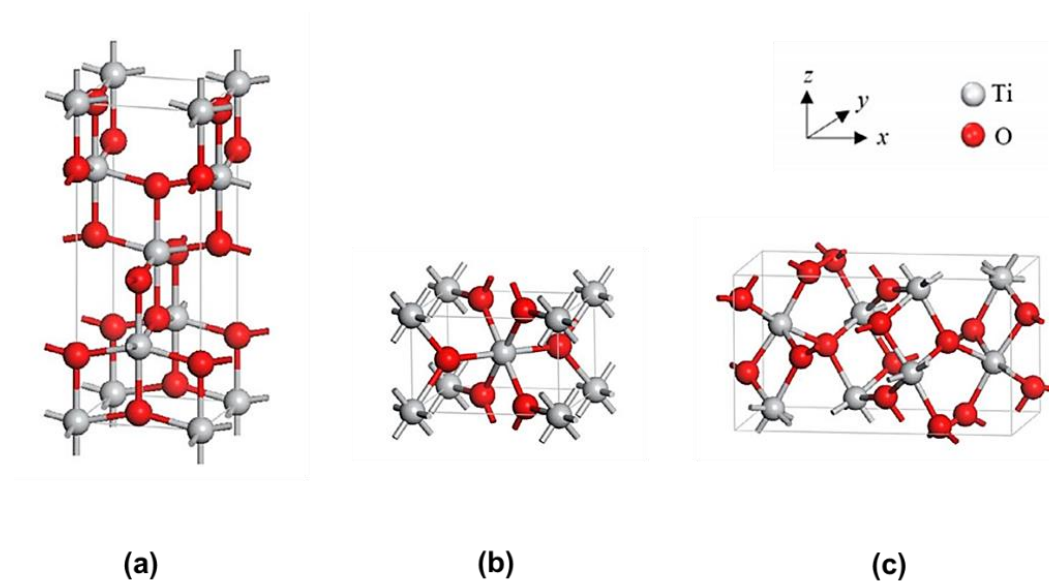


Figure 1.4: The unit cell of TiO₂ crystallites (a) anatase, (b) rutile and (c) brookite³⁶.

TiO₂ is by far the most used photoanode for DSSCs because of its stability, easy availability, less toxicity, low cost, bio-compatibility, and favourable energetics³⁷. For different types of electrolytes being used, only stainless steel and TiO₂ have been proven to be chemically stable with the traditionally used corrosive iodine electrolyte³⁸. There are three polymorphs of TiO₂ namely, anatase, rutile and brookite (see Figure 1.4). The use of mesoporous TiO₂ especially of anatase crystalline structure for soaking the sensitizer is expected to enhance the performance of the cell due to its larger band gap in comparison to the rutile phase. In addition, the faster electron transport in the anatase layer due to inter-particle connectivity of densely packed particles results in improved photocurrent³⁹. Brookite is not an alternative in DSSCs application due to the complexity of its preparation⁴⁰.

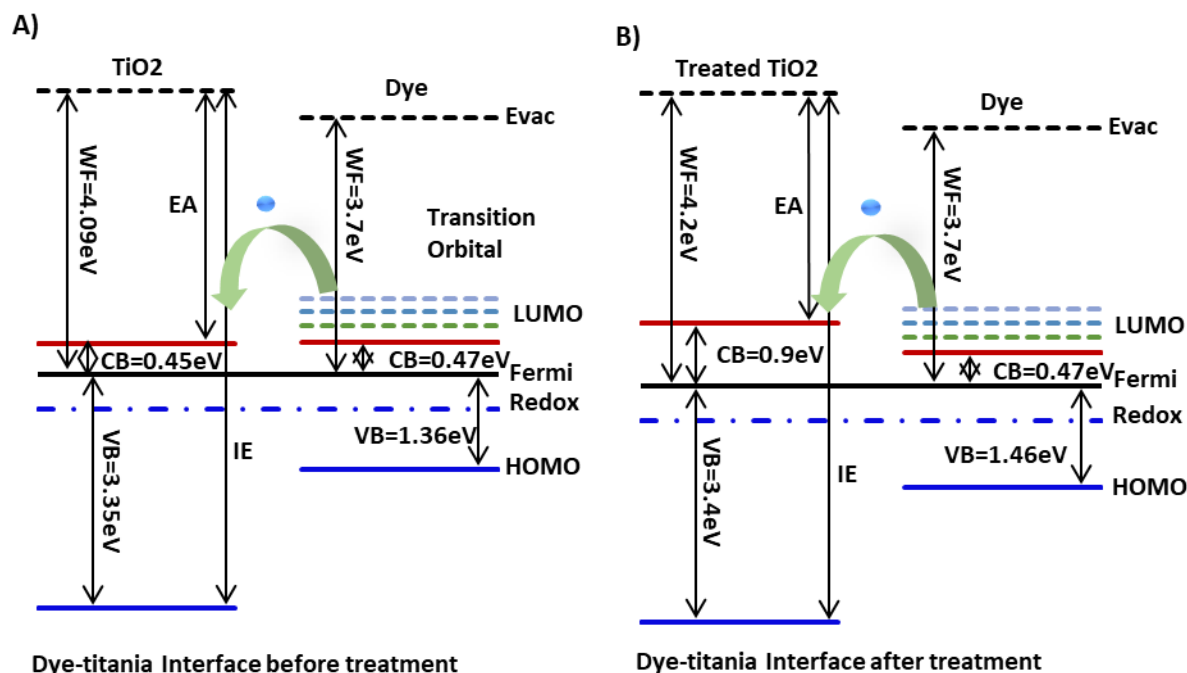


Figure 1.5: The TiO_2 -dye interface before TiCl_4 treatment (A) and after treatment (B) ⁴¹. Reprinted with permission from AIP Publishing.

To further improve the functionalities of TiO_2 substrate different techniques are used to elevate the overall cell performance which includes the construction of nano-architecture like nanoparticles, nanotubes, and nanorods just to name a few, different treatments- TiCl_4 treatment ⁴¹, heating treatments ⁴², acidic treatments ⁴³, interfacial engineering, doping, light scattering layer ⁴⁴ and composites which are better described in the review by Fan et al ⁴⁵. Figure 1.5 illustrates the effect of TiCl_4 treatment in shifting the CB of the TiO_2 and hence reducing the recombination consequently improving the cell performance. The factors affecting dye performance due to the TiO_2 substrate are mentioned below:

1.1.1.1 Morphology

The increase in net surface area of the TiO_2 deposited on FTO increases the dye loading subsequently enhancing the J_{sc} ⁴⁶. The increased surface area as an outcome of the formation of surface structure results in promoting surface defects thus, developing the trap sites ⁴⁷ which adversely affects the cell performance. In addition, for a given porosity and pore size, the increment in thickness of the deposited TiO_2 film leads to improved J_{sc} value owing to an increase in internal surface area with enhanced dye adsorption ⁴⁷⁻⁴⁸. However, a further increase in TiO_2 thickness increases the distance to the back contact, thus elevating the chances of recombination ⁴. Likewise, with certain resistance of TiO_2 that increases with thickness, results in an increase in the electron path length, which ultimately improves the dye absorbance ⁴⁹.

Similarly, the cross-section also influences dye adsorption. On one hand, a cross-section smaller than the area occupied by the sensitizer is unable to adsorb incident light and therefore limits the photo injection. On the other hand, multi-layer deposition of dye does not promote absorption, thus, TiO_2 with a larger surface area enhances light absorption and improved performance⁴. Different treatments of TiO_2 result in a decrease in porosity with an increase in the surface area of TiO_2 consequently increasing the average particle diameter⁵⁰⁻⁵¹. Nevertheless, a further decrease in porosity provides limited space for dye adsorption as well as limits the diffusion kinetics in the electrolyte⁴⁷. Additionally, the crystallinity affects the cell performance, the presence of rutile type TiO_2 leads to stronger scattering than anatase type owing to the higher refractive index of rutile⁴⁶.

1.1.1.2 Electronic Structure and Trap State

The electronic structure and trap state distribution influence the electron transport and the recombination reaction in DSSCs, and therefore different techniques of surface modification of the deposited TiO_2 layer are employed which include adding a layer of metal oxide on TiO_2 substrate or doping TiO_2 with certain metal. The purpose of these surface modifications is upward shifting in the CB edge⁴¹ and decreasing the surface trap states to hinder the electron recombination at the interface by suppressing the dark current and the recombination reaction sites and enhancing the V_{oc} ⁵¹⁻⁵². The surface trap states can be reduced by modification of the TiO_2 surface however, it is difficult to get rid of the bulk trap state which is responsible for the decreased cell performance of DSSCs for the treated photoanodes as the electrons in bulk traps exchange electrons in the CB and participate in recombination through the surface trap state⁴⁷. Thereupon, it is important to passivate the trap states from bulk and surface during the preparation of the photoanode⁵².

1.3.2. Sensitizer

DSSCs also known as excitonic solar cells are based on dye adsorbed on a photoanode substrate. The dye adsorbs on the substrate via chemisorption and physisorption⁵³. Physisorption is a weak interaction between the adsorbent and the adsorbate via van der Waals forces and hence chemisorption, being stronger interaction, is preferred⁵⁴. The dye or sensitizer acts as a light harvester. The charge separation takes place at the semiconductor-dye interface. Therefore, the optimisation of spectral properties can be done through the modification of the dye alone⁵⁵. Since 1991, different types of dyes have been synthesised and used as a chromophore to enhance PV performance and make DSSCs commercially viable.

The general properties an efficient dye possesses are:

- a. An extended absorption ranging from the whole visible region to IR or NIR region with a molar extinction coefficient high enough to enable efficient light harvesting with a thinner semiconductor layer ⁵⁶.
- b. The LUMO is localised near the anchoring group and above the CB of the semiconductor electrode for efficient electron ejection ⁵⁷.
- c. The HOMO is located below the redox potential of the electrolyte to promote efficient dye regeneration ⁵⁸.
- d. The donor, as the site for the localisation of positive charge resulting after electron ejection from the dye must be located far from the semiconductor surface to avoid recombination of injected electrons with the oxidised dye ⁵⁹.
- e. The hydrophobic periphery of the dye minimizes the contact of the dye with the electrolyte. Consequently, prevents water-induced dye desorption and increases stability ⁵⁸.
- f. The dye should not aggregate to avoid the non-radiative decay of the dye ⁶⁰.

Based on research interest and sensitizer synthesis, the dyes can be classified into the following broad classes; 1. Organo-metallic dyes especially, Ru-based dyes and porphyrin dyes 2. Metal-free Organic dye, and 3. Natural dyes.

Ru complexes are gaining interest basically due to their favourable photoelectrochemical properties, high stability in the oxidised state, long-lived excited state, and metal-ligand charge transfer (MLCT) in the visible region ¹. Many different types of Ru-based sensitizers have been synthesised and used in DSSCs. From the original prototype N3, many other dyes such as N719, Z907 and black dye with different ligands were made. The change in the type of ancillary ligands can influence the PV performance of the DSSCs ⁵⁷. The introduction of hydrophobic ligand to the Ru complexes decreases the chances of dye desorption due to the traces of water and thereupon, the amphiphilic heteroleptic Ru-complex Z907 was seen stable under light soaking test at 55-60 °C for 25000 hrs ⁶¹. The substitution of bipyridyl ligand with alkyl-thiophene or carbazole tuned the HOMO-LUMO level to extend the absorption spectrum of the dye ⁶²⁻⁶³. The use of a cyclodextrin unit attached to an ancillary ligand was found to improve the dye regeneration in iodide, and tri-iodide redox ⁶⁴. Additionally, the use of thiocyanate ligand and triarylamine donor group improved the excited state lifetime and henceforth reduced recombination ⁶⁵⁻⁶⁶. The series of dyes JK, synthesised with di-methyl fluorenyl amino moiety with bipolar character, provide stability against light and temperature and prevent degradation correspondingly the presence of thiophene units with the aliphatic chain provided resistance

against water present in the electrolyte and a cyano acrylic acid moiety as an acceptor and anchoring group maintained stability with solvent-free electrolyte ⁶⁷. The incorporation of a terthiophene donor unit to the Z907Na dye increased the molar extinction coefficient with a red shift in the metal to ligand charge transfer (MLCT) transition with remarkable stability under a full-light soaking test ⁶⁸.

Furthermore, the performance of the cell can also be altered by the concentration of dye, use of solvent, and dipping time ⁶⁹. In N3-derived dyes, the protonation also affects the electronic property of the dye; a fully protonated species showed the smallest HOMO-LUMO gap, whereas a fully deprotonated species showed large excitation energy. Thus, mono-protonated and di-protonated dyes are of good choice due to the compromise between the light-harvesting capability and excited state alignment with the CB edge of the semiconductor ^{1, 69}. Besides, the presence of a carboxylic anchoring group in dye promotes efficient charge ejection ⁶⁹. The reason for incorporating the carboxylic group in the ligand is to increase the molar extinction coefficient, to facilitate anchoring of the sensitizer to the substrate, and to ensure high electronic coupling between its excited-state wave function and the CB of the semiconductor ⁵⁷. The dye with a high molar extinction coefficient K19 was found more stable and maintained 92% of stability under both thermal and light stress for 1000 hrs ⁷⁰. An organic dye C203 with a high molar extinction coefficient and a di-thienothiophene unit provided low energy for solvation in high polarity electrolyte and was stable with solvent-free electrolyte ⁷¹.

Table 1.1: The PV parameter of dyes with different cations present in the molecule adapted from ⁷². Reprinted with permission from John Wiley and Sons.

Dyes	Eff [%]	Jsc [mA/cm ²]	Voc [mV]	FF
2TBA ⁺ (N3,2H ⁺)	8.45	14.9	797	0.71
Na ⁺ (N3,2H ⁺)	7.6	15	777	0.66

Likewise, the type of counter-ion/s present in dyes influences the cell performance as shown in Table 1.1. This is possible because of the influence of counter ions on dye adsorption. N3 dye, with 4H⁺ counter ions, adsorbs faster than the N719 dye with three TBA⁺ and one H⁺ ion on the photoanode substrate ¹. The replacement of 2H⁺ by 2Na⁺ in N3 dye maintained 99% stability under light soaking for 1000 hrs ⁷². Among many other factors, the anchoring mode of the dye to the semiconductor surface also affects the stability of the dye. Through Fourier Transform Infrared (FTIR) study, the bidentate chelating and bidentate bridging modes of attachment of the carboxylic group to the TiO₂ substrate showed better stability than the unidentate mode.

Moreover, the attachment of phosphonic acid was stronger than the carboxylic acid group and so was more stability in the presence of a trace of water in-situ ⁷³.

The other factor seen to influence the activity of the sensitizer is the pH value, the acidic environment blue-shifted the absorption spectra and thus, with a decrease in pH value Jsc improved ⁷⁴. Farther decreased pH resulted in a decrease in performance parameters due to defect formation on the photoanode and dye-leaching from the photoanode substrate under a strong acid environment ⁷⁵. On the contrary, the increased pH value facilitates the conductivity which is attributed to the formation of strong polar bonds with improved dye adsorption. However, this phenomenon is limited to the acidic environment ⁷⁶.

As Ru is an expensive and rare element, metal-free organic dyes appear as cost-effective, and environment-friendly alternatives. The gaining interest in metal-free organic dye synthesis is due to their tuneable absorption and electrochemical properties through molecular designing, cost-efficient and eco-friendly, comparatively higher extinction coefficient than the Ru-dyes, and higher efficiency ⁵⁶. Some of the popular metal-free dyes include hemicyanine dye, polyene-diphenyl aniline dye, thienyl fluorene dye, phenothiazine dye, thienothiophene-thiophene derived dye, phenyl-conjugated polyene dye, N, N-dimethylaniline-cyanoacetic acid, oligothiophene dye, coumarin dye, indoline dye, oligo-phenylenevinylene-unit dye. An organic dye is donor- π -acceptor or D- π -A structure. The structure of organic dye is tuned to alter the LUMO-HOMO and electronic properties in favour of PV performance. To date, the highest efficiency recorded 14.3% has been achieved by organic dye ADEKA-1 in association with another organic dye LEG4 as a co-sensitizer ². Undoubtedly, organic dyes have been successful to achieve near-target efficiency. However, the issues with the organic dye are instability and aggregation. Aggregation causes intermolecular quenching, other molecules that are not functionally attached to TiO₂ act as filters. Thence, aggregation is avoided by introducing a co-adsorbent with the dye on the electrode substrate. Aggregation results in a dye-multilayer with partial or complete island formation on the absorbent surface as illustrated in Figure 1.6. Nonetheless, a different effect is observed in different types of dye. Indoline with n-octyl substitution in dye D205 increased Voc than the origin dye D149 without the n-octyl, and alkyl substitution of dyes improved Voc ⁷⁷. Thus, controlling dye aggregation improves photo generation. An ideal co-adsorbent must possess the (i) ability to co-adsorb competitively with the sensitizer to occupy the void spaces on the photoanode substrate which create a barrier and provides shielding against the unwanted recombination ⁷⁸, (ii) the ability to avoid π - π stacking of the dye molecule and promote monolayer formation ⁷⁹, (iii) presence of hydrophobic end to

prevent dye-desorption caused by the water molecules ⁸⁰, and, (iv) ability to shift the CB of the semiconductor towards a negative potential ⁸¹.

Porphyrins are among the sensitizer group which is gaining the attention of researchers due to their strong absorption in the visible region, tuneable electronic structure, and easy modification of the dye core. The porphyrins have successfully outperformed most of the Ru-based dyes and hold the capability to represent future DSSCs. Some of the efficient porphyrin dyes are; SM315 ($\eta=13\%$), SM371 ($\eta=12\%$) ⁸², LD4 ($\eta=10.6\%$) ⁸³, LD14 ($\eta=10.17\%$) ⁸³, YD2-o-C8 ($\eta=12.29\%$) ⁸⁴, ZnPBT ($\eta=10.1\%$) ⁸⁵, and GY50 ($\eta=12.75\%$) ⁸⁶. The efficient dye structure and the cell configuration is provided by Figure 8.1 and Table 8.1.

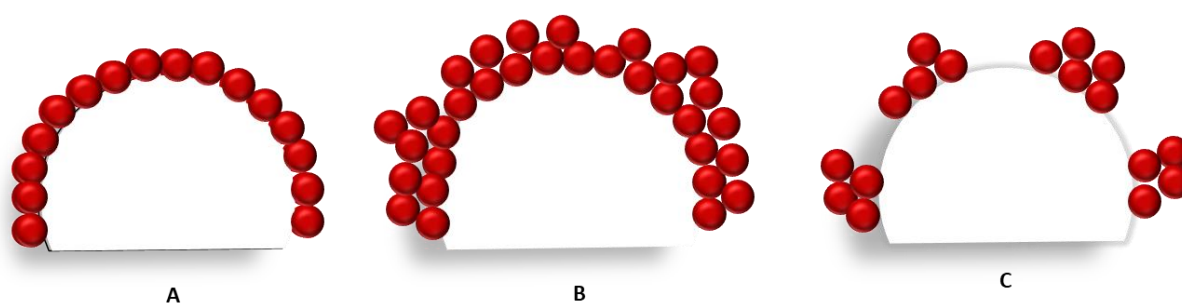


Figure 1.6: Diagrammatic illustration of complete monolayer dye coverage (A), complete multilayer dye coverage (B) and partial coverage with island formation (C).

1.3.3. Electrolytes

The efficiency of DSSCs under operating conditions is affected by the mentioned four processes: light harvesting, recombination of an electron with the oxidised dye molecule or the electrolyte, diffusion of triiodide to CE and reduction of triiodide at the CE. Except for the light-harvesting, all the other processes can be suppressed or enhanced by the proper selection of electrolytes and their components. For instance, the transportation of the redox couple influences the value of J_{sc} ; V_{oc} is directly affected by the redox potential of the electrolyte and FF is affected by the diffusion of the charge carrier and the charge transfer resistance. On that account, electrolyte plays an important role in enhancing the PV properties of the DSSCs by regenerating the dye and itself during cell operation.

The electrolyte used in DSSCs is broadly classified as (i) Liquid electrolytes, (ii) Quasi-solid electrolytes and (iii) Solid electrolyte. Liquid electrolytes are so far from the most efficient electrolyte system used in DSSCs. However, it is undeniable that the use of liquid electrolytes by volatilisation and evaporation is disadvantageous. Moreover, the problem of corrosion, dye desorption and photodegradation, and precipitation of salts are other issues leading to cell

degradation and instability⁸⁷. To follow that, different ionic liquids with high viscosity and negligible vapour pressure are included in the liquid electrolyte. The issue of volatility was attempted to resolve by efforts like gelation⁸⁸⁻⁹⁰ or solidification of liquid electrolyte or by introducing polymeric solid⁹¹⁻⁹⁶, or molecular hole-conductors but this could not achieve the performance capability of the liquid electrolyte. The most popular strategy is the use of ionic liquid as a solvent. The ionic solvents are a good option because of their low volatility, wide electrochemical window, and negligible vapour pressure. However, the high viscosity is the reason that inhibits the charge flow and decreases the performance of the cell. This leads to the use of a combination of organic and ionic solvents⁹⁷. The use of organic liquid with an ionic liquid to exploit the property of viscosity address the problem of mass-transport limitation⁹⁸. Some modifications introduced in ionic liquids were seen to improve the cell performance and stability. The use of supercooling series of 1-alkyl-3-alkyl-imidazolium iodides as electrolyte solvent reduced the viscosity of the electrolyte and provided high efficiency with good stability under light soaking test at 60 °C⁹⁹. The use of fluorinated ionic solvents improved cell performance by enhancing the interfacial charge transfer¹⁰⁰. Other solvents used in electrolytes, acetylacetone¹⁰¹, butyronitrile¹⁰², gamma butyrolactone, carbonates, alcohols and nitriles have shown good performance¹⁰³⁻¹⁰⁴. However, one must consider, the electrolyte and its components are dye-selective¹⁰⁵⁻¹⁰⁸.

The next important component of electrolytes is the redox reagent. The redox couple helps in the regeneration of dye and itself under a working scenario. Different redox couples have been used in electrolyte systems. I^-/I_3^- is the most used redox couple in DSSCs because of its capacity to fast dye regeneration, especially in Ru-based dyes¹⁰⁹, high solubility with electrolyte components, slow back electron transfer and high diffusion length¹¹⁰. However, the drawbacks include a large potential difference between the Fermi level and HOMO of dye¹¹¹ and high absorption of visible light¹¹². Consequently, alternative redox couples are being explored to replace the traditional I^-/I_3^- . The alternative redox reagent investigated is pseudohalogen-based redox couple, organic redox couple, metal complex redox couple, and ferricenium/ferrocene redox couple¹¹³. The record efficiency to date is obtained from a Co-based redox couple². However, the stability analysis of the recorded system is not yet studied. Apart from this, the use of binary redox couple in electrolytes has also been investigated. The binary redox system results in the positive shift of the potential consequently, improving Voc and suppressing dark current¹¹⁴.

The third component of the electrolyte system is electrolyte-additives. The additives are used to improve the initial performance of the cell and to promote cell stability. The additives have a positive influence on some cell parameters whereas they influence negatively on the other.

Different N-based compounds are very popular electrolyte additives in DSSC systems. Mostly, the additives help in shifting the CB of the TiO_2 substrate upwards and hereinafter increase the value of V_{oc} . In particular, the use of TBP increased the V_{oc} and increased the electron lifetime due to the shift in the CB edge whereas the J_{sc} decreased due to a decrease in the diffusion coefficient of the electrons ¹¹⁵. However, a combination of TBP and Li^+ showed a stable performance for 70 hrs under dark ageing ¹¹⁶. The use of NMBI and TBP in electrolytes improved V_{oc} . Further, NMBI was found to smoothen the high iodine concentration effects, which otherwise would increase the charge recombination and hence decrease J_{sc} . Likewise, the use of TBP additives in electrolytes is crucial to enhance the initial performance of the cell ¹¹⁷. GuNCS as an additive that improved both the J_{sc} and V_{oc} . Nonetheless, different effects were observed in different electrolyte configurations ¹¹⁵. Furthermore, new additives as an alternate to traditional ones are investigated to improve cell performance and stability under different stress conditions. For instance, DNP (4,4'-dinonyl-2,2'-bipyridine) as an alternative to TBP is investigated which improved the thermal stability of N719 dye when exposed to thermal stress of 80 °C for 1000 hrs ¹¹⁸. Despite this, in ionic liquid-based electrolytes, because of the mass transport limitation, the use of a single additive result in improved V_{oc} with decreased J_{sc} but the use of binary additives help to achieve efficiency comparable to standard AN (acetonitrile) based electrolyte and improved cell stability under thermal stress ¹¹⁹⁻¹²⁰.

Various cationic salts as electrolyte additives have shown improvement in V_{oc} in DSSCs. The shift in the CB edge due to the presence of cations was proportional to the cationic radius when compared among Li^+ , Na^+ , K^+ and Cs^+ cations (see Figure 1.7). The direct influence of CB edge shift was observed in electron lifetime which improved with the shift ¹²¹. Therefore, the V_{oc} increased with the increase in cation radius but J_{sc} was found to decrease ¹²². Likewise, Benzimidazolium as an additive in electrolytes improved the V_{oc} but decreased the value of J_{sc} . The increase in V_{oc} depended on the decrease in molecular size of the imidazolium additives. Furthermore, the increase in J_{sc} was concerning the increase in an absolute difference between the dipole moment of the additive and the solvent ¹²³. The use of different volume ratios of types of imidazolium melts as electrolyte solvents has maintained 93% of efficiency under visible light soaking at 60 °C ¹²⁴. On the contrary, the use of MBI as an electrolyte additive with I^-/I_3^- redox resulted in the formation of crystals. This unwanted crystallisation affects the concentration of electrolyte and energy band structure eventually decreasing the cell stability ¹²⁵. Moreover, the use of CaI_2 or MgI_2 as an electrolyte additive have suppressed the UV effect on cell and improved stability ¹²⁶. Thus, the best recipe for optimum cell performance is unknown and defining a specific combination and concentration is still a challenge.

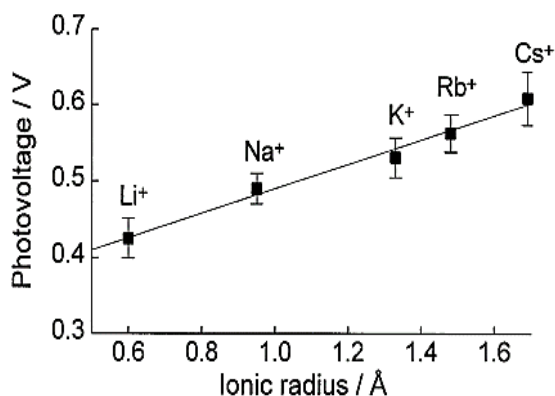


Figure 1.7: The effect of cation on the open circuit voltage with a 10:1 ratio of alkali iodide and iodine in the electrolyte system ¹²². Reprinted with permission from Elsevier.

A very limited study is related to the effect of water as an electrolyte additive on cell performance. The presence of water increased the V_{oc} which was proportional to water concentration in electrolytes due to the shifting of the CB ¹²⁷. The effect of water is observed more as a blocking effect than the CB edge shifting that contributes increment in V_{oc} ¹²². On the contrary, the J_{sc} decreases with increasing water concentration in the electrolyte which is expected due to dye desorption or ligand exchange ¹²² or the presence of water in the DSSC system may help in the oxidation of I^- into iodate IO_3^- which results in depletion in I_3^- and eventual decrease in the cell performance ¹²⁷.

Among different approaches to enhance the performance and stability of DSSCs other than the use of fore-mention additives in electrolyte system includes dye and co-adsorbent as an additive for the electrolyte. The use of dye molecules as an electrolyte additive helps in improving the dye stability by suppressing the dye desorption from the TiO_2 substrate ¹²⁸. With ageing, the parameter that diminishes the efficiency of the cell is J_{sc} , which is due to dye degradation under different stress conditions. Therefore, employing this simple technique during cell fabrication is seen to decrease the dye-desorption rate and improve the stability of the cell when tested in the dark.

Similarly, the modification in cell fabrication by introducing co-adsorbent as electrolyte-additive. The use of co-adsorbent with dye molecules as surface-adsorbent is a common procedure of dye sensitisation. The technique of using co-adsorbent with dye and electrolyte conjointly, first introduced by Daeneke et al with Fc/Fc^+ redox system, successfully achieved comparable efficiency with the traditional I/I_3^- redox ¹¹¹. This concomitant use of co-adsorbent with dye and electrolyte was not limited to the Fc/Fc^+ redox system after Salvotri et al. investigated it with I/I_3^- and $Co(II)/(III)$ redox couples. Although, this technique did not influence the PV parameter of the cell using the I/I_3^- electrolyte system ¹²⁹. The electrical

measurement confirmed the presence of co-adsorbent in both electrolyte and dye reduced the recombination of $\text{TiO}_2/\text{electrolyte}$ and TiO_2/FTO interface by Co (I/II) redox improving the PV parameter by a factor of 2¹³⁰. Nevertheless, this technique requires more investigation under realistic stress levels.

1.3.4. Counter Electrodes

CE is the component in DSSC which affects both the PV parameter and the device cost. Although platinum (Pt) is an expensive and rare element, because of its conductivity, stability, and good catalytic property it still holds the title of the best-performing CE catalyst. The Pt act as a catalyst for the regeneration of I^- and I_3^- and helps in the collection of electrons through the external load to the electrolyte. The electrolyte regenerates the oxidised dye by I^- which is an electron donor in the electrolyte. The oxidation of I^- produces I_3^- which further regenerates I^- by accepting the electrons from the external load which is collected at the CE¹³¹. Pt because it is rare and expensive various attempts have been made to investigate an efficient substitute. There are different materials gaining attraction which includes, carbonaceous materials like carbon black, CNTs, graphene, polymers and transition metals and alloys.

Carbonaceous compounds are good substitutes for Pt because of their large internal surface area, and pore volume with tuneable pore diameter. These compounds, with rich micropores and mesopores and relatively high specific surface area with excellent electrochemical activity towards redox, are cost-effective. Graphene and graphene-based composites for example, because of its property like high mobility, large surface area, excellent conductivity, and high optical transparency is a very promising alternate. However, these C-based materials have not yet succeeded in achieving the performance level of Pt¹³²⁻¹³³. Besides, these materials suffer corrosion under continuous cell-operating conditions¹³⁴. Added, to improve the catalytic property of this material the thickness is increased by increasing the loading. But by increasing the thickness the adhesion for FTO is compromised which results in instability issues for long-term use¹³⁵⁻¹³⁶. Moreover, different forms of CNTs demand functional treatment to improve the catalytic property¹³⁴. The use of composite materials integrates the property and improves the durability and functionality of the CE for instance, the polymer has lower conductivity and carbon has less catalytic property. For this reason, polymer-supported graphene CE possesses the property of carbon for rapid charge transfer and redox performance for conductive polymers¹³⁷. The use of composite CE approached the efficiency of the Pt catalyst (see Table 1.2).

Table 1.2: The PV parameter of C-based graphene and conducting polymer PANI and their composite ¹³⁷. Reprinted with permission from Elsevier.

Counter Electrode	η [%]	Jsc [mA/cm ²]	Voc [mV]	FF
Bare FTO	0.19	3.87	495	0.10
Graphene	2.82	12.08	601	0.39
PANI	4.78	12.86	683	0.54
PANI/Graphene	6.09	13.28	685	0.67
Pt	6.88	14.20	695	0.70

The conducting polymer because of its excellent catalytic property, charge transfer ability and excellent optical transparency in the visible region is also included in the list. Among many, different polymers investigated, PANI has been proven better for bi-facial solar cells ¹³⁸ but commercialisation demands stability with low cost which still is far away as the cost-effective polymer has poor performance and the polymer with comparable performance to Pt is expensive ¹³⁶.

Transition metals are also included in the list because of their excellent catalytic activity towards popular redox couples. These transition metal compounds possess Pt-like catalytic properties but their performance is still poor ¹³⁶. Thus, alloys were introduced. The alloys when compared to a single metal-based catalyst can be manipulated to change the intrinsic electronic property that influences the catalysis. For instance, the use of high electronegative metal with Pt increased the active catalytic sites. Likewise, the doping of Pt into the metal improved the catalytic property of the alloy ¹³⁹. The performance of Pt/Co and Pt/Ni was higher than the standard Pt electrode ¹³⁹⁻¹⁴⁰. As evidence, the influence of the ratios of CoPt alloy on the PV performance of DSSCs is enlisted in Table 1.3. Likewise, the Pt-free alloy Fe-Se achieved transparency of 70% in comparison to 45% of standard Pt electrodes which makes alloys popular with bi-facial cells ¹⁴¹. This technique has resulted in considerable improvement with a reduction in manufacturing cost but demands further investigation of stability under different stress factors.

Table 1.3: The PV parameter of CoPt alloy with performance parameter high compared to standard Pt-based electrode ¹⁴². Reprinted with permission from the American Chemical Society.

Counter Electrode	η [%]	Jsc [mA/cm ²]	Voc [mV]	FF
CoPt0.01	8.29	16.75	705	0.70
CoPt0.02	10.23	18.53	735	0.75
CoPt0.04	9.18	17.46	721	0.73
CoPt0.1	8.43	16.95	715	0.70
CoPt0.2	7.59	14.95	688	0.74
Pt	6.52	13.93	714	0.66
Co	1.84	5.78	643	0.50

Besides, all the other possibilities, even the function and performance of Pt-based electrodes are still under investigation. Different factors were found to influence the catalytic capacity of Pt. The deposition technique ^{104, 143}, fabrication method ¹⁴⁴, thickness ¹⁴⁵, the Pt-structure ¹⁴⁶ are just a few. Pt is so far considered stable under ageing. However, some studies indicate the dissolution of Pt as a reason for the decrease in cell performance ¹⁴⁷ while others support the stability of Pt under real working scenarios for more than a year ¹⁴⁸. Though, it is very important to consider the experimental set-up and techniques involved in the above-mentioned studies varied.

1.4. Dye Anchoring Modes

The molecular packing of dye influences the availability of the binding sites of the absorbate that determines the molecular coverage which directly influences the Jsc and the photoelectric conversion capability ¹⁴⁹. The operation of DSSCs is initiated by an interfacial charge separation at the dye-TiO₂ interface; it is therefore crucial to understand the interfacial properties and different processes occurring between the absorbent and the absorbate. The molecular packing of the dye also defines the availability of the TiO₂ to the redox electrolyte and reduces the Voc via limiting unwanted recombination. Therefore, it is highly desirable to obtain detailed structural information on the absorbent-absorbate interface and its influence on the PV performance and stability of the device ¹⁵⁰. In this study, we fully intend to understand by comparing the structural change of dye molecules under ageing.

Dye anchoring influences the electron transfer in the photoexcitation process and the charge injection efficiency which strongly depends on the type of binding modes suggesting that surface anchoring plays an important role in determining the cell efficiency and stability in the cell performance ¹⁵⁰. For instance, the formation of a covalent-like linkage that decreases charge

on the bipyridine ligand was seen to improve the Voc¹⁴⁹. Therefore, various attempts have been made to investigate the binding modes of different dye structures using different experimental techniques and computational methods to understand the undertaking processes better. Figure 1.8 depicts the possible anchoring modes available for the carboxylic group to attach to the metal oxide substrate.

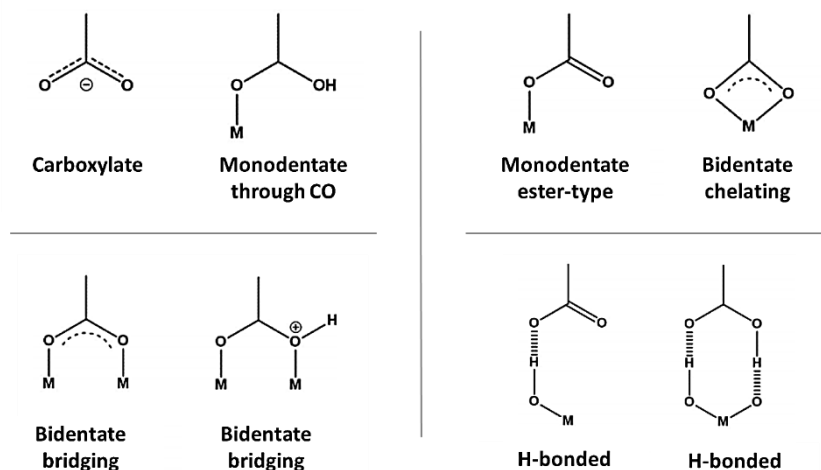


Figure 1.8: Available modes for the carboxylate anchoring group to bind to metal oxide substrate¹⁵¹.

Different dyes are structured and investigated to compete the performance of the Si-based solar cells. In addition, to test the compatibility of the dyes with the adsorbate different techniques are used. For better performance of the cell, different factors come into play, mainly for dye, a broad adsorption band over the visible region, type of aggregation, and dye anchoring modes are of interest. There are many techniques used to illustrate the dye adsorption modes on the substrates, like X-ray reflectometry, XAS (X-ray absorption spectrometry), EXAFS (Extended X-ray Absorption Fine Structure Spectroscopy), UV-Vis, FTIR, X-ray Photoelectron Spectroscopy (XPS), Raman. Some of the popular techniques are enlisted below.

1.4.1. UV Vis

UV-vis is used to investigate the absorption bands and the emission bands. The absorption bands indicate different electronic transitions occurring in the dye molecule upon the absorption of UV-rays. Additionally, the difference between the absorption and emission UV spectra indicates the reorganization of the molecule via dipole change or the presence of an excited state reaction preferably due to proton exchange. A blue shift in the UV-vis spectra indicates H-type aggregation (Hypsochromic shift) and a red shift is an indication of J-type aggregation (Bathochromic shift)¹⁵² (see Figure 1.9). Nonetheless, the comparison of UV-vis absorption spectra of the dye solution and the dye adsorbed on a substrate with a Hypsochromic shift

indicates the anchoring group is in its deprotonated form. It is difficult to confirm the adsorption modes via UV vis only and the result is often complimented by Density functional theory (DFT) and time dependent DFT (TD-DFT) calculations¹⁵³. In addition, the adsorption shifts towards lower energy are ascribed to good interaction between the dye and adsorbent¹⁴⁹⁻¹⁵⁰. On the contrary, the band shift towards higher energy elucidates a weak electron coupling between the dye and adsorbent¹⁵⁴. The red shift in the absorption threshold of the dye-adsorbed TiO₂ suggests the loss in energy due to increased delocalisation as a result of interaction between the carboxylate group and TiO₂¹⁵⁵. The dye adsorption when compared between Oxalic acid treated and non-treated TiO₂, the high absorbance indicated high dye loading in the former substrate. Again, a slight blue shift in the low energy MLCT band signifies an increase in the energy of LUMO of the ligand since the shape of the absorbance curve has no significant change, the concept of aggregation was ruled out. In addition, a slight red shift noted in the high-energy MLCT indicates the increased delocalisation due to different anchoring of the dye to the oxalic acid-treated TiO₂¹⁵⁶.

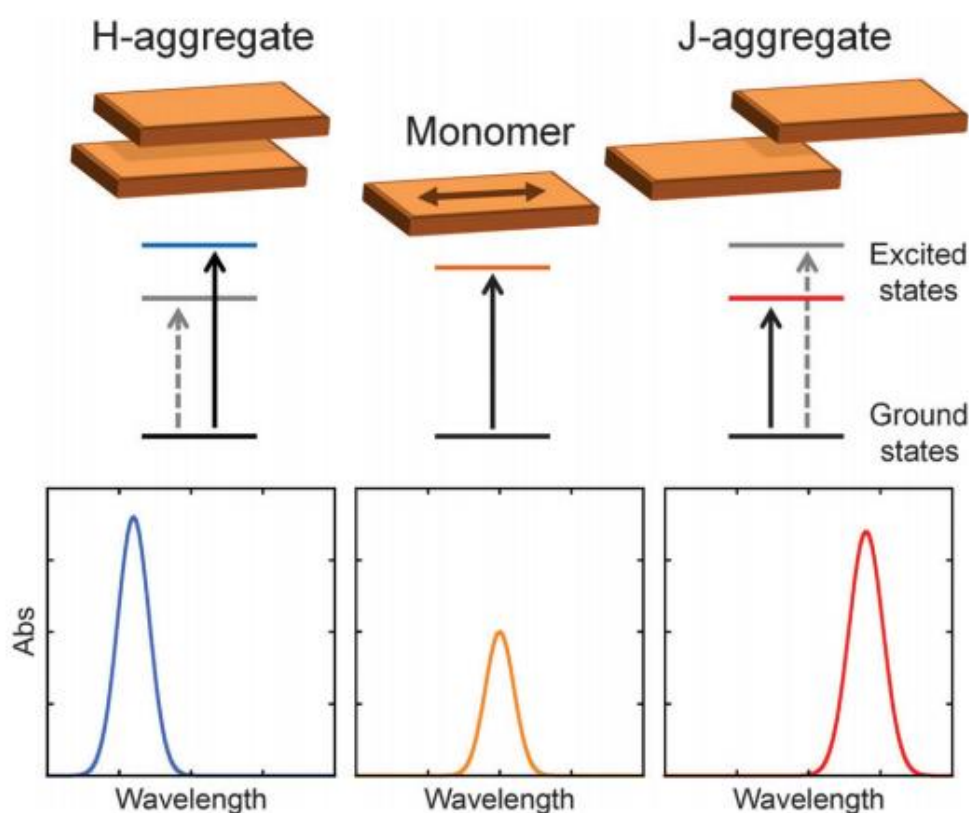


Figure 1.9: The illustration of H- and J-aggregates on the absorption of π -conjugated dye molecule¹⁵⁷. Reprinted with permission from the Royal Society of Chemistry.

1.4.2. XPS

Although, in some cases, XPS has not been proven as a good technique to confirm the dye adsorption modes¹⁵³. XPS with argon-sputtering is used to characterise the dye adsorption modes via depth profiling. The atomic percentage of representative elements for instance Ru and N to Ti was evaluated before and after sputtering. After sputtering a drastic drop in the Ru peak indicated the dye concentration towards the surface. The widening of the Oxygen peak was attributed to the carboxyl group being adsorbed on the oxide surface¹⁵⁸. In the comparison of non-adsorbed and adsorbed TiO₂, the presence of two additional O 1s peaks supports the adsorption via carboxylic species¹⁵⁹.

1.4.3. Fourier Transform Infrared (FTIR)

Fourier Transform Infrared (FTIR) is a very popular and non-destructive technique to observe the change in the dye conformation upon adsorption. However, FTIR results are taken to compliment other observations. Attenuated Total Reflectance- Fourier Transform Infrared (ATR-FTIR) measurement of a coumarin dye, NKX-2753, powder dye and the dye adsorbed on the TiO₂ substrate the carboxylic acid positioned at 1666 cm⁻¹ disappeared and instead, two new peaks at 1540 cm⁻¹ and 1371 cm⁻¹ appeared, assigned to asymmetric and symmetric modes of carboxylate respectively¹⁵⁵. According to Phillips and Deacon¹⁶⁰, the frequency difference between the symmetric and asymmetric bands especially the carboxylate band for N719 dye is considered to conclude the anchoring mode¹⁵⁰ when investigated for oxalic acid treated and non-treated dye-loaded TiO₂ two spectral features were observed for treated photoanodes representing C=O functional group, 1698 cm⁻¹ and 1719 cm⁻¹. The 1719 cm⁻¹ arises from the dye, but the former is from oxalic acid. Upon comparing the intensity of the former decreased indicating for an oxalic acid-treated substrate the dye adsorption involved oxalate ions in binding. Further, with the NCS group, the shift in the peak with a significant reduction in intensity indicates the involvement of the NCS group in dye anchoring¹⁵⁶. Finally, the disappearance of the peak associated with the C=S of NCS and the reappearance of the peak associated with Ru-O in the oxalic acid-treated sample suggests the involvement of NCS in absorption resulting in Ru-O as an interaction of the dye with the oxalate ions. These results were confirmed using FTIR as elucidated in Figure 1.10.

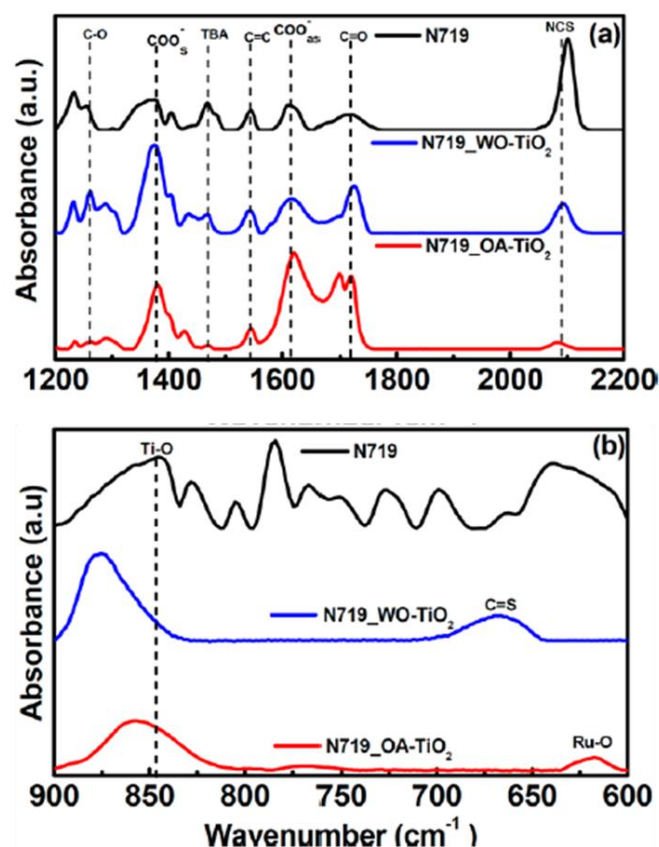


Figure 1.10: FTIR spectra of N719 powder as well as N719 dye adsorbed on oxalic acid treated TiO₂ (OA-TiO₂) and without (WO-TiO₂) in the frequency range (a) 1200-2000 cm^{-1} (b) 900-600 cm^{-1} ¹⁵⁶. Reprinted with permission from the American Chemical Society.

1.4.4. Raman

Raman is a widely used complementary technique to support the anchoring and dye adsorption modes. It is capable of investigating the IR vibrational bands which are inactive in FTIR¹⁶¹. However, the low concentration of the sample is a disadvantage which was overcome by Resonance Raman Spectroscopy (RRS) and Time-resolved Raman Spectroscopy (TRRS)¹⁶¹. The influence of Raman which limits the spectral measurement due to the fluorescence effect was resolved using Surface Enhanced Raman without the resonance¹⁵⁰. For N719 powder, the shift in the C=N line of NCS positioned at 2080 cm^{-1} with low intensity indicate that the NCS ligand does not participate in adsorption directly but the change in the dye structure due to adsorption affects this mode. Nevertheless, on adsorption, a large redshift for the C=N line was observed. On the contrary, for N3 the NCS was observed not participating in dye adsorption. This could be due to the different systems involved¹⁵⁴. However, a difference in structural configuration leading to the disappearance of spectral features is also observed upon continuous irradiation with excitation wavelength ~ 632.8 nm due to thermal degradation. However, with radiation of excitation wavelength ~ 532 nm a good quality spectrum was obtained due to partial quenching of the fluorescence effect. Further, to avoid thermal degradation, the signal

from different spots was taken into account ¹⁵⁰. Table 1.4 includes the list of popular techniques used in the investigation of dye anchoring modes along with the expertise of measurement.

Table 1.4: The list of equipment used in investigating dye anchoring modes with their criteria of measurement ¹⁶¹.

INSTRUMENTS	WHAT IS MEASURED?
Fourier Transform-Infrared	Functional groups and/or bonding present in the dye molecule and change in bonding group when attached to TiO ₂ .
Raman	Vibrational bands that are inactive in IR measurement.
Photoelectron Spectroscopy	Changes in Binding Energies and surface composition.
X-ray Absorption Spectroscopy	Chemical bonding near the surface.
Single crystal X-ray diffraction	Indirect information from bond geometry of dye.
X-ray reflectometry	Orientation and molecular density of dyes on TiO ₂ .
Scanning Tunnelling Microscopy	Absorption geometry and electronic characterisation of dye/ TiO ₂ interface at the atomic. Scale
X-ray Diffraction	Crystal structure of metal oxide absorbent.
Small Angle X-ray Scattering	To determine averaged particle size, shape, and distribution of particles along with their surface-to-volume ratio.
Scanning Electron Microscopy	Sample topography, particle size and elemental composition.
Transmission Electron Microscopy	Sample morphology, composition, and crystal structure.
Atomic Force microscopy	Surface morphology and film roughness.
UV Vis spectroscopy	Effect of anchors on optical properties of the dye molecule and dye adsorption.

Here, we aim to understand the dye anchoring modes of N719 onto the TiO₂ substrate, which can further be compared and investigated to observe changes in the dye structure and its

influence on dye anchoring with ageing. The techniques applied in this study are the AR-XPS, a non-destructive technique, in which tilting the sample probing depth is changed. AR-XPS helps in determining the concentration depth profile of the dye adsorbed onto TiO₂. Furthermore, FTIR gives information about the structural change of the adsorbed dye molecule upon adsorption and with ageing.

1.5. Ageing and Degradation in DSSCs

For the past three decades, DSSCs have been widely researched. Various dye molecules and electrolyte solutions have been designed to improve conversion efficacy and cell stability¹⁶², however, little attention has been paid to researching cell stability under real-world operational conditions. An appropriate ageing investigation can shed light on cell efficiency improvement, perform reliability assessment, assist in lowering cell manufacturing costs, support performance prediction, and aid in understanding the environmental impact on the cell system. Ageing research in DSSCs is not a new field of study, yet there are numerous variations in sample size and ageing setup. Much PV research focuses on improving cell efficiency, with very few considering ageing as a topic. Furthermore, there is a necessity for a systematic ageing study that considers an acceptable number of sample cells to boost statistical reliability, as well as periodic characterisation for device performance, including both dark and illuminated ageing analysis. Until far, no ageing test has included the investigation of cell component deterioration and the relationship to changes in the electrical and compositional structure of the cell interface. The ageing investigation employs JV analysis as a technique to track the device performance throughout the ageing period. The JV parameters, J_{sc} which determines the light-harvesting efficiency decrease mainly due to any degradation introduced in dye components¹⁶³, which could be either dye desorption or dye decomposition resulting in the low ejection of photoelectrons¹⁶⁴. In many aged samples, a decrease in J_{sc} has been the main reason for to decrease in the overall cell efficiency¹⁶⁵. The V_{oc} is mainly affected by the shifting of the CB edge of the semiconductor which increases with an increase in electron flux¹⁶⁴. The next parameter is the FF which is related to better contact between the electrolyte and CE and is usually seen improving with ageing owing to better electrolyte absorption into TiO₂ with time¹⁶⁴. The decrease of FF indicated a poor connection between the electrolyte and CE possibly due to counter catalyst degradation¹⁶⁶. The overall efficiency which depends on J_{sc}, V_{oc} and FF eventually decreases with ageing. However, to confirm what is the reason for the change in the PV parameter demands other analysis techniques involved in parallel. Under different stress conditions, the potential reasons for the instability of DSSCs, proposed by different literatures are due to dye degradation is because of dye desorption, ligand loss and

formation of different complexes; and electrolyte loss or change in electrolyte composition that degrades the electrolyte with time⁸⁷. The study of the degradation of cells on a molecular level mostly involves the FTIR and/or Raman with Electrochemical impedance spectroscopy (EIS) techniques for analysis. The EIS give information about the change in electrochemical properties while FTIR and Raman are used to determine any chemical change introduced with ageing under stress.

The ageing study of different components under different stress factors reports different phenomena. Under high temperatures, the degradation of the cell was faster than under illumination and/or thermal stress below 50 °C¹⁶⁷. The effect of heat on cell performance parameters was recovered when the cell was again aged in the dark¹⁶⁸ indicating that the changes introduced in situ are reversible. Under operating conditions, the decomposition of the dye molecule was observed due to rupturing of the Metal-Ligand bond¹⁶⁹⁻¹⁷¹. The phenomenon of ligand loss in dye molecules was supported by Raman measurement^{170, 172-173}. The degradation was enhanced in the absence of electrolytes¹⁷¹. Further, the presence of water in the electrolyte or the electrolyte solvent induced dye desorption under different stress factors^{163, 174-175}. In some cases, the additives used to improve the cell efficiency triggered degradation, for instance, the deprotonation of carboxylic ligand by TBP additive^{116, 163}. However, most dyes with ionic liquid and proper sealing technique have shown better stability for a long time giving stability for 15 years¹¹⁶. This indicates the major degradation initiation is due to the electrolyte and improper sealing technique used in the cell configuration.

Apart from electrolyte leakage and evaporation mainly for the AN-based liquid electrolyte, electrolyte degradation under different stress conditions has been reported. One should keep in mind the degradation of electrolytes depends on the stress factor and the electrolyte ingredient¹⁷⁶⁻¹⁷⁷. For instance, the use of TBP in electrolyte systems promotes dye desorption¹⁶⁷. Therefore, it is very crucial to select the right electrolyte recipe, like a solvent, redox couple, additives, and their concentration concerning the dye. Cells with liquid electrolyte and I⁻/I₃⁻ redox couple show a decrease in I₃⁻ concentration to cause degradation^{116, 178}. This changes the ingredients of electrolytes and affects the regeneration cycle¹⁷⁹. Some ageing tests have reported the formation of iodine crystals when aged under short-circuit conditions¹⁸⁰ and iodate compound formation causing electrolyte bleaching¹⁸¹ and resulting in iodine loss¹⁷¹. The effect of ageing was also observed on the TiO₂ substrate. The CB edge of TiO₂ shifted with ageing. The possible reason suggested is due to stress factors and electrolytes which promote proton intercalation and/ or water inhalation due to ineffective sealing¹⁶⁸. The presence of air and moisture on the TiO₂ adversely affected its electronic properties^{173, 182}. Further, the cracks

introduced due to ageing under stress factors increased cell resistance ¹⁷⁰. The effect of ageing was observed to adversely affect the inter-particle bonding of the TiO₂ network ¹⁷⁹.

For CE, Pt because of its superior catalytic property and high conductivity is very popular and mostly used as the counter catalyst. Pt is considered a stable catalyst. However, heat harms it. Although the effect of light and dark ageing is negligible on Pt, chemical dissolution of Pt has been reported in the presence of water which decreased the catalytic property of the CE with ageing ^{166, 179}. The catalytic property of Pt before and after ageing even in the absence of water decreased under thermal stress ¹⁷⁰. The dissolution of Pt into electrolytes is suggested to possibly affect the electrolyte concentration and retard dye regeneration ¹⁷⁹.

The DSSCs exhibit specific advantages over the commercialised Si-based solar cell, including easy fabrication, low manufacturing cost, eco-friendliness and flexibility. However, the commercialisation of dye-sensitised solar cells is still a question. From an industrial point of view, the main concern related to DSSCs is their efficiency, comparable to Si-based cells, and stability. Much research is ongoing to optimise cell efficiency in addition to testing cell stability based on different components that are used to improve cell performance. As a result, many ageing and stability tests are gaining mass attention. About 50% of the tests have serious short-coming ¹⁸³, as some tests were performed on a single cell or a limited number of cells that lack uniformity and repeatability. Therefore, different factors need to be considered and procedures are needed to follow, to result from a valid ageing test including a good sample size, application of real-life environment conditions, and operation under load are a few to mention. In addition, different stress factors applied should be included and clarified in the study like, illumination light intensity, humidity, and temperature. The ageing test should aim at determining the lifespan of the cell which require a long time to expose the cell to certain stress condition and it demands a better and more reliable technique to determine the acceleration test and degradation factor which is still a limit.

The research on ageing in DSSCs can be summarised as follows:

- In the case of DSSCs, ageing has been performed under different stress factor which includes either heat, light or dark. The focus is mostly kept on the change in PV-parameter to determine the stability of the specific cell configuration.
- The decrease in J_{sc} is attributed to the change introduced in the dye properties under different stress conditions, for instance, dye desorption, ligand exchange, and dye decomposition which directly affects the light-harvesting efficiency ¹⁶⁵.
- The change in V_{oc} however is attributed to the shifting of the CB edge of the semiconductor substrate which affects the electron transport ¹⁶⁴. Shifting of CB of TiO₂ with ageing was

suggested due to the intercalation and/or water inhalation due to poor sealing technique ¹⁶⁸. Further, the cracks introduced on the TiO₂ increased the internal cell resistance ¹⁷⁰.

- The FF was seen to improve with ageing which was related to improved connection between the electrolyte and CE with time ¹⁶⁶.
- The electrochemical properties are investigated using the EIS technique ¹⁸⁴, while the chemical change is observed employing FTIR and Raman on the aged photoanodes ^{163, 182}.
- Rapid ageing in cells was observed under temperatures higher than 50 °C, and the effect of ageing was recovered when aged in the dark ¹⁶⁸. Moreover, the degradation is enhanced in the absence of the electrolyte ¹⁷¹.
- The effect of ageing on dye was observed as dye rupturing due to ligand loss confirmed via Raman ¹⁶⁹⁻¹⁷¹.
- Cells with ionic liquid electrolytes and proper sealing technique showed better stability for 15 years ¹¹⁶.
- The poor stability of liquid electrolytes depended on the stress factor and the cell components and electrolyte constituents.
- For I⁻/I₃⁻ electrolytes the reasons reported as causes for electrolyte degradation are, a decrease in I₃⁻ ^{116, 178}, I crystallisation ¹⁸⁰ and iodate formation causing electrolyte bleaching ¹⁸¹ and I loss ¹⁷¹.
- The Pt catalyst dissolution was reported due to the presence of water that decreased the catalytic property of the CE ¹⁷⁹. However, even in the absence of water but under high temperatures the dissolution was still observed ¹⁷⁰.

Ageing in DSSCs is not a new topic to study. However, it does include many discrepancies. The ageing test demands a complete analysis of all the components and establishing an effective, yet easy and non-destructive technique is the interest of this study. Further, to implement the technique and investigate the degradation of different cell components under different stress conditions is the project's aim. Thus, we aim to set up a methodology for investigating the ageing of the cell effectively. We propose a technique of rinsing the aged photoanode and using the rinsed-off solution to prepare a drop-cast substrate. On investigating the rinsed-off photoanode along with the drop-cast substrate we expect to observe the change in dye structure along with the degrading component with their respective ratios.

The application of XPS, and FTIR to investigate the change in the dye structure and NICISS to compare the concentration depth profile of aged photoanode, we expect to observe changes introduced onto the TiO₂-dye-electrolyte interface along with the change in the PV properties.

1.6. Commercial and Future Perspective of DSSCs

DSSCs have the potential to produce electricity under low light conditions including indoor lighting. The structural design and use of different coloured dyes in the cell feature colour, transparency, light weight, flexibility and now availability of the roll-to-roll technique, which make them an excellent choice for architecture like electrochromic windows, interior applications, electronic devices, and portable power systems. DSSCs models have the potential to provide higher power output on cloudy days than other thin film solar cells (see Figure 1.11). The first commercial application of DSSCs was in 2009, created by G24i's, used in solar panels built into backpacks which could be used to recharge electronic devices such as cell phones, e-books, cameras, and portable LED lighting systems. In addition, this technology has been successful in attracting military attention for tents and fabrics with the capability to produce 1 kW of energy to power a few lights and other essential electronics like laptops. Further, a lightweight wearable solar panel that could recharge electrical devices like telephones, cameras, and portable electronic the military carry, will eliminate the need to carry extra battery packs. In 2013, the SwissTech convention centre installed the world's first multi-coloured DSSCs panes expected to generate 8000 kWh of electricity annually, which is a step forward towards building integrated photovoltaics (BIPV) applications of DSSCs. DSSCs have also been investigated in the Agrovoltaic field as panels for the greenhouse application which shows promising results ¹⁸⁵.

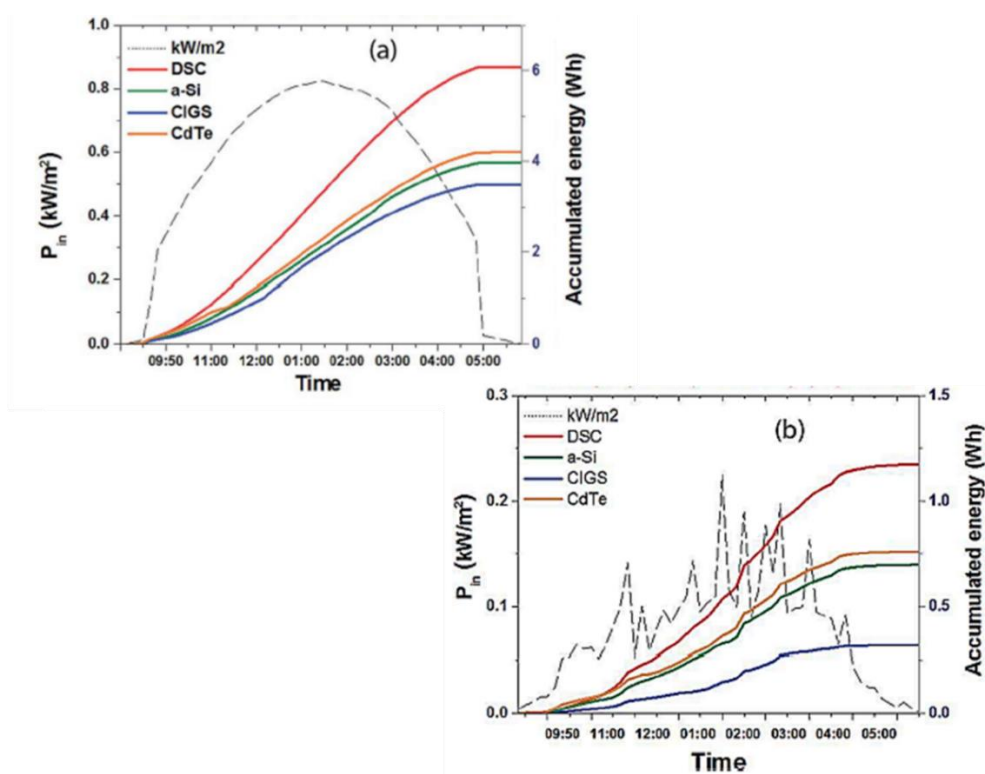


Figure 1.11: The performance comparison of different PV technologies on (a) Sunny day and (b) Cloudy day¹⁸⁶. Reprinted with permission from the Royal Society of Chemistry.

Nevertheless, with the increase of dependence on tech for entertainment, informatics, communication, health, security and many other purposes, an energy source that is portable, wireless convenient recharging and sustainable is needed to meet the energy demands of charging the battery of the devices. The textile DSSCs have potentiality as they can be easily woven into fabrics to absorb sunlight across 360° angle which will increase the possibility of optimum absorption of direct and scattered light¹⁸⁷.

DSSCs have also shown promising results in photocatalysis for effective water splitting. A schematic diagram illustrating the water splitting process in DSSCs is described in Figure 1.12. With the use of an appropriate chromophore in DSSCs the photo absorption can be extended to improve charge transfer which ultimately increases the hydrogen production¹⁸⁸. This has attracted many researchers' attention to the modification of dye structure, and cell structures¹⁸⁹⁻¹⁹⁰ to improve hydrogen production.

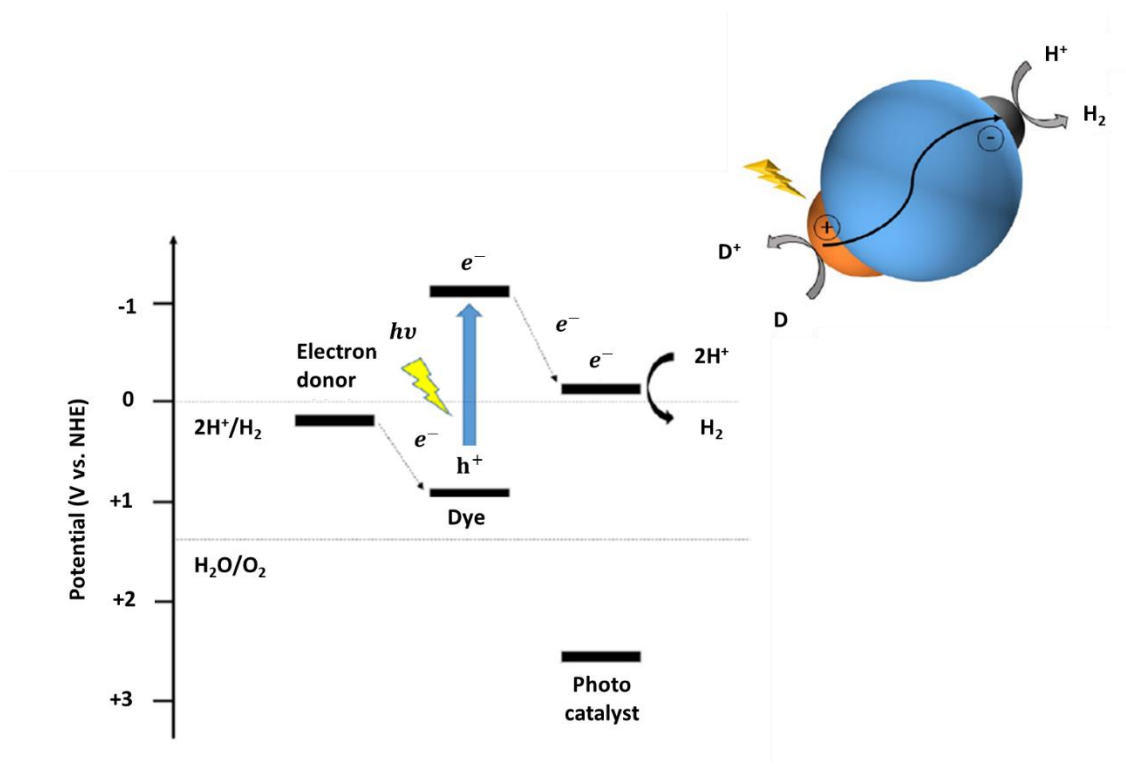


Figure 1.12: The schematic illustration of Dye-sensitised photocatalysts for hydrogen production¹⁸⁸.

1.7. Appendix

In the appendix, the record keeping cell efficiencies with the cell components is tabulated and further includes the molecular structure of efficient dyes.

1.8. References

1. Grätzel M. Dye-sensitized solar cells. *Journal of photochemistry and photobiology C: Photochemistry Reviews*. 2003;4(2):145-53.
2. Kakiage K, Aoyama Y, Yano T, Oya K, Fujisawa J-i, Hanaya M. Highly-efficient dye-sensitized solar cells with collaborative sensitization by silyl-anchor and carboxy-anchor dyes. *Chemical communications*. 2015;51(88):15894-7.
3. Ren Y, Zhang D, Suo J, Cao Y, Eickemeyer FT, Vlachopoulos N, et al. Hydroxamic acid pre-adsorption raises the efficiency of cosensitized solar cells. *Nature*. 2023;613(7942):60-5.
4. Jyoti D, Mohan D, Singh A, Ahlawat DS, editors. A critical review on mesoporous photoanodes for dye-sensitized solar cells. *Materials Science Forum*; 2014: Trans Tech Publ.
5. Liu W, Liu Y, Liu F, Yang Y. Regeneration performance tolerance of dye-sensitized solar cells based on continuous repeated electric erasure/re-sensitization. *Electrochimica Acta*. 2019;307:488-94.
6. Roy JK, Kar S, Leszczynski J. *Development of Solar Cells: Theory and Experiment*: Springer; 2021.
7. Hsiao P-T, Tung Y-L, Teng H. Electron transport patterns in TiO₂ nanocrystalline films of dye-sensitized solar cells. *The Journal of Physical Chemistry C*. 2010;114(14):6762-9.
8. Listorti A, O'regan B, Durrant JR. Electron transfer dynamics in dye-sensitized solar cells. *Chemistry of Materials*. 2011;23(15):3381-99.
9. Archer MD, Nozik AJ, Ai X, Benson-smith J. *Nanostructured and photoelectrochemical systems for solar photon conversion*: World Scientific; 2008.
10. Robson KC, Bomben PG, Berlinguette CP. Cycloruthenated sensitizers: improving the dye-sensitized solar cell with classical inorganic chemistry principles. *Dalton Transactions*. 2012;41(26):7814-29.
11. An Z, Zheng C, Tao Y, Chen R, Shi H, Chen T, et al. Stabilizing triplet excited states for ultralong organic phosphorescence. *Nature Materials*. 2015;14(7):685-90.
12. Vlček Jr An. The life and times of excited states of organometallic and coordination compounds. *Coordination Chemistry Reviews*. 2000;200:933-78.
13. Ardo S, Meyer GJ. Photodriven heterogeneous charge transfer with transition-metal compounds anchored to TiO₂ semiconductor surfaces. *Chemical Society Reviews*. 2009;38(1):115-64.
14. Haque SA, Palomares E, Cho BM, Green AN, Hirata N, Klug DR, et al. Charge separation versus recombination in dye-sensitized nanocrystalline solar cells: the minimization of kinetic redundancy. *Journal of the American Chemical Society*. 2005;127(10):3456-62.
15. Sima C, Grigoriu C, Antohe S. Comparison of the dye-sensitized solar cells performances based on transparent conductive ITO and FTO. *Thin Solid Films*. 2010;519(2):595-7.
16. Sheehan S, Surolia P, Byrne O, Garner S, Cimo P, Li X, et al. Flexible glass substrate based dye sensitized solar cells. *Solar energy materials and solar cells*. 2015;132:237-44.
17. Weerasinghe HC, Huang F, Cheng Y-B. Fabrication of flexible dye sensitized solar cells on plastic substrates. *Nano Energy*. 2013;2(2):174-89.
18. Frank AJ, Kopidakis N, Van De Lagemaat J. Electrons in nanostructured TiO₂ solar cells: transport, recombination and photovoltaic properties. *Coordination Chemistry Reviews*. 2004;248(13-14):1165-79.
19. Bhatti K, Khan M, Saleem M, Alvi F, Raza R, Rehman S. Analysis of multilayer based TiO₂ and ZnO photoanodes for dye-sensitized solar cells. *Materials Research Express*. 2019;6(7):075902.

20. Siwatch S, Kundu VS, Kumar A, Kumar S, Chauhan N, Kumari M. Morphology correlated efficiency of ZnO photoanode in dye sensitized solar cell. *Materials Research Express*. 2019;6(10):1050d3.
21. Rani RA, Zoolfakar AS, Rusop M, editors. Photovoltaic performance of dye-sensitized solar cells based nanoporous-network Nb₂O₅. *AIP Conference Proceedings*; 2019: AIP Publishing LLC.
22. Latini A, Panetta R. Test of different sensitizing dyes in dye-sensitized solar cells based on Nb₂O₅ photoanodes. *Energies*. 2018;11(4):975.
23. Prasittichai C, Hupp JT. Surface modification of SnO₂ photoelectrodes in dye-sensitized solar cells: significant improvements in photovoltage via Al₂O₃ atomic layer deposition. *The Journal of Physical Chemistry Letters*. 2010;1(10):1611-5.
24. Gayathri R, Raja G, Rajeswaran P. High stable with efficient dye-sensitized solar cell-based Al₂O₃/graphene hybrid photoanode fabricated by simple household microwave irradiation technique. *JOURNAL OF MATERIALS SCIENCE-MATERIALS IN ELECTRONICS*. 2020.
25. Duan J, Zou S, Yang C, Liu W, Wu H, Chen T. Full SnO₂ double-layer dye-sensitized solar cells: Slowly increasing phenomenon of power conversion efficiency. *Solar Energy*. 2020;196:99-106.
26. Cheema H, Delcamp JH. SnO₂ Transparent Printing Pastes from Powders for Photon Conversion in SnO₂-Based Dye-Sensitized Solar Cells. *Chemistry—A European Journal*. 2019;25(62):14205-13.
27. Rashid NM, Kishi N, Soga T. Effects of nanostructures on iron oxide based dye sensitized solar cells fabricated on iron foils. *Materials Research Bulletin*. 2016;77:126-30.
28. Shang X, Guo Z, Gan W, Zhou R, Ma C, Hu K, et al. Dye-sensitized solar cells with 3D flower-like α -Fe₂O₃-decorated reduced graphenes oxide as photoanodes. *Ionics*. 2016;22(3):435-43.
29. Leandri V, Liu P, Sadollahkhani A, Safdari M, Kloo L, Gardner JM. Excited-State Dynamics of [Ru (bpy) ₃] ²⁺ Thin Films on Sensitized TiO₂ and ZrO₂. *ChemPhysChem*. 2019;20(4):618-26.
30. Yin X, Xie X, Song L, Zhou Y, Du P, Xiong J. The application of highly flexible ZrO₂/C nanofiber films to flexible dye-sensitized solar cells. *Journal of Materials Science*. 2017;52(18):11025-35.
31. Gholamrezaei S, Salavati-Niasari M. An efficient dye sensitized solar cells based on SrTiO₃ nanoparticles prepared from a new amine-modified sol-gel route. *Journal of Molecular Liquids*. 2017;243:227-35.
32. Das PP, Roy A, Agarkar S, Devi PS. Hydrothermally synthesized fluorescent Zn₂SnO₄ nanoparticles for dye sensitized solar cells. *Dyes and Pigments*. 2018;154:303-13.
33. Fattahi AR, Asemi M, Ghanaatshoar M. The influence of plasma treatment on the photovoltaic performance of DSSCs fabricated from hydrothermally prepared Zn₂SnO₄ nanoparticles. *Journal of Materials Science: Materials in Electronics*. 2019;30(14):13525-33.
34. Roose B, Pathak S, Steiner U. Doping of TiO₂ for sensitized solar cells. *Chemical Society Reviews*. 2015;44(22):8326-49.
35. Yang Y, Niu S, Han D, Liu T, Wang G, Li Y. Progress in developing metal oxide nanomaterials for photoelectrochemical water splitting. *Advanced Energy Materials*. 2017;7(19):1700555.
36. Samat M, Ali A, Taib M, Hassan O, Yahya M. Hubbard U calculations on optical properties of 3d transition metal oxide TiO₂. *Results in physics*. 2016;6:891-6.
37. O'regan B, Grätzel M. A low-cost, high-efficiency solar cell based on dye-sensitized colloidal TiO₂ films. *nature*. 1991;353(6346):737-40.
38. Jun Y, Kim J, Kang MG. A study of stainless steel-based dye-sensitized solar cells and modules. *Solar energy materials and solar cells*. 2007;91(9):779-84.

39. Park N-G, Van de Lagemaat J, Frank, AJ. Comparison of dye-sensitized rutile-and anatase-based TiO₂ solar cells. *The Journal of Physical Chemistry B*. 2000;104(38):8989-94.
40. Al-Alwani MA, Mohamad AB, Ludin NA, Kadhum AAH, Sopian K. Dye-sensitized solar cells: development, structure, operation principles, electron kinetics, characterisation, synthesis materials and natural photosensitisers. *Renewable and Sustainable Energy Reviews*. 2016;65:183-213.
41. Adhikari SG, Shamsaldeen A, Andersson GG. The effect of TiCl₄ treatment on the performance of dye-sensitized solar cells. *The Journal of Chemical Physics*. 2019;151(16):164704.
42. More V, Mokurala K, Bhargava P. Influence of different heat treatment methods of titania film on performance of DSSCs. *Applied Physics A*. 2018;124(4):345.
43. Sireesha P, Sun W-G, Su C, Kathirvel S, Lekphet W, Akula SB, et al. Enhancement of Power Conversion Efficiency of TiO₂-Based Dye-Sensitized Solar Cells on Various Acid Treatment. *Journal of Nanoscience and Nanotechnology*. 2017;17(1):354-62.
44. Watson T, Charbonneau C, Bryant D, Worsley D. Acid treatment of titania pastes to create scattering layers in dye-sensitized solar cells. *International Journal of Photoenergy*. 2012;2012.
45. Fan K, Yu J, Ho W. Improving photoanodes to obtain highly efficient dye-sensitized solar cells: a brief review. *Materials Horizons*. 2017;4(3):319-44.
46. Deb Nath NC, Subramanian A, Hu RY, Lim BO, Lee J-J. Effects of TiCl₄ post-treatment on the efficiency of dye-sensitized solar cells. *Journal of Nanoscience and Nanotechnology*. 2015;15(11):8870-5.
47. Lee S-W, Ahn K-S, Zhu K, Neale NR, Frank AJ. Effects of TiCl₄ treatment of nanoporous TiO₂ films on morphology, light harvesting, and charge-carrier dynamics in dye-sensitized solar cells. *The Journal of Physical Chemistry C*. 2012;116(40):21285-90.
48. Sedghi A, Miankushki HN. Influence of TiCl₄ treatment on structure and performance of dye-sensitized solar cells. *Japanese Journal of applied physics*. 2013;52(7R):075002.
49. Myat S, Khine S. Optical properties of dye solutions for dye-sensitized solar cell. *International Journal of Scientific and Research Publications*. 2018;8(12):32-6.
50. Sommeling P, O'Regan BC, Haswell R, Smit H, Bakker N, Smits J, et al. Influence of a TiCl₄ post-treatment on nanocrystalline TiO₂ films in dye-sensitized solar cells. *The Journal of Physical Chemistry B*. 2006;110(39):19191-7.
51. Huang N, Liu Y, Peng T, Sun X, Sebo B, Tai Q, et al. Synergistic effects of ZnO compact layer and TiCl₄ post-treatment for dye-sensitized solar cells. *Journal of Power Sources*. 2012;204:257-64.
52. Zhang J, Feng J, Hong Y, Zhu Y, Han L. Effect of different trap states on the electron transport of photoanodes in dye sensitized solar cells. *Journal of Power Sources*. 2014;257:264-71.
53. Hirose F, Kuribayashi K, Shikaku M, Narita Y, Takahashi Y, Kimura Y, et al. Adsorption density control of N719 on TiO₂ electrodes for highly efficient dye-sensitized solar cells. *Journal of The Electrochemical Society*. 2009;156(9):B987.
54. Ishihara T, Tokue J, Sano T, Shen Q, Toyoda T, Kobayashi N. Effect of ligand carboxylation on adsorption and photosensitization in Ru (II)-complex dye-sensitized nanocrystalline TiO₂ solar cell. *Japanese journal of applied physics*. 2005;44(4S):2780.
55. Pourtois G, Beljonne D, Moucheron C, Schumm S, Kirsch-De Mesmaeker A, Lazzaroni R, et al. Photophysical properties of ruthenium (II) polyaaromatic compounds: A theoretical insight. *Journal of the American Chemical Society*. 2004;126(2):683-92.
56. Hagfeldt A, Boschloo G, Sun L, Kloo L, Pettersson H. Dye-sensitized solar cells. *Chemical reviews*. 2010;110(11):6595-663.

57. Dayan O, Özdemir N, Yakuphanoglu F, Şerbetçi Z, Bilici A, Çetinkaya B, et al. Synthesis and photovoltaic properties of new Ru (II) complexes for dye-sensitized solar cells. *Journal of Materials Science: Materials in Electronics*. 2018;29(13):11045-58.
58. Sharma K, Sharma V, Sharma S. Dye-sensitized solar cells: fundamentals and current status. *Nanoscale research letters*. 2018;13(1):1-46.
59. Ning Z, Zhang Q, Wu W, Pei H, Liu B, Tian H. Starburst triarylamine based dyes for efficient dye-sensitized solar cells. *The Journal of organic chemistry*. 2008;73(10):3791-7.
60. Mishra A, Fischer MK, Bäuerle P. Metal-free organic dyes for dye-sensitized solar cells: From structure: Property relationships to design rules. *Angewandte Chemie International Edition*. 2009;48(14):2474-99.
61. Harikisun R, Desilvestro H. Long-term stability of dye solar cells. *Solar Energy*. 2011;85(6):1179-88.
62. Chen CY, Lu HC, Wu CG, Chen JG, Ho KC. New ruthenium complexes containing oligoalkylthiophene-substituted 1, 10-phenanthroline for nanocrystalline dye-sensitized solar cells. *Advanced Functional Materials*. 2007;17(1):29-36.
63. Chen CY, Chen JG, Wu SJ, Li JY, Wu CG, Ho KC. Multifunctionalized ruthenium-based supersensitizers for highly efficient dye-sensitized solar cells. *Angewandte Chemie*. 2008;120(38):7452-5.
64. Faiz J, Philippopoulos AI, Kontos AG, Falaras P, Pikramenou Z. Functional supramolecular ruthenium cyclodextrin dyes for nanocrystalline solar cells. *Advanced Functional Materials*. 2007;17(1):54-8.
65. Clifford JN, Palomares E, Nazeeruddin MK, Grätzel M, Nelson J, Li X, et al. Molecular control of recombination dynamics in dye-sensitized nanocrystalline TiO₂ films: Free energy vs distance dependence. *Journal of the American Chemical Society*. 2004;126(16):5225-33.
66. Karthikeyan CS, Wietasch H, Thelakkat M. Highly efficient solid-state dye-sensitized TiO₂ solar cells using donor-antenna dyes capable of multistep charge-transfer cascades. *Advanced Materials*. 2007;19(8):1091-5.
67. Choi H, Baik C, Kang SO, Ko J, Kang MS, Nazeeruddin MK, et al. Highly efficient and thermally stable organic sensitizers for solvent-free dye-sensitized solar cells. *Angewandte Chemie*. 2008;120(2):333-6.
68. Sauvage F, Fischer MK, Mishra A, Zakeeruddin SM, Nazeeruddin MK, Bäuerle P, et al. A Dendritic Oligothiophene Ruthenium Sensitizer for Stable Dye-Sensitized Solar Cells. *ChemSusChem: Chemistry & Sustainability Energy & Materials*. 2009;2(8):761-8.
69. Nazeeruddin MK, De Angelis F, Fantacci S, Selloni A, Viscardi G, Liska P, et al. Combined experimental and DFT-TDDFT computational study of photoelectrochemical cell ruthenium sensitizers. *Journal of the American Chemical Society*. 2005;127(48):16835-47.
70. Wang P, Klein C, Humphry-Baker R, Zakeeruddin SM, Graetzel M. A high molar extinction coefficient sensitizer for stable dye-sensitized solar cells. *Journal of the American Chemical Society*. 2005;127(3):808-9.
71. Qin H, Wenger S, Xu M, Gao F, Jing X, Wang P, et al. An organic sensitizer with a fused dithienothiophene unit for efficient and stable dye-sensitized solar cells. *Journal of the American Chemical Society*. 2008;130(29):9202-3.
72. Andrade L, Zakeeruddin SM, Nazeeruddin MK, Aguilar Ribeiro H, Mendes A, Grätzel M. Influence of Sodium Cations of N3 Dye on the Photovoltaic Performance and Stability of Dye-Sensitized Solar Cells. *ChemPhysChem*. 2009;10(7):1117-24.
73. Wang P, Klein C, Moser J-E, Humphry-Baker R, Cevey-Ha N-L, Charvet R, et al. Amphiphilic ruthenium sensitizer with 4, 4'-diphosphonic acid-2, 2'-bipyridine as anchoring ligand for nanocrystalline dye sensitized solar cells. *The Journal of Physical Chemistry B*. 2004;108(45):17553-9.

74. Chang H, Wu H, Chen T, Huang K, Jwo C, Lo Y. Dye-sensitized solar cell using natural dyes extracted from spinach and ipomoea. *Journal of Alloys and Compounds*. 2010;495(2):606-10.
75. Abodunrin T, Obafemi O, Boyo A, Adebayo T, Jimoh R. The effect of electrolyte on dye sensitized solar cells using natural dye from mango (*M. indica* L.) Leaf as Sensitizer. *Advances in Materials Physics and Chemistry*. 2015;5.
76. Faqih P, Nurosyid F, Kusumaningsih T, editors. Effect of acidic level (pH) of red dragon fruit (*Hylocereus costaricensis*) peels extract on DSSC efficiency. *AIP Conference Proceedings*; 2020: AIP Publishing LLC.
77. Ito S. Investigation of dyes for dye-sensitized solar cells: Ruthenium-complex dyes, metal-free dyes, metal-complex porphyrin dyes and natural dyes. *Solar Cells-Dye-Sensitized Devices*. 2011:19-48.
78. Manthou VS, Pefkianakis EK, Falaras P, Vougioukalakis GC. Co-Adsorbents: A Key Component in Efficient and Robust Dye-Sensitized Solar Cells. *ChemSusChem*. 2015;8(4):588-99.
79. Choi IT, Ju MJ, Song SH, Kim SG, Cho DW, Im C, et al. Tailor-Made Hole-Conducting Coadsorbents for Highly Efficient Organic Dye-Sensitized Solar Cells. *Chemistry—A European Journal*. 2013;19(46):15545-55.
80. Wang P, Zakeeruddin S, Humphry-Baker R, Moser J, Grätzel M. Molecular-scale interface engineering of TiO₂ nanocrystals: improving the efficiency and stability of dye-sensitized solar cells. *Advanced Materials*. 2003;15:2101-4.
81. Ren X, Feng Q, Zhou G, Huang C-H, Wang Z-S. Effect of cations in coadsorbate on charge recombination and conduction band edge movement in dye-sensitized solar cells. *The Journal of Physical Chemistry C*. 2010;114(15):7190-5.
82. Mathew S, Yella A, Gao P, Humphry-Baker R, Curchod BF, Ashari-Astani N, et al. Dye-sensitized solar cells with 13% efficiency achieved through the molecular engineering of porphyrin sensitizers. *Nature chemistry*. 2014;6(3):242-7.
83. Wang C-L, Chang Y-C, Lan C-M, Lo C-F, Diao EW-G, Lin C-Y. Enhanced light harvesting with π -conjugated cyclic aromatic hydrocarbons for porphyrin-sensitized solar cells. *Energy & Environmental Science*. 2011;4(5):1788-95.
84. Yella A, Lee H-W, Tsao HN, Yi C, Chandiran AK, Nazeeruddin MK, et al. Porphyrin-sensitized solar cells with cobalt (II/III)-based redox electrolyte exceed 12 percent efficiency. *science*. 2011;334(6056):629-34.
85. Kurotobi K, Toude Y, Kawamoto K, Fujimori Y, Ito S, Chabera P, et al. Highly Asymmetrical Porphyrins with Enhanced Push–Pull Character for Dye-Sensitized Solar Cells. *Chemistry—A European Journal*. 2013;19(50):17075-81.
86. Yella A, Mai CL, Zakeeruddin SM, Chang SN, Hsieh CH, Yeh CY, et al. Molecular engineering of push–pull porphyrin dyes for highly efficient dye-sensitized solar cells: The role of benzene spacers. *Angewandte Chemie*. 2014;126(11):3017-21.
87. Mozaffari S, Nateghi MR, Zarandi MB. An overview of the Challenges in the commercialization of dye sensitized solar cells. *Renewable and Sustainable Energy Reviews*. 2017;71:675-86.
88. Boschloo G, Hagfeldt A. Characteristics of the iodide/triiodide redox mediator in dye-sensitized solar cells. *Accounts of chemical research*. 2009;42(11):1819-26.
89. Gutmann V. Empirical parameters for donor and acceptor properties of solvents. *Electrochimica Acta*. 1976;21(9):661-70.
90. Wang X, Kulkarni SA, Ito BI, Batabyal SK, Nonomura K, Wong CC, et al. Nanoclay gelation approach toward improved dye-sensitized solar cell efficiencies: an investigation of charge transport and shift in the TiO₂ conduction band. *ACS applied materials & interfaces*. 2013;5(2):444-50.

91. Dong R-X, Shen S-Y, Chen H-W, Wang C-C, Shih P-T, Liu C-T, et al. A novel polymer gel electrolyte for highly efficient dye-sensitized solar cells. *Journal of materials chemistry A*. 2013;1(29):8471-8.
92. Chen K, Liou C, Lee C, Chen F, editors. Development of solid polymeric electrolyte for DSSC device. 2010 35th IEEE Photovoltaic Specialists Conference; 2010: IEEE.
93. Lee SY, Yoo B, Lim MK, Lee T-k, Priya AS, Kim K-J. Influence of Nylon 6 in I³-/I⁻ Redox Electrolyte on the Photovoltaic Performance and Stability of Dye-Sensitized Solar Cells. *Langmuir*. 2010;26(9):6638-42.
94. Park SJ, Yoo K, Kim J-Y, Kim JY, Lee D-K, Kim B, et al. Water-based thixotropic polymer gel electrolyte for dye-sensitized solar cells. *ACS nano*. 2013;7(5):4050-6.
95. Tsai C-H, Lu C-Y, Chen M-C, Huang T-W, Wu C-C, Chung Y-W. Efficient gel-state dye-sensitized solar cells adopting polymer gel electrolyte based on poly (methyl methacrylate). *Organic electronics*. 2013;14(11):3131-7.
96. Wang P, Zakeeruddin SM, Moser JE, Nazeeruddin MK, Sekiguchi T, Grätzel M. A stable quasi-solid-state dye-sensitized solar cell with an amphiphilic ruthenium sensitizer and polymer gel electrolyte. *Nature materials*. 2003;2(6):402-7.
97. Tedla A, Tai Y. Influence of binary solvent system on the stability and efficiency of liquid dye sensitized solar cells. *Journal of Photochemistry and Photobiology A: Chemistry*. 2018;358:70-5.
98. Yusof SMM, Yahya WZN. Binary ionic liquid electrolyte for dye-sensitized solar cells. *Procedia engineering*. 2016;148:100-5.
99. Fei Z, Kuang D, Zhao D, Klein C, Ang WH, Zakeeruddin SM, et al. A supercooled imidazolium iodide ionic liquid as a low-viscosity electrolyte for dye-sensitized solar cells. *Inorganic Chemistry*. 2006;45(26):10407-9.
100. Abate A, Petrozza A, Roiati V, Guarnera S, Snaith H, Matteucci F, et al. A polyfluoroalkyl imidazolium ionic liquid as iodide ion source in dye sensitized solar cells. *Organic Electronics*. 2012;13(11):2474-8.
101. Gondane V, Bhargava P. Acetylacetone: A promising electrolyte solvent for dye sensitized solar cells. *RSC advances*. 2016;6(43):37167-72.
102. Sauvage F, Chhor S, Marchioro A, Moser J-E, Graetzel M. Butyronitrile-based electrolyte for dye-sensitized solar cells. *Journal of the American Chemical Society*. 2011;133(33):13103-9.
103. Hara K, Horiguchi T, Kinoshita T, Sayama K, Arakawa H. Influence of electrolytes on the photovoltaic performance of organic dye-sensitized nanocrystalline TiO₂ solar cells. *Solar Energy Materials and Solar Cells*. 2001;70(2):151-61.
104. Lin C-Y, Lin J-Y, Wan C-C, Wei T-C. High-performance and low platinum loading electrodeposited-Pt counter electrodes for dye-sensitized solar cells. *Electrochimica Acta*. 2011;56(5):1941-6.
105. Hara K, Nishikawa T, Kurashige M, Kawauchi H, Kashima T, Sayama K, et al. Influence of electrolyte on the photovoltaic performance of a dye-sensitized TiO₂ solar cell based on a Ru (II) terpyridyl complex photosensitizer. *Solar energy materials and solar cells*. 2005;85(1):21-30.
106. Tichnell CR, Miller JN, Liu C, Mukherjee S, Jakubikova E, McCusker JK. Influence of electrolyte composition on ultrafast interfacial electron transfer in Fe-sensitized TiO₂-based solar cells. *The Journal of Physical Chemistry C*. 2020;124(3):1794-811.
107. Kuang D, Wang P, Ito S, Zakeeruddin SM, Grätzel M. Stable mesoscopic dye-sensitized solar cells based on tetracyanoborate ionic liquid electrolyte. *Journal of the American Chemical Society*. 2006;128(24):7732-3.
108. Kuang D, Klein C, Zhang Z, Ito S, Moser JE, Zakeeruddin SM, et al. Stable, high-efficiency ionic-liquid-based mesoscopic dye-sensitized solar cells. *small*. 2007;3(12):2094-102.

109. Clifford JN, Palomares E, Nazeeruddin MK, Grätzel M, Durrant JR. Dye dependent regeneration dynamics in dye sensitized nanocrystalline solar cells: evidence for the formation of a ruthenium bipyridyl cation/iodide intermediate. *The Journal of Physical Chemistry C*. 2007;111(17):6561-7.
110. Peter LM. Characterization and modeling of dye-sensitized solar cells. *The Journal of Physical Chemistry C*. 2007;111(18):6601-12.
111. Daeneke T, Kwon T-H, Holmes AB, Duffy NW, Bach U, Spiccia L. High-efficiency dye-sensitized solar cells with ferrocene-based electrolytes. *Nature chemistry*. 2011;3(3):211-5.
112. Nath NCD, Sarker S, Ahammad AS, Lee J-J. Spatial arrangement of carbon nanotubes in TiO₂ photoelectrodes to enhance the efficiency of dye-sensitized solar cells. *Physical Chemistry Chemical Physics*. 2012;14(13):4333-8.
113. Nath NCD, Lee J-J. Binary redox electrolytes used in dye-sensitized solar cells. *Journal of Industrial and Engineering Chemistry*. 2019;78:53-65.
114. Nath NCD, Lee HJ, Choi W-Y, Lee J-J. Electrochemical approach to enhance the open-circuit voltage (Voc) of dye-sensitized solar cells (DSSCs). *Electrochimica Acta*. 2013;109:39-45.
115. Stergiopoulos T, Rozi E, Karagianni C-S, Falaras P. Influence of electrolyte co-additives on the performance of dye-sensitized solar cells. *Nanoscale research letters*. 2011;6(1):307.
116. Nakade S, Kanzaki T, Kambe S, Wada Y, Yanagida S. Investigation of cation-induced degradation of dye-sensitized solar cells for a new strategy to long-term stability. *Langmuir*. 2005;21(24):11414-7.
117. Gao J, Achari MB, Kloo L. Long-term stability for cobalt-based dye-sensitized solar cells obtained by electrolyte optimization. *Chemical Communications*. 2014;50(47):6249-51.
118. Nguyen PT, Do Nguyen NP. 4, 4'-dinonyl-2, 2'-bipyridine as an alternative electrolyte additive for improving the thermal stability of ruthenium dyes in dye-sensitized solar cells. *Journal of Physics and Chemistry of Solids*. 2018;122:234-8.
119. Lee H-S, Bae S-H, Jo Y, Kim K-J, Jun Y, Han C-H. A high temperature stable electrolyte system for dye-sensitized solar cells. *Electrochimica acta*. 2010;55(24):7159-65.
120. Lee H, Bae S, Han C, Sekhon S. Efficiency enhancement of dye-sensitized solar cells with addition of additives (single/binary) to ionic liquid electrolyte. *Bulletin of Materials Science*. 2012;35(6):1003-10.
121. Fredin K, Nissfolk J, Boschloo G, Hagfeldt A. The influence of cations on charge accumulation in dye-sensitized solar cells. *Journal of Electroanalytical Chemistry*. 2007;609(2):55-60.
122. Liu Y, Hagfeldt A, Xiao X-R, Lindquist S-E. Investigation of influence of redox species on the interfacial energetics of a dye-sensitized nanoporous TiO₂ solar cell. *Solar Energy Materials and Solar Cells*. 1998;55(3):267-81.
123. Kusama H, Arakawa H. Influence of benzimidazole additives in electrolytic solution on dye-sensitized solar cell performance. *Journal of Photochemistry and Photobiology A: Chemistry*. 2004;162(2-3):441-8.
124. Bai Y, Cao Y, Zhang J, Wang M, Li R, Wang P, et al. High-performance dye-sensitized solar cells based on solvent-free electrolytes produced from eutectic melts. *Nature materials*. 2008;7(8):626-30.
125. Fischer A, Pettersson H, Hagfeldt A, Boschloo G, Kloo L, Gorlov M. Crystal formation involving 1-methylbenzimidazole in iodide/triiodide electrolytes for dye-sensitized solar cells. *Solar energy materials and solar cells*. 2007;91(12):1062-5.
126. Hinsch A, Kroon J, Kern R, Uhlendorf I, Holzbock J, Meyer A, et al. Long-term stability of dye-sensitized solar cells. *Progress in Photovoltaics: Research and Applications*. 2001;9(6):425-38.

127. Law C, Pathirana SC, Li X, Anderson AY, Barnes PR, Listorti A, et al. Water-based electrolytes for dye-sensitized solar cells. *Advanced Materials*. 2010;22(40):4505-9.
128. Heo N, Jun Y, Park JH. Dye molecules in electrolytes: new approach for suppression of dye-desorption in dye-sensitized solar cells. *Scientific reports*. 2013;3(1):1-6.
129. Salvatori P, Marotta G, Cinti A, Anselmi C, Mosconi E, De Angelis F. Supramolecular interactions of chenodeoxycholic acid increase the efficiency of dye-sensitized solar cells based on a cobalt electrolyte. *The Journal of Physical Chemistry C*. 2013;117(8):3874-87.
130. Konstantakou M, Falaras P, Stergiopoulos T. Blocking recombination in Ru (II) complex-sensitized solar cells by incorporating co-adsorbents as additives in the Co (II)/(III)-based redox electrolytes. *Polyhedron*. 2014;82:109-15.
131. Thomas S, Deepak T, Anjusree G, Arun T, Nair SV, Nair AS. A review on counter electrode materials in dye-sensitized solar cells. *Journal of Materials Chemistry A*. 2014;2(13):4474-90.
132. Li Gr, Wang F, Jiang Qw, Gao Xp, Shen Pw. Carbon nanotubes with titanium nitride as a low-cost counter-electrode material for dye-sensitized solar cells. *Angewandte Chemie International Edition*. 2010;49(21):3653-6.
133. Li G, Wang F, Song J, Xiong F, Gao X. TiN-conductive carbon black composite as counter electrode for dye-sensitized solar cells. *Electrochimica Acta*. 2012;65:216-20.
134. Tang Q, Duan J, Duan Y, He B, Yu L. Recent advances in alloy counter electrodes for dye-sensitized solar cells. A critical review. *Electrochimica Acta*. 2015;178:886-99.
135. Murakami TN, Ito S, Wang Q, Nazeeruddin MK, Bessho T, Cesar I, et al. Highly efficient dye-sensitized solar cells based on carbon black counter electrodes. *Journal of the Electrochemical Society*. 2006;153(12):A2255.
136. Wu J, Lan Z, Lin J, Huang M, Huang Y, Fan L, et al. Counter electrodes in dye-sensitized solar cells. *Chemical Society Reviews*. 2017;46(19):5975-6023.
137. Wang G, Xing W, Zhuo S. The production of polyaniline/graphene hybrids for use as a counter electrode in dye-sensitized solar cells. *Electrochimica Acta*. 2012;66:151-7.
138. Tai Q, Chen B, Guo F, Xu S, Hu H, Sebo B, et al. In situ prepared transparent polyaniline electrode and its application in bifacial dye-sensitized solar cells. *Acs Nano*. 2011;5(5):3795-9.
139. He B, Meng X, Tang Q, Li P, Yuan S, Yang P. Low-cost CoPt alloy counter electrodes for efficient dye-sensitized solar cells. *Journal of Power Sources*. 2014;260:180-5.
140. He B, Tang Q, Yu L, Yang P. Cost-effective alloy counter electrodes as a new avenue for high-efficiency dye-sensitized solar cells. *Electrochimica Acta*. 2015;158:397-402.
141. Liu J, Tang Q, He B, Yu L. Cost-effective, transparent iron selenide nanoporous alloy counter electrode for bifacial dye-sensitized solar cell. *Journal of Power Sources*. 2015;282:79-86.
142. He B, Meng X, Tang Q. Low-cost counter electrodes from CoPt alloys for efficient dye-sensitized solar cells. *ACS applied materials & interfaces*. 2014;6(7):4812-8.
143. Priani W, Nurosyid F, Suryana R, editors. The effect of Pt-counter electrode deposition methods on the efficiency of Dye-Sensitized Solar Cells. *Journal of Physics: Conference Series*; 2019: IOP Publishing.
144. Song MY, Chaudhari KN, Park J, Yang D-S, Kim JH, Kim M-S, et al. High efficient Pt counter electrode prepared by homogeneous deposition method for dye-sensitized solar cell. *Applied energy*. 2012;100:132-7.
145. Fang X, Ma T, Guan G, Akiyama M, Kida T, Abe E. Effect of the thickness of the Pt film coated on a counter electrode on the performance of a dye-sensitized solar cell. *Journal of Electroanalytical Chemistry*. 2004;570(2):257-63.

146. Jeong H, Pak Y, Hwang Y, Song H, Lee KH, Ko HC, et al. Enhancing the charge transfer of the counter electrode in dye-sensitized solar cells using periodically aligned platinum nanocups. *Small*. 2012;8(24):3757-61.
147. Syrokostas G, Siokou A, Leftheriotis G, Yianoulis P. Degradation mechanisms of Pt counter electrodes for dye sensitized solar cells. *Solar Energy Materials and Solar Cells*. 2012;103:119-27.
148. Sacco A, Pugliese D, Lamberti A, Castellino M, Chiodoni A, Virga A, et al. A long-term analysis of Pt counter electrodes for Dye-sensitized Solar Cells exploiting a microfluidic housing system. *Materials Chemistry and Physics*. 2015;161:74-83.
149. Murakoshi K, Kano G, Wada Y, Yanagida S, Miyazaki H, Matsumoto M, et al. Importance of binding states between photosensitizing molecules and the TiO₂ surface for efficiency in a dye-sensitized solar cell. *Journal of Electroanalytical Chemistry*. 1995;396(1-2):27-34.
150. Pérez León C, Kador L, Peng B, Thelakkat M. Characterization of the adsorption of Ru-bpy dyes on mesoporous TiO₂ films with UV– Vis, Raman, and FTIR spectroscopies. *The Journal of Physical Chemistry B*. 2006;110(17):8723-30.
151. Holliman PJ, Kershaw C, Connell A, Jones EW, Hobbs R, Anthony R, et al. A perspective on using experiment and theory to identify design principles in dye-sensitized solar cells. *Science and Technology of Advanced Materials*. 2018;19(1):599-612.
152. Eisfeld A, Briggs J. The J-and H-bands of organic dye aggregates. *Chemical Physics*. 2006;324(2-3):376-84.
153. Chen H, Gong Y, Vázquez-Mayagoitia AI, Zhang J, Cole JM. Dye Aggregation, Photostructural Reorganization and Multiple Concurrent Dye... TiO₂ Binding Modes in Dye-Sensitized Solar Cell Working Electrodes Containing Benzothiadiazole-Based Dye RK-1. *ACS Applied Energy Materials*. 2019;3(1):423-30.
154. Shoute LC, Loppnow GR. Excited-state metal-to-ligand charge transfer dynamics of a ruthenium (II) dye in solution and adsorbed on TiO₂ nanoparticles from resonance Raman spectroscopy. *Journal of the American Chemical Society*. 2003;125(50):15636-46.
155. Wang Z-S, Hara K, Dan-oh Y, Kasada C, Shinpo A, Suga S, et al. Photophysical and (photo) electrochemical properties of a coumarin dye. *The Journal of Physical Chemistry B*. 2005;109(9):3907-14.
156. Singh J, Gusain A, Saxena V, Chauhan A, Veerender P, Koiry S, et al. XPS, UV– vis, FTIR, and EXAFS studies to investigate the binding mechanism of N719 dye onto oxalic acid treated TiO₂ and its implication on photovoltaic properties. *The Journal of Physical Chemistry C*. 2013;117(41):21096-104.
157. Pescitelli G, Di Bari L, Berova N. Application of electronic circular dichroism in the study of supramolecular systems. *Chemical Society Reviews*. 2014;43(15):5211-33.
158. Patrocínio AOT, Paniago EB, Paniago RM, Iha NYM. XPS characterization of sensitized n-TiO₂ thin films for dye-sensitized solar cell applications. *Applied Surface Science*. 2008;254(6):1874-9.
159. Zubavichus Y, Slovokhotov YL, Nazeeruddin MK, Zakeeruddin S, Grätzel M, Shklover V. Structural characterization of solar cell prototypes based on nanocrystalline TiO₂ anatase sensitized with Ru complexes. X-ray diffraction, XPS, and XAFS spectroscopy study. *Chemistry of materials*. 2002;14(8):3556-63.
160. Deacon G, Phillips R. Relationships between the carbon-oxygen stretching frequencies of carboxylato complexes and the type of carboxylate coordination. *Coordination chemistry reviews*. 1980;33(3):227-50.
161. Zhang L, Cole JM. Anchoring groups for dye-sensitized solar cells. *ACS applied materials & interfaces*. 2015;7(6):3427-55.
162. Sharma K, Sharma V, Sharma S. Dye-sensitized solar cells: fundamentals and current status. *Nanoscale research letters*. 2018;13:1-46.

163. Lohrasbi M, Pattanapanishawat P, Isenberg M, Chuang SS, editors. Degradation study of dye-sensitized solar cells by electrochemical impedance and FTIR spectroscopy. 2013 IEEE Energytech; 2013: IEEE.
164. Lai SC, Connor KNP, Ke L. Degradation mechanisms and electron kinetics analysis in aging dye sensitized solar cell using electrochemical impedance spectroscopy. *Journal of the Electrochemical Society*. 2011;158(12):H1193.
165. Jiang R, Anderson A, Barnes PR, Xiaoe L, Law C, O'Regan BC. 2000 hours photostability testing of dye sensitised solar cells using a cobalt bipyridine electrolyte. *Journal of Materials Chemistry A*. 2014;2(13):4751-7.
166. Lee C-H, Lee K-M, Tung Y-L, Wu J-M. Degradation analysis of thermal aged back-illuminated dye-sensitized solar cells. *Journal of The Electrochemical Society*. 2012;159(4):B430.
167. Sommeling PM, Späth M, Smit H, Bakker N, Kroon J. Long-term stability testing of dye-sensitized solar cells. *Journal of Photochemistry and Photobiology A: Chemistry*. 2004;164(1-3):137-44.
168. Yum J-H, Humphry-Baker R, Zakeeruddin SM, Nazeeruddin MK, Grätzel M. Effect of heat and light on the performance of dye-sensitized solar cells based on organic sensitizers and nanostructured TiO₂. *Nano Today*. 2010;5(2):91-8.
169. Grünwald R, Tributsch H. Mechanisms of instability in Ru-based dye sensitization solar cells. *The Journal of Physical Chemistry B*. 1997;101(14):2564-75.
170. Xue G, Guo Y, Yu T, Guan J, Yu X, Zhang J, et al. Degradation mechanisms investigation for long-term thermal stability of dye-sensitized solar cells. *Int J Electrochem Sci*. 2012;7(2):1496-511.
171. Kohle O, Grätzel M, Meyer AF, Meyer TB. The photovoltaic stability of, bis (isothiocyanato) ruthenium (II)-bis-2, 2' bipyridine-4, 4'-dicarboxylic acid and related sensitizers. *Advanced Materials*. 1997;9(11):904-6.
172. Agrell HG, Lindgren J, Hagfeldt A. Coordinative interactions in a dye-sensitized solar cell. *Journal of Photochemistry and Photobiology A: Chemistry*. 2004;164(1-3):23-7.
173. Greijer H, Lindgren J, Hagfeldt A. Resonance Raman scattering of a dye-sensitized solar cell: mechanism of thiocyanato ligand exchange. *The Journal of Physical Chemistry B*. 2001;105(27):6314-20.
174. Kwak CH, Baeg JH, Yang IM, Giribabu K, Lee S, Huh YS. Degradation analysis of dye-sensitized solar cell module consisting of 22 unit cells for thermal stability: Raman spectroscopy study. *Solar Energy*. 2016;130:244-9.
175. Agrell HG, Lindgren J, Hagfeldt A. Degradation mechanisms in a dye-sensitized solar cell studied by UV-VIS and IR spectroscopy. *Solar Energy*. 2003;75(2):169-80.
176. Nakajima S, Katoh R. Mechanism of degradation of electrolyte solutions for dye-sensitized solar cells under ultraviolet light irradiation. *Chemical Physics Letters*. 2015;619:36-8.
177. Kato N, Higuchi K, Tanaka H, Nakajima J, Sano T, Toyoda T. Improvement in long-term stability of dye-sensitized solar cell for outdoor use. *Solar Energy Materials and Solar Cells*. 2011;95(1):301-5.
178. Kato N, Takeda Y, Higuchi K, Takeichi A, Sudo E, Tanaka H, et al. Degradation analysis of dye-sensitized solar cell module after long-term stability test under outdoor working condition. *Solar Energy Materials and Solar Cells*. 2009;93(6-7):893-7.
179. Mohanty SP, More V, Bhargava P. Effect of aging conditions on the performance of dip coated platinum counter electrode based dye sensitized solar cells. *RSC advances*. 2015;5(24):18647-54.
180. Krašovec UO, Bokalič M, Topič M. Ageing of DSSC studied by electroluminescence and transmission imaging. *Solar Energy Materials and Solar Cells*. 2013;117:67-72.

181. Ciani L, Catelani M, Carnevale EA, Donati L, Bruzzi M. Evaluation of the aging process of dye-sensitized solar cells under different stress conditions. *IEEE Transactions on Instrumentation and Measurement*. 2014;64(5):1179-87.
182. Likodimos V, Stergiopoulos T, Falaras P, Harikisun R, Desilvestro J, Tulloch G. Prolonged light and thermal stress effects on industrial dye-sensitized solar cells: a Micro-Raman investigation on the long-term stability of aged cells. *The Journal of Physical Chemistry C*. 2009;113(21):9412-22.
183. Tiihonen A, Miettunen K, Halme J, Lepikko S, Poskela A, Lund PD. Critical analysis on the quality of stability studies of perovskite and dye solar cells. *Energy & Environmental Science*. 2018;11(4):730-8.
184. Wang Q, Moser J-E, Grätzel M. Electrochemical impedance spectroscopic analysis of dye-sensitized solar cells. *The Journal of Physical Chemistry B*. 2005;109(31):14945-53.
185. Barichello J, Vesce L, Mariani P, Leonardi E, Braglia R, Di Carlo A, et al. Stable semi-transparent dye-sensitized solar modules and panels for greenhouse application. *Energies*. 2021;14(19):6393.
186. Fakharuddin A, Jose R, Brown TM, Fabregat-Santiago F, Bisquert J. A perspective on the production of dye-sensitized solar modules. *Energy & Environmental Science*. 2014;7(12):3952-81.
187. Chae Y, Park JT, Koh JK, Kim JH, Kim E. All-solid, flexible solar textiles based on dye-sensitized solar cells with ZnO nanorod arrays on stainless steel wires. *Materials Science and Engineering: B*. 2013;178(17):1117-23.
188. Watanabe M. Dye-sensitized photocatalyst for effective water splitting catalyst. *Science and Technology of advanced MaTerialS*. 2017;18(1):705-23.
189. Yu Z, Li F, Sun L. Recent advances in dye-sensitized photoelectrochemical cells for solar hydrogen production based on molecular components. *Energy & Environmental Science*. 2015;8(3):760-75.
190. Sherman BD, McMillan NK, Willinger D, Leem G. Sustainable hydrogen production from water using tandem dye-sensitized photoelectrochemical cells. *Nano Convergence*. 2021;8:1-15.

CHAPTER 2 RESEARCH PROJECT

2.1. Aims and scope

From previous chapters and prior studies in DSSCs, it is evident that $\text{TiO}_2/\text{dye}/\text{electrolyte}$ interface has a direct influence on the efficacy and stability of the DSSCs. Hence, even though plenty of research is available, this dissertation emphasises not merely investigating the changes in the interface of DSSCs but on establishing a method to investigate the electronic properties and the interfacial changes brought up by the dye/ TiO_2 or dye/ $\text{TiO}_2/\text{electrolyte}$ interface of the DSSCs under different conditions using the surface sensitive analytical tools.

2.2. Research Project

The dissertation includes three experimental chapters enlisted as follows:

2.2.1. Anchoring modes of Ru-based N719 dye onto TiO_2 substrate

Chapter 4, this study aims to investigate the anchoring mode of N719 dye. The anchoring modes has direct influence on the stability and efficiency of the DSSCs. Understanding the anchoring modes of the N719 dye and how the anchoring modes is affected under ageing will give us insight into how the change introduced in the anchoring modes will influence on cell stability and instigate cell ageing. In this study, the dye anchoring modes of extensively studied N719 dye was re-investigated using the FTIR and ARXPS. The anchoring mode investigation of N719 is not a new topic to study, however, with many variations in the dye anchoring modes and different dye- TiO_2 configuration, the aim is to gain a broader understanding in the anchoring mode of the dye- TiO_2 configuration of our interest.

The research approach includes studying the possible anchoring modes of dye by investigating the anchoring modes of individual functional group. For this purpose, formic acid, phenyl isothiocyanate and TBA-Br salt were investigated. Further, with discrepancies in understanding the role of TBA^+ a re-sensitising test was also performed. Further using FTIR the anchoring mode of N719 dye was found to be combination of different modes of attachment, like bidentate bridging via COO^- , ester bonding and weak interaction of NCS to the TiO_2 substrate. The ARXPS helped in obtaining concentration depth profile of the dye- TiO_2 configuration. The concentration depth profile suggested that the dye is mainly concentrated towards the surface than depth. Further, the COO^- penetrates deeper into the substrate.

2.2.2. Exploring Alteration in Electrochemical Interface of Dye Sensitised Solar Cells-An Experimental Set-up for Ageing Investigation

The aim of this research study Chapter-5 is to establish an effective methodology to investigate ageing and application of various technique to explore different aspects of cell degradation.

The research approach includes establishment an effective technique to open the cell and to access the interface and further to analyse degradation at the interface. To begin with, a methodology to rinse-off the opened cell to get rid of the excess electrolyte onto the photoanode surface was analysed. A procedure of ethanol rinsing of the photoanode was applied and the alteration introduced by the procedure were investigated using surface sensitive techniques. The rinsed off solution was further analysed by drop-casting it on to blank TiO₂ substrate. Thus, the effect of ethanol rinsing on to the due adsorbed TiO₂ was quantified. The results conclude the effect of ethanol rinsing to be negligible.

Further, to comprehend the application of different techniques in inspecting the degradation at the cell interface and, to correlate the interfacial degradation with the decrease in cell performance, surface sensitive techniques such as XPS, UPS and NCISS were used to investigate the aged photoanodes. The applied techniques proved to identify the changes in the elemental composition, valence band structure and molecular concentration at the dye-TiO₂ interface of the aged photoanodes. The use of both He and Ne projectile in NCISS were investigated. Overall, an effective technique to investigate interfacial degradation in the DSSCs was developed that could correlate the decrease in the cell performance with the interfacial degradation.

2.2.3. Unveiling the Ageing Effect at the Interface of N719 Dye Sensitised Solar Cells

The aim of this research study, Chapter-6, is to investigate the changes introduced in different cell components and to determine the cause of ageing over time by applying different techniques to track the changes at device level and at the cell-interface level. In other words, it is a modified application of the methodology determined in Chapter 5.

The study intends to investigate causes of ageing in DSSCs. After reproducing the cell structure of interest, the cells are planned to age under different stress factors like dark and light. In the dark, the sample was kept under room temperature. This study uses device level analytic techniques such as JV characterisation and EIS analysis to track changes in the PV performance of the cell as well as the contribution of internal resistance to cell performance. Furthermore,

surface analytical methods such as XPS, MIES, UPS, and NCISS aid in determining the overriding factor to cell degradation.

In the study, the device level analysis and surface analysis combinedly supported in investigating the potential cause for the cell degradation. The dark ageing with stable cell performance and interfacial resistance suggests no degradation phenomenon occurring in dark ageing. For light aged sample, XPS and NCISS confirmed the I penetration into the dye-layer with overtime. Further, UPS supported the electrolyte penetrating deeper into the dye layer responsible for cell degradation and the presence of electrolyte at the surface is essential to continue the cell's functioning. FTIR confirmed upon electrolyte injection into dye layer forms dye-iodine complex which is needed to continue dye regeneration cycle which is maintained in dark aged samples but decomposes in light aged sample. Thus, the main reason for the cell degradation proposed by the study is the I penetration into the dye layer.

2.2.4. Conclusion and Outlook

This chapter summarises the key understanding of the interfacial structure of dye adsorbed TiO_2 substrate, the stability investigation of DSSCs under dark and the causative for cell degradation in light. The study's novelty is that it answers many unanswered questions related to ageing and causative of cell degradation on the PV performance of DSSCs and correlates the interfacial degradation with the decrease in cell performance. Furthermore, it involves additional development of the work covered in the thesis, potentially leading to future work and application of alternative approaches for the analysis of cell disintegration, as well as prospective application of the methodology to other fields of study. In addition, it includes the future application and advancement of DSSCs in several fields, including, IoTs, textiles and photocatalysis.

CHAPTER 3 EXPERIMENTAL METHODS

3.1. Analysis Techniques

Different surface analysis techniques applied in this study are generally employed in electron and ion spectroscopy. These techniques are used to investigate the composition and electronic properties of the samples and to analyse the changes introduced to the sample under different influential factors. Ion-spectroscopy is applied to investigate the concentration depth profile and the penetration depth of Ru and I into the TiO₂ adsorbate with ageing. The FTIR and ARXPS combined to understand the dye anchoring on the TiO₂. Table 3.1 illustrates different techniques with their probing depth, with the potential information obtained and their resolution.

Table 3.1: Enlisting different techniques applied in the study with their probing depth, the information extracted and the resolution.

Techniques	Probe	Probing Depth	Information	Resolution
<i>XPS</i>	X-ray photons- 1253.6 eV	1-10 nm	Chemical Composition and Chemical states	0.2 eV
<i>UPS</i>	UV photons- 21.2 eV	2-3 nm	Valence band structure	0.5 eV
<i>MIES</i>	Metastable He*-19.8 eV	< 0.3 nm	Electronic Structure and Molecular Orientation	0.5 eV
<i>NICISS</i>	Rare gas ions (He/Ne)-10 keV	20 nm	Concentration Depth profile (atomic level)	0.5 nm
<i>ARXPS</i>	X-ray photons- 1253.6 eV	10 nm	Concentration Depth profile (Chemical states)	0.2 eV
<i>FTIR</i>	IR radiation	Approx. in terms of micrometre	Identification of chemical bonds	3 cm ⁻¹

3.1.1. JV Characterisation

Upon illumination, the DSSCs convert sunlight into electrical energy. The PV parameters are measured to evaluate the cell performance. The cell conversion efficiency of DSSCs is measured using a solar simulator. A solar simulator consists of a source of light that represents the solar spectrum, with a 1.5 air-mass coefficient and total power density of 1000 W/m². It is crucial to follow the standard testing condition (STC) according to IEC 609043 while tracking cell performance ¹. The general concept behind JV characterisation is to apply a series of voltages through the cell device and to measure the current flowing through the cell at each voltage. In this study, a Keithley 2400/2450 source meter, operated by LabVIEW software was used. The source meter is capable of measuring current simultaneously by supplying voltage.

Efficiency is mathematically defined as the ratio of the product of open circuit voltage (V_{oc}), short circuit current (J_{sc}) and fill factor (FF) to the power of the incident light (P_{in}), given by Equation 3.1.

$$\eta = \frac{J_{sc} \cdot V_{oc} \cdot FF}{P_{in}} \times 100\% \quad \text{Equation 3.1}$$

The J_{sc} is the integral of the product of the spectral wavelength $\phi(\lambda)$ and the incident photon-to-current efficiency $IPCE(\lambda)$, refer to Equation 3.2.

$$J_{sc} = \int_{\lambda_1}^{\lambda_2} \phi(\lambda) IPCE(\lambda) d\lambda \quad \text{Equation 3.2}$$

where incident photon to current efficiency (IPCE) is the product of light harvesting efficiency $\eta_{LH}(\lambda)$, charge injection efficiency $\eta_{INJ}(\lambda)$, and charge collection efficiency $\eta_{COL}(\lambda)$, see Equation 3.3.

$$IPCE(\lambda) = \eta_{LH}(\lambda) \eta_{INJ}(\lambda) \eta_{COL}(\lambda) \quad \text{Equation 3.3}$$

The PV parameter that determines the cell performance is further used to understand the degradation phenomenon. Different alterations either intrinsic or extrinsic, introduced in DSSC under various stress factors affect the PV parameter. For instance, the V_{oc} depends on the shifting of the difference between the quasi-fermi level and the redox potential of the electrolyte. In other words, fixed redox potential shifting in the CB edge of the semiconductor can influence the V_{oc} , given by Equation 3.4.

Mathematically, for DSSCs ²,

$$V_{oc} = \frac{E_{CB}}{q} + \frac{kT}{q} \ln\left(\frac{n}{N_{CB}}\right) - \frac{E_{redox}}{q} \quad \text{Equation 3.4}$$

where, n is the number of electrons in the CB of the semiconductor, N_{CB} is the effective density of states (DOS), and E_{redox} is the Nernst potential of the redox mediator.

Alike, J_{sc} depends on the absorption coefficient of the sensitizer and the intensity of incident light. However, for different intensities of the incident light, both the J_{sc} and V_{oc} shall change. The FF on the other hand indicates the connectivity between the electrolyte and the CE.

From a typical JV and PV curve, the following electrical parameters are derived, namely, J_{sc} , V_{oc} , FF, efficiency, the maximum power (P_{MPP}), current (J_{MPP}) and voltage (V_{MPP}), refer to Figure 3.1.

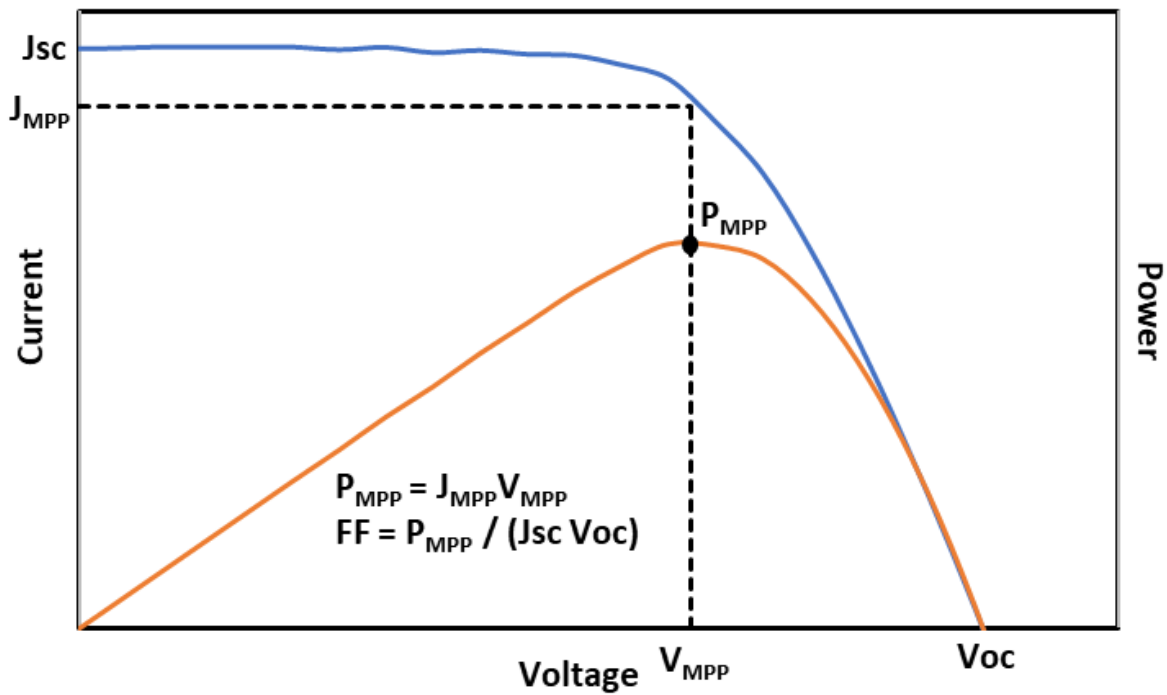


Figure 3.1: Typical JV characterisation curve ³. Reprinted with permission from Elsevier.

The J_{sc} is defined as the highest current drawn from the solar cell at zero potential. Hence, the power generated is also zero, see Equation 3.5.

$$J_{sc} = J(V = 0) \quad \text{Equation 3.5}$$

Likewise, V_{oc} is defined as the highest potential voltage where the current flow through the cell is zero, given by Equation 3.6.

$$V_{oc} = V(J = 0) \quad \text{Equation 3.6}$$

The Power generated by the solar cell (P) is given by Equation 3.7,

$$P = J \cdot V \quad \text{Equation 3.7}$$

FF on the other hand is the ratio of maximum generated power to the theoretically expected value, see Equation 3.8.

$$FF = \frac{P_{MPP}}{P_{Theo}} = \frac{J_{MPP} V_{MPP}}{J_{sc} V_{oc}} \quad \text{Equation 3.8}$$

Further, the power loss due to internal cell resistance demands the evaluation of series resistance (R_s) and shunt resistance (R_{sh}). The R_s can be estimated by taking the inverse of the slope of the JV curve near zero V_{oc} , Figure 3.2. It must be noted that V_{oc} is not affected by R_s since the current flow is zero. For an ideal cell, R_s is zero and the slope increases with a decrease in R_s .

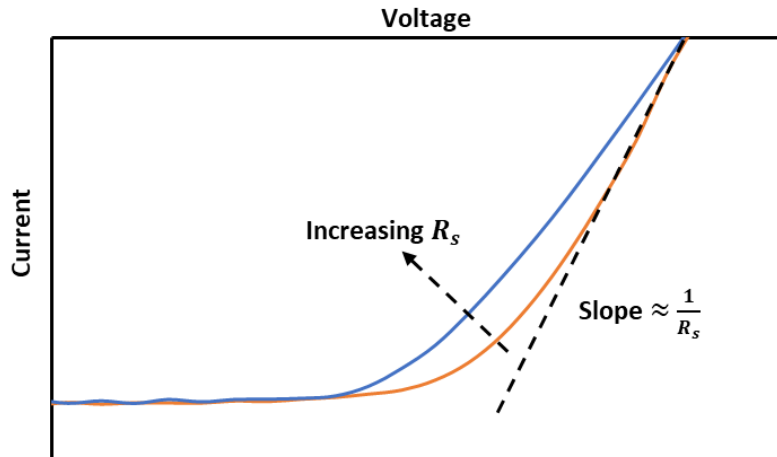


Figure 3.2: Schematic JV curve illustrating the influence of R_s .

The inverse of the slope of the JV curve near J_{sc} is used to determine R_{sh} (see Figure 3.3). For an ideal cell, R_{sh} is infinite. The decrease in R_{sh} increases the slope.

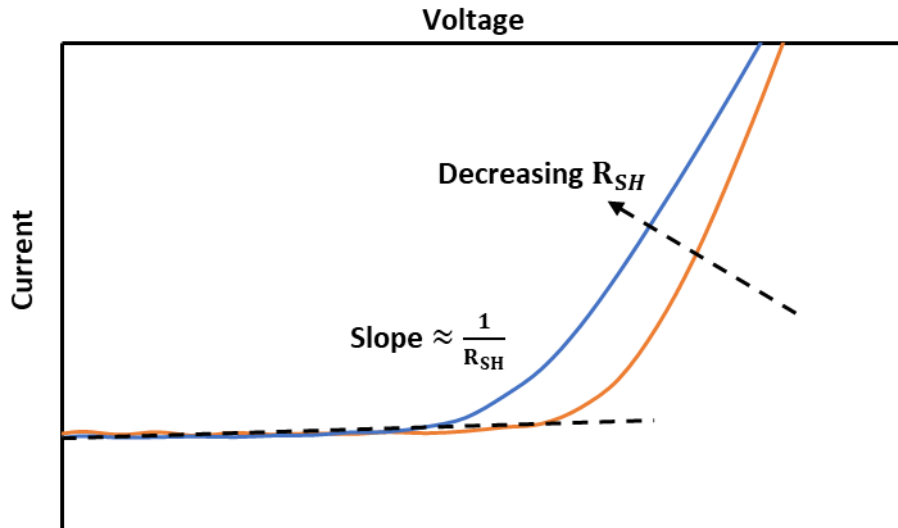


Figure 3.3: Schematic JV curve illustrating the influence of R_{sh} .

The traditional equivalent circuit diagram with the fundamental four constituent parts of the solar cell, namely photocurrent source, diode, series resistor, and shunt resistor are represented in Figure 3.4.

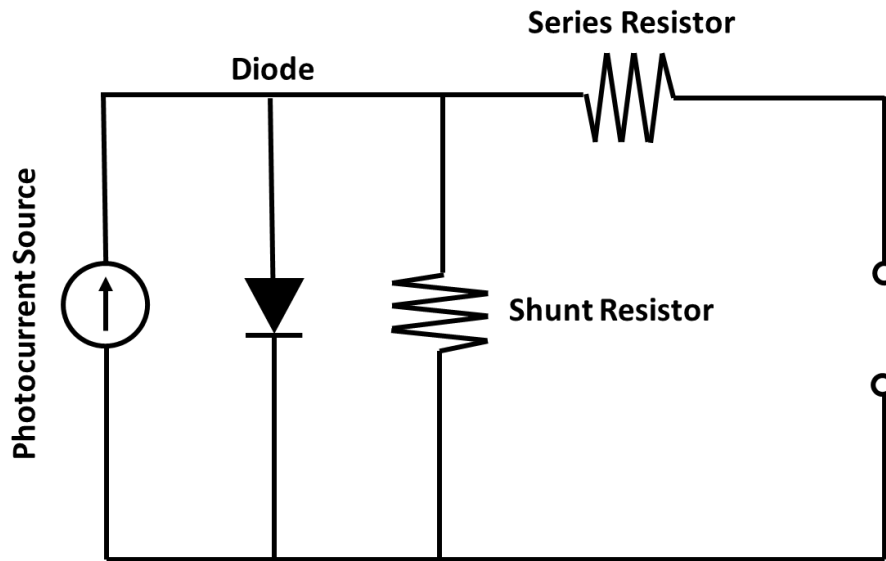


Figure 3.4: The traditional circuit model for the solar cell.

The photocurrent is the outcome of the photon absorption resulting in photoelectrons, the diode represents the electron-hole recombination at the p-n junction, and the series resistor and the shunt resistor model the internal resistance and current leakage of the cell respectively (see Equation 3.9).

Mathematically,

$$J = J_0 \left[\exp \left(\frac{e(V - JR_s)}{nk_B T} \right) - 1 \right] + \frac{V - JR_s}{R_{sh}} - J_{ph} \quad \text{Equation 3.9}$$

where, J_0 is the reverse bias saturation current density, e is the elementary charge, R_s is the series resistance, n is the diode ideality factor, k_B is Boltzmann's constant, T is the temperature and, R_{sh} is the shunt resistance.

According to the p-n junction theory of Shockley, for an ideal p-n junction diode, at $n = 1$, J_0 represents the saturation current density at reverse bias and according to Shockley-Read-Hall recombination due to defect states that at the p-n junction diode models developed for $n > 1$ the first expression, recombination current accounts for how the solar cell acts as a diode in the dark. The second expression represents the shunt current, cell leakage due to sources like pinholes that result in parasitic current moving directly from one electrode to the other⁴. In this study, different sample cells will be measured and tracked to observe changes in PV parameters with time under different stress factors.

3.1.2. Photoelectron Spectroscopy (PES)

Photoelectron Spectroscopy or Photoemission Spectroscopy is a non-destructive technique based on the photoelectric effect. In PES, either X-ray or UV photons impinge on the surface of the targeted sample in a UHV environment $\sim 10^{-10}$ bar, to avoid interference of electrons with gas molecules. The PES is a three-step process, first, the incident photon is absorbed by the electron resulting in photoexcitation. The photoexcited electron reaches the final state above Fermi; however, the electron lies within the potential field of the solid sample. This electron gets transported within the solid sample and finally escapes to a vacuum⁵. In PES the kinetic energy (KE) of the emitted electron is measured using an analyser from which the binding energy (BE) is calculated. The energy of the incident photon can be in a different regime which is further classified as UPS (UV regime $h\nu = 5-100$ eV), Soft XPS (Soft X-ray regime $h\nu = 100-1000$ eV) and XPS (X-ray regime $h\nu > 1000$ eV)⁶. The energy of the incident photon determines whether the electrons will be ejected from the core level or valence level. Figure 3.5 illuminates the difference between the XPS and UPS processes.

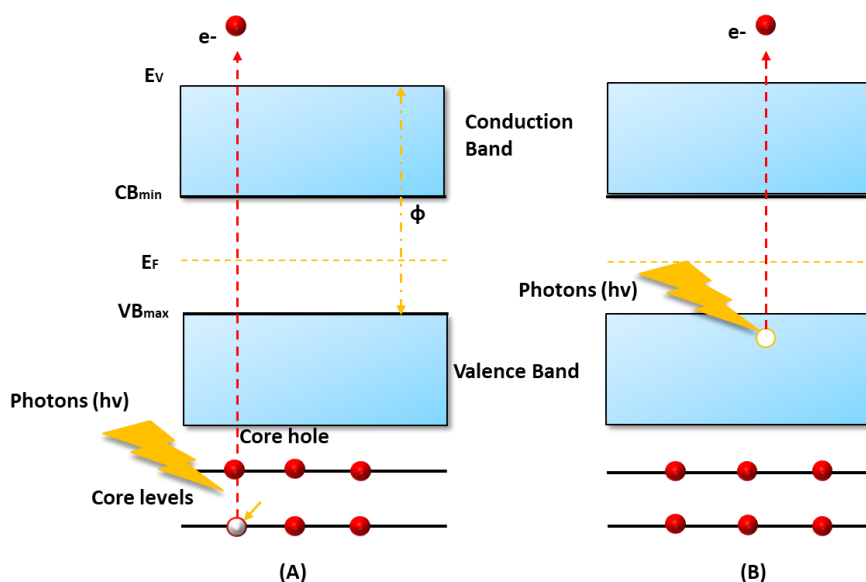


Figure 3.5: The Schematic Diagram of the photoemission Process (A) XPS and (B) UPS (modified from ⁷).

3.1.2.1. X-ray Photoelectron Spectroscopy (XPS)

XPS or Electron Spectroscopy for Chemical Analysis (ESCA) is a commonly used material characterisation technique for surface analysis. In thin film solar cells, understanding the surface properties is very crucial. The surface atoms have a bonding potential variant than the bulk atoms which makes the surface atoms more reactive and the properties of surface atoms differ from the bulk ⁸. This technique provides information about the elemental and chemical states and electronic structure information of the sample within the depth of 10 nm. XPS is based on the photoelectric effect where the X-rays irradiated on the sample surface knock out the core level electrons Figure 3.5 (A). The photons being chargeless and massless a complete transfer of energy occurs to the photoelectrons before annihilation. The concomitant photo-emitted electrons have discrete KE which is the characteristic of the emitting atoms and their BE as given in the photoelectric equation below (see Equation 3.10),

$$E_b = h\nu - E_k + \phi_{spec} \quad \text{Equation 3.10}$$

where, E_b is the electron BE in the solid, $h\nu$ is the incident photon energy, E_k is the electron KE, and ϕ_{spec} is the work function of the spectrometer, 4.15 eV calibrated with graphite sample.

The characteristic BE is the fingerprint for each core atomic level and every element; each element will produce a characteristic peak in the photoelectron spectrum ⁹. Furthermore, the peak intensity or peak area can be related to the relative concentration of the element within the

sample region ⁹. The XPS surface sensitivity is due to the electron emission from near the surface 3λ , where λ lambda is the inelastic mean free path (IMFP), which has a very small value for solids, that contributes to the XPS signal resulting in the XP spectrum. On photon penetration through the sample surface, the constituting molecules and ions from the sample undergo reactions such as inelastic collisions, recombination, and excitation which increase with the depth thus hindering the overall photoelectron ejection. The intensity of electron attenuated in the bulk decreases as the function of the distance the photoelectron has to travel to the surface is given by Equation 3.11 ¹⁰,

$$E_b = h\nu - E_k + \phi_{spec} \quad \text{Equation 3.11}$$

where, d is the measuring depth, θ is the angle between the direction of the detector and the surface normal, $\lambda(E)$ is the electron mean a free path, and I_0 is the maximum intensity.

An XPS setup consists of an X-ray source, a hemispherical analyser and a detector portrayed in Figure 3.6. A monoenergetic X-ray source (Mg, $K\alpha$) with energy $h\nu = 1253.6$ eV is used to irradiate the sample under UHV. The reason for selecting either is they produce stable beams influenced by $K\alpha_{1,2}$ which makes them nearly monochromatic ¹¹. The photons due to their limited penetrating power mostly interact with the surface atoms causing electrons to emit from the surface, creating a hole in the atomic core. The electron deficit atom relaxes either through the electronic transition from higher energy to lower energy level or through Auger electrons, where the excess leftover energy is passed to another high energy level to eject the electrons ¹²⁻¹³. The emitted photoelectron is passed through the spectrometer, and the analyser is set at a pass energy of 10 eV which would allow electrons with a certain K.E. range to pass through, which is amplified by channeltron and recorded by the detector. The angle between the X-ray source and the detector is 54.74° . This angle is also known as the “*magic angle*” because at this angle the photocurrent depends on the total cross-section (σ) and independent from the effect of light polarization or the symmetry of the initial state or the angular momenta of the photoelectron wavefunction ¹⁴. The hemispherical structure of the analyser either accelerates or decelerates the electrons that travel through the analyser by applying a floating potential and in consequence electrons with specific KE reach the channeltron analyser and get detected as discrete events. The XPS records the number of photoemitted electrons and their KE that have escaped into the vacuum level after irradiation. The known values for core-level BE and photoemission cross-section of specific element makes it easy to quantitatively analyse the spectrum, peak area and peak heights, and determine the elemental composition of the sample ¹⁵. Further, the shift in the BE in the spectrum indicates the change in the chemical

environment of the sample due to changes in the chemical potential and polarizability of elemental components ¹⁵. In this study, all the XPS measurement was conducted under transmission optimised mode with slit size 7mmx20mm.

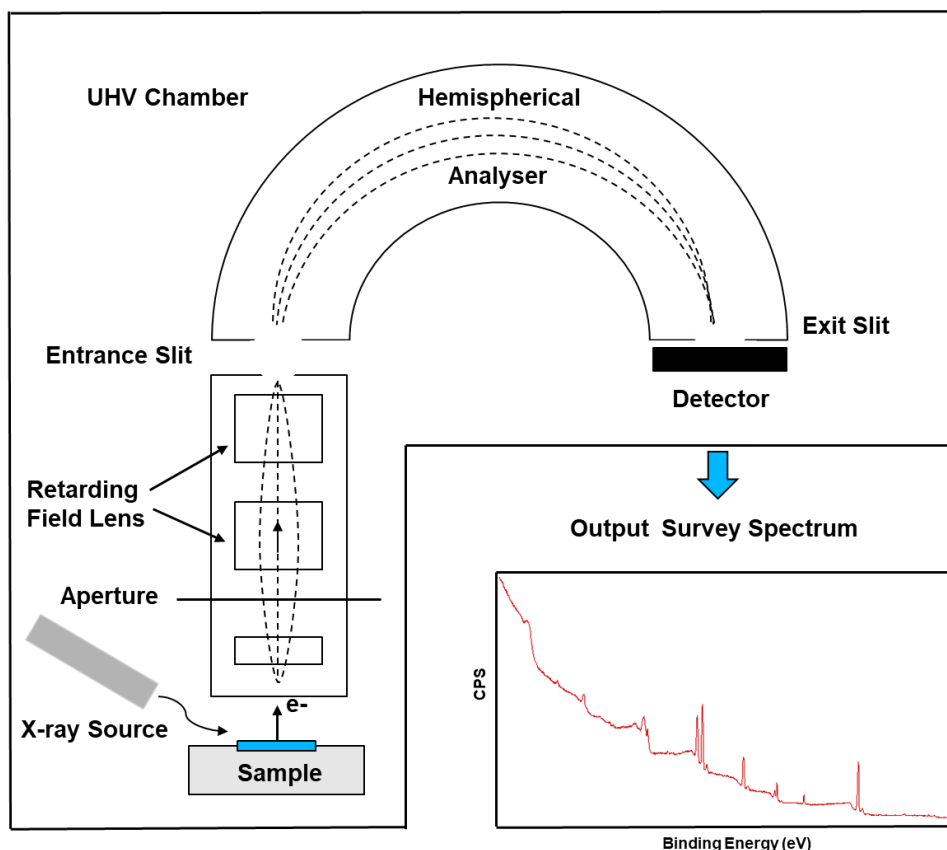


Figure 3.6: Schematic diagram illustrating the working of XPS ⁹. Reprinted with permission from Springer.

On photoemission, the possibility of electron-matter interaction than photon-matter interaction is higher due to the path length of photons and electrons, in order of a few microns and tens of Angstrom respectively. Only the electrons originating from within the tens of Angstrom depth leave with no energy loss and contribute to the spectrum. The electrons located deeper undergo inelastic energy loss before leaving the sample contributing to the background ¹⁶. The measured spectra, both the survey and high-resolution scan are plotted as a function of BE. The pass energy value for the survey spectrum and high-resolution spectrum were maintained at 40 eV and 10 eV respectively. The lower pass energy applied to high-resolution helps in decreasing the background noise by decreasing thermal de-excitation. The high-resolution scan is then fitted with Shirley's background. Shirley's background is the combination of Gaussian (70%) and Lorentzian (30%) functions. Shirley's Background incorporates the influence of the instrument and other factors included in the profile of the XPS spectrum. In Shirley's background, the background intensity at BE is proportional to the intensity of the total peak

area above the background in the lower BE range. Hence, it is the most chosen background type ¹⁷. All the peak position for the respective elements is then calibrated with the peak position of Carbon (285 eV) because the C 1s peak representing C-C/C-H bonds from adventitious carbon is established and found on many sample substances, however, a few consider it as not a good reference for calibration specifically with Al and Au foils ¹⁸. Further, quantitative analysis is obtained from the peak areas, and the peak position and the shift help in determining the chemical state ¹⁶. The probability of X-ray interaction is different for different elements, which results in different sensitivity factors or photoionization cross-sections ¹¹. The observed elemental intensity is divided by the atomic sensitivity factor (ASF) of respective elements to determine the number of atoms per cm³ ¹⁹. For a homogenous sample in analysis volume, the number of photoelectrons emitted per second, contributing to a specific spectral peak is given by Equation 3.12 ¹⁶,

$$I = n f \sigma \theta \gamma \lambda A T \quad \text{Equation 3.12}$$

where, n is the number of atoms of the elements per cm³, f is the X-ray flux in photons/cm² sec, σ is the photoelectric cross-section for the atomic orbital in cm², θ is the angular efficiency factor for the instrumental arrangement depending on the angle between the incident photon and the detected electron, γ is the efficiency for the formation of photoelectrons in the photoelectric process, λ is the IMFP, A is the area of the sample from where the photoelectrons are detected, and T is the detection efficiency of the emitted photoelectrons.

Thus,

$$n = \frac{I}{f \sigma \theta \gamma \lambda A T} \quad \text{Equation 3.13}$$

Here, the denominator in Equation 3.13 is the ASF ¹⁶.

Table 3.2 represents the ASF of the elements investigated in the study.

Table 3.2: The ASF of different elements investigated in the study using an X-ray source at an angle of 54.7° relative to the analyser ¹⁶. Reprinted with permission from John Wiley and Sons.

Elements	ASF for X-ray at 54.74°
C	0.296
O	0.71
Ti	2.0
Ru	4.27
N	0.48
S	0.67
I	6.21
F	1.0

The elemental composition of element A on the sample surface is thus calculated using Equation 3.14 ²⁰,

$$C_A(\%) = \frac{\frac{I_A}{S_A}}{\sum_i \frac{I_i}{S_i}} \times 100 \quad \text{Equation 3.14}$$

where, I_A is the integrated peak intensity of element A, and S_A is the ASF of element A.

Using XPS, we aim to investigate the change in the dye and the electrolyte components introduced with ageing and its influence on the TiO₂/dye/electrolyte interface and how the changes affect the interfacial electron transfer.

3.1.2.1.1. Angle-resolved X-ray Photoelectron Spectroscopy (ARXPS)

The analysis of ARXPS is based on The Beer-Lamberts Law with an assumption that with the increase in analysis depth ds , the photoelectron flux intensity I suffers an attenuation dI which is proportional to the flux intensity and the distance travelled, given by Equation 3.15,

$$dI = -IAds \quad \text{Equation 3.15}$$

The negative sign indicates the attenuation of photoelectron flux.

The attenuation coefficient A has the dimension of per unit length and on further integration the expression obtained by Equation 3.16,

$$\frac{I}{I_0} = e^{-As} \quad \text{Equation 3.16}$$

In XPS, the attenuation coefficient A and s are substituted by λ (IMFP) and $\frac{z}{\cos\theta}$ where z is the projection of s onto the vector perpendicular to the sample surface and θ is the photoemission angle.

Thus, Equation 3.17 is obtained,

$$I = I_0 e^{\frac{-z}{\lambda \cos\theta}} \quad \text{Equation 3.17}$$

Unlike other depth profiling techniques, ARXPS is a non-destructive method which works on the simple principle of tilting the sample to increase the surface sensitivity ²¹. XPS typically is conducted with an analyser normal to the sample which is noted as $\theta = 0^\circ$ in ARXPS, where θ is the emission angle, the angle between the analyser and the surface normal. At this angle, the electron emission occurs normally to the sample surface with less surface sensitivity ²². In other words, at this angle the take-off angle $\alpha = 90^\circ$, the angle between the analyser and the sample surface. Further, by increasing the emission angle θ or decreasing the take-off angle α , the distance travelled by the electron through the solid changes which increases the surface sensitivity and a series of consecutive measurements with different angles is then analysed to determine the concentration depth profile ²³.

The average sampling depth depends on the sine of α or cosine of θ , given by Equation 3.18,

$$d' = d \sin\alpha = d \cos\theta \quad \text{Equation 3.18}$$

The ARXPS is an in-depth analysis technique in which by varying the emission angle (θ) and considering the dependence of escape depth (d) and IMFP for photoelectrons (λ), the information depth varies such that, $d \leq 3\lambda \cos\theta$ where $\theta > 0^\circ$ (7) as illustrated in Figure 3.7.

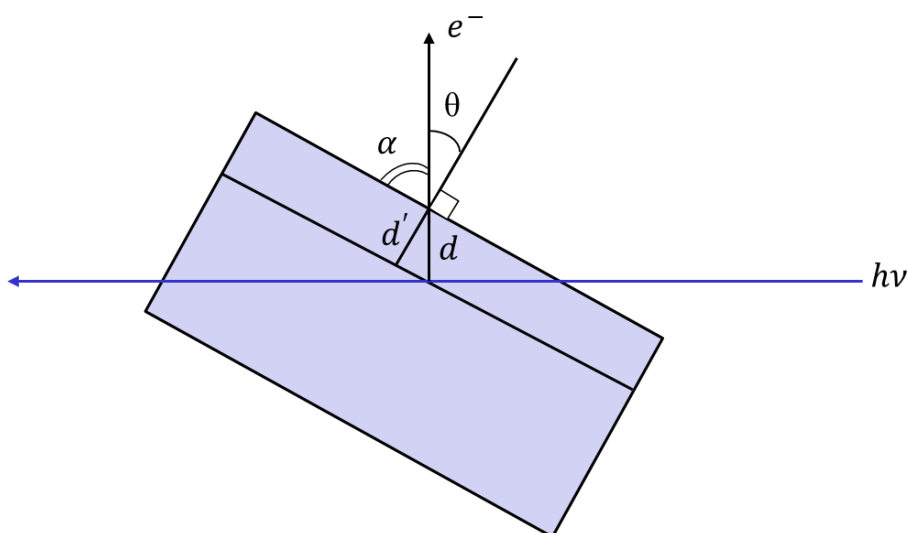


Figure 3.7: Schematic illustration of the basic working principle of ARXPS and dependence of take-off angle (α) or emission angle (θ) on the information depth probe of the sample ²⁴⁻²⁵. Reprinted with permission from the American Chemical Society.

The ARXPS analysis is based on the consideration that the intensity of the photoelectron is the function of the emission angle. The emission angle θ and the attenuation affected by the inelastic interaction of electrons within the sample influences the intensity of photoelectrons emitted from different species from different depths.

In this study, the concentration depth profile of the dye adsorbed onto the TiO_2 substrate is obtained by considering the following assumptions:

1. The sample is treated as a series of finite layers where EAL depends on the layer composition.
2. The electron mean free path depends on the KE of the electron which is calculated using NIST EAL Database for the elemental species of each layer.
3. The observed depth is inversely proportional to the cosine of the electron emission angle (θ).
4. The atomic density of the composition of each layer is used as an input parameter.

Thus, the intensity of electrons emitted I from the species i at an emission angle θ is given by²⁶,

$$I(i, \theta) = fT(E) \left(\frac{d\sigma}{d\Omega} \right) \int_0^\infty n_i(d) \cdot \exp\left(\frac{-d}{\lambda \cos\theta}\right) d(d) \quad \text{Equation 3.19}$$

where, n_i is the number density of species i , d is the depth, f is the X-ray flux, $T(E)$ is the transmission function of the spectrometer, E is the KE, $\frac{d\sigma}{d\Omega}$ is the differential photoionization cross-section of the core level, and λ is the attenuation length.

The intensity of electrons given by Equation 3.19 accounts for the intensity of electrons emitted from all layers at a certain emission angle. However, considering the effect of attenuation on the electron intensity with the depth that changes with the emission angle. It is important to apply certain algorithms on different sets of measurements taken by varying the emission angle to obtain the concentration depth profile of the sample. Hence, for simplification, the sample is divided into different layers and the intensity of electrons coming from each layer is calculated using Equation 3.20²⁶,

$$I(i, j, \theta) = fT_i \frac{d\sigma_i}{d\Omega} n_i(j) \lambda_j(\theta) \left[1 - \exp\left(-\frac{d_j}{\lambda_j(\theta)}\right) \right] \prod_{m=1}^{j-1} \exp\left(-\frac{d_m}{\lambda_m(\theta)}\right) \quad \text{Equation 3.20}$$

Equation 3.21 is the entire sum of the contribution of the species in each layer, given by²⁷,

$$I(i, \theta) = \sum_1^j \left\{ fT_i \frac{d\sigma_i}{d\Omega} n_i(j) \lambda_j(\theta) \left[1 - \exp\left(-\frac{d_j}{\lambda_j(\theta)}\right) \right] \prod_{m=1}^{j-1} \exp\left(-\frac{d_m}{\lambda_m(\theta)}\right) \right\} \quad \text{Equation 3.21}$$

where j is the number of layers.

ARXPS will help in investigating the layer composition of the samples and modelling the concentration depth profile.

3.1.3. Ultra-violet Photoelectron Spectroscopy (UPS)

UPS is based on the photoelectric effect explained in Figure 3.5 (B). In UPS, He I, 584- Å resonance lines are used to irradiate the sample and probe the valence orbitals of the sample surface. The He-I have energy 21.2 eV sufficient to ionize electrons from most of the valence molecular orbitals that can constitute chemical bonds²⁸. On irradiation, the valence level

electrons get ejected which passes through the hemispherical analyser. An additional bias (- 10 V) is applied to ensure the secondary electrons emitted with added KE of the electrons reach the detector. The added bias deconvolutes the true work function from the work function of the spectrometer. This bias is accounted for in determining the BE of the electrons (see Equation 3.22).

$$E_b = h\nu - (E_k + 10 \text{ eV}) - \phi_{spec} \quad \text{Equation 3.22}$$

where, E_b is the electron BE in the solid, $h\nu$ is the incident photon energy 21.2 eV, E_k is the electron KE, and ϕ_{spec} is the work function of the spectrometer.

UPS exhibits high sensitivity for lesser depth than XPS. This is due to short *IMFP* for electrons (λ) within a solid. As shown in Figure 3.8, for XPS, the depth information is 3λ which is 10 nm but for UPS the information depth is within 2-3 nm. This makes UPS more surface sensitive. Unlike XPS, the low energy of the incident photon is smaller than the BE of the core level electrons, limiting the photon interaction to the valence level electrons which makes it possible to investigate the valence band structure of the sample surface⁹. The application of UPS is in determining the orbital involvement in the bonding between the adsorbate and adsorbent²⁹.

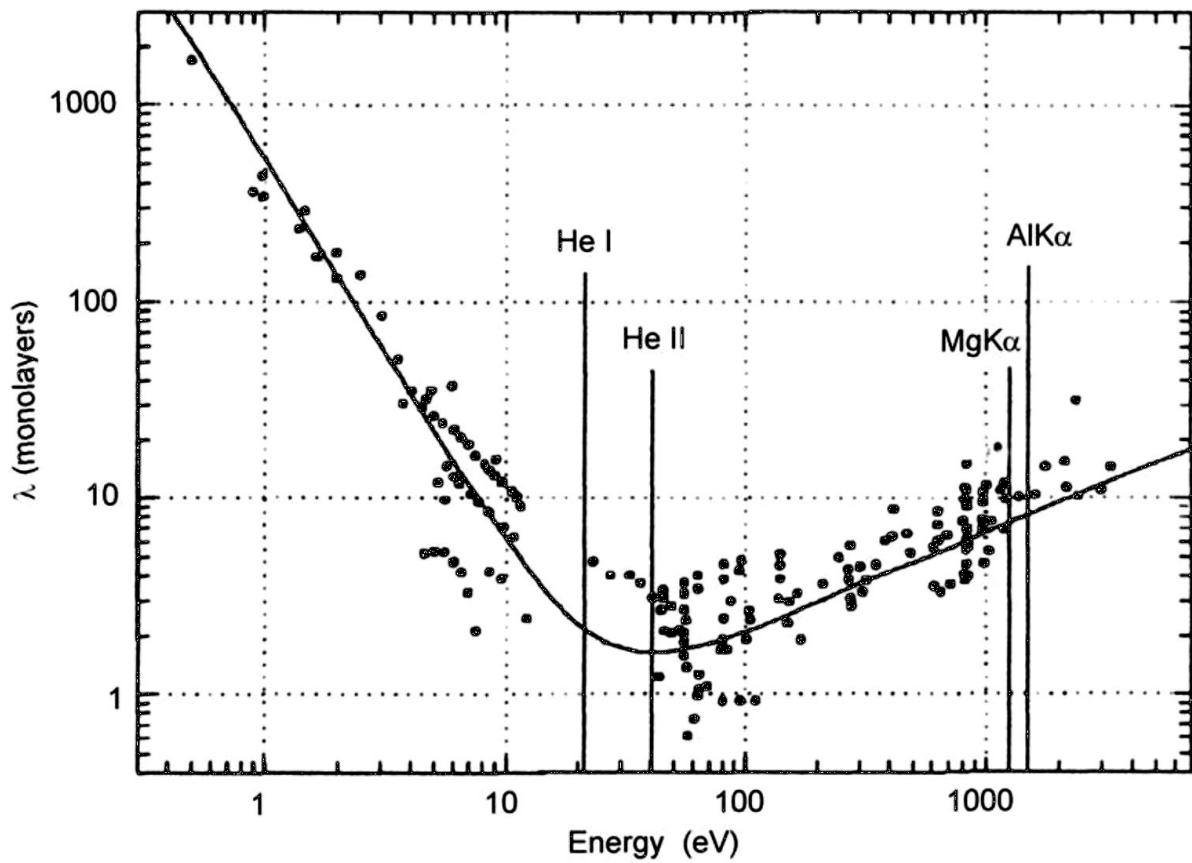


Figure 3.8: The IMFP (λ) for solid as a function of applied energy for XPS and UPS photon sources³⁰. Reprinted with permission from John Wiley and Sons.

Further, the UP spectra are used to determine the work function of the sample. Taken from Figure 3.9 the work function of the sample is derived using the Equation 3.23.

$$\phi_{sample} = h\nu - (\text{High energy cut-off } E_b - E_F) \quad \text{Equation 3.23}$$

Valence band structure carries crucial information about molecular bonding and charge transfer in the sample.

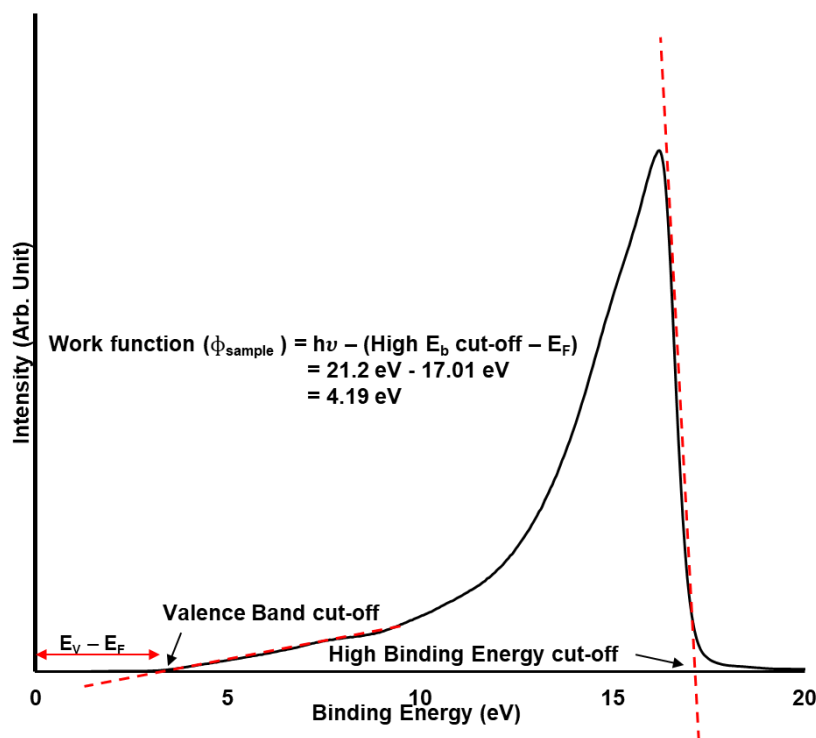


Figure 3.9: An illustration for calculating the work function of the sample from the UP spectrum.

In this study, we aim to investigate the influence of trap state density of the dye-TiO₂ interface with ageing.

3.1.4. Meta-stable Induced Electron Spectroscopy (MIES)

MIES is based on a principle that utilises slow, rare gas metastable atoms (He* 2³S, 2¹S) to eject electrons from the sample surface³¹. MIES instrument consists of a two-stage cold cathode gas discharge (MFS, Clausthal-Zellerfeld, Germany) which generates He*- 3S₁ (19.8 eV) and UV- photons (21.2 eV) which is separated by a mechanical chopper set at frequency 2000 Hz. The chopper separates the signal from photons and He* implies the time of flight (TOF) technique³². These He* atoms with their long-lived excited state and the inability to any other orbital transition increase the probability of transferring the energy into the target surface to eject the electron³³. During this interaction, the energy of He* gets transferred via three different mechanisms, Resonance Ionisation (RI), Auger Neutralization (AN*) and Auger De-excitation (AD), which depend on the electronic structure and work function of the sample under investigation³¹.

For samples with low work function, RI followed by AN* occurs as a de-excitation mechanism of He*. RI refers to the process in which 2s electron from the outer orbital of He* tunnels into an empty surface state with resonant energy through ionization thus forming He⁺³⁴. These He⁺ ions are further neutralised through a two-electron event, AN*. In AN*, an electron from the

surface fills the $\text{He}^+ 1s$, simultaneously emitting another electron with excess energy in Equation 3.24³⁵. The RI + AN* result in broad-spectrum, shown in Figure 3.10, process 1 and 2 illustrates RI and AN* simultaneously.

$$E_k = E'_i - 2(\phi + \varepsilon) \quad \text{Equation 3.24}$$

where, E_k is the KE of the emitted electron via the AN* process, ϕ is the work function of the sample surface, and ε average BE of the electrons involved in AN*.

For insulators, with medium to large work function the RI process gets hindered due to the unavailability of an empty level opposite to the excited level of He^* ³³. Thus, quenching of He^* occurs via AD²³. In AD, the surface electron from the occupied state transits to the inner vacant orbital ($\text{He}^+ 1s$) with simultaneous ejection of an electron from the outer orbital $\text{He } 2s$ ³³. AD is a one-electron transfer from valence bands and hence results in a spectrum with sharp features³², illustrated in Figure 3.10 Process 3.

In electron spectroscopy, the information depth limits in the range of tenths of nanometres to several nanometres due to its dependence on the IMFP³⁶. However, MIES uses low energetic He atoms which limits the damage to the surface of the targeted sample³⁴ and limits the probing depth making it surface sensitive with information depth of 1 to 2 atomic layers³⁶ owing to the large de-excitation cross-section of He^* ³⁴. Further, the limitation of rare gas to penetrate the van der Waals surface makes it more extremely surface sensitive³⁴. MIES being a surface-sensitive analysis technique provides information about the electronic properties of the outermost layer including, valence band structure, molecular orientation and reorientation on the sample surface³⁷. Further comparison with the computational calculations the spectra can be co-related with different DOS to the different functional groups of the compound under investigation³⁷.

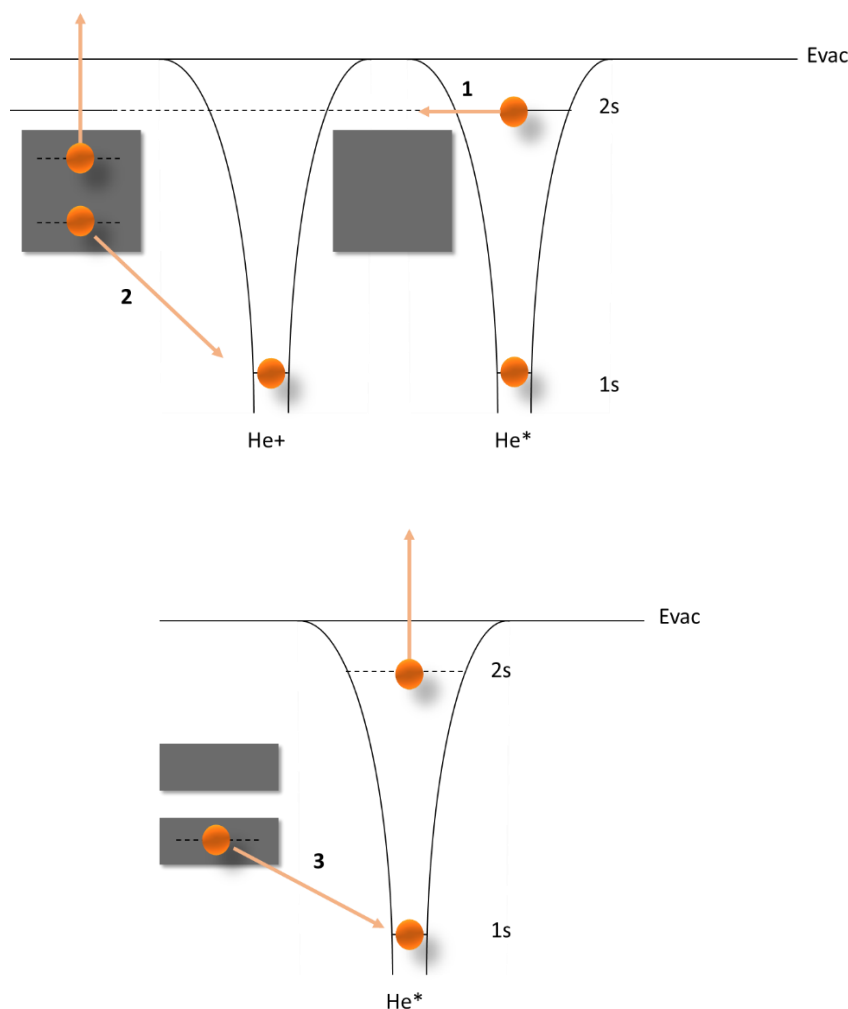


Figure 3.10: The schematic illustration of energy transfer processes in MIES 1 and 2 indicating RI and AN* occurring in solids with low work function respectively and 3.

3.1.5. Neutral Impact Collision Ion Scattering Spectroscopy (NICISS)

NICISS is an ion scattering technique used to quantitatively investigate the composition of the surface near bulk with a depth of 20 nm with a resolution of 1-3 Å³⁸, that is, the depth profile and the molecular concentration within the depth of 10 Å of the target³⁹. NICISS analysis is determined by ions-matter interaction, which includes charge transfer processes, elastic transfer of KE and inelastic energy transfer like electronic excitations or eradication of atoms or molecules by sputtering³⁶.

NICISS mainly consists of an ion source, a deflector, and a detector within a UHV chamber, Figure 3.11. The ion source uses inert gas such as Helium (He⁺) as a projectile with an energy range of ~ 3 keV which gets backscattered with an angle ~180° and the detector detects the TOF of the backscattered ions from the target. Meanwhile, an electrostatic deflector plays a role in permitting only the neutrals to be analysed by the detector. The He⁺ penetrates through the sample and then gets backscattered. During this process, the ion loses its energy, and the energy

loss directly depends on the atomic mass of the target atom and the depth penetration. The TOF determines the time taken by the projectile to reach the detector which is further used to analyse the energy loss⁴⁰. Additionally, the energy loss reveals the identity and the depth of the target atom.

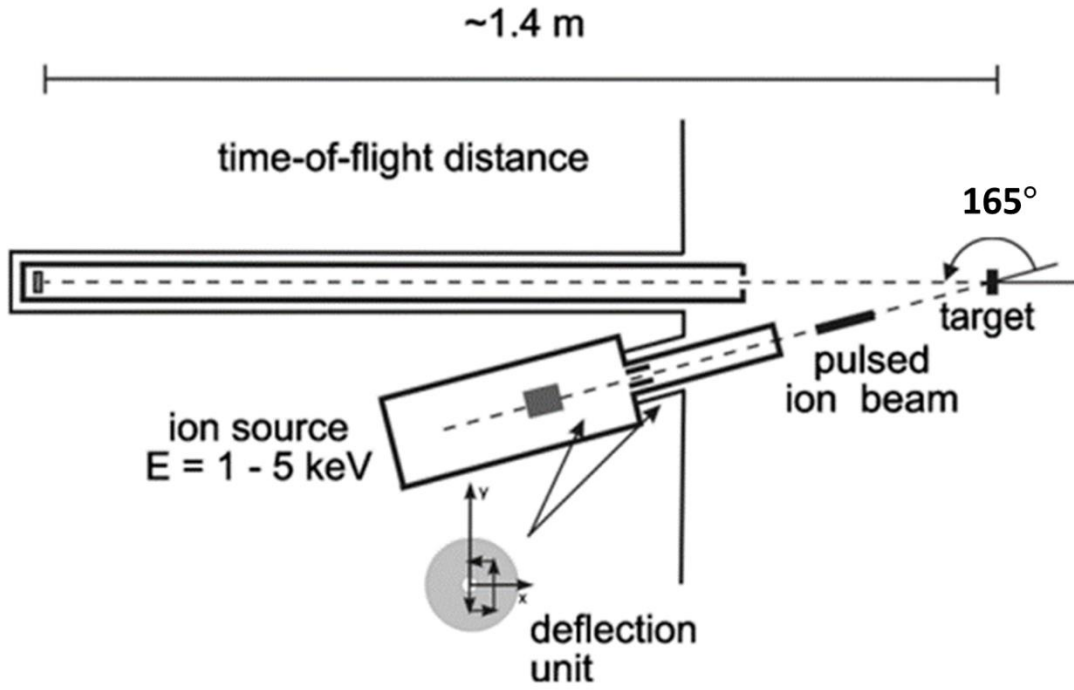


Figure 3.11: The diagrammatic representation of the NICISS experimental set-up⁴¹. Reprinted with permission from the American Institute of Physics

The energy loss of the backscattered projectiles occurs via several small-angle and large-angle-scattering events. These energy losses are summarised as two different energy losses; the large loss in energy, the elastic energy loss, in the backscattered projectile which appears once is due to the collision of the projectile with the target atom and the loss is proportional to the mass of the target atom²⁶⁻²⁷ (via momentum conservation) which is given by Equation 3.25,

$$E_{final} = E_0 \frac{(\cos\theta + (A^2 - \sin^2\theta)^{\frac{1}{2}})^2}{(1 + A)^2} - Q_{in} \quad \text{Equation 3.25}$$

Where E is the energy of the projectile, θ is the detector angle ($\sim 165^\circ$), Q_{in} is the inelastic energy loss due to backscattering, A is the ratio of the mass of the target element to the mass of the projectile. The schema of the NICISS principle is shown in Figure 3.12.

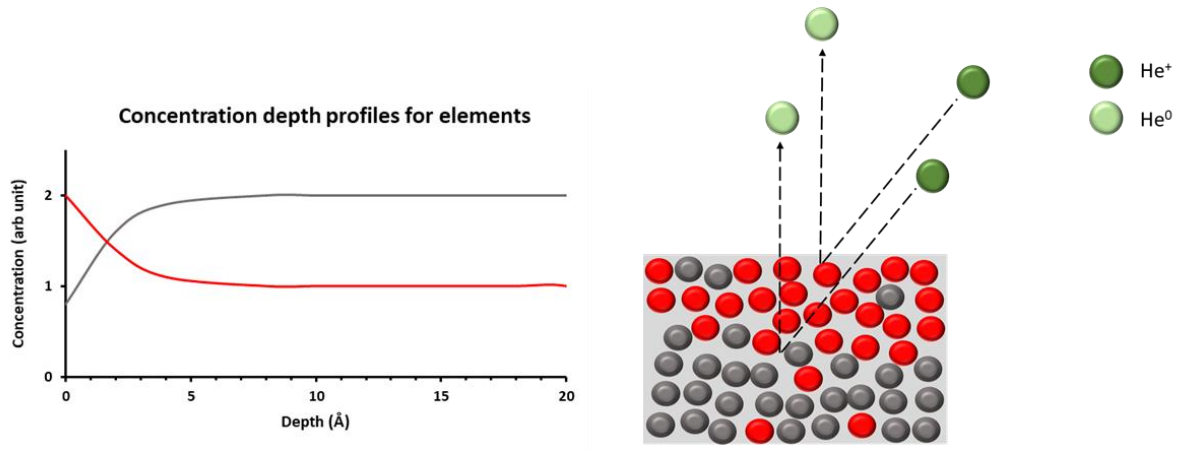


Figure 3.12: The schematic presentation of the NICISS principle.

The small and continuous inelastic energy losses due to small angle scattering within the sample bulk, also termed stopping power, appear multiple times throughout a single trajectory. This small angle scattering energy loss from TOF relates to the depth of the target atom ³⁵ by the following expression,

The TOF spectrum is converted into an energy spectrum using Equation 3.26,

$$I(E) = I(t) \frac{\Delta t}{\Delta E} \frac{1}{d\sigma/d\Omega(E)} \frac{1}{\text{det}(E)} \quad \text{Equation 3.26}$$

where, $I(E)$ is the energy loss spectrum, $I(t)$ is the contribution of a specific element in the TOF spectrum, t is the TOF, $d\sigma/d\Omega(E)$ is the differential impact cross-section of the target elements in the projectile and $\text{det}(E)$ is the detector sensitivity factor with $\frac{\Delta t}{\Delta E}$, a factor considered for a non-linear relation between the TOF and the energy. Further, the Energy loss spectrum is converted into a depth profile by Equation 3.27,

$$I(d) = I(E) \frac{dE}{dz} f \quad \text{Equation 3.27}$$

where z is the elemental depth and f is the factor co-relating backscattered projectile and the concentration yield.

The NICIS spectra record different steps, and each step is determined by the mass of the element detected from the sample, refer to Figure 3.13 for elemental steps in the TQ1 sample. The TOF of the onset is inversely dependent on the mass of the target element ²⁷. The heavier elements appear earlier in the TOF spectra as they are more likely to lose less energy during a collision.

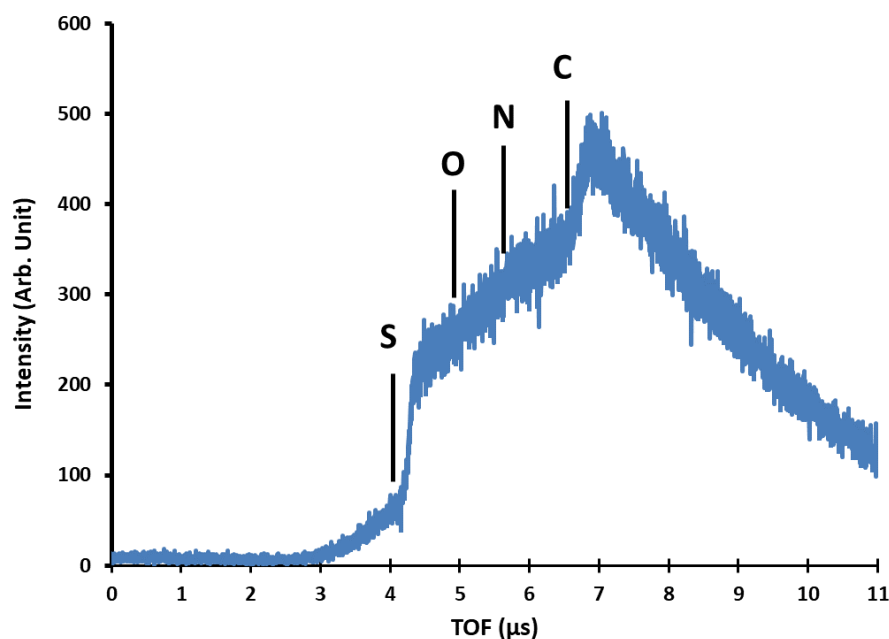


Figure 3.13: NICIS spectra of TQ1 with the onset representing the elements present in the target system.

The study aims to use NICISS to quantitatively measure the molecular concentration of Ru and I present in the sample and how ageing affects them. Due to the incapability of He projectile to separate the Ru from I, Ne is used as a projectile. He is replaced by a heavier projectile Ne, as using a heavier projectile increases the energy loss between the backscattering from the elements. Hence, the energy difference between Ru and I get larger when the heavier projectile is used.

3.1.6. Fourier Transform Infrared Spectroscopy (FTIR)

Infrared (IR) spectroscopy is the study of the interaction of matter with electromagnetic waves in the IR region of the spectrum. Generally, IR radiation excites vibrational motion in molecules and solids. Molecules have different modes of vibrations, and each vibrational mode has a corresponding frequency or energy⁴². When the molecule absorbs the IR radiation its atoms vibrate causing stretching and contraction of chemical bonds, as well as bending and twisting of the molecular structure. However, one needs to consider that not all vibrational modes can absorb energy. Only the modes that create a changing dipole moment during the vibration motion have the potential to absorb IR radiation. In this study, the mid-IR radiation from a broadband source $4000\text{ cm}^{-1} - 400\text{ cm}^{-1}$ is used to expose the molecules. On exposure, the molecules may absorb the IR light provided the frequency matches a natural vibrational frequency of the molecule. The probability of absorption, and thus excitation to a higher

vibrational state depends on the magnitude of the changing dipole moment, while the absorption energy is equal to the difference between the initial and final vibrational levels. For excitation of a single quanta of a vibration mode the energy of the incident radiation is, mathematically represented by ⁴²,

$$E_{IR} = \Delta E_{vib} = \frac{h}{2\pi} \sqrt{\frac{k_{vib}}{\mu_{vib}}} = h\nu_{vib} \quad \text{Equation 3.28}$$

where, E_{IR} is the energy of the radiation, ΔE_{vib} is the change in the vibrational energy, k_{vib} is the force constant of the mode of vibration, μ_{vib} is the reduced mass, and ν_{vib} is the vibrational frequency.

From Equation 3.28 the frequency of the vibrational mode depends on the reduced mass and the force constant which, in turn, depends on the bond strengths. These parameters are characteristic of different functional groups and thus valuable information about molecular structure can be extracted from the spectrum.

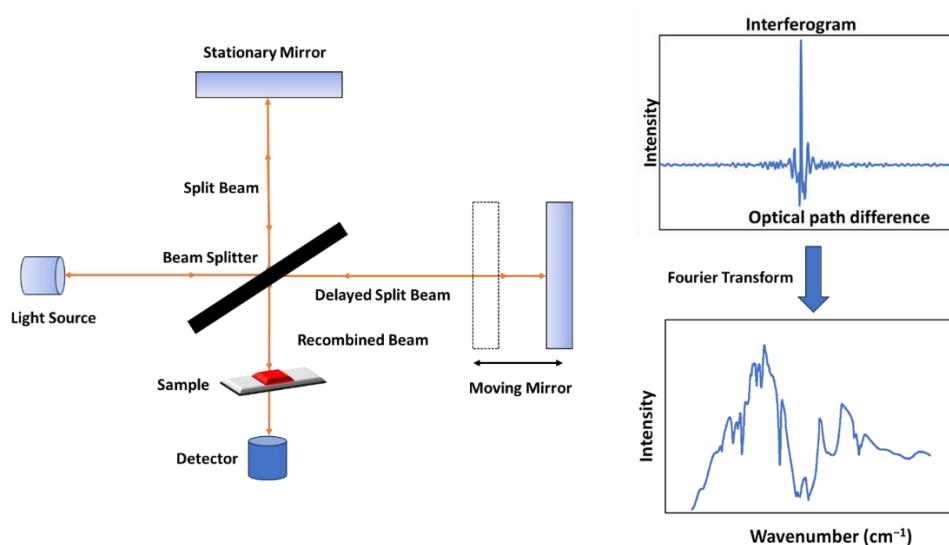


Figure 3.14: The schema of FTIR instrumentation and operating principle (Reformatted from ⁴³).

Most FTIR consists of the Michelson Interferometer with a beam splitter that divides the radiation beam from the IR source into two equal parts (ideally) as shown in Figure 3.14. A part of the radiation is directed towards the stationary mirror, while the second part is directed towards the moving mirror. The moving mirror results in an optical path difference (OPD) between the two separated beams and consequently causes a phase change between them. These beams get reflected and recombine at the beam splitter thus resulting in interference. The magnitude of interference is the result of variation in the OPD travelled by the two reflected IR

beams. If the distance between the two mirrors from the beam splitter is equal ($OPD = 0$), the reflected beams are in phase with each other, resulting in constructive interference for all wavelengths and sending the maximum signal to the detector. This is the centre-burst in the interferograms. When the two reflected beams are out of phase by 180° , ($OPD \frac{\lambda}{2}$), they result in destructive interference (zero signal to the detector). Since the IR source is broadband, and thus composed of many wavelengths, the signal at the detector is a superposition of interference effects of all the wavelengths. The detector response as a function of the OPD is called the interferogram⁴³. Finally, the interferogram is converted from the time domain into the frequency domain using the Fourier transformation. This results in a spectrum giving the intensity of the IR source as a function of light frequency. If an absorbing medium is placed in the beam path, then the absorbed frequencies will be missing from the resulting intensity spectrum.

The transmittance of a sample is given by Equation 3.29,

$$T = \frac{I}{I_0} \quad \text{Equation 3.29}$$

where I is the intensity of transmitted light, and I_0 is the intensity of the incident radiation.

Accordingly, the absorbance spectrum is derived using the Beer-Lambert relationship given by Equation 3.30,

$$A = -\log\left(\frac{I}{I_0}\right) = \epsilon cl \quad \text{Equation 3.30}$$

where, ϵ is the molecular absorption coefficient, c is the concentration, and l is the sample path length.

FTIR is popularly used to compare the similarities or differences between or among different molecules. Every different molecule has a unique set of vibrational modes and thus different frequencies of vibration and absorption coefficients. Accordingly, the IR spectrum is taken as a fingerprint of the molecule⁴⁴. Likewise, the IR spectrum also helps in identifying the presence or absence of specific functional groups in the molecule or changes introduced due to external factors.

3.1.7. Electrochemical Impedance Spectroscopy (EIS)

Electrochemical impedance is based on the application of an AC potential to an electrochemical system and measuring the current through the cell. The response to the applied AC potential is an AC signal. EIS is a common method applied to measure the current response of a device as a function of the frequency for an applied AC voltage. EIS is a steady-state technique that utilises potentiostat to probe signal relaxations over a wide range of frequencies, by the application of harmonically modulated small amplitude AC voltage to detect small perturbations on the system to investigate both the bulk and surface properties of the system⁴⁵⁻⁴⁶. It is a non-destructive tool used to investigate the stability and kinetics along with the intrinsic charge transport in DSSCs. In simple words, it is a tool to understand the movement of charge through the cell device. The intrinsic stability of the cell depends on the irreversible kinetics occurring within the cell interface which is photo-electrochemical and thermal degradation of dye and/or electrolyte components occurring during cell operation hence characterisation of the inner cell parameter under ageing is required^{45, 47}.

Theory:

The general approach of EIS is to apply an electrical stimulus (sinusoidal potential) to an electrochemical system and measure the output (sinusoidal current) response as a function of frequency⁴⁶. The electrochemical impedance is measured using a small excitation signal to obtain a pseudo-linear response, which means the applied potential is a sinusoidal result in the sinusoidal current but shifted in phase Figure 3.15.

The applied sinusoidal potential is given by Equation 3.31,

$$E_t = E_0 \sin(\omega t) \quad \text{Equation 3.31}$$

where, E_t is the potential at time t , E_0 is the amplitude of the signal, ω is the radial frequency (in rad/sec), and

$$\omega = 2\pi f \quad \text{Equation 3.32}$$

Here in Equation 3.32, f is the frequency (in Hz). Thus, the output current response is sinusoidal with different amplitude I_0 and a phase shift Φ , given by Equation 3.33,

$$I_t = I_0 \sin(\omega t + \phi) \quad \text{Equation 3.33}$$

Following Ohm's law, the impedance is given by Equation 3.34,

$$Z(\omega) = \frac{E_t}{I_t} = \frac{E_0 \sin(\omega t)}{I_0 \sin(\omega t + \phi)} = Z_0 \frac{\sin(\omega t)}{\sin(\omega t + \phi)} \quad \text{Equation 3.34}$$

Further, from Euler's Equation 3.35 is obtained,

$$\exp(j\phi) = \cos \phi + j \sin \phi \quad \text{Equation 3.35}$$

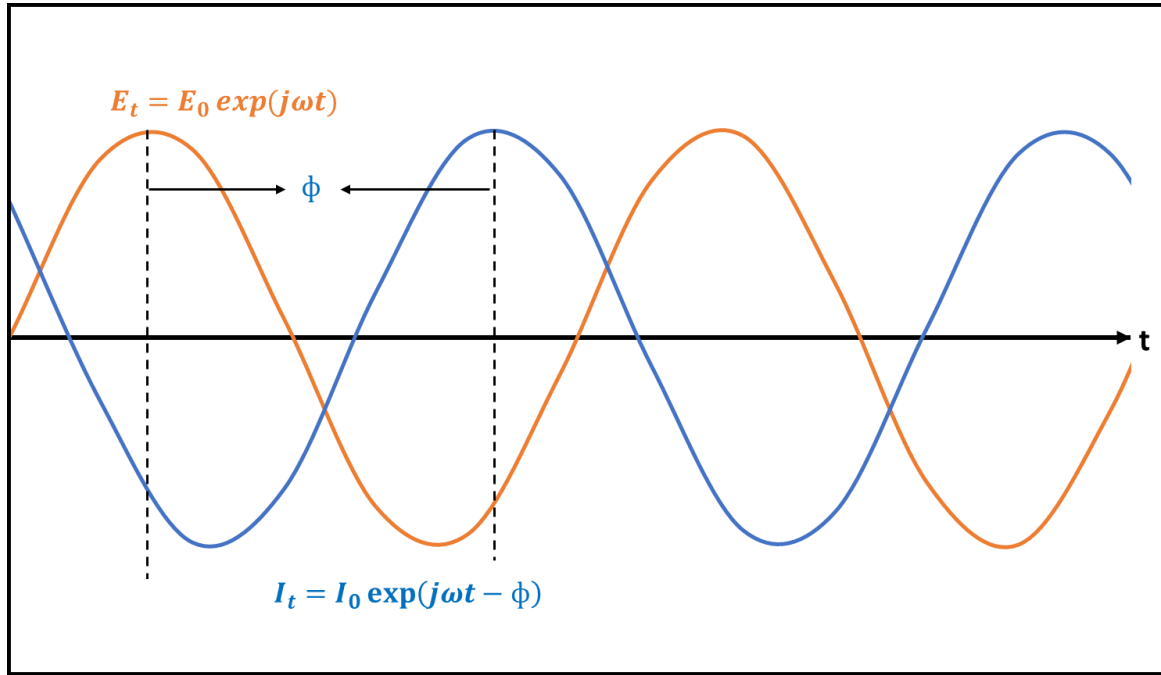


Figure 3.15: The sinusoidal current response (I) for the sinusoidal potential (E) applied in EIS.

The potential is represented in terms of a complex function as (see Equation 3.36),

$$E_t = E_0 \exp(j\omega t) \quad \text{Equation 3.36}$$

The output current response is given by Equation 3.37,

$$I_t = I_0 \exp(j\omega t - \phi) \quad \text{Equation 3.37}$$

Thus, the impedance in terms of complex numbers becomes,

$$Z(\omega) = \frac{E}{I} = Z_0 \exp(j\phi) = Z_0 (\cos \phi + j \sin \phi) \quad \text{Equation 3.38}$$

Data Presentation:

From Equation 3.38, the expression $Z(\omega)$ is composed of a real and an imaginary part. On plotting the real part on the x-axis and the imaginary part on the y-axis, we obtain a Nyquist plot which is also known as the ‘Cole-Cole’ plot.

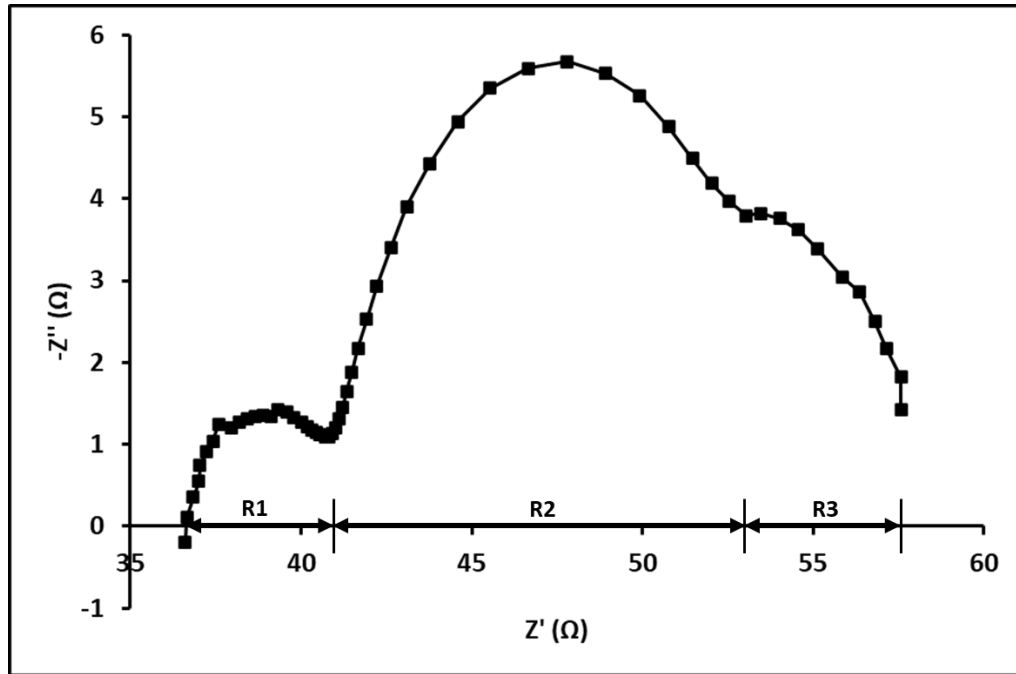


Figure 3.16: Typical Nyquist plot of DSSC with different interfacial resistance labelled, namely R1-charge transfer resistance at the CE and electrolyte interface, R2-charge transfer resistance at photoanode and R3-Nernst diffusion of I_3^- in the electrolyte.

The Nyquist plot in Figure 3.16 illustrates the imaginary impedance (Z''), which results from the capacitive and inductive character of the cell versus the real impedance (Z') as a set of three semi-circular plots and the bode plot shows the magnitude of the total impedance as a function of the frequency⁴⁸⁻⁴⁹. The semi-circle at the high-frequency region represents the charge transfer process at the CE/electrolyte interface. Likewise, the middle or the central semi-circle represents the diffusion recombination process in the photoanodes/electrolyte. Likewise, the third semi-circle at the low-frequency region represents the Nernst diffusion of I/I_3^- in the electrolyte⁵⁰.

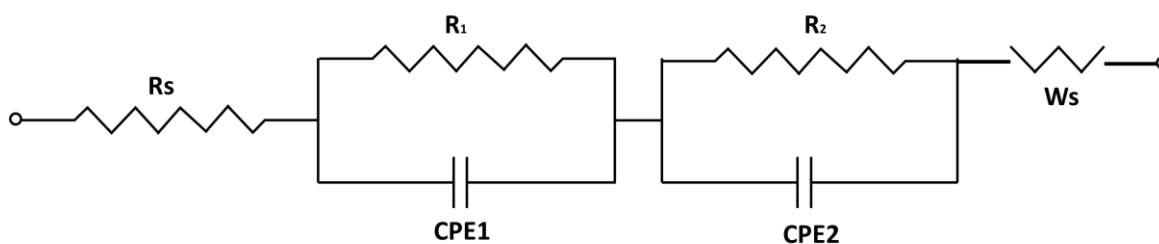


Figure 3.17: The equivalent circuit diagram of the electrochemical system of DSSC.

An equivalent circuit is used to model the impedance refer to Figure 3.17. The equivalent circuit consists of resistors and capacitors. At every interface, there is resistance to charge mobility which causes charge collection. Further diffusive charge transfer is modelled by a combination of Warburg elements (Ws), representing the resistance of the I^-/I_3^- redox couple in the electrolyte. Rs circuit component represents the Ohmic series resistance of the FTO/electrolyte. Likewise, the R_1 and R_2 components represent the charge transfer resistance at the CE/electrolyte and PA/electrolyte interface respectively, with CPE1 and CPE2 as the corresponding constant phase element ⁵¹. EIS helps in obtaining the following parameters, series resistance, charge transfer resistance of the CE, diffusion resistance of the electrolyte, the resistance of electron transport and recombination in the TiO_2 and the chemical capacitance of the porous TiO_2 electrode. In DSSCs, the Nyquist plots are commonly used as a plot of Z-imaginary plotted against Z-real and appears as a set of three semi-circular plot and a bode plot shows the magnitude of the total impedance as a function of the frequency.

In this study, the EIS measurement was performed using a FRA2 μ Autolab potentiostat/galvanostat with an impedance module under dark-bias voltage conditions, with the bias voltage -0.9V. The frequency range of 10^5 Hz to 0.1 Hz was applied. The spectra were measured using Metrohm Autolab NOVA 2, a data acquisition software. Further, the acquired spectra were fitted using Z-View2 software using appropriate equivalent circuits. Here, as the cell has only two electrodes, the reference terminal was connected to the CE during the measurement.

3.2. Materials

- **Electrodes:** Fluorine doped tin oxide (FTO) ($15 \Omega \text{ cm}^{-2}$ and $7 \Omega \text{ cm}^{-2}$, 100 mm x 100 mm x 2.2 mm) for photoanode and CE was bought from Dyesol.
- **Adsorbent:** TiO_2 pastes 18NR-AO blend of active anatase with average particle size ~ 20 nm and anatase scatter particle size ≤ 450 nm was obtained from Greatcell. For the treatment of the photoanode titanium tetrachloride (purity 99.99%) was purchased from Sigma-Aldrich.

- **Chromophore:** N719 dye, Molecular formula: $C_{58}H_{86}N_8O_8RuS_2$ (Greatcell), Molecular structure in Figure 3.18.

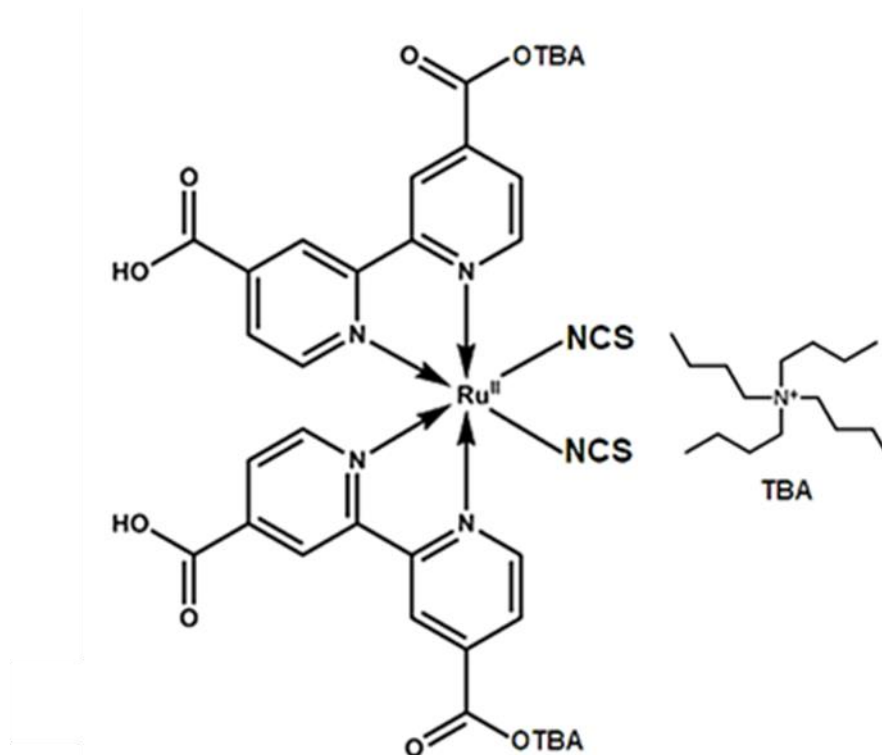


Figure 3.18: The molecular structure of N719 dye.

- **Catalyst:** Chloroplatinic acid hydrate (99.99%, Sigma-Aldrich).
- **Electrolyte components:** BMII (1-Butyl-3-Methylimidazolium iodide, purity 99%, Sigma-Aldrich), TBP (4-Tertbutyl pyridine, purity 96%, TCI), Iodine (purity 98%, TCI), DMPIImI (1,2-Dimethyl-3-Propyl-1H-imidazol-3-ium iodide, purity > 95%, Synthonix), LiI (Lithium iodide, purity 99.9%, Sigma-Aldrich), DMII (1,3-Dimethyl-1H-imidazole-3ium iodide, purity 97%, Ambeed).
- **Solvents:** AN (Merck), VN (Valeronitrile, purity 99.5%, Sigma-Aldrich), MPN (3-Methoxypropionitrile purity \geq 98%, Sigma-Aldrich), Et-OH (Ethanol, purity 100%, Chem-supply).
- **Sealant:** Surlyn frame (inner 9 mm x 9 mm, outer 11 mm x 11 mm, 60 μ m thickness) from Solaronix.

3.3. Cell Preparation Procedure

DSSCs were fabricated using standard protocols as described in ⁵² and ⁵³. For a complete detailed description and diagrammatic illustration on DSSC preparation refer to Figure 3.19 and Figure 3.20 respectively.

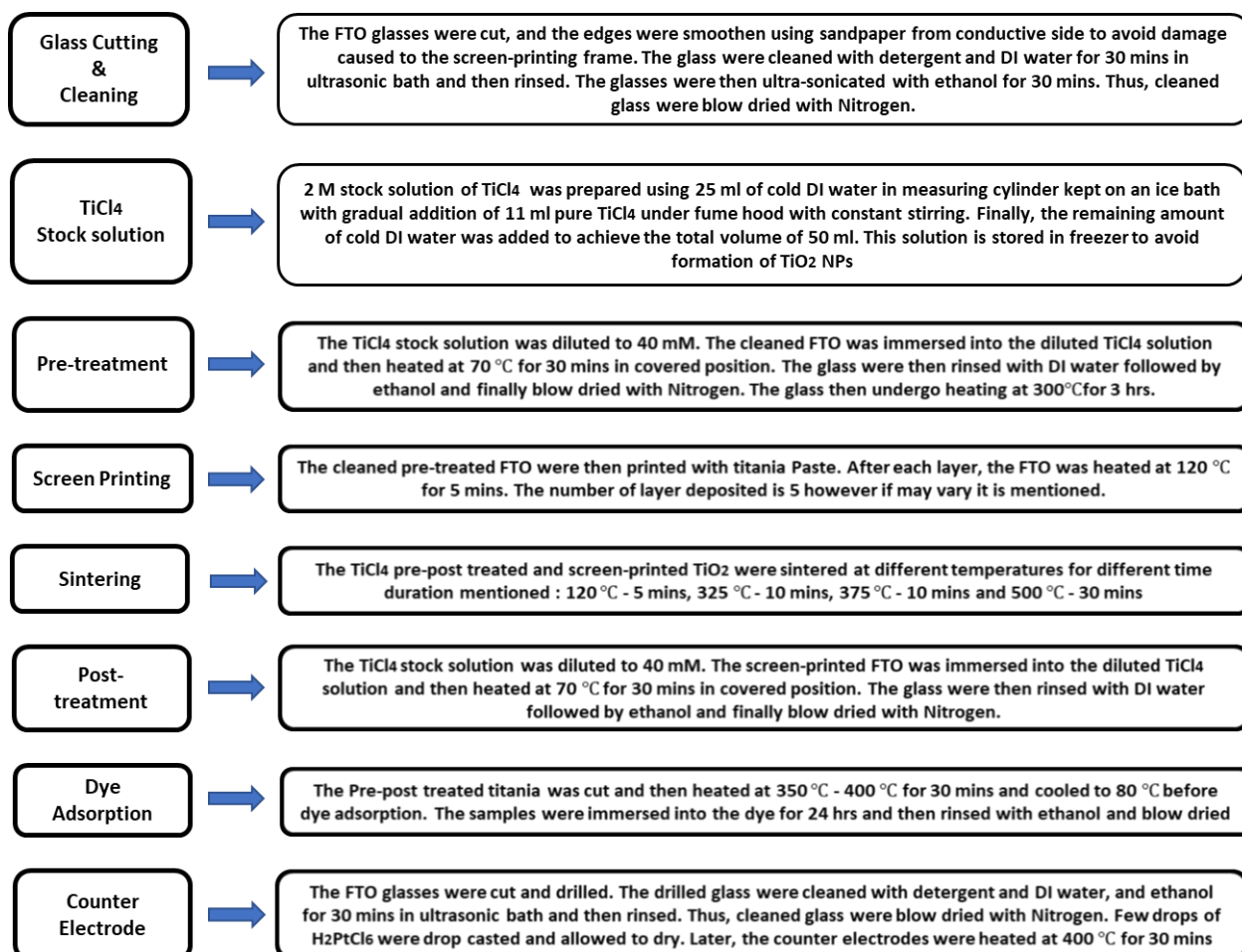


Figure 3.19: Detailed information about the DSSC preparation applied in the study.

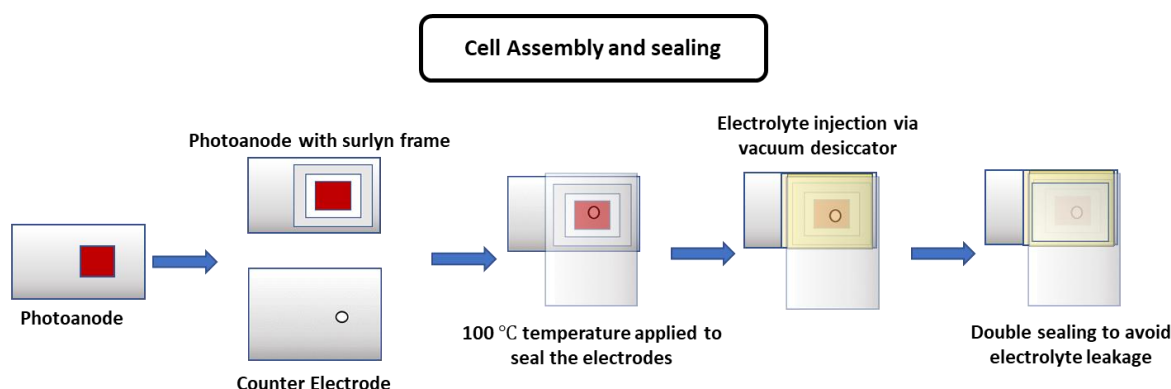


Figure 3.20: The diagrammatic representation of the cell assembly and the cell sealing used in the study.

3.4. References

1. Gueymard, C. A.; Myers, D.; Emery, K., Proposed Reference Irradiance Spectra for Solar Energy Systems Testing. *Solar energy* **2002**, 73, 443-467.
2. Khan, M. I., *A Study on the Optimization of Dye-Sensitized Solar Cells*; University of South Florida, 2013.
3. Dirnberger, D., Photovoltaic Module Measurement and Characterization in the Laboratory. In *The Performance of Photovoltaic (Pv) Systems*, Elsevier: 2017; pp 23-70.
4. Servaites, J. D.; Ratner, M. A.; Marks, T. J., Organic Solar Cells: A New Look at Traditional Models. *Energy & Environmental Science* **2011**, 4, 4410-4422.
5. Riviere, J. C.; Myhra, S., *Handbook of Surface and Interface Analysis: Methods for Problem-Solving*; CRC press, 2009.
6. Hüfner, S., *Photoelectron Spectroscopy: Principles and Applications*; Springer Science & Business Media, 2013.
7. Wagner, J. M., *X-Ray Photoelectron Spectroscopy*; Nova Science Publishers, Incorporated, 2014.
8. Van der Heide, P., *X-Ray Photoelectron Spectroscopy: An Introduction to Principles and Practices*; John Wiley & Sons, 2011.
9. Verma, H. R., *Atomic and Nuclear Analytical Methods*; Springer, 2007.
10. Fuggle, J.; Fabian, D.; Watson, L., Electron Energy Loss Processes in X-Ray Photoelectron Spectroscopy. *Journal of Electron Spectroscopy and Related Phenomena* **1976**, 9, 99-109.
11. Andrade, J. D., *Surface and Interfacial Aspects of Biomedical Polymers: Volume 1 Surface Chemistry and Physics*; Springer Science & Business Media, 2012.
12. Oswald, S., X-Ray Photoelectron Spectroscopy in Analysis of Surfaces. *Encyclopedia of Analytical Chemistry: Applications, Theory and Instrumentation* **2006**.
13. O'Connor, D. J.; Sexton, B. A.; Smart, R. S., *Surface Analysis Methods in Materials Science*; Springer Science & Business Media, 2013; Vol. 23.
14. Mariani, C.; Stefani, G., Photoemission Spectroscopy: Fundamental Aspects. In *Synchrotron Radiation*, Springer: 2015; pp 275-317.
15. Reinert, F.; Hüfner, S., Photoemission Spectroscopy—from Early Days to Recent Applications. *New Journal of Physics* **2005**, 7, 97.
16. Moulder, J. F., Handbook of X-Ray Photoelectron Spectroscopy. *Physical electronics* **1995**, 230-232.
17. Seah, M., Quantification in Aes and Xps. In *Quantitative Microbeam Analysis*, Routledge: 2017; pp 1-42.
18. Greczynski, G.; Hultman, L., The Same Chemical State of Carbon Gives Rise to Two Peaks in X-Ray Photoelectron Spectroscopy. *Scientific Reports* **2021**, 11, 1-5.
19. Wagner, C., Sensitivity Factors for Xps Analysis of Surface Atoms. *Journal of electron spectroscopy and related phenomena* **1983**, 32, 99-102.
20. Philippe, B.; Man, G. J.; Rensmo, H., Photoelectron Spectroscopy Investigations of Halide Perovskite Materials Used in Solar Cells. In *Characterization Techniques for Perovskite Solar Cell Materials*, Elsevier: 2020; pp 109-137.
21. Paynter, R., An Arxps Primer. *Journal of Electron Spectroscopy and Related Phenomena* **2009**, 169, 1-9.
22. Watts, J. F.; Wolstenholme, J., An Introduction to Surface Analysis by Xps and Aes. **2003**.
23. Chambers, B. Spectroscopic Studies of 2d Nanomaterials. Flinders University, College of Science and Engineering., 2018.
24. Schneider, T.; Artyushkova, K.; Fulghum, J. E.; Broadwater, L.; Smith, A.; Lavrentovich, O. D., Oriented Monolayers Prepared from Lyotropic Chromonic Liquid Crystal. *Langmuir* **2005**, 21, 2300-2307.

25. Merzlikin, S., Depth Profiling by X-Ray Photoelectron Spectroscopy. *Fakultät für Chemie* **2007**.
26. Wang, C.; Andersson, G. G., Measuring Concentration Depth Profiles at Liquid Surfaces: Comparing Angle Resolved X-Ray Photoelectron Spectroscopy and Neutral Impact Collision Scattering Spectroscopy. *Surface Science* **2011**, *605*, 889-897.
27. Wang, C.; Kan, A.; Liu, Z.; Zhang, G.; Lin, X.; Fu, H., Using Neutral Impact Collision Ion Scattering Spectroscopy and Angular Resolved X-Ray Photoelectron Spectroscopy to Analyze Surface Structure of Surfactant Solutions. *Colloid and Polymer Science* **2015**, *293*, 1655-1666.
28. Kimura, K., *Handbook of Hei Photoelectron Spectra of Fundamental Organic Molecules*; Halsted Press, 1981.
29. Atkins, P.; Atkins, P. W.; de Paula, J., *Atkins' Physical Chemistry*; Oxford university press, 2014.
30. Seah, M. P.; Dench, W., Quantitative Electron Spectroscopy of Surfaces: A Standard Data Base for Electron Inelastic Mean Free Paths in Solids. *Surface and interface analysis* **1979**, *1*, 2-11.
31. Odenbach, S., *Colloidal Magnetic Fluids: Basics, Development and Application of Ferrofluids*; Springer, 2009; Vol. 763.
32. Krishnan, G. Investigation of Ligand Protected Gold Clusters on Defect Rich Ald Titania Using Electron Spectroscopies. Flinders University, College of Science and Engineering., 2018.
33. Harada, Y.; Masuda, S.; Ozaki, H., Electron Spectroscopy Using Metastable Atoms as Probes for Solid Surfaces. *Chemical Reviews* **1997**, *97*, 1897-1952.
34. Read, S. T. Metastable Induced Electron Spectroscopy of Iron Pentacarbonyl on Gold. University of Guelph, 2014.
35. Trilaksana, H. Analysis of the Dye/Titania Interface as Photo-Anode in Dye Sensitized Solar Cells. Flinders University, College of Science and Engineering., 2018.
36. Andersson, G.; Morgner, H., Thermodynamics and Structure of Liquid Surfaces Investigated Directly with Surface Analytical Tools. *Annalen der Physik* **2017**, *529*, 1600230.
37. Alshehri, N.; Bennett, T.; Metha, G. F.; Andersson, G. G., Transfer of Ordered Phospholipid Films onto Solid Substrates from a Drained Foam Film. *The Journal of Physical Chemistry C* **2015**, *119*, 22496-22503.
38. Ridings, C.; Andersson, G. G., Deconvolution of Niciss Profiles Involving Elements of Similar Masses. *Nuclear Instruments and Methods in Physics Research Section B: Beam Interactions with Materials and Atoms* **2014**, *340*, 63-66.
39. Andersson, G.; Morgner, H., Impact Collision Ion Scattering Spectroscopy (Iciss) and Neutral Impact Collision Ion Scattering Spectroscopy (Niciss) at Surfaces of Organic Liquids. *Surface science* **1998**, *405*, 138-151.
40. Andersson, G.; Morgner, H.; Pohl, H., Energy-Loss Straggling of Helium Projectiles at Low Kinetic Energies: Deconvolution of Concentration Depth Profiles of Inorganic Salt Solutes in Aqueous Solutions. *Physical Review A* **2008**, *78*, 032904.
41. Ridings, C.; Andersson, G. G., Determining Concentration Depth Profiles of Thin Foam Films with Neutral Impact Collision Ion Scattering Spectroscopy. *Review of Scientific Instruments* **2010**, *81*, 113907.
42. Shodiev, M. Determining the Structure and Orientation of the Alamethicin Ion Channel in Lipid Membranes Using Atr and Electrochemical Pmirras. University of Guelph, 2015.
43. Rees, O. J., *Fourier Transform Infrared Spectroscopy: Developments, Techniques and Applications*; Nova Science Publ., 2010.
44. Pavia, D. L.; Lampman, G. M.; Kriz, G. S.; Vyvyan, J. A., *Introduction to Spectroscopy*; Cengage Learning, 2008.

45. Wang, Q.; Moser, J.-E.; Grätzel, M., Electrochemical Impedance Spectroscopic Analysis of Dye-Sensitized Solar Cells. *The Journal of Physical Chemistry B* **2005**, *109*, 14945-14953.
46. Macdonald, J. R.; Johnson, W. B., Fundamentals of Impedance Spectroscopy. *Impedance spectroscopy: theory, experiment, and applications* **2018**, 1-20.
47. Kern, R.; Sastrawan, R.; Ferber, J.; Stangl, R.; Luther, J., Modeling and Interpretation of Electrical Impedance Spectra of Dye Solar Cells Operated under Open-Circuit Conditions. *Electrochimica acta* **2002**, *47*, 4213-4225.
48. Fu, D. Back Contact Dye-Sensitized Solar Cells. Monash University, 2012.
49. Weerasinghe, H. C. Development and Characterization of Flexible Dye Sensitized Solar Cells. Monash University, 2010.
50. Sarker, S.; Seo, H. W.; Kim, D. M., Electrochemical Impedance Spectroscopy of Dye-Sensitized Solar Cells with Thermally Degraded N719 Loaded Tio₂. *Chemical Physics Letters* **2013**, *585*, 193-197.
51. Hwang, D.-K.; Lee, B.; Kim, D.-H.; Chang, R. P., Efficiency Enhancement in Dye-Sensitized Solar Cells by Three-Dimensional Photonic Crystals. *Applied Physics Express* **2012**, *5*, 122301.
52. Sedghi, A.; Miankushki, H. N., Influence of TiCl₄ Treatment on Structure and Performance of Dye-Sensitized Solar Cells. *Japanese Journal of applied physics* **2013**, *52*, 075002.
53. Adhikari, S. G.; Shamsaldeen, A.; Andersson, G. G., The Effect of TiCl₄ Treatment on the Performance of Dye-Sensitized Solar Cells. *The Journal of Chemical Physics* **2019**, *151*, 164704.

CHAPTER 4 ANCHORING MODES OF RU-BASED N719 DYE ONTO TITANIA SUBSTRATE

This chapter is a reformatted and edited version of a manuscript for a journal article published in a peer-reviewed journal. See the Contextual Statement section for details on the co-author's contribution to the published version of the manuscript.

Reference for the published version:

Adhikari, S. G., Gascooke, J. R., Alotabi, A. S., & Andersson, G. G. (2024). Anchoring Modes of Ru-Based N719 Dye onto Titania Substrates. The Journal of Physical Chemistry C.

Abstract

Dye anchoring plays a vital role in determining cell efficiency and extensively influences the stability of DSSCs. The investigation and the characterisation of the dye complex adsorption on the TiO₂ substrate are crucial for understanding the sensitisation process of the TiO₂ surface and for optimising the quantum yield of DSSCs. Many dyes used in DSSCs consist of either a carboxylic group or a cyanoacrylic acid group as dye anchors. However, with the growing interest in DSSCs new dyes with different anchoring groups have been developed and evaluated.

The present study investigates the anchoring mode of the dye-TiO₂ system with FTIR and ARXPS. The FTIR results support that the carboxylic group deprotonates and that the COO⁻ anchors to TiO₂ via multiple modes, i.e., bidentate chelating and ester bonds. However, the changes in the features of NCS in FTIR also suggest the partial involvement of the thiocyanate ligand in the dye attachment. In addition, the depth profile obtained from ARXPS indicates that the COO⁻ group is found dominantly at the dye/TiO₂ interface and thus is the main anchoring group for the dye-TiO₂ system. The application of the techniques in understanding anchoring modes is not limited to the investigation of N719 and can be applied to other dye-adsorbed systems of interest.

4.1. Introduction

DSSCs are a cost-effective, flexible, stable, eco-friendly substitute for traditional silicon cells and have indeed attracted a lot of scientific and technological interest since the breakthrough in 1991¹. The adsorption mode of the dye on the photoanode plays a crucial role in the

efficiency and durability of the cells ². To achieve the adsorption of the dye on the photoanode an anchoring group is introduced into the dye molecule. The anchoring group directly influences the donor and acceptor function of the molecule which can ultimately affect the LUMO and HOMO energy ³. An efficient dye molecule has its LUMO localised near the anchoring group and above the CB of the semiconductor electrode for efficient electron injection into the photoanode ⁴ and HOMO between the redox potential of the electrolyte and the VB to promote efficient dye regeneration under operating circumstances ⁵. A dye molecule can attach to the substrate via different anchoring groups, which could be, either strong attachments like covalent attachment, electrostatic interaction, hydrogen bonding, hydrophobic interaction, or weak attachments like van der Waals forces or physical entrapment ⁶. Most DSSCs employ a dye that attaches covalently to the titania substrate to ensure strong coupling for improved stability and homogenous dye distribution ². The most popular anchoring groups are the carboxylic and cyanoacrylic acid groups. However, due to recent research interest, other anchoring groups are being explored too.

Ru-based dyes, since their application in the first designed DSSCs, are profoundly used as sensitisers and utilises trimeric Ru-complex. Later, Nazeeruddin et. al synthesised panchromatic dyes with Ru complex with carboxylated terpyridyl and 3NCS group as ligands ⁷⁻¹⁰. Ru-sensitisers are popular due to their favourable photoelectrochemical properties, high stability in the oxidised state, long-lived excited state, and MLCT in the visible region ^{1, 6}. The highest efficiency recorded is 11.2 % for Ru-based N719 DSSCs with a pair of NCS ligands and TBA⁺ as a counter ion. As Ru is an expensive and rare element, metal-free organic dyes appear as cost-effective, and environment-friendly alternatives. The gaining interest in metal-free organic dye synthesis is due to their tuneable absorption and electrochemical properties through molecular designing, cost-efficient and eco-friendly, comparatively higher extinction coefficient than the Ru-dyes and higher efficiency ¹¹. Some of the popular metal-free dyes include hemicyanine dye, polyene-diphenyl aniline dye, thienyl fluorene dye, phenothiazine dye, thienothiophene-thiophene derived dye, phenyl-conjugated polyene dye, N, N-dimethylaniline-cyanoacetic acid, oligothiophene dye, coumarin dye, indoline dye, oligo-phenylenevinylene-unit dye. An organic dye is donor- π -acceptor or D- π -A structure. The structure of organic dye is tuned to alter the LUMO-HOMO and electronic properties in favour of PV performance. Undoubtedly, organic dyes have been successful to achieve near-target efficiency. However, the issues with the organic dye are instability and aggregation. Aggregation causes intermolecular quenching, other molecules that are not functionally attached to TiO₂ act as filters. Thence, aggregation is avoided by introducing a co-adsorbent with the dye on the electrode substrate. The highest efficiency

recorded 14.3% has been achieved by organic dye ADEKA-1 in association with another organic dye LEG4 as a co-sensitiser ¹² and recently a new record efficiency has been achieved by SL9 dye co-sensitised with SL10 with hydroxamic acid pre-adsorption on TiO₂ adsorbent ¹³. The efficiency of DSSC based on single organic sensitisers achieved 12.5% with C275 dye ¹⁴. Porphyrins are among the sensitiser group which is gaining the attention of researchers due to their strong absorption in the visible region, tuneable electronic structure, and easy modification of the dye core. The porphyrins have successfully outperformed most of the Ru-based dyes and hold the capability to represent future DSSCs. The highest recorded efficiency for porphyrin-based DSSCs is 13 % that utilises SM315 dye ¹⁵.

The Ru-based N719, cis-bis(isothiocyanato) bis (2,2'-bipyridyl-4,4'- dicarboxylato) ruthenium (II) bis-tetrabutylammonium (Ru(dcbpy)₂(NCS)₂ 2TBA) are functionalised by carboxyl groups for anchoring onto titania. Due to N719 being amphiphilic with effective electrostatic binding onto the titania substrate at low pH and increased stability in comparison to other Ru-based dyes, it makes N719 one of the highest-performing dyes developed for DSSCs with a recorded efficiency of 11% ¹⁶. However, few publications still support anchoring via the NCS group. Figure 4.1 shows the possible available anchoring modes of the N719 dye molecule onto the TiO₂ substrate. Physisorption of the dye is possible through H-bonding in either monodentate or bidentate fashion and is also possible through the NCS group. The dye molecule can chemisorb through the COOH acid group via the carbonyl oxygen ¹⁷. The dissociative (deprotonated) chemisorption includes monodentate binding through C=O, bidentate chelating, and bidentate bridging. In the N719 molecule, the anchoring mode influences the photo-conversion efficiency, with ester-like linkages observed on cells with higher efficiencies and high or improved Voc due to a decrease in charge of the bipyridine ligand because of the covalent bond ².

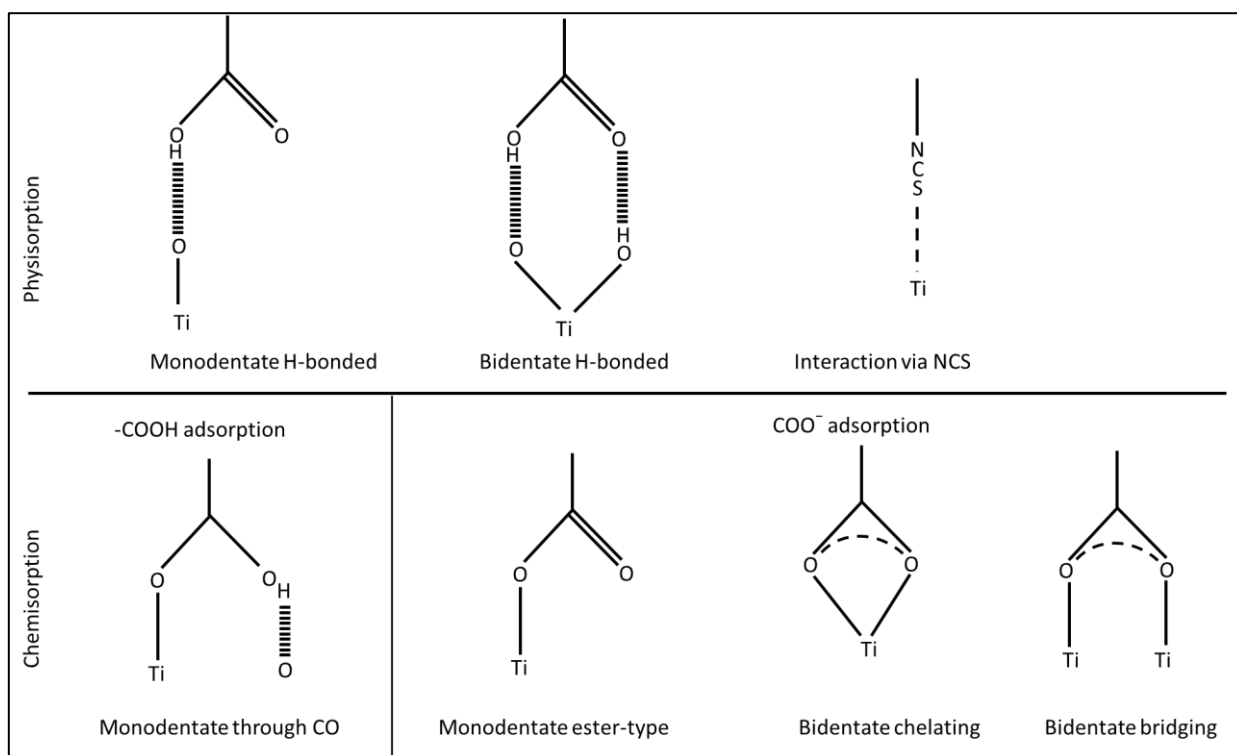


Figure 4.1: The possible anchoring modes of Ru-based dye molecule on the TiO₂ substrate via COOH acid group and NCS.

The influence of dye anchoring on the electrochemical properties of N719 with the modification introduced in P25 titania films, which is an electrochemical treatment of the substrate or dye adsorption under reflux, was investigated employing IR spectroscopy. The IR spectroscopy revealed a higher absorption of the C=O stretch mode than for the OCO asymmetrical modes concluding the presence of unidentate (ester-like) anchoring mode which contributed to an improved Voc and FF². Further, a photoacoustic FTIR investigation was performed to study the influence of protons on Ru-based chromophore immobilization using dyes N3, N719 and N712, where these dyes differ in the number of TBA⁺ in their molecular structure by 4, 2 and 0 respectively by Nazeeruddin, Md K., et al in ref¹⁷. For N719 molecule adsorption, the study concluded the involvement of either carboxylic or carboxylate or both in the N719 adsorption, further suggesting the dominance of the two-carboxylic groups in trans configuration over the NCS in contributing to the anchoring, with a carboxylic adsorption configuration in either bidentate chelation or bridging mode¹⁷. An investigation into dye anchoring suggested chemisorption and physisorption of dye onto the titania substrate and dye interaction onto the substrate via electrostatic/H-bonding in addition to the bidentate bridging which was supported by Raman results¹⁸. The Raman results supported no direct involvement of NCS in adsorption but the blue shifting of the peak supported the change in the dye structure upon adsorption¹⁹. Contradicting, Johansson et al in an XPS investigation

observed NCS interaction on titania to occur through S and the presence of mixed binding modes via the carboxylate group partly with TBA^+ as a counterion²⁰.

Owing to the discrepancies previously observed in the modes of dye attachment investigated to date, and with only a few investigations focussing on the involvement of NCS and TBA^+ in the adsorption, here we aim to investigate the anchoring modes of N719 by applying the techniques of FTIR and ARXPS. We note that recent studies have indicated an influence on the efficiency of DSSCs upon varying pH of the dye solution²¹⁻²³ which may result from changes in the anchoring modes, however, it is our aim to investigate the anchoring modes in cells created using typical construction protocols. The investigation of the anchoring mode through FTIR is quite common. Complementing FTIR results, the concentration depth profiling technique ARXPS allows the determination of which anchoring modes identified using FTIR are responsible for the actual adsorption of the dye on the titania surface. FTIR is extremely sensitive to the functional group and provides information about molecular interactions and conformational changes but does not have any sensitivity for the location of a functional group in the dye layer. On the contrary, ARXPS is sensitive to the surface chemistry and elemental composition of a material and can reveal detailed information about the concentration depth profiles. Combining these two techniques we aim to understand the dye anchoring modes along with the depth profile of the adsorbed dye onto TiO_2 .

4.2. Experimental

4.2.1. Materials

Fluorine-doped tin oxide (FTO) transparent conductive glass ($15 \, \Omega \, \text{cm}^{-2}$ and $7 \, \Omega \, \text{cm}^{-2}$, 100 mm x 100 mm x 2.2 mm) from Dyesol was used for the photoanode. TiO_2 pastes 18NR-AO with a blend of active anatase with average particle size $\sim 20 \, \text{nm}$ and anatase scatter particle size $\leq 450 \, \text{nm}$ was obtained from Greatcell for fabricating the TiO_2 porous anode. Titanium tetrachloride (purity 99.99%) from Sigma-Aldrich was used for the treatment of the TiO_2 anode. N719 complex [di-tetrabutylammonium cis-bis(isothiocyanato) bis(2,2'-bipyridyl-4,4'-dicarboxylato) Ru (II), purity 95%] obtained from Greatcell, PITC (phenyl isothiocyanate, purity 98%) was purchased from Merck, RF-sputtered titania was prepared via the method described in ref²⁴.

4.2.2. Sample Preparation

4.2.2.1. Preparation of substrate

The substrate for FTIR measurements was fabricated by the standard protocol of photoanode preparation for DSSCs²⁵⁻²⁶. The FTO was cleaned using ultrasonication first with deionised (DI) water and detergent and followed by ethanol for 30 mins each. The cleaned FTO was then treated with 40 mM of TiCl_4 aqueous solution by heating at 70 °C for 30 mins. Pre and post-treatment of the photoanode with TiCl_4 has been shown experimentally to improve cell efficiency and thus implemented in this study²⁷. The pre-treated FTO was sintered in a furnace at 300 °C for 3 hrs. The pre-treated FTO was then screen-printed with 5 layers of titania to obtain the required thickness, refer to Figure 8.2 for SEM image of the cross section of 4 layered titania and plot of thickness versus number of layers deposited. It must be noted that each layer was dried at 120 °C for 5 minutes before the application of each layer. After complete deposition, the titania layer was sintered by stepwise heating with the following steps: 120 °C for 5 mins, 325 °C for 10 mins, 375 °C for 10 mins, and 500 °C for 30 mins. The sintered titania substrate was again treated with 40 mM of TiCl_4 solution.

For ARXPS analysis mesoporous titania is not a viable substrate and instead, a model flat substrate was needed. Hence, the RF-sputter deposited titania on the Si wafer was used as described in ref²⁴.

4.2.2.2. FTIR sample preparation

The samples for FTIR analysis were prepared either by drop-casting the respective substance directly onto the substrate or by immersing the substrate into the respective compound solution. Drop-cast samples were kept covered overnight before measurement. For the dye-adsorbed sample, TiO_2 substrates were immersed in 0.3 mM of N719 solution for 24 hrs. The solvent used was a 1:1 ratio of tert-butanol and AN. For RF-sputtered substrates, the dye solution was drop-cast to allow complete coverage of the substrate.

4.2.2.3. Samples for Dye re-sensitisation

The samples for re-sensitisation purposes were prepared by dipping the pre and post- TiCl_4 treated (PPT) 5 layered mesoporous TiO_2 into 0.3 mM dye solution for 24 hrs. In this experiment, different TiO_2 substrates were dipped into the same dye solution. The resultant dye solution following multiple dipping events was drop-cast onto a TiO_2 substrate to compare with a fresh dye solution absorbed onto a TiO_2 substrate.

4.2.3. Spectroscopic Measures

4.2.3.1. Fourier Transform Infrared Spectroscopy

The ATR-FTIR spectra presented in this study were measured using a Bruker FTIR spectrometer (Vertex 80v) with a diamond ATR crystal and a broadband mid-IR source $4000\text{ cm}^{-1} - 400\text{ cm}^{-1}$. The spectra represent an average of 100 scans recorded with a resolution of 2 cm^{-1} . The spectra do not have any corrections applied for penetration depth, incidence angle, or refractive index. A scaled TiO_2 spectrum was subtracted from the spectra of samples adsorbed on TiO_2 substrate to reveal the adsorbate's contribution alone.

4.2.3.2. ARXPS

XPS was used to identify the elemental and chemical states and electronic structural information of the sample within the depth of 10 nm. The spectroscopy apparatus is best described in ref ²⁸. The Mg anode with photon energy 1253.6 eV (XR-50, SPECS) was used. Each spectrum was calibrated to the C1s spectral line at a BE of 285 eV. The background signal due to electron scattering was fitted with a Shirley background. To fit the intrinsic shape of the high-resolution spectra, the peaks were fitted with a 30% and 70% Lorentz and Gaussian function contribution, respectively.

A quantitative depth profile analysis was conducted by ARXPS. By changing the angle between the analyser and the surface normal probing depth changes thus, revealing the concentration depth profiles. The angle of observation ranged from 0° to 60° . The analysis and mathematical fitting procedure used are best described by Eschen et al. ²⁹. The electron mean-free path required for the fitting was obtained via the NIST EAL database ³⁰. The XPS technique was experimentally proven to cause no damage to the sample. Refer to Figure 8.3 for the variation in different dye elements with continuous exposure of an X-ray source for 2 hrs.

4.3. Results and Discussion

4.3.1. FTIR

To understand the anchoring behaviour of the potential binding groups on the N719, namely the carboxyl group, thiocyanate ligand, and TBA^+ ion, the model compounds formic acid, PITC, and TBA-Br salt were chosen for adsorption studies on TiO_2 . The PPT 5 layered TiO_2 was immersed into the respective compounds and the substrates were investigated using FTIR.

4.3.1.1. Formic acid adsorption

Formic acid has a carboxylic acid group which can function as an anchoring group. Formic acid has previously been found to adsorb on metal oxide surfaces through two methods ³¹:

1. Adsorption via the formate anion following deprotonation of formic acid during adsorption.
2. Physisorption of molecular formic acid.

The deprotonated formate was found to adsorb through different coordination modes; monodentate via ester or CO binding, bidentate bridging, bidentate chelating, and H-bonded structures ³².

The ATR-FTIR spectra of liquid formic acid and formic acid adsorbed on TiO₂ are shown in Figure 4.2. The peak positions observed in the formic acid spectrum are close to that of the IR transmission mode spectra reported previously ³³. From Figure 4.2 it is obvious that upon adsorption the formic acid peaks positioned at 1170 cm⁻¹ (C-O stretching) and 1688 cm⁻¹ (C=O stretching) disappeared and weak new peaks with a moderate shift towards high wavenumber appeared at 1208 cm⁻¹, and 1710 cm⁻¹, respectively. Moreover, a new intense peak at 1552 cm⁻¹ and another peak at 1362 cm⁻¹ appear upon adsorption and are readily assigned to the carboxylate group asymmetric and symmetric stretching modes respectively ³¹, suggesting the dominant mode of attachment is via the deprotonation of formic acid into formate species to bind to the surface. The broad peak at 1354 cm⁻¹ in the liquid formic acid spectrum has previously been assigned to the combination band of (O-OH) + (C-O) stretching ³⁴ and is seen to disappear upon adsorption consistent with the disappearance of the C-O peak at 1170 cm⁻¹. The new, weak, shifted C-O and C=O peaks observed at 1208 cm⁻¹ and 1710 cm⁻¹ could be a result of a physisorption species or evidence of ester linkage formation. For a physisorbed species, the observed peak shift would require strong interactions with the substrate, whereas the new peaks lie in the expected range for esters and thus we suggest there is also a small contribution from binding through an ester linkage.

The assignments of the vibrational modes of different adsorbed species following formic acid adsorption observed in this study are summarised in Table 4.1.

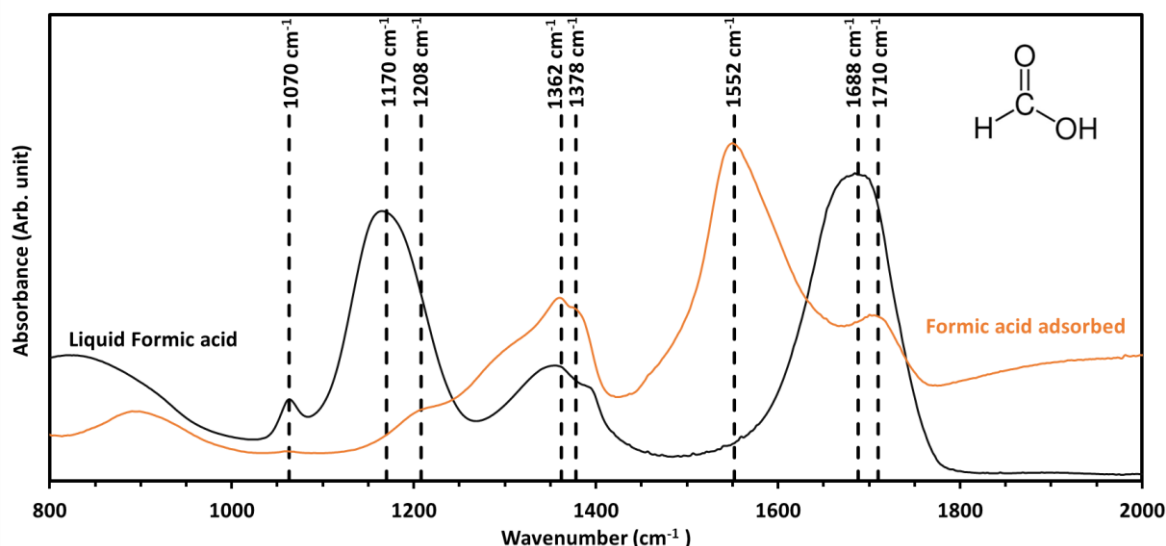


Figure 4.2: The FTIR spectra of formic acid (black) and formic acid adsorbed on TiO₂ (orange), the formic acid adsorbed spectrum has had the TiO₂ contribution removed. The secondary axis represents the absorbance for the formic acid adsorbed.

Table 4.1: Vibrational mode assignments of adsorbed species for formic acid observed in the adsorption onto the TiO₂ substrate using ATR-FTIR.

Liquid Formic Acid			
Species		Vibrational Modes	Wavenumber (cm ⁻¹)
Formic acid	Solution	$\nu(\text{C=O})$	1688
		$\nu(\text{CO})$	1170
Adsorbed Species			
Species		Vibrational Modes	Wavenumber (cm ⁻¹)
Formate	Bridged Bidentate	$\nu_{as}(\text{OCO})$	1552
		$\nu_s(\text{OCO})$	1362
		δCH	1378
Formic acid	Ester	$\nu(\text{C=O})$	1710
		$\nu(\text{CO})$	1208

Philips and Deacon reviewed the IR spectra of many carboxylate compounds and subsequently proposed an empirical formula to determine the anchoring geometry of a carboxylate group based on the frequency separation ($\Delta\nu$) of the symmetric $\nu_s(\text{OCO})$ and asymmetric $\nu_{as}(\text{OCO})$ stretching modes of the carboxylate group³⁵. They found that $\Delta\nu$ values span a large range from $<100 \text{ cm}^{-1}$ to almost 400 cm^{-1} and the frequency difference is in order

of unidentate $>$ ionic \cong bidentate bridging $>$ bidentate chelating^{31, 35-36}. From Table 4.1 the difference between the symmetric and asymmetric carboxylate group observed in the study is 190 cm^{-1} which is close to the frequency difference observed for ionic sodium formate which was measured to be 201 cm^{-1} ³⁷⁻³⁸. Therefore, we suggest the dominant binding of formic acid on titania occurs through a bridging bidentate mode, with a minor contribution from ester binding.

Combining all the possible anchoring modes observed, Figure 4.3 shows the adsorption model of formic acid attachment to titania substrate.

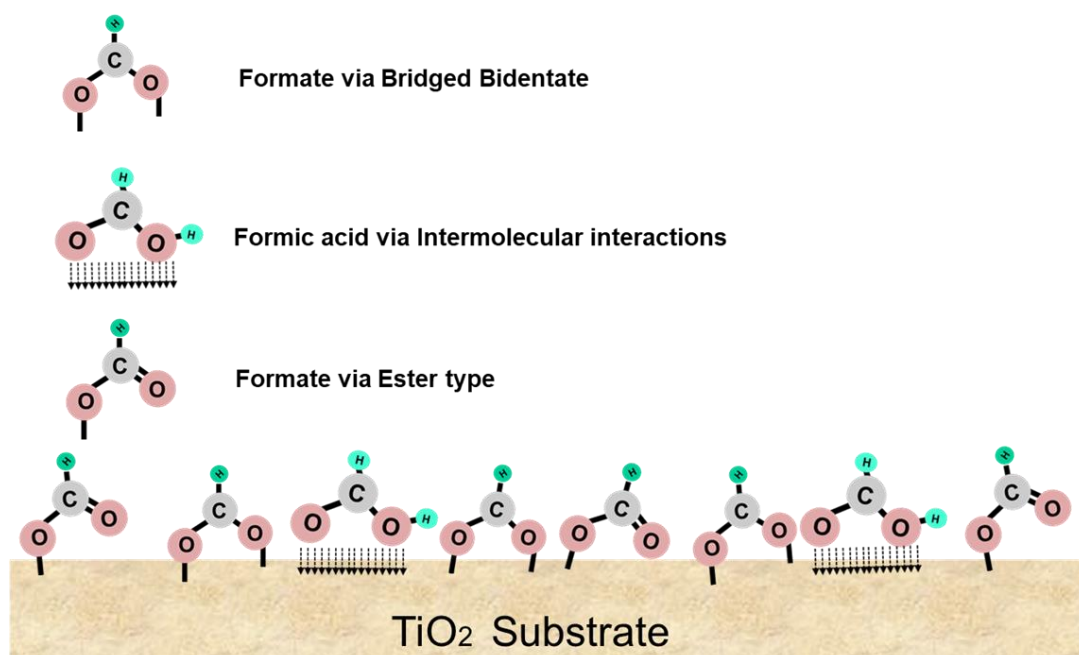


Figure 4.3: The adsorption model for adsorbate formic acid and adsorbent TiO_2 .

4.3.1.2. Phenyl isothiocyanate (PITC) Adsorption

To understand the interaction of the thiocyanate ligand, NCS^- , on TiO_2 substrates the adsorption of PITC was investigated. PITC was drop-cast onto a mesoporous TiO_2 substrate and then measured under different conditions using FTIR (refer Figure 8.4 for IR spectra of PITC adsorbed on titania with and without rinsing in N_2 purged condition and in vacuum). Figure 4.4 displays the IR spectra for neat PITC liquid and PITC adsorbed onto titania substrate measured both under an N_2 purged environment and under vacuum conditions. The NCS peak for the liquid PITC was observed at 2030 cm^{-1} , however, on adsorption and under a nitrogen atmosphere, the intensity of the NCS peak is drastically reduced and observed to shift to $\sim 2100\text{ cm}^{-1}$. This peak vanishes upon the evacuation of the sample chamber, but other PITC peaks remain. This indicates the dominant mode of adsorption is through the destruction

of the N=C=S moiety, and possibly under atmospheric conditions there is a small contribution from either a physisorbed species or a layer of PITC molecules above the chemisorbed species that is easily removed under vacuum.

Following adsorption, many new peaks appear in the 1200-1345 cm^{-1} range, a range of new peaks, comprised of multiple peaks, is observed at 1500-1660 cm^{-1} , and a single strong broad peak centred at 3205 cm^{-1} also appears. The 3205 cm^{-1} peak can be assigned to an N-H stretch, presumably of a secondary amine given that only a single peak is observed, although the peak position is at the lower wavenumber range of expected values. Further evidence of the presence of an amine includes the observation of new peaks in the 1200-1345 cm^{-1} region, which can be attributed to the C-N-C asymmetric stretch of an aromatic secondary amine. We tentatively assign the 1545 cm^{-1} peak to N-H bending motion but note that this is expected to be weak in secondary amines. The appearance of N-H assigned peaks and the disappearance of the NCS peak suggests that the PITC undergoes breaking of the N=C=S bonds and subsequent reaction with surface hydroxyl groups to form an amine species upon adsorption.

Samples of adsorbed PITC on titania were subjected to rinsing with ethanol to give some indication of the binding strength of PITC onto titania. Following ethanol rinsing, no evidence of any adsorbed species remained, indicating that upon adsorption only a weak chemisorbed species is formed and is easily removed with rinsing. The complete information about the wavenumber and peak assignments for the PITC liquid and adsorbed onto titania substrate can be found in the appendix section (see Table 8.2).

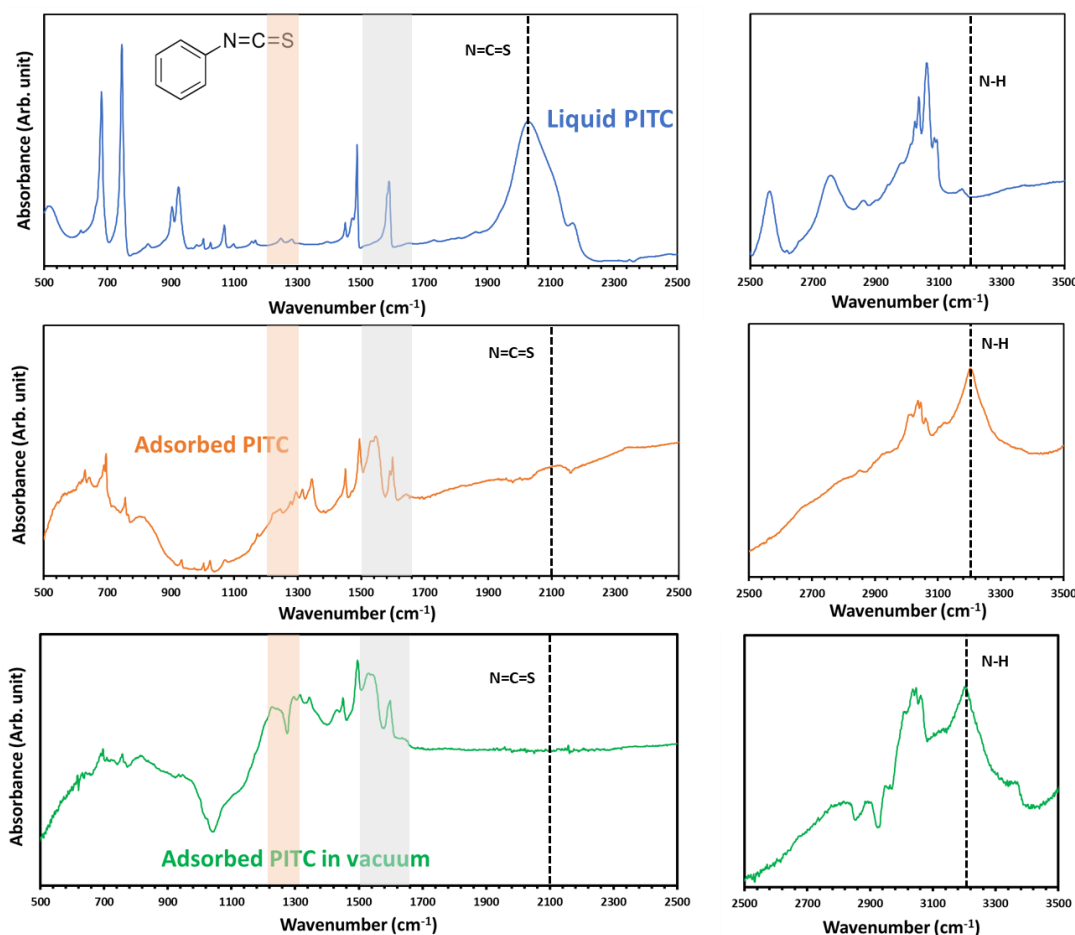


Figure 4.4: The ATR-FTIR spectra of phenyl isothiocyanate (PITC) liquid and PITC adsorbed on TiO_2 substrate from region $500\text{--}2500\text{ cm}^{-1}$ and from region $2500\text{--}3500\text{ cm}^{-1}$. The adsorbed PITC spectrum has the TiO_2 background subtracted.

4.3.1.3. TBA-Br Adsorption

To have a better understanding of the potential involvement of TBA^+ in dye anchoring, TBA-Br salt was selected and investigated using FTIR. Pure TBA-Br powder and 1M TBA-Br solution adsorbed onto TiO_2 substrate were analysed under vacuum conditions. The FTIR spectrum shows only minor changes after TBA-Br adsorption when compared with the pure powder spectrum suggesting the physisorption of TBA-Br on the TiO_2 substrate (see appendix section Figure 8.5).

4.3.1.4. N719-dye Adsorption

To investigate the anchoring modes of N719 onto the TiO_2 substrate the dye adsorbed sample was investigated and compared with the pure N719 powder. Figure 4.5, shows the IR spectrum of N719 powder (orange) and the subtracted spectrum (green) that represents the difference

between the dye-adsorbed TiO_2 and blank TiO_2 . The peak positions of the main features of the dye powder and the dye adsorbed on TiO_2 are shown in Table 4.2.

Table 4.2: The IR modes of N719 powder and the adsorbed dye on TiO_2 substrate with the peak assignment.

IR modes	Dye Powder (cm^{-1})	Dye adsorbed on TiO_2 (cm^{-1})
C-O	1228	1234
Sym (COO^-)	1372	1372
Bpy	1405	1407
TBA (CH₂)	1466	1466
C=C	1542	1542
Asym (COO^-)	1607	1602
C=O	1705	1734
NCS	2095	2096
TBA	2873	2854

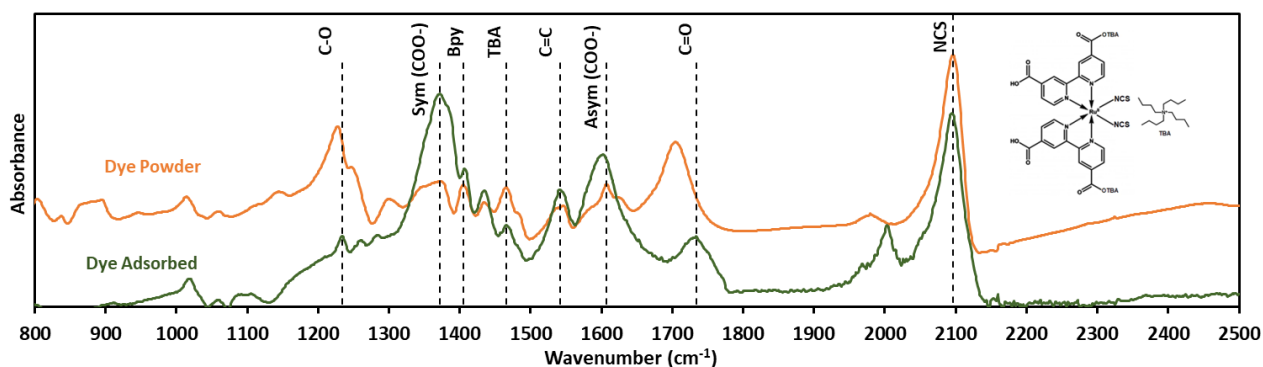


Figure 4.5: FTIR spectra of N719 powder (orange) and N719 solution adsorbed on TiO_2 substrate subtracted from blank TiO_2 (green).

The changes in the IR spectra between the dye powder and dye adsorbed onto TiO_2 , Figure 4.5, closely resemble the differences observed for the adsorption of formic acid, Figure 4.2. The intensity of the C-O stretch in the dye powder spectrum is significantly reduced and the C=O peak intensity is also reduced with a shift towards higher wavenumber. New peaks corresponding to the symmetric and asymmetric stretches of COO^- appear in the spectrum upon adsorption. All these observations were noted in the formic acid adsorption and thus, like formic acid, the dye dominantly binds through a carboxylate group with some evidence of an ester binding mode. Although it is clear that deprotonation of the carboxylic acid group

is occurring, we note that carboxylate binding may occur via the existing carboxylate group in the dye molecule or deprotonation of the acid moiety^{18, 39}.

Although no significant feature change in the C-H stretch region was observed for TBA-Br salt adsorbing on TiO₂, a significant change in the saturated aliphatic C-H stretch region for the dye molecule adsorbed on TiO₂ was observed, see appendix Figure 8.5 and Figure 4.6. The C-H bands of TBA⁺ positioned at 2873 cm⁻¹, 2933 cm⁻¹, and 2960 cm⁻¹ was observed to strongly alter upon adsorption suggesting a change in the TBA⁺ interaction upon dye adsorption. Although we have previously shown that TBA-Br adsorption onto TiO₂ is a physisorption process, the TBA⁺ within the dye was found to interact differently with the Ru- complex after the complex adsorbs to the TiO₂ substrate. In addition, the lack of carboxylic acid features in the IR spectrum upon dye adsorption suggests complete deprotonation of all carboxylic acid groups, however, it is sterically impossible to anchor via all the carboxylate groups in the complex. Thus, we suggest the changes in the C-H region are due to the interaction of TBA⁺ with the binding carboxylate and potentially bridging between the bound and unbound carboxylate groups.

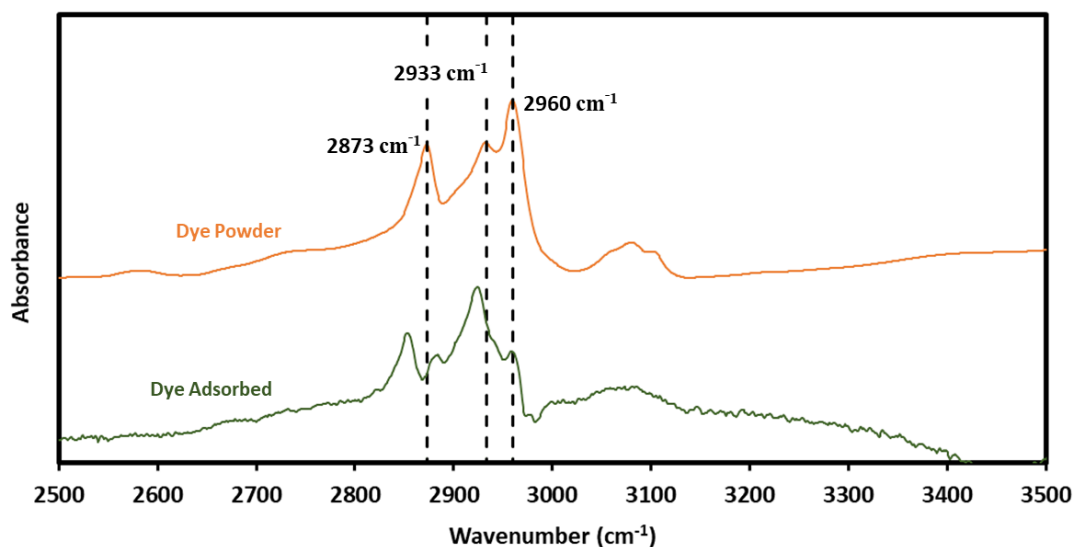


Figure 4.6: FTIR spectrum of N719 powder (orange) and dye adsorbed onto TiO₂ (green) in high wavenumber region 2700-3200 cm⁻¹.

Furthermore, no shift in the NCS peak at 2095 cm⁻¹ rules out the involvement of NCS as a dominant mode in dye anchoring in this case. However, a new peak appears in this region at 2050 cm⁻¹ which we assign to another form of NCS within the dye complex which we suggest is due to a non-covalent interaction with the TiO₂ substrate.

Moreover, considering the Phillips and Deacon rule, bidentate coordination results in separation equivalent to the free salt. The frequency separation for the dye powder calculated from the observed peak positions is 235 cm^{-1} and that for the adsorbed dye molecule is 230 cm^{-1} . The small difference in the wavenumber of the adsorbed symmetric COO^- and asymmetric COO^- with the pure dye suggests bidentate bridging.

In summary, the N719 anchors onto the TiO_2 substrate via multiple modes, which could be bidentate chelating and/or ester bonding through COO^- with partial interaction through NCS. Figure 4.7 below represents the simplified adsorption model for dye- TiO_2 configuration based on FTIR results. The possible modes of attachment for N719 onto the TiO_2 substrate are bidentate bridging and ester bond because of deprotonation of the carboxylic group, in addition, the NCS has a partial interaction with the TiO_2 substrate during adsorption, a similar result was proposed by ref ²⁰. Thus, we conclude from our observation that any possible combination of the three modes of attachment is the anchoring mode for the dye TiO_2 configuration.

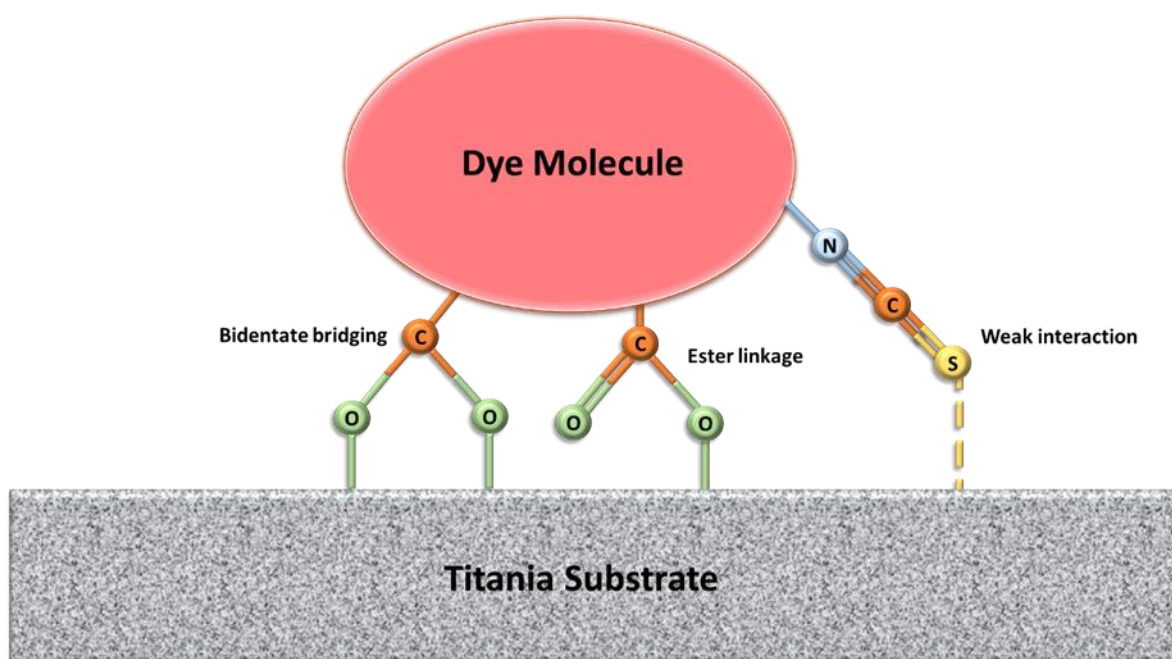


Figure 4.7: The dye anchoring model illustrating the individual anchoring modes of N719 onto the TiO_2 substrate based on the results observed from FTIR.

4.3.2. ARXPS

The sample substrate used in ARXPS analysis is flat. The crystallinity of the flat substrate and that of the mesoporous substrate is the same and was confirmed via XRD, see appendix section Figure 8.6. ARXPS was performed on the N719 adsorbed TiO_2 sample. The functional groups

representing the N719 and TiO_2 were considered and the variation in the intensity of the functional group with different observation angles was quantified.

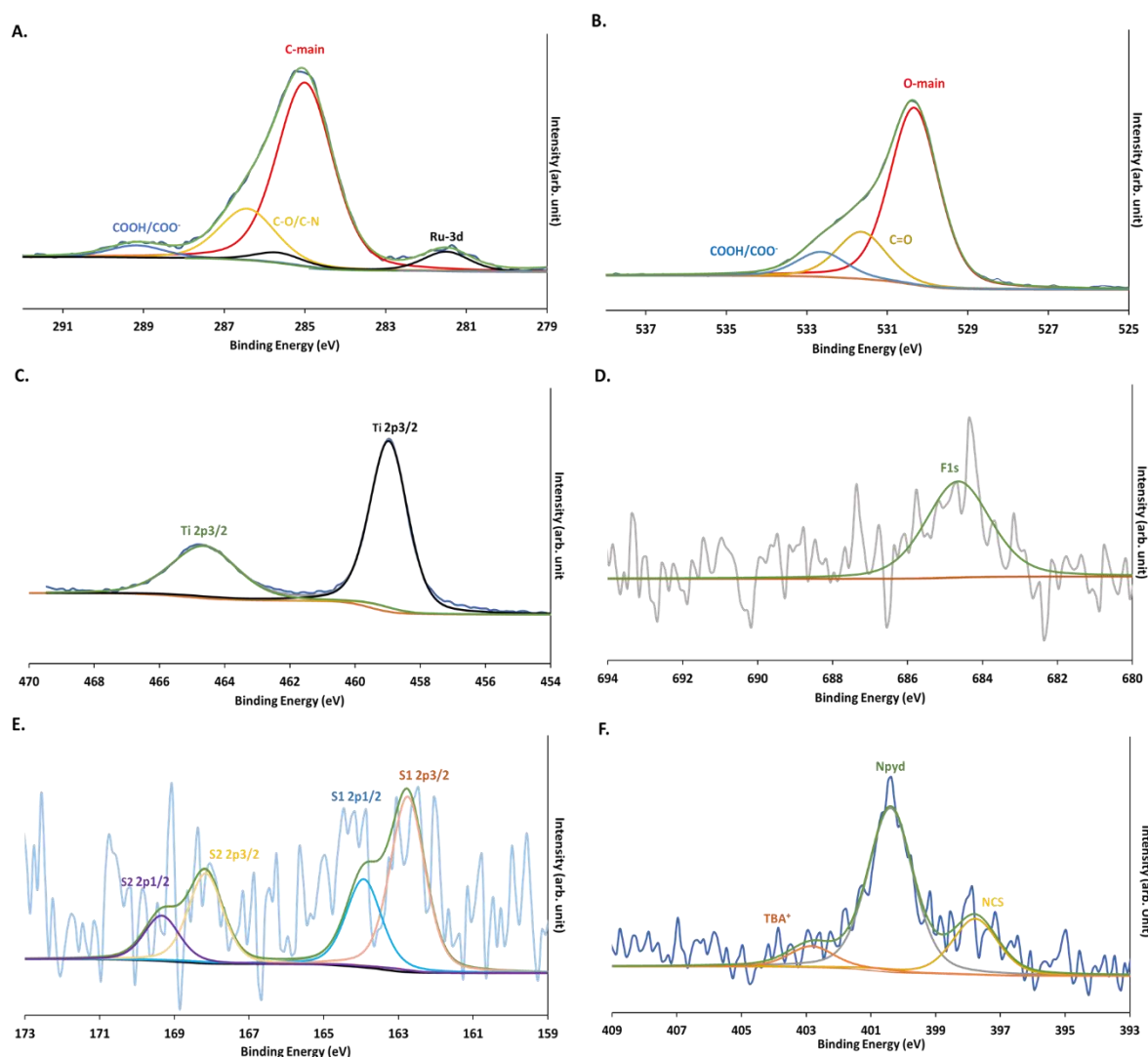


Figure 4.8: High-resolution XPS spectra of N719 adsorbed onto RF-sputtered TiO_2 measured at 0° emission angle, fitted with Shirley background, representing the relative intensity of (A). C1s/Ru3d, (B). O1s, (C). Ti2p, (D). F1s, (E). S2p, and (F). N1s for dye adsorbed onto RF- sputtered TiO_2 measured at 0° emission angle.

Figure 4.8 shows the high-resolution scan of the respective elements obtained after XPS analysis of the dye adsorbed onto RF-sputtered TiO_2 substrate at an emission angle of 0° , i.e., parallel to the surface normal. The C 1s/Ru 3d spectra revealed five peaks upon deconvolution, three related to carbon 1s and two related to Ru 3d. The largest contribution at 285.0 eV represents the main carbon peak (C-C bonds), 286.4 ± 0.2 eV represents C-O and C-N, and 289.2 ± 0.2 eV represents COO^-/COOH . All C1s peaks can be assigned to the various functional groups of the dye. Unlike FTIR, in XPS it is difficult to identify precisely the exact chemical nature of the C-peaks. Ru 3d $_{5/2}$ positioned at 281.5 ± 0.2 eV is the metal component

from the dye molecule ⁴⁰⁻⁴¹. The XPS high resolution of O1s peak at 530.3 ± 0.2 eV represents the main oxygen peak from titania ⁴⁰ and 531.6 ± 0.2 eV represents O⁻ and Ti-OH from titania substrate and C=O from dye molecule ⁴⁰, and COO⁻/COOH at 532.6 ± 0.2 eV ⁴¹. Apart from the COO⁻/COOH group, all O groups can be assigned to the TiO₂ substrate. Ti2p is resolved into two peaks the main peak at 459.0 ± 0.2 eV for 2p_{3/2} peak and its doublet ⁴². The S2p region includes two doublets 162.8 ± 0.2 eV (2p_{3/2}) for the S from NCS denoted as S-1 ⁴³ and 168.2 ± 0.2 eV (2p_{3/2}) for oxidised sulphur (S⁶⁺) possibly a sulphate noted as S-2 ⁴⁴. The high-resolution scan of N1s includes three peaks the high contributing pyridine at 400.4 ± 0.2 eV the N-main peak attributed to the organometallic functional group N719 being an organometallic dye, the contribution from NCS at 397.8 ± 0.2 eV and TBA⁺ at 402.8 ± 0.2 eV ^{43, 45}. All N and S components can be assigned to functional groups of the dye. Finally, the high-resolution scan for F1s was positioned at 684.6 ± 0.2 eV, which is present in the FTO but not in the TiO₂ paste. The relative peak intensities for the elements of dye-titania are shown in the appendix section Figure 8.7 and the relative intensity of N species are shown in Figure 8.8.

Further, for the extraction of the concentration depth profile, the algorithms used in this study are described by Eschen et. al. ²⁹. The measured intensity ratios for individual species were compared to the fitted intensity ratio and with the minimalization of the difference between the intensity ratios the concentration depth profile was obtained.

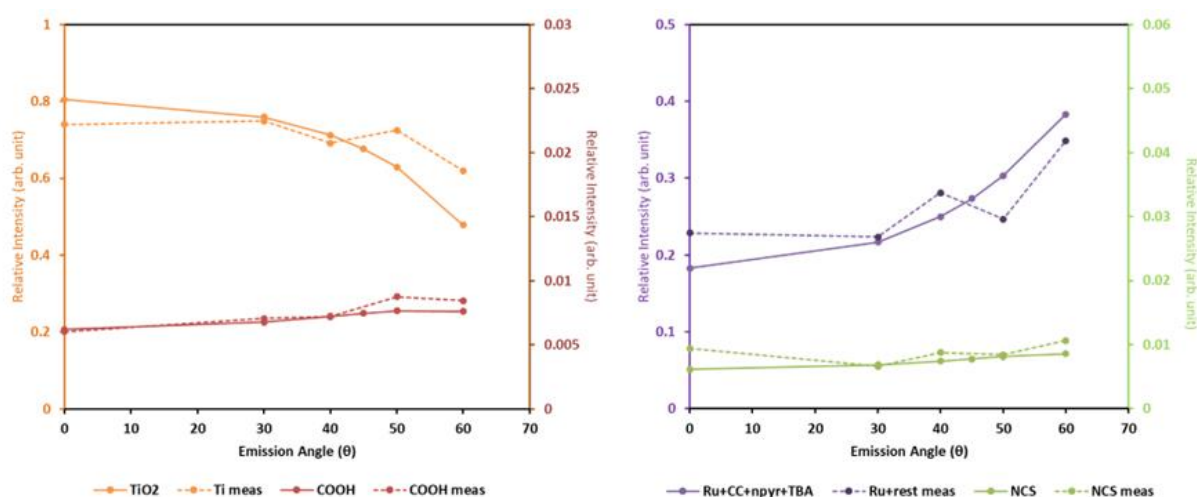


Figure 4.9: The variation in the XPS intensity of different components, namely TiO₂ (includes Ti at BE 459 eV and O1s at BE 530 eV and O-COOH at BE 533 eV), COO⁻/COOH (includes C-COOH at BE 289 eV), NCS (includes NCS at BE, S-1 at BE and S-2 at BE), and rest of the dye molecule (includes a combination of Ru, CC, CN, CO, Npyd, and TBA), (solid lines) and the fitted intensity ratio (dashed lines) with the emission angles.

To understand the depth profile of the various functional groups of the dye and the substrate, the intensity ratios of the elemental groups were classified as either coming from the substrate, which comprises the intensity of the Ti and main O peak, or from the dye component which incorporates the remaining peak intensities. Here, the dye layer was modelled as a combination of three main components, the COO⁻/COOH group, the NCS group, and the Ru +CC +Npyd +TBA representing the rest of the dye.

In Figure 4.9 the relative intensities as measured by ARXPS for the three groups representing the dye as described above and the TiO₂ are shown. The relative intensity of the peaks representing TiO₂ decreases with increasing emission angle. The peaks representing the three parts of the dye are increasing with increasing emission angle. This is what is expected for dye adsorbed on a flat TiO₂ surface.

The geometry of the adsorbed dye can be determined by fitting quantitatively the relative intensities as shown in Figure 4.9. For correct interpretation of the ARXPS data, it needs to be noted that the intensity of emitted electrons decreases with increasing depth due to the attenuation of the electrons when passing through matter. Shifting a layer to a larger depth then has a consequence that the number of atoms forming the layer has to increase to maintain the intensity of electrons emitted from this layer. In this study, two models were considered for the dye adsorption onto the TiO₂ substrate. Both models consist of four layers: TiO₂, COO⁻/COOH, NCS and the rest of the dye. In both models, TiO₂ forms the bottom layer (largest depth) and the rest of the dye the top layer (lowest depth). In model 1 the COO⁻/COOH is attached to the TiO₂ followed by the NCS. In the second model, the order of COO⁻/COOH and NCS are reversed as can be seen in Figure 4.10. For both models, the thickness of each layer is the fitting parameter. Both models fit the measured data equally well. However, as can be seen in Figure 4.10 in model 1 the thickness of the COO⁻/COOH and NCS layers are almost the same while in the second model the NCS layer is twice as thick as the COO⁻/COOH layer. Given that the number of atoms in the COO⁻/COOH and NCS layers is the same, the second model can be excluded. This infers that ARXPS shows that the main anchoring group is the COO⁻/COOH group.

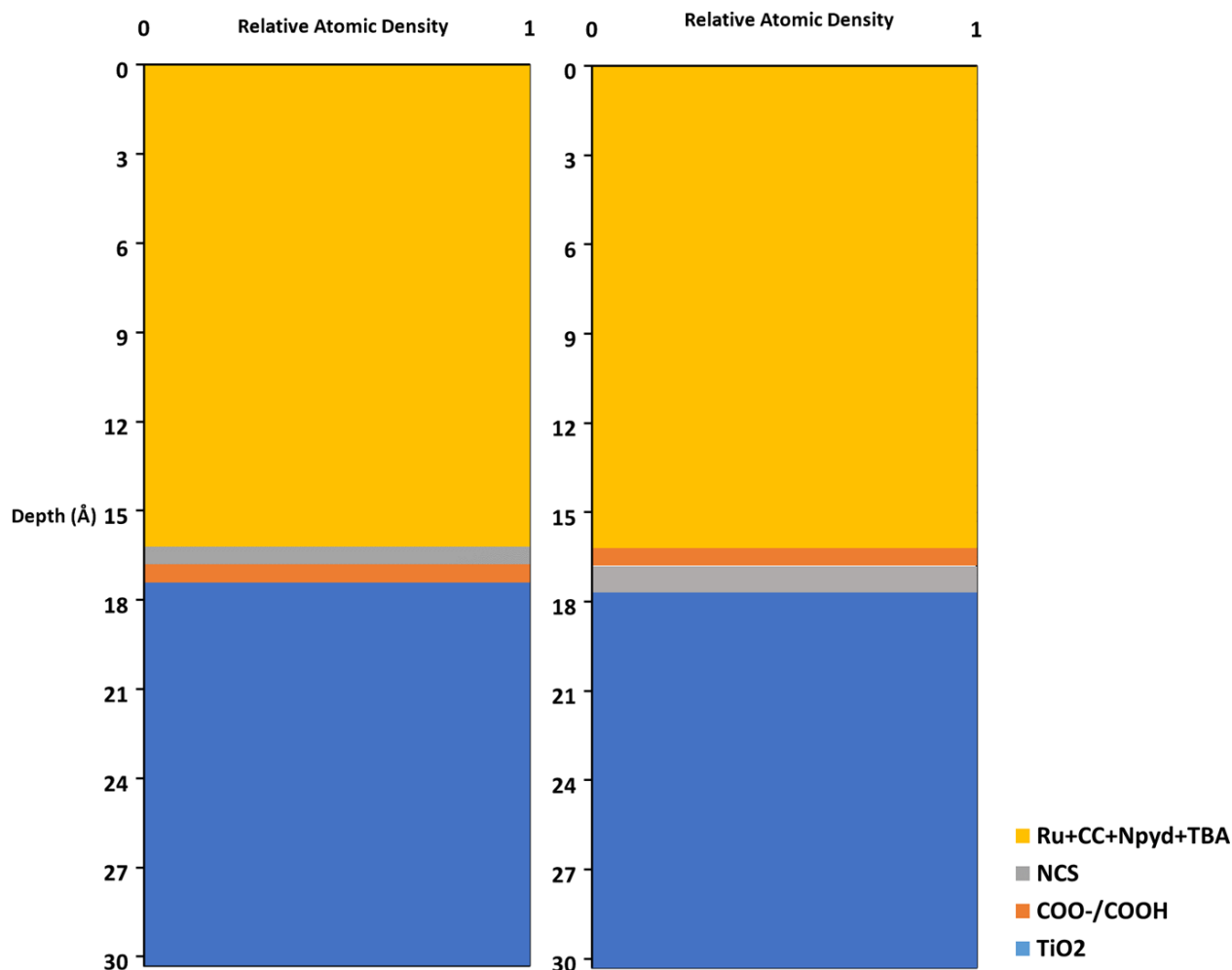


Figure 4.10: ARXPS concentration depth profile models for N719 drop-cast on RF-sputtered TiO₂. The left profile illustrates COO⁻/COOH group is binding to the TiO₂, and the right profile demonstrates the NCS group binding to the TiO₂ substrate. (Note: In the right profile the thickness of the NCS layer is significantly thicker than COO⁻/COOH).

4.3.3. XPS analysis for the re-sensitising test for analysing the TBA⁺ adsorption

The presence of TBA⁺ on the TiO₂ substrate is not addressed in many papers and hence different assumptions are made. Among them, ref ¹⁹ suggests the TBA⁺ gets washed away after rinsing the photoanodes. To understand the adsorption of TBA⁺ as a component of N719 on the TiO₂ substrate, a re-sensitising test was performed.

Fresh TiO₂/FTO substrates were immersed in the very same dye solution with an initial concentration of 0.3 mM for 24 hours each and then rinsed with ethanol. 20 such repetitions were performed. Of the 20 prepared samples five samples were analysed with XPS. Figure 4.11 shows the fresh dye solution versus the dye solution after the 20th sample immersion and

indicates the change in dye colouration indicating a decrease in dye concentration due to multiple sensitisations.

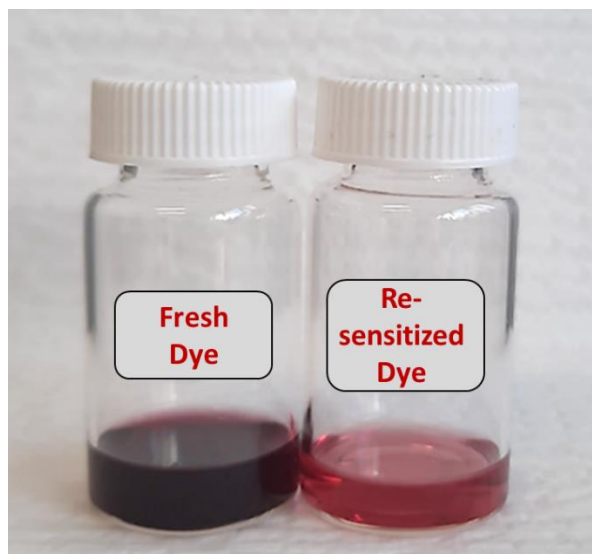


Figure 4.11: The colour comparison of freshly prepared dye and the dye after 20 consequent re-sensitising.

The complete chart with the peak intensity ratio and peak position of the multiple adsorbed samples can be found in the appendix section Table 8.3 and Table 8.4 respectively.

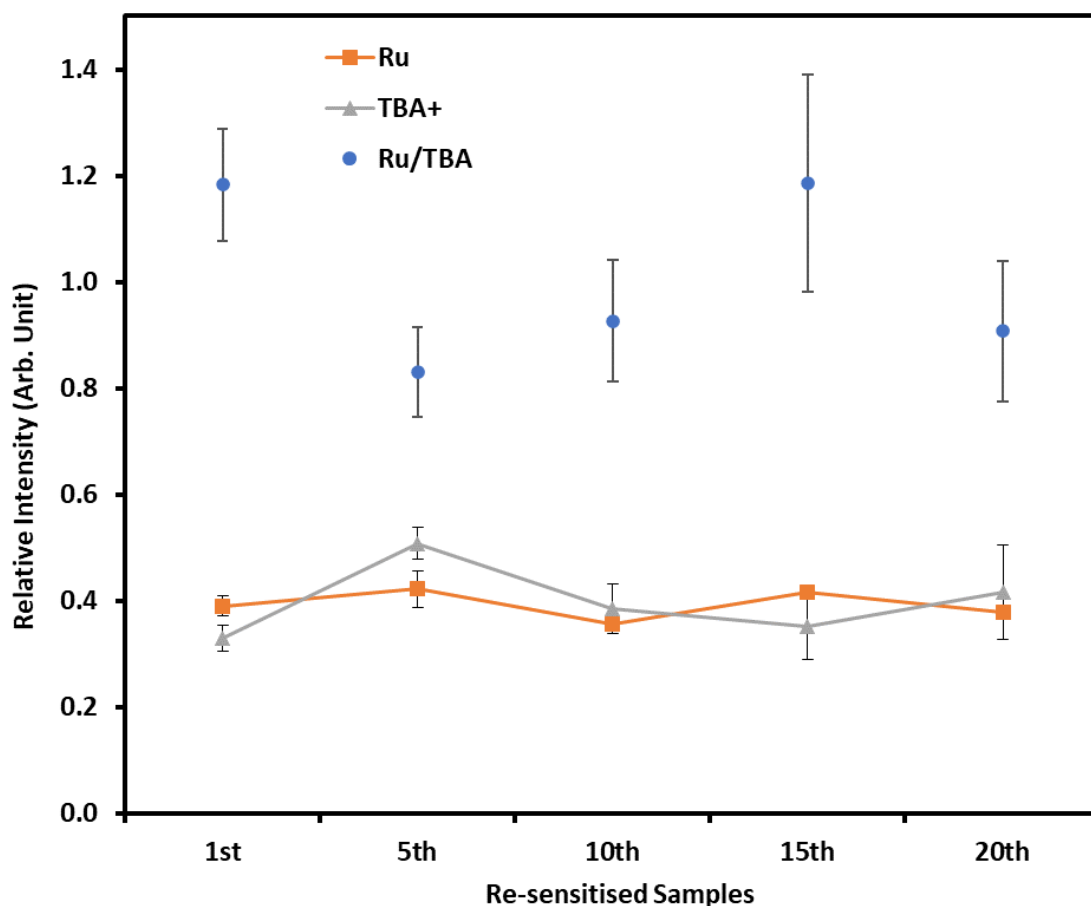


Figure 4.12: The XPS relative intensity ratio of Ru and TBA⁺ adsorbed onto the TiO₂ substrate on multiple sensitisations and the ratio of Ru/TBA⁺. The procedure for determining the relative intensities from XPS data is described in the experimental section.

Figure 4.12 shows the relative intensities of Ru and TBA⁺ and the ratio of Ru to TBA⁺ for the five samples investigated. The adsorption of the Ru and TBA⁺ components of N719 stays constant within the error bars as well as their ratio. This means that both parts of N719 adsorb in equal amounts. A complete plot for the ratio of individual dye elements to TiO₂ substrate is given in the appendix section Figure 8.9.

Figure 4.12 shows that the Ru/TBA⁺ ratio is unity within experimental uncertainty which means that TBA⁺ adsorbs onto the substrate with the same amount as Ru and that the TBA⁺ does not get lost on rinsing. This contradicts the report presented by Pérez León, Carmen, et al.¹⁹ that in dye solution the TBA⁺ counterions dissociate from the dye molecule and upon adsorption these counterions are rinsed off and remain in the rinsed solvent. It is to be noted that all the samples in the study were measured after rinsing with ethanol to make sure that excess or non-adsorbed dye molecules were removed from the substrate. Our findings support the study of Johansson et al.²⁰, that TBA⁺ adsorbs onto the TiO₂ substrate and participates in

charge compensation of carboxylate during adsorption. The analysis of the starting solution and the solution after 20 immersions for the relative intensity ratio of Ru/TBA⁺ is shown in the appendix Figure 8.9 which further confirms that all dye components decrease in concentration through repeated immersion. Refer to Table 8.5 for elemental ratios of fresh dye and the re-sensitised dye solutions drop-cast on TiO₂ substrate and analysed with XPS. Further, the XPS intensity ratio of Ru/TBA⁺ of the fresh dye and dye after multiple sensitisations drop-cast onto TiO₂ substrate show no notable change within experimental uncertainty (see Figure 8.10).

4.4. Conclusion

In the current study, the techniques FTIR and ARXPS have been applied to investigate the adsorption of N719 onto TiO₂ surfaces. FTIR is a chemical-sensitive technique but not a surface-sensitive technique and provides information about dye anchoring and dye conformation on the TiO₂ substrate. ARXPS is a surface-sensitive technique and allows for determining concentration depth profiles. In combination, the dye adsorption mode of N719 on TiO₂ was determined. FTIR for higher wavenumber suggests the interaction of TBA⁺ with the binding carboxylate and potentially bridging between the bound and unbound carboxylate groups. Supported by XPS results for dye re-sensitisation that addressed the discrepancies for TBA⁺ and confirmed that TBA⁺ adsorbs onto the TiO₂ in correspondence to the Ru of the dye molecule. Thus, the dye binding occurs via COO⁻ onto the TiO₂ however, we cannot rule out the possibility of COO⁻/TBA⁺ attachment.

4.5. Acknowledgements

The authors acknowledge the facilities, and the scientific and technical assistance of Microscopy Australia and the Australian National Fabrication Facility (ANFF) under the National Collaborative Research Infrastructure Strategy, at the South Australian Regional Facility, Flinders Microscopy and Microanalysis, Flinders University. The authors thank Dr. Yanting Yin for assistance in performing the SEM analysis.

4.6. Appendix

In the appendix section, SEM analysis for determining the thickness of TiO₂ on the FTO as the function of the number of layers deposited is included. The change in the relative intensity of different element species via XPS, to investigate the potential damage caused by X-ray exposure on the sample during XPS analysis. The analysis of the FTIR of phenyl

isothiocyanate (PITC) with and without rinsing in different environments namely N_2 purged and under vacuum is shown. It further includes a table comparing the wavenumber of liquid PITC and PITC adsorbed onto TiO_2 substrate with their respective peak assignment. Further, FTIR for TBA-Br powder and TBA-Br solution adsorbed on TiO_2 is shown. The XRD analysis for the mesoporous TiO_2 and the RF-sputtered TiO_2 is shown. In addition, the ARXPS analysis for the variation in the elemental species of dye adsorbed on RF-sputtered TiO_2 , with different emission angles, is incorporated both as a plot and illustrated in a table. The XPS peak position and variation in the intensity among the re-sensitised sample is detailed in a table.

4.7. References:

1. Grätzel M. Dye-sensitized solar cells. *Journal of Photochemistry and Photobiology C: Photochemistry Reviews*. 2003;4(2):145-53.
2. Murakoshi K, Kano G, Wada Y, Yanagida S, Miyazaki H, Matsumoto M, et al. Importance of binding states between photosensitizing molecules and the TiO₂ surface for efficiency in a dye-sensitized solar cell. *Journal of Electroanalytical Chemistry*. 1995;396(1-2):27-34.
3. Li Z, Smeu M, Ratner MA, Borguet E. Effect of anchoring groups on single molecule charge transport through porphyrins. *The Journal of Physical Chemistry C*. 2013;117(29):14890-8.
4. Dayan O, Özdemir N, Yakuphanoglu F, Şerbetçi Z, Bilici A, Çetinkaya B, et al. Synthesis and photovoltaic properties of new Ru (II) complexes for dye-sensitized solar cells. *Journal of Materials Science: Materials in Electronics*. 2018;29:11045-58.
5. Ning Z, Zhang Q, Wu W, Pei H, Liu B, Tian H. Starburst triarylamine based dyes for efficient dye-sensitized solar cells. *The Journal of organic chemistry*. 2008;73(10):3791-7.
6. Zhang L, Cole JM. Anchoring groups for dye-sensitized solar cells. *ACS applied materials & interfaces*. 2015;7(6):3427-55.
7. Nazeeruddin MK, Liska P, Moser J, Vlachopoulos N, Grätzel M. Conversion of light into electricity with trinuclear ruthenium complexes adsorbed on textured TiO₂ films. *Helvetica Chimica Acta*. 1990;73(6):1788-803.
8. Nazeeruddin MK, Pechy P, Grätzel M. Efficient panchromatic sensitization of nanocrystalline TiO₂ films by a black dye based on a trithiocyanato-ruthenium complex. *Chemical Communications*. 1997(18):1705-6.
9. Nazeeruddin MK, Kay A, Rodicio I, Humphry-Baker R, Müller E, Liska P, et al. Conversion of light to electricity by cis-X₂bis (2, 2'-bipyridyl-4, 4'-dicarboxylate) ruthenium (II) charge-transfer sensitizers (X= Cl-, Br-, I-, CN-, and SCN-) on nanocrystalline titanium dioxide electrodes. *Journal of the American Chemical Society*. 1993;115(14):6382-90.
10. Nazeeruddin MK, Pechy P, Renouard T, Zakeeruddin SM, Humphry-Baker R, Comte P, et al. Engineering of efficient panchromatic sensitizers for nanocrystalline TiO₂-based solar cells. *Journal of the American Chemical Society*. 2001;123(8):1613-24.
11. Hagfeldt A, Boschloo G, Sun L, Kloo L, Pettersson H. Dye-sensitized solar cells. *Chemical reviews*. 2010;110(11):6595-663.
12. Kakiage K, Aoyama Y, Yano T, Oya K, Fujisawa J-i, Hanaya M. Highly-efficient dye-sensitized solar cells with collaborative sensitization by silyl-anchor and carboxy-anchor dyes. *Chemical communications*. 2015;51(88):15894-7.
13. Ren Y, Zhang D, Suo J, Cao Y, Eickemeyer FT, Vlachopoulos N, et al. Hydroxamic acid pre-adsorption raises the efficiency of cosensitized solar cells. *Nature*. 2023;613(7942):60-5.
14. Yao Z, Zhang M, Wu H, Yang L, Li R, Wang P. Donor/acceptor indenoperylene dye for highly efficient organic dye-sensitized solar cells. *Journal of the American Chemical Society*. 2015;137(11):3799-802.
15. Mathew S, Yella A, Gao P, Humphry-Baker R, Curchod BF, Ashari-Astani N, et al. Dye-sensitized solar cells with 13% efficiency achieved through the molecular engineering of porphyrin sensitizers. *Nature chemistry*. 2014;6(3):242-7.
16. Kroon JM, Bakker N, Smit H, Liska P, Thampi K, Wang P, et al. Nanocrystalline dye-sensitized solar cells having maximum performance. *Progress in Photovoltaics: Research and Applications*. 2007;15(1):1-18.

17. Nazeeruddin MK, Humphry-Baker R, Liska P, Grätzel M. Investigation of sensitizer adsorption and the influence of protons on current and voltage of a dye-sensitized nanocrystalline TiO₂ solar cell. *The Journal of Physical Chemistry B*. 2003;107(34):8981-7.
18. Lee KE, Gomez MA, Elouatik S, Demopoulos GP. Further understanding of the adsorption mechanism of N719 sensitizer on anatase TiO₂ films for DSSC applications using vibrational spectroscopy and confocal Raman imaging. *Langmuir*. 2010;26(12):9575-83.
19. Pérez León C, Kador L, Peng B, Thelakkat M. Characterization of the adsorption of Ru-bpy dyes on mesoporous TiO₂ films with UV–Vis, Raman, and FTIR spectroscopies. *The Journal of Physical Chemistry B*. 2006;110(17):8723-30.
20. Johansson EM, Hedlund M, Siegbahn H, Rensmo H. Electronic and molecular surface structure of Ru (tcterpy)(NCS) 3 and Ru (dcbpy) 2 (NCS) 2 adsorbed from solution onto nanostructured TiO₂: a photoelectron spectroscopy study. *The Journal of Physical Chemistry B*. 2005;109(47):22256-63.
21. Chang H, Wu H, Chen T, Huang K, Jwo C, Lo Y. Dye-sensitized solar cell using natural dyes extracted from spinach and ipomoea. *Journal of Alloys and Compounds*. 2010;495(2):606-10.
22. Abodunrin T, Obafemi O, Boyo A, Adebayo T, Jimoh R. The effect of electrolyte on dye sensitized solar cells using natural dye from Mango (*M. indica* L.) leaf as sensitizer. *Advances in Materials Physics and Chemistry*. 2015;5(06):205.
23. Faqih P, Nurosyid F, Kusumaningsih T, editors. Effect of acidic level (pH) of red dragon fruit (*Hylocereus costaricensis*) peels extract on DSSC efficiency. *AIP Conference Proceedings*; 2020: AIP Publishing.
24. Daughtry J, Alotabi AS, Howard-Fabretto L, Andersson GG. Composition and properties of RF-sputter deposited titanium dioxide thin films. *Nanoscale Advances*. 2021;3(4):1077-86.
25. Sedghi A, Miankushki HN. Influence of TiCl₄ treatment on structure and performance of dye-sensitized solar cells. *Japanese Journal of applied physics*. 2013;52(7R):075002.
26. Vesce L, Riccitelli R, Soscia G, Brown TM, Di Carlo A, Reale A. Optimization of nanostructured titania photoanodes for dye-sensitized solar cells: Study and experimentation of TiCl₄ treatment. *Journal of Non-crystalline solids*. 2010;356(37-40):1958-61.
27. Adhikari SG, Shamsaldeen A, Andersson GG. The effect of TiCl₄ treatment on the performance of dye-sensitized solar cells. *The Journal of Chemical Physics*. 2019;151(16):164704.
28. Acres RG, Ellis AV, Alvino J, Lenahan CE, Khodakov DA, Metha GF, et al. Molecular structure of 3-aminopropyltriethoxysilane layers formed on silanol-terminated silicon surfaces. *The Journal of Physical Chemistry C*. 2012;116(10):6289-97.
29. Eschen F, Heyerhoff M, Morgner H, Vogt J. The concentration-depth profile at the surface of a solution of tetrabutylammonium iodide in formamide, based on angle-resolved photoelectron spectroscopy. *Journal of Physics: Condensed Matter*. 1995;7(10):1961.
30. NIST Electron Effective-Attenuation-Length Database [Internet]. NIST. 2021. Available from: <https://www.nist.gov/property-fieldsection/nist-standard-reference-database-82>
31. Nanayakkara CE, Dillon JK, Grassian VH. Surface adsorption and photochemistry of gas-phase formic acid on TiO₂ nanoparticles: the role of adsorbed water in surface coordination, adsorption kinetics, and rate of photoproduct formation. *The Journal of Physical Chemistry C*. 2014;118(44):25487-95.
32. Galoppini E. Linkers for anchoring sensitizers to semiconductor nanoparticles. *Coordination Chemistry Reviews*. 2004;248(13-14):1283-97.
33. Chapman D. 48. The infrared spectra of liquid and solid formic acid. *Journal of the Chemical Society (Resumed)*. 1956:225-9.

34. Tomlinson GE, Curnutte B, Hathaway C. Temperature dependence of the Raman and infrared spectrum of liquid formic acid. *Journal of Molecular Spectroscopy*. 1970;36(1):26-33.
35. Deacon G, Phillips R. Relationships between the carbon-oxygen stretching frequencies of carboxylato complexes and the type of carboxylate coordination. *Coordination chemistry reviews*. 1980;33(3):227-50.
36. Uznanski P, Zakrzewska J, Favier F, Kazmierski S, Bryszewska E. Synthesis and characterization of silver nanoparticles from (bis) alkylamine silver carboxylate precursors. *Journal of Nanoparticle Research*. 2017;19(3):1-20.
37. Nakamoto K. *Infrared and Raman spectra of inorganic and coordination compounds, part B: applications in coordination, organometallic, and bioinorganic chemistry*: John Wiley & Sons; 2009.
38. Nolan NT, Seery MK, Pillai SC. Spectroscopic investigation of the anatase-to-rutile transformation of sol–gel-synthesized TiO₂ photocatalysts. *The Journal of Physical Chemistry C*. 2009;113(36):16151-7.
39. Falaras P. Synergetic effect of carboxylic acid functional groups and fractal surface characteristics for efficient dye sensitization of titanium oxide. *Solar Energy Materials and Solar Cells*. 1998;53(1-2):163-75.
40. Singh J, Gusain A, Saxena V, Chauhan A, Veerender P, Koiry S, et al. XPS, UV–vis, FTIR, and EXAFS studies to investigate the binding mechanism of N719 dye onto oxalic acid treated TiO₂ and its implication on photovoltaic properties. *The Journal of Physical Chemistry C*. 2013;117(41):21096-104.
41. Zen S, Inoue Y, Ono R. Low temperature (150° C) fabrication of high-performance TiO₂ films for dye-sensitized solar cells using ultraviolet light and plasma treatments of TiO₂ paste containing organic binder. *Journal of Applied Physics*. 2015;117(10):103302.
42. Bharti B, Kumar S, Lee H-N, Kumar R. Formation of oxygen vacancies and Ti³⁺ state in TiO₂ thin film and enhanced optical properties by air plasma treatment. *Scientific reports*. 2016;6(1):1-12.
43. Oscarsson J, Fredin K, Ahmadi S, Eriksson AI, Johansson EM, Rensmo H. Molecular degradation of D35 and K77 sensitizers when exposed to temperatures exceeding 100° C investigated by photoelectron spectroscopy. *Physical Chemistry Chemical Physics*. 2016;18(12):8598-607.
44. Siow KS, Britcher L, Kumar S, Griesser HJ. XPS study of sulfur and phosphorus compounds with different oxidation states. *Sains Malaysiana*. 2018;47(8):1913-22.
45. Hahlin M, Johansson EM, Scholin R, Siegbahn H, Rensmo H. Influence of water on the electronic and molecular surface structures of Ru-dyes at nanostructured TiO₂. *The Journal of Physical Chemistry C*. 2011;115(24):11996-2004.

CHAPTER 5 EXPLORING ALTERATION IN ELECTROCHEMICAL INTERFACE OF DYE SENSITISED SOLAR CELLS-AN EXPERIMENTAL SET-UP FOR AGEING INVESTIGATION

Abstract

Interfaces play a crucial role in determining the efficiency and long-term stability of DSSCs. While an ageing and degradation study in DSSCs is not a new topic to explore, there are still many open questions concerning investigating the changes occurring at the electrochemical interfaces through ageing. A comprehensive degradation analysis will help in developing a more stable and sustainable electrochemical system in DSSCs. Here, we develop a systematic methodology to explore the degradation at the various cell interfaces. For investigating the interfaces, the components forming an interface, in particular the anode/electrolyte interface, are separated to allow for applying surface analytical methods. The influence of the separation procedure on the interfaces is studied. It is investigated whether electrolyte extraction is possible via a rinsing method. Subsequently, the interface components are analysed with XPS, UPS and MIES to understand the impact of the rinsing technique on the chemical and electronic structure of the dye-adsorbed layer. The application of surface analytical technique in investigating the interfacial degradation is presented by employing XPS, UPS and NISS.

5.1. Introduction

As a low-cost alternative to traditional PV systems, DSSCs have been thoroughly researched¹⁻². They have reached efficiencies of up to 15.2%³. Being economical, flexible, and eco-friendly with the ability to operate indoors under low light conditions, DSSCs have the potential to expand their application in the sector of IoTs, textiles and in building integrated PV. To further improve the cell performance and durability, it is important to understand the degradation mechanisms in DSSCs. Within DSSC, several interfaces exist and efficient transport over the interfaces is necessary for their smooth and efficient operation. Charges generated in the cell have to be transported across the interfaces. Degradation at the cell interfaces can severely impact the performance of the cell. A systematic procedure to investigate the change at the interfaces in DSSCs is needed to understand the mechanisms leading to their degradation.

Prior ageing investigations have found various mechanisms responsible for the degradation of DSSCs over time under various stress factors. Under light, dye disintegration due to ligand loss was confirmed via Raman spectroscopy ⁴⁻⁶. For I-based electrolytes, several reasons for the electrolyte degradation were reported mainly due to a decrease in I_3^- concentration ⁷⁻⁸. The reasons proposed for the decrease in I_3^- are I crystallisation ⁹ and iodate formation causing electrolyte bleaching ¹⁰. I loss has also been observed in cells with improper sealing ⁶. For the CE, Pt-catalyst dissolution was reported due to the presence of water that decreased the catalytic property of the CE ¹¹. However, even in the absence of water, under high temperatures, the dissolution was still observed ¹². In another case degradation of the TiO_2 was reported due to the shifting of the CB with ageing and the reason suggested is the intercalation or water inhalation as a result of poor sealing technique ¹³. Further, the cracks occurring in the porous TiO_2 layer of the anode increased the internal cell resistance upon prolonged light exposure ¹². It is worth noting that existing studies of the degradation did not effectively correlate the decrease in cell performance with the interfacial degradations. Hence, it is important to develop a systematic procedure to explore comprehensively the changes in interfaces related to the degradation in DSSCs. A systematic approach for the ageing analysis developed for these electrochemical interfaces in DSSCs could then also be applied to other electrochemical systems efficiently.

The overall aim of the present work is to develop and test a procedure that can investigate the change at the interfaces in DSSCs, which also takes into account the alteration of the interfaces due to the applied analysis. The procedure must be relevant for investigating the interfaces and must not cause any change at the interfaces or at least allow to quantify the change in the interfacial properties upon application of the procedure. For analysing the electrochemical interfaces, the electrolyte must be removed from the respective electrode and subsequently both the electrolyte and the anode must be analysed regarding their chemical composition and their electronic structure. Rinsing of the aged photoanode is important to remove the top-electrolyte layer and to extract the electrolyte from the aged sample cells for further investigation. This study includes an investigation of the effect of ethanol rinsing on the photoanode to determine if it is a good procedure for rinsing and electrolyte extraction.

A combination of XPS, MIES, and UPS was employed to understand the changes in chemical and electronic properties of the dye-adsorbed layer upon rinsing and in aged photoanodes upon prolonged light exposure. Further, the application of He^+ and Ne^+ projectiles in NICISS to quantify the dye and electrolyte penetration in aged photoanode was investigated.

5.2. Experimental

5.2.1. Materials

The FTO ($15 \Omega \text{ cm}^{-2}$ and $7 \Omega \text{ cm}^{-2}$) is bought from Dyesol. TiO_2 pastes 18NR-AO blend of active anatase with average particle size $\sim 20 \text{ nm}$ and anatase scatter particle size $\leq 450 \text{ nm}$ was obtained from Greatcell, titanium tetrachloride (purity 99.99%) was purchased from Sigma-Aldrich, N719 dye (Greatcell), Chloroplatinic acid hydrate (99.99%, Sigma-Aldrich), BMII (1-Butyl-3-Methylimidazolium iodide, purity 99%, Sigma-Aldrich), TBP (4-Tertbutyl pyridine, purity 96%, TCI), I (purity 98%, TCI), LiI (Lithium iodide, purity 99.9%, Sigma-Aldrich), AN (Merck), VN (purity 99.5%, Sigma-Aldrich), MPN (3-Methoxypropionitrile purity $\geq 98\%$, Sigma-Aldrich), Et-OH (Ethanol, purity 100%, Chem-supply). Surlyn frame (inner $9 \text{ mm} \times 9 \text{ mm}$, outer $11 \text{ mm} \times 11 \text{ mm}$, $60 \mu\text{m}$ thickness).

5.2.2. Sample Preparation

5.2.2.1. Photoanodes for ethanol rinsing test

For the present study, four different photoanodes were prepared by immersing the $20 \mu\text{m}$ thick TiO_2 into 3 ml each of 0.5 mM N719 in Et-OH solution for 24 hrs. To investigate the effect of ethanol rinsing on the dye-adsorbed layer, each photoanode was analysed using XPS. The measured sample photoanodes were immersed in 3 ml of ethanol solution each with constant stirring for 2 mins. The rinsed photoanodes were thus dried using dry N_2 gas and re-measured to record the changes introduced in the dye layer with rinsing. The rinsed-off ethanol solution thus obtained was used to investigate the dye components that degrade due to rinsing. For this purpose, 3 drops of rinsed-off solution were drop-cast on the blank TiO_2 and further investigated for any traces of dye elements.

5.2.2.2. Preparation of the Cells

DSSCs were fabricated using standard protocols as described in ¹⁴ and ¹⁵. The FTO (TEC 15) was rinsed using ultrasonication in detergent and ethanol respectively. 40 mM of TiCl_4 in deionized water was used to treat the FTO by immersing it into the TiCl_4 solution and heating it at 70°C for 30 min and further heating it at 300°C for 3 hrs. Photoanodes with an effective area of $0.6 \times 0.6 \text{ cm}^2$ were prepared by depositing TiO_2 paste via screen printing and further heated in a furnace at 120°C for 5 min, 325°C for 10 min 375°C for 10 min and 500°C for 30 min, respectively. The prepared sintered TiO_2 was post-treated with 40 mM of TiCl_4 solution. To dye the porous TiO_2 layer, the TiO_2 substrate was soaked in a dye solution for 24 hr. The dye concentration used was 0.5 mM N719 dye in ethanol solution. After the preparation of the dye-adsorbed TiO_2 substrate, a pre-drilled Pt-coated FTO that acts as a CE is placed over

the dyed TiO₂ substrate and sealed together using a sealant surlyn frame. The surlyn frame acts as the spacer between the electrode and the seal. The electrolytes are filled into the cells by using a vacuum. The electrolyte composition used is I₂ (0.03 M), BMII (0.6 M), TBP (0.5 M), and LiI (0.1 M) in an 85:15 ratio of AN to VN. The hole is further sealed using a surlyn frame and glass coverslip.

5.2.3. Analysis Measures

5.2.3.1. JV characterisation

The power conversion efficiency of the cell is quantified by measuring JV curves. Each sample cell was illuminated with an Oriel solar simulator equipped with a Xenon lamp, with an output of 100 mW/cm² at AM 1.5, which is equivalent to one sun. A Si reference cell was used to calibrate the distance of the sample cell from the light source. The efficiency was measured using LabVIEW software, and a Keithley 2400 source meter.

5.2.3.2. XPS

XPS was applied to determine the elemental and chemical composition of the samples. XPS analysis was performed using an X-ray source with Mg anode with a photon energy of 1253.6 eV (XR-50, SPECS). A detailed description of the instrument can be found in ref ¹⁶. Survey spectrum scans were recorded with pass energy 40 eV using a SPECS PHOIBOS-HSA 3500 hemispherical analyser equipped with channeltrons. High-resolution scans for C, O, N, S, Ti, Ru and I were conducted with a pass energy of 10 eV. Each spectrum was calibrated at the main C1s peak at a BE of 285.0 eV. A Shirley background was used to fit the spectra with the background signal from electron scattering. A contribution of 30% and 70% of the Lorentz and Gaussian functions, respectively, were used to fit the inherent shape of the high-resolution spectra.

5.2.3.3. UPS and MIES

UPS was used to investigate the valence electron states of the sample surface and to observe the change in the orientation of the dye molecule upon ethanol rinsing. For aged sample cells, UPS is applied to determine the change in the DOS of the photoanode over time. UP spectra were recorded with the same experimental set as used for the XPS analysis with a sample bias at -10 eV. A two-stage gas discharge produces both the metastable He (He*, 19.8 eV) atoms as well as the He I (21.2 eV) radiation. MIES was used to determine the valence electron spectra for the outermost layer of the sample and to identify the change in dye orientation upon ethanol rinsing in the outermost layer of the dye-adsorbed sample. MIES uses the He*

for exiting electrons in the samples. Due to the large cross-section of He* with other matter, the probing depth is restricted to the outermost layer¹⁷.

5.2.3.4. NICISS

NICISS is used to obtain the depth profile of the aged photoanode by using both He⁺ and Ne⁺ as projectiles. The measurement is conducted at a high vacuum ($\sim 10^{-7}$ mbar). The NICISS experiment determines the concentration depth profiles of the elements in a sample up to a depth of 30 nm with a depth resolution of a few angstroms. The experimental set-up details are best described in references¹⁷⁻¹⁸. In NICISS, He⁺ projectiles are directed at a sample and the energy of the backscattered projectiles is determined from their TOF. Two factors cause energy losses. First, backscattering from the atoms forming the sample. The amount of energy lost depends on the mass of the element from which the He⁺ projectile is backscattered, which is given by Equation 5.1,

$$E_{final} = E_0 \frac{(\cos\theta + (A^2 - \sin^2\theta)^{\frac{1}{2}})^2}{(1 + A)^2} - Q_{in} \quad \text{Equation 5.1}$$

where E is the energy of the projectile, θ is the detector angle ($\sim 165^\circ$), Q_{in} is the inelastic energy loss due to backscattering, A is the ratio of the mass of the target element to the mass of the projectile. The second energy loss is a steady energy loss brought on by electronic excitation and small angle scattering along the trajectory of the He projectiles. This energy loss is proportional to the depth from which the He projectile has been backscattered.

5.2.3.5. Accelerated Ageing Set-up

An ATLAS- Sun-test CPS⁺ was used to perform the acceleration stability test. DSSCs were continuously exposed to bright light and a temperature of 60 °C for 600 hours before being removed at specific periods for characterisation, refer to Figure 8.11 for the sun-test equipment set-up with a sample loaded on the loading compartment.

The experimental techniques have been selected to cover the aspects which need to be applied for investigating the interfaces in DSSCs in an ageing study. The study employs JV characterisation which is a popular technique and profoundly used to track the changes in the PV parameter over time. XPS is a surface-sensitive technique to analyse the elemental and chemical composition of the sample surface. XPS is applied to investigate the changes introduced by ethanol rinsing of the dye layer adsorbed onto the TiO₂. XPS is further employed to investigate and compare the changes in the composition of the dye-TiO₂-

electrolyte interface upon light exposure. UPS and MIES reveal information about the changes in the orientation of the dye molecule with ethanol rinsing. Further, UPS and MIES determine the changes in the DOS of the photoanodes with ageing. To determine the molecular concentration of dye and electrolyte species penetrating the dye-TiO₂ interface, NICISS is applied with Ne⁺ as a projectile.

5.3. Result and Discussion

5.3.1. Electrolyte Extraction method via ethanol rinsing

To investigate the changes in the adsorbed dye layer over time it is important to open the DSSC cells and rinse the aged sample substrate to remove the electrolyte layer allowing access for investigation of the dye layer through techniques typically used for surface analysis. Further, the rinsing technique must have no measurable effect on the dye-adsorbed layer or at least an effect which can be quantified. The effect of ethanol rinsing on the photoanode was conducted and investigated with different techniques to compare the changes in the dye composition before and after the rinsing procedure. To account for variations, four samples each for the given condition were investigated. The dye-soaked substrates were analysed with XPS, UPS and MIES. After analysis, the same samples were rinsed with ethanol and re-analysed with XPS, UPS and MIES.

XPS

Figure 5.1 shows the high-resolution spectra of the elements forming the dye layer. The C1s/Ru3d region was fitted with five peaks, three related to C1s and two related to Ru3d. The largest contribution at 285.0 eV is the main C peak representing the C-C bonds¹⁹, 286.1±0.2 eV represents C-O/ C- N¹⁹, and 288.6±0.2 eV represents COOH¹⁹. These species could be either from the dye, the solvent residue, or adventitious hydrocarbons. Ru 3d5/2 positioned at 281±0.2 eV is the metal component from the dye molecule¹⁹. The XPS high resolution of O1s peak at 530.0±0.2 eV represents the main O peak from TiO₂¹⁹ and 531.4±0.2 eV represents O⁻ and Ti-OH from the TiO₂ substrate¹⁹ and COOH at 532.6±0.2 eV¹⁹. Ti2p_{3/2} is found at 458.8±0.2 eV for peak¹⁹. The S2p region includes two peaks 162.1±0.2 eV (2p_{3/2}) for the S from NCS denoted by S-1¹⁹ and 169.0±0.2 eV (2p_{3/2}) for oxidised S, possibly a sulphate, noted as S-2¹⁹. The high-resolution scan of N1s includes three peaks with the high contributing pyridine at 400.1±0.2 eV the N-main peak attributed to the organometallic functional group N719 being an organometallic dye, the contribution from NCS at 398.1±0.2 eV and TBA⁺ at 402.1±0.2 eV¹⁹.

The same samples were investigated by XPS after undergoing ethanol rinsing. The summary of the peak shifting and the change in the relative intensity ratio of the core elements is illustrated in Table 5.1 and Table 5.2, respectively.

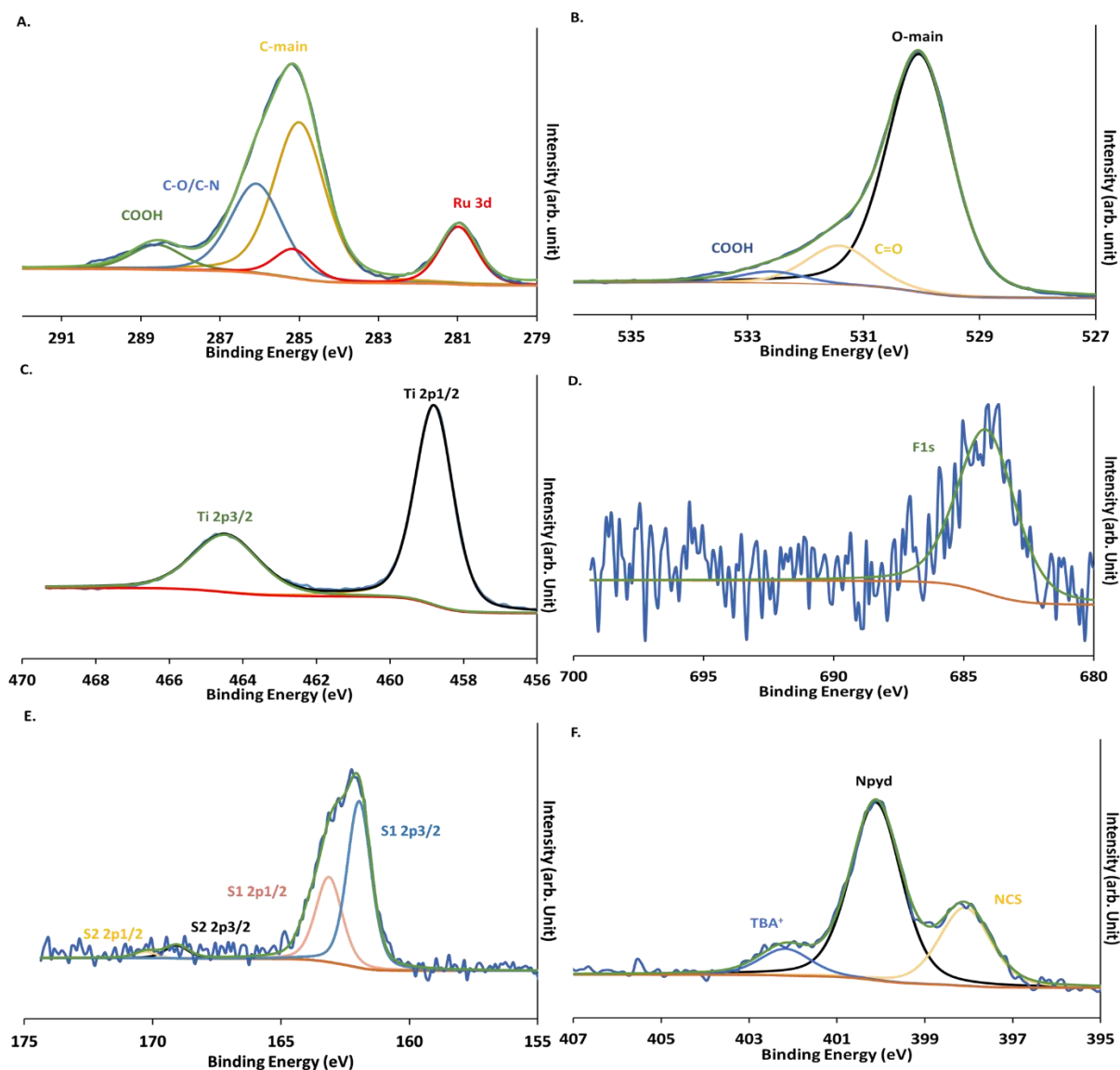


Figure 5.1: High-resolution XPS spectra of the core dye elements in 0 hrs photoanode, fitted with a Shirley background, representing the relative intensity of (A.) C1s/Ru3d, (B.) O1s, (C.) Ti2p, (D.) F1s, (E.) S2p, and (F.) N1s. Here, 0 hrs aged sample refers to the cell with electrolyte injected and stored in the dark for 24 hrs.

Table 5.1: The elemental peak positions of the elements in the adsorbed dye on the TiO₂ substrate before and after ethanol rinsing. The peak position is an average of the four samples investigated and the error is the instrumental error.

Elemental Group	Before	After
Ru	281.0 ± 0.2	281.0 ± 0.2
Npyd	400.1 ± 0.2	400.1 ± 0.2
NCS	398.1 ± 0.2	397.9 ± 0.2
TBA	402.1 ± 0.2	402.1 ± 0.2
S-1	162.1 ± 0.2	162.3 ± 0.2
S-2	169.0 ± 0.2	168.5 ± 0.2

From Table 5.1, no significant changes in the peak shift are noticed after ethanol rinsing. This confirms ethanol rinsing to have no change in the chemical states of the dye elements on the dye-TiO₂ substrate.

Table 5.2: The elemental ratios (atomic percentage) of elements representing adsorbed dye on TiO₂ substrate before and after ethanol rinsing. The elemental ratio is an average of four samples.

Elements	Sample-1		Sample-2		Sample-3		Sample-4		Difference
	Before	After	Before	After	Before	After	Before	After	
Ru	0.6	0.5	0.6	0.5	0.5	0.5	0.5	0.5	0.0
Npyd	3.3	3.1	3.2	3.2	3.1	3.0	3.0	3.5	0.0
NCS	1.4	1.0	1.4	1.0	1.3	1.0	1.3	1.0	-0.4
TBA	0.5	0.3	0.5	0.3	0.5	0.3	0.6	0.3	-0.2
S-1	1.0	1.0	1.0	0.5	1.0	0.6	1.0	0.7	-0.3
S-2	0.1	0.1	0.1	0.3	0.0	0.3	0.1	0.2	0.2

The change in the intensities of the dye elements due to ethanol rinsing shown as a difference in the last column of Table 5.2 was determined by calculating the difference in relative intensity of the average of the four samples before and after ethanol rinsing. After ethanol rinsing the ethanol obtained was drop-cast onto a PPT-5 layered TiO₂ and again investigated using XPS. From Table 5.2, it is confirmed that Ru and Npyd are unaffected while NCS, TBA⁺ and S-1 decrease upon rinsing. On the contrary, the intensity of oxidised S increased, which is due to the oxidation of dye and or TiO₂ substrate. Thus, Ru and Npyd components appear

to be unaffected by the rinsing procedure; but NCS, TBA^+ and S-1 are slightly affected and show a decrease upon rinsing.

Further to investigate the dye desorption due to rinsing and understand how it might influence the investigation of rinsed-off electrolyte solution later, the rinse-off ethanol solution was drop-cast onto the blank TiO_2 and measured using XPS. Table 5.3 shows the elemental ratios of different elements drop-cast on PPT TiO_2 after rinsing. Here, the N-species N-1 combinedly represent Npyd from the dye (400.1 ± 0.2 eV) and N atoms from molecularly adsorbed N-compounds that are observed in blank TiO_2 substrate (400.5 ± 0.2 eV), refer to Table 8.6 and Table 8.7 for the variation in the relative intensities of various elemental species of dye and blank TiO_2 substrate upon rinsing. Likewise, N-2 represents NCS (398.1 ± 0.2 eV) and substitutional N in oxide lattice in TiO_2 (398.7 ± 0.2 eV), and TBA^+ (402.1 ± 0.2 eV) from the dye molecule.

Table 5.3: The elemental ratios of the elements after XPS analysis of rinsed-off solution drop cast onto PPT-5 layered TiO_2 substrate. Here, N1 represents a combination of Npyd from the dye molecule and N atoms from molecularly adsorbed N-species; N-2 represents NCS and substitutional N in the oxide lattice of TiO_2 .

Elements	Sample-1	Sample-2	Sample-3	Sample-4	Average	Error
Ru	0.0	0.0	0.0	0.0	0.0	0.0
N-1	0.2	0.5	0.2	0.6	0.4	0.2
N-2	0.1	0.1	0.1	0.0	0.1	0.0
TBA^+	0.0	0.0	0.1	0.2	0.1	0.1
S-NCS	0.0	0.1	0.0	0.0	0.0	0.0
S-2	0.1	0.1	0.0	0.1	0.1	0.0

Table 5.3 shows no trace of Ru in any of the samples under investigation, which strongly supports the stability of Ru of dye adsorbed layer under the ethanol rinsing procedure. Adversely, the presence of other N-related peaks especially N-1, N-2, TBA^+ , and S-2 from the oxidised S species suggest the possibility of dye desorption. The peaks N-1, N-2 and S-2 are present on the blank TiO_2 substrate (more information about the relative intensity ratio can be found in the appendix Table 8.7). Thus, these elements, N-1, N-2 and S-2 cannot be considered as the dye remanent that is lost due to the rinsing effect. In contrast, the presence of TBA^+ peaks in the drop casted samples but being absent in the blank TiO_2 indicates nominal desorption of TBA^+ upon rinsing.

The XPS result confirmed the stability of the Ru dye N719 to ethanol rinsing. Although a slight decrease in the relative intensity of NCS, TBA⁺ and S-1 was observed, the presence of the N-2 peak in blank TiO₂ makes it difficult to quantify the loss of N-2 upon rinsing. The absence of TBA⁺ and S-1 in blank TiO₂ helps in quantifying their loss with rinsing which is ~1%. Furthermore, the decrease in intensity of S-NCS and increase in the intensity of S-2 in photoanodes, with the stability of S-2 in blank TiO₂ concludes the conversion of S-NCS to a higher oxidation state upon rinsing. Hence, based on the observation from XPS the procedure of ethanol rinsing is an acceptable technique for electrolyte collection.

UPS/MIES

UPS and MIES are used to investigate the changes in the orientation of the dye molecule through rinsing. For the interpretation of MIES and UPS in the context of XPS, it needs to be taken into account that the first two methods are more surface-sensitive than the latter. Figure 5.2 shows the UP and MIE spectra for the dye-adsorbed surface before and after ethanol rinsing. In the UP spectra, the feature at 8 eV decreased upon rinsing and for the MIE spectra the features in the regions 6-8 eV and 11 eV decreased. From DFT calculations, the peaks positioned at 6-8 eV and 11 eV are assigned to the functional groups NCS, Ru, pyridine, and carboxyl of the dye molecule,²⁰. Through the XPS analysis, no significant change in Ru and Npyd was observed but NCS slightly decreased and O-COOH increased with rinsing. Combining this information, the changes observed in the UP and MIE spectra are due to the change in the orientation of the dye molecule upon ethanol rinsing. The potential reasons for dye re-orientation are a small loss of dye components with rinsing, an increase in COOH due to solvent, and conversion of S-NCS to higher oxidised S upon rinsing which is evident from XPS analysis. Table 8.6 provides the relative changes in the intensities of different elemental compositions of the dye-TiO₂ substrate measured before and after ethanol rinsing.

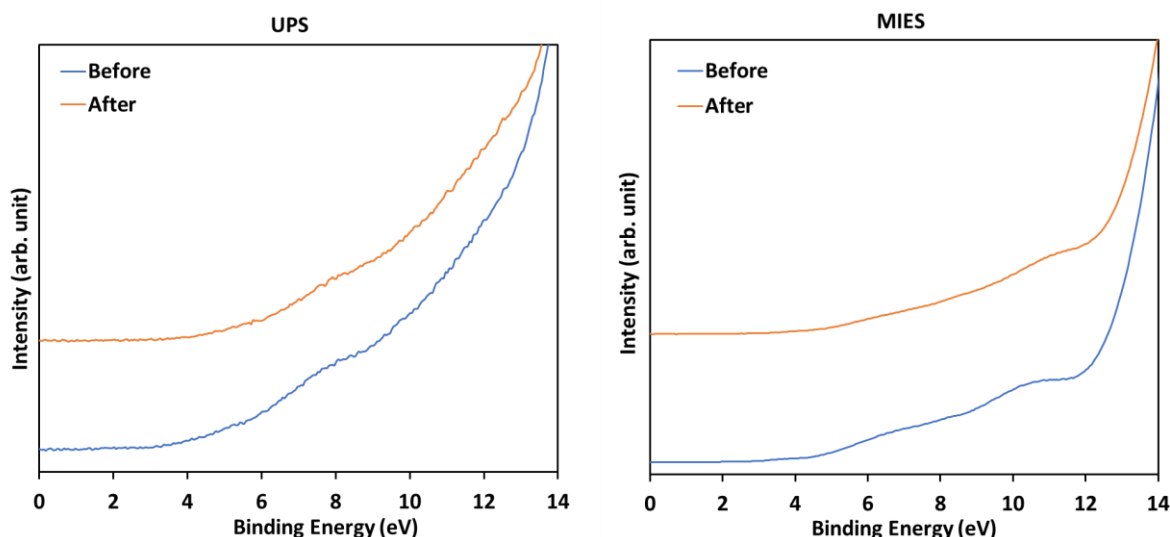


Figure 5.2: The UP (left) and MIE (right) spectra of the photoanode before and after ethanol rinsing.

Overall, from the observation from XPS, MIES and UPS we conclude that ethanol rinsing is an efficient technique to extract electrolytes from the aged sample and possesses a nominal effect on the elemental species of the adsorbed dye. However, a change in the molecular orientation of the dye was observed from UPS and MIES.

5.3.2. Ageing Investigation of DSSCs

5.3.2.1. Device Level Analysis

The sample cells were aged under light illumination. Over time, a gradual decrease in the J_{sc} , V_{oc} and efficiency was observed; FF is seen to increase and then slightly decrease after 240 hrs. After 600 hrs of illumination, the J_{sc} decreased by $67.0 \pm 4.0\%$, the V_{oc} decreased by $19.89 \pm 0.05\%$, and the FF increased by $0.2 \pm 0.2\%$ with an overall decrease in efficiency by $74.3 \pm 0.3\%$. This concludes that degradation has a strong influence on J_{sc} but not much influence on FF. The changes in the trend of the individual PV parameters are shown in Figure 8.12 and Table 8.8. The 0 hr sample represents the cell with the electrolyte injected and stored in the dark for 24 hr and the 600 hrs sample represents 600 hrs of continuous illumination.

5.3.2.2. Surface Analysis

5.3.2.2.1. XPS

A. Effect of ageing on adsorbed dye layer

In Figure 5.3 the relative elemental intensities of the sample aged for 600 hrs are compared to the 0 hrs sample to analyse the changes in the dye elements of interest. Before XPS analysis both the samples were opened, and the anode was rinsed with ethanol. More information about the elemental species and their relative intensity ratios can be found in Table 8.9. The changes in the spectra of Ru, S and N were used to investigate the application of XPS to understand the degradation of the dye-TiO₂-electrolyte interface. From Figure 5.3 we can see that the relative intensities of Ru, NCS, and S1 decreased upon constant illumination for 600 hrs relative to the 0 hrs sample. Upon constant illumination, for 600 hrs the relative intensity ratio of dye species Ru, NCS, S1 and S2 changed. No significant shift in the BE of the elemental species confirmed no change in the chemical environment and hence no new products were formed. Table 8.10 enlists the peak position of different elemental species of aged photoanode for 0 hrs and 600 hrs aged sample cells. With ageing, the peak intensity of dye species, Ru, NCS, S1 and S2 decreased, which indicate the possibility of either dye desorption or dye disintegration. Further by comparing the relative change in one dye component with respect to the other the above two mechanisms for dye degradation can be distinguished. For dye desorption, an equal relative loss of the respective peak intensities is expected. Likewise, a disproportional change with significantly different uncertainties will conclude the dye desorption.

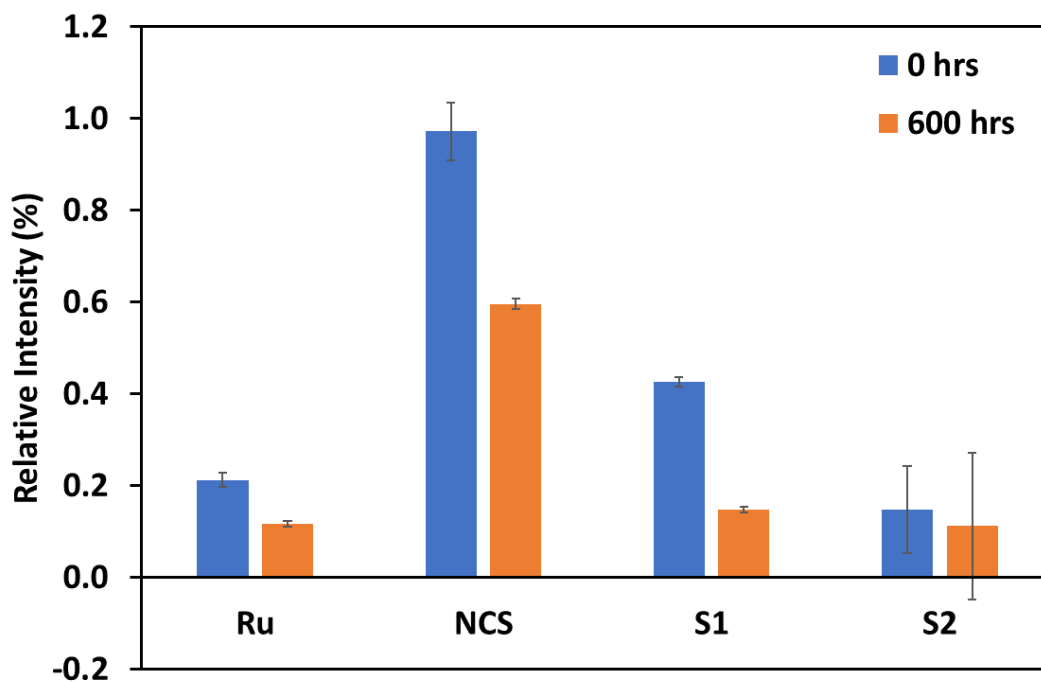


Figure 5.3: The column chart comparing the changes in the atomic intensity of respective dye elements at 0 hrs and 600 hrs. Here, the 0 hrs sample represents the cell which was stored in the dark for 24 hrs.

B. Effect of Ageing on Electrolyte and Redox Cycle

Further, XPS was used to analyse which electrolyte components adsorbed onto the dye-TiO₂ interface from the electrolyte. Figure 5.4 shows the high-resolution scan of I obtained from the photoanode of the cell aged for 0 hrs in light but stored in the dark for 24 hrs. The peak positioned at 618.4 ± 0.2 eV is assigned to I1 represents I^- ²¹, I2 at 621 ± 0.2 eV for I_3^- ²² and I3 at higher BE 623 or 624 eV for the higher oxidised state of I-species²¹.

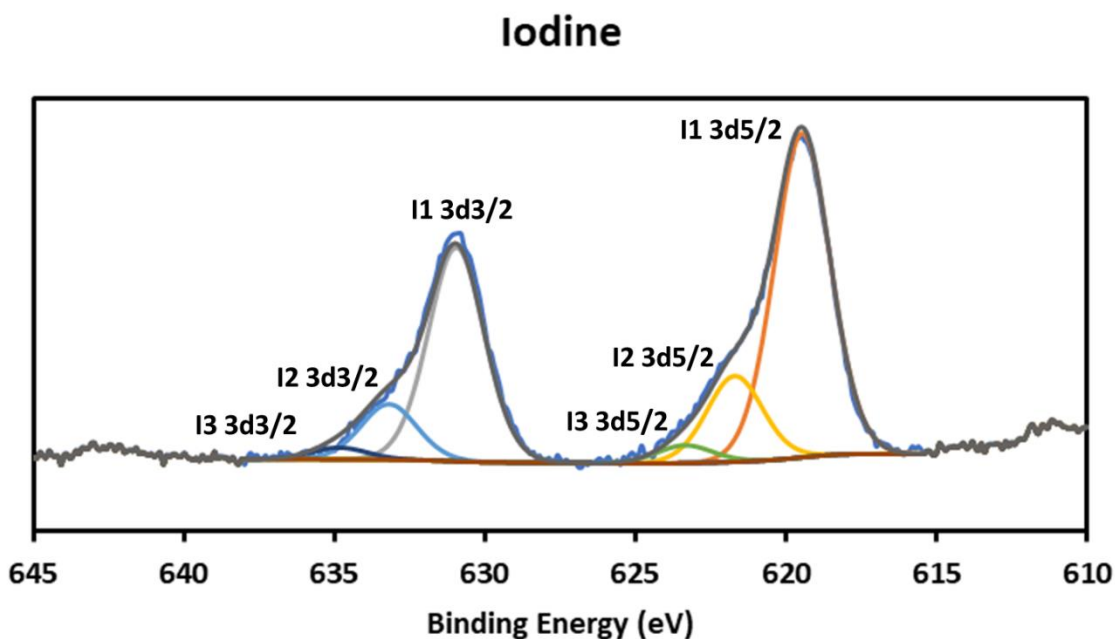


Figure 5.4: The high-resolution XP spectra of the I element in 0 hrs photoanode fitted with Shirley background. I1 represents I^- , I2 represent I_3^- and I3 represents higher oxidised I species. Here, the 0 hrs sample represents the cell which was stored in the dark for 24 hrs.

Figure 5.5 shows the change in the relative intensity of different species of I analysed, before and after the ageing for 600 hrs. I^- and I_3^- are found to be increased with ageing, on the contrary, the intensity of higher oxidised I-species is decreased. All the samples were subjected to ethanol rinsing before XPS analysis. The increase in intensity of I^- and I_3^- in 600 hrs aged sample, suggests I^- and I_3^- penetration into the dye layer upon illumination for 600 hrs. The decrease in intensity of higher oxidised I-species could potentially be due to rinsing. This supports the application of XPS in determining the elemental and chemical changes in the dye-TiO₂-electrolyte interface over time.

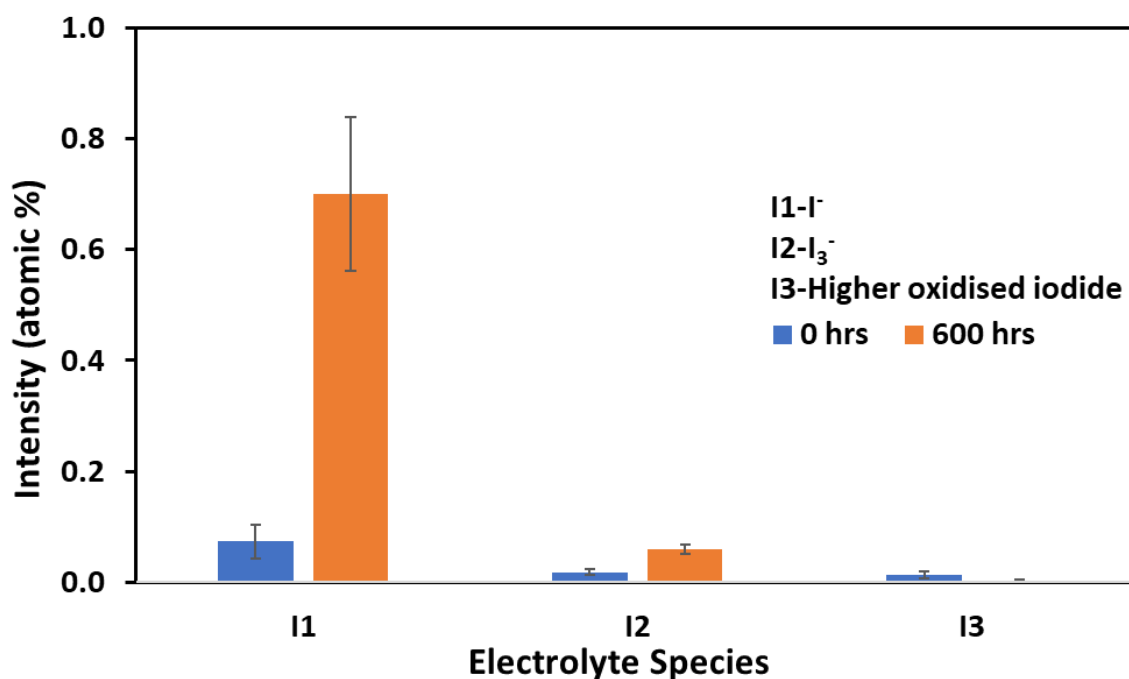


Figure 5.5: Changes in the XPS relative intensity of the electrolyte components for 0 hrs and 600 hrs aged cells. Here, the 0 hrs sample represents the cell which was stored in the dark for 24 hrs.

C. Drop-cast Samples

To further understand whether components of the dyed photoanode desorbed into the electrolyte with ageing, the solution obtained by rinsing off the aged photoanode was drop-cast onto a TiO_2 substrate and analysed. The components, Ru, S-1, and I-2 were not observed in the 0 hrs and 600 hrs drop-cast samples demonstrating their stability over time. The relative intensity of C-C, C-COOH, C-N, and O1s increased in 600 hrs drop-cast sample. This could be from the solvent used for rinsing or may be an effect of prolonged light exposure on aged photoanodes. Further, the relative intensity of C=O, O-COOH, Npyd, and I^- decreases over time arguing for improved chemical stability. The decrease in the relative intensity of Ti, O1s and F however, is due to an increase in adsorption of electrolyte species. For the elemental ratio of different species for 0 hrs and 600 hrs aged samples refer to Table 8.11. TiO_2 substrate was employed in the drop-casting investigation to ensure consistency in the adsorption of the cell remnants. The majority of elemental species found in the sample cells are present in the TiO_2 substrate, and only Ru and TBA represent the dye while the three I species represent the electrolyte. The remaining species in the XP spectra cannot be used to derive information about degradation.

5.3.3. UPS

Figure 5.6 shows the UP spectra for the 600 hrs cell, the 0 hrs aged cells and the difference between them. Each spectrum represents an average of three spectra and the difference spectrum represents the relative change in the valence bands of 600 hrs samples upon light exposure. Referring to appendix Figure 8.13 for UP spectra of reference dye and electrolyte adsorbed on TiO_2 , the peak between 2- 3 eV is present in both the dye and electrolyte; and the peak in the 4-5 eV region is present in the electrolyte. The molecular orbital calculation for the dye/I combined system adsorbed onto the TiO_2 sample assigns the peak between 3-4 eV and 5.2 eV to Ru and NCS from the dye molecule and I from the electrolyte ²⁰. As evident from XPS the relative intensity of most of the dye elements has decreased after light exposure for 600 hrs, the peak feature in the difference spectrum thus, represents the I from the electrolyte. This observation allows to conclude that the concentration of the electrolyte in the photoanodes has increased upon continuous illumination for 600 hrs which is in line with the XPS results. UPS thus has proven to be a powerful technique in determining the relative changes in the valence band of the photoanodes with ageing.

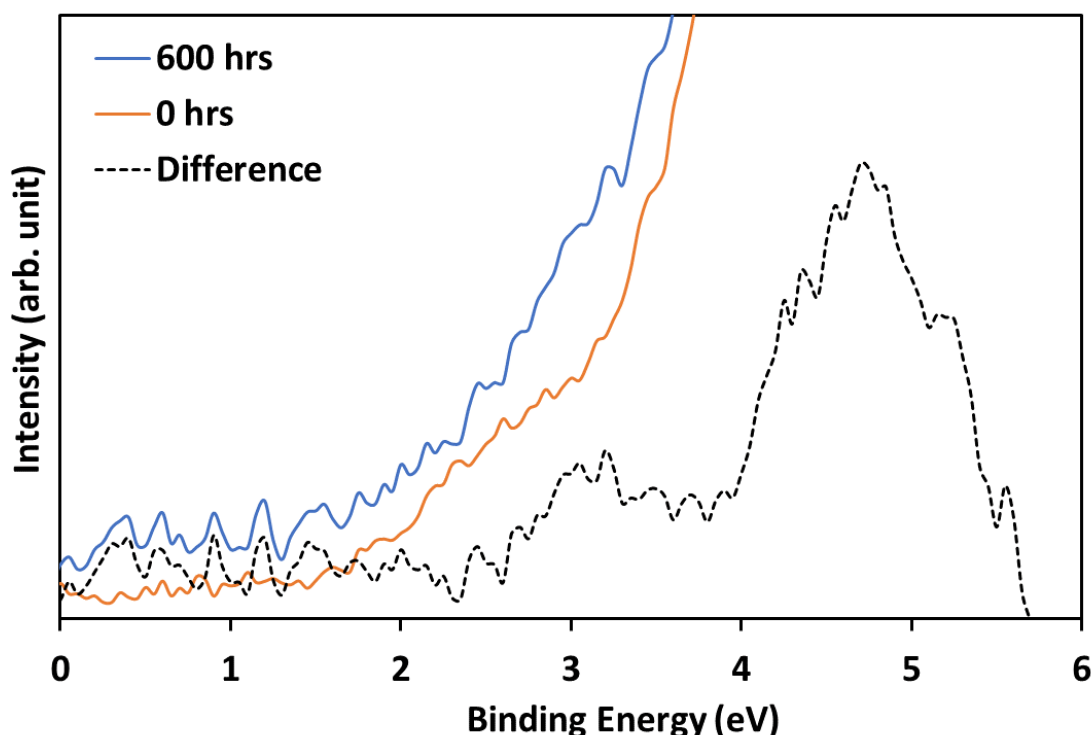


Figure 5.6: The UP spectra for the 0 hrs and 600 hrs aged samples and their spectral difference. The spectra difference refers to the difference of 0 hrs from 600 hrs aged photoanode.

5.3.4. NCISS implementation in ageing investigation

NCISS with He^+ as a projectile in the energy range of 2 to 5 keV is a technique to determine the molecular concentration depth profiles at soft matter surfaces¹⁷. NCISS is used here to quantify the molecular coverage of I and Ru in the dye layer.

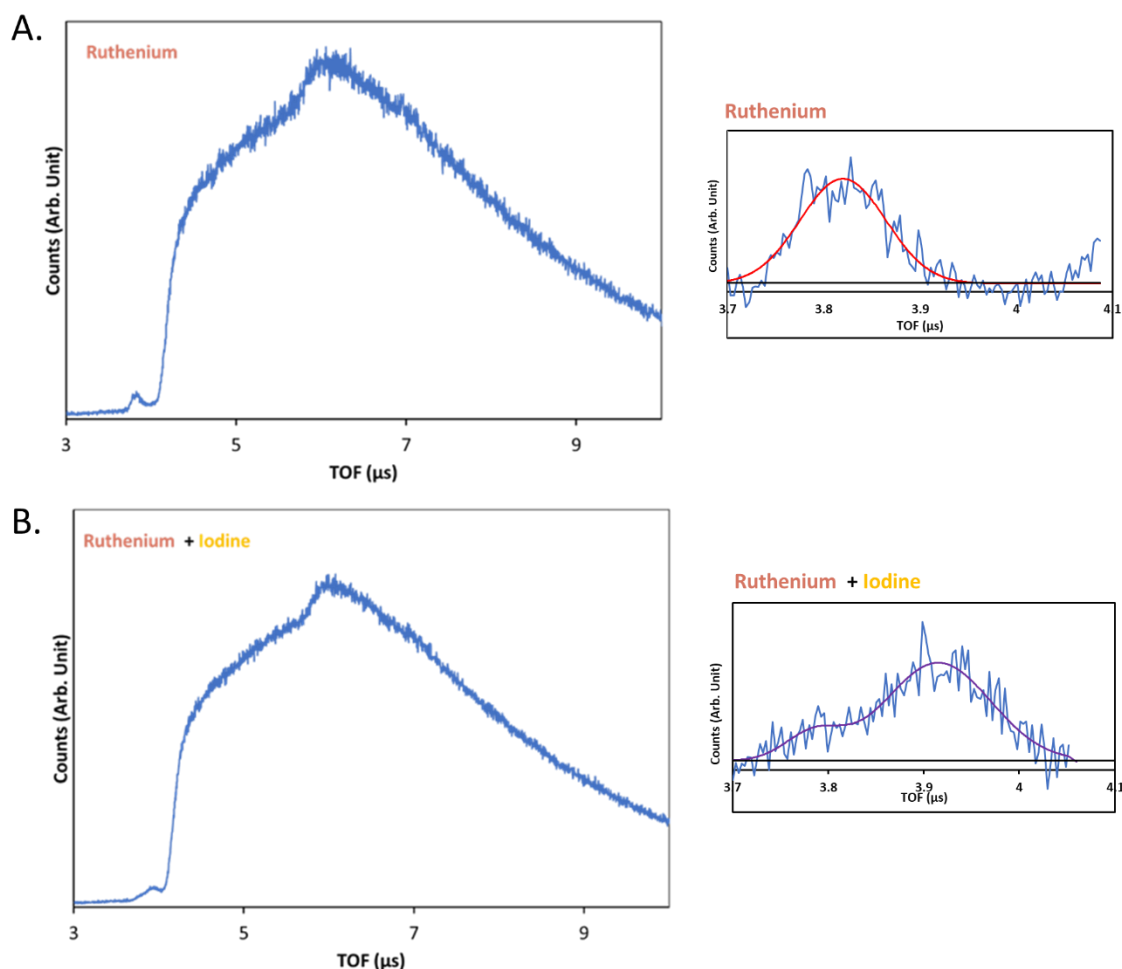


Figure 5.7: The NCISS spectra representing dye adsorbed TiO_2 (A), and aged photoanode with dye and electrolyte (B). Here, He^+ is used as the projectile.

When He^+ is used as a projectile in NCISS to probe dye adsorbed sample a symmetric peak for Ru was observed, as can be seen in Figure 5.7 (A.) above. In the figure, the background is fitted for the recoil-H and the area above the background indicates Ru. On probing an aged sample that consists of both dye and electrolyte onto the TiO_2 substrate, overlapping peaks for I and Ru were observed as can be seen in Figure 5.7 (B) The region above the background indicates combined contribution from Ru and I. The reason for the overlapping of Ru and I peak is that the atomic mass of Ru (101.7 amu) and I (126.9 amu) are very similar relative to that of the projectile He. The overlapping of the Ru and I peak complicate resolving the molecular concentration of the species. Hence, to address this issue, the projectile He^+ was

replaced by Ne^+ as a projectile. On using a heavier projectile, the value of A decreases where A represents the ratio of the mass of the target to the mass of the projectile (see Equation 5.1). This increases the energy separation between I and Ru and results in clearly separated peaks for I and Ru (see Figure 5.8) which can be further analysed to determine the relative molecular coverage based on the peak area. When He^+ is used as projectile the energy loss correlates well to the mass of the target atom and its depth. Hence, concentration depth profiles can be obtained. On using Ne^+ as projectile, the energy loss does not correlate well with the depth but correlates well with the mass of the target atom. Hence, although with Ne^+ the concentration depth profile cannot be determined, the molecular concentration can be quantified²³ as needed for the present study. Thus, using Ne^+ as a projectile the molecular coverage of both the dye element Ru and electrolyte element I can be analysed to investigate the penetration of I into the dye layer.

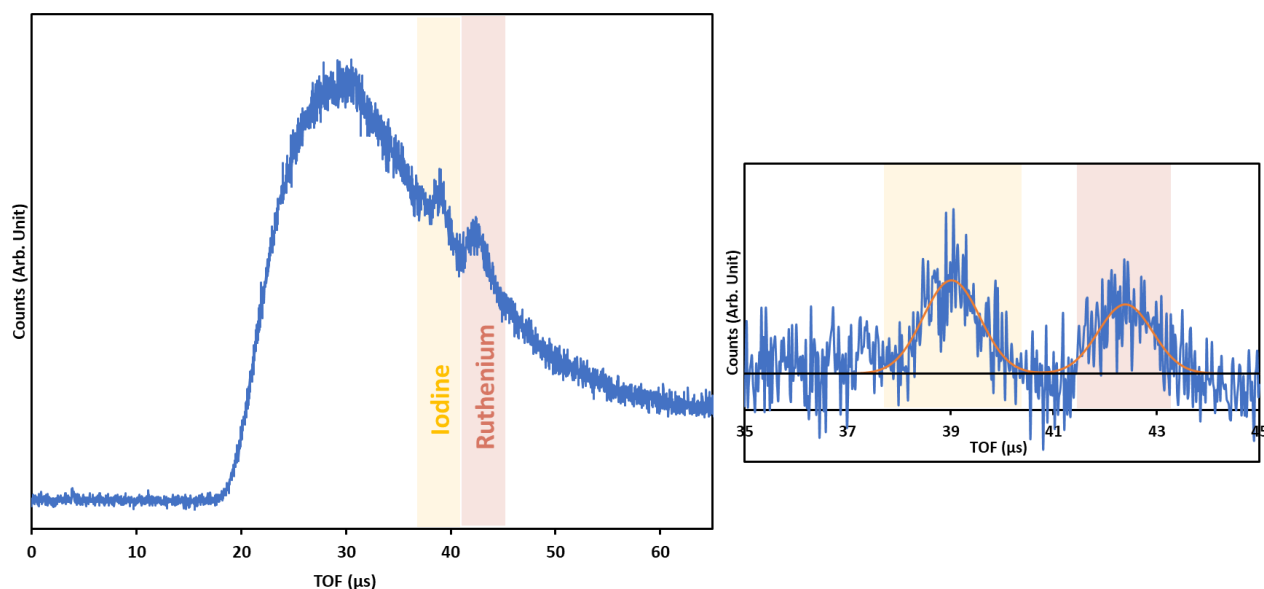


Figure 5.8: NICISS spectrum of aged cell showing I and Ru peaks shaded, yellow and red respectively. Here, Ne^+ is used as the projectile.

In NICISS, by substituting He^+ with Ne^+ the potential risk of sample damage is increased as a heavier projectile is used. Hence, it is important to consider the dosing of the ion beam onto the sample surface to avoid sample sputtering due to heavier ion beams (~ 3 keV) on the samples²⁴. Hence, to decrease ion dosing and to ensure that the ions dosing remains below 5×10^{13} ions/cm² for every sample, 16 different spots were measured each for 15 mins to avoid the possible damage caused to the sample surface due to Ne^+ sputtering. Thus, the NICISS

technique with Ne^+ can reveal information on how the dye and electrolyte species adsorb onto the sample with ageing and quantifying it.

5.4. Conclusion

In conclusion, an effective strategy to access the cell interface after cell operation was determined. A procedure to open the cell and rinsing-off the electrolyte layer to excess the dye-layer was applied. Further, the effect of the procedure on the dye layer was investigated. Additionally, the rinsed-off solution was analysed by drop-cast onto blank TiO_2 substrate. Through the application of surface sensitive techniques, XPS, MIES, and UPS, the changes brought into the photoanodes via the procedure was quantified. The results confirm that the ethanol rinsing procedure endure negligible effect on the photoanodes. Further, a systematic methodology to investigate changes introduced at the cell interface over time is established which will help to correlate the decrease in cell performance with the interfacial degradation.

The surfaces-analytical techniques XPS, UPS and NICISS have proved to identify the changes in the elemental composition, valence band structure and molecular concentration at the dye- TiO_2 interface of the aged photoanodes. The XPS result provides information about the changes in the elemental and chemical composition of the sample with ageing. The XPS observation indicate the possibility of dye degradation with ageing. With UPS investigating the changes in the valence band structure of the aged photoanode, the UPS result for the difference spectrum shows the relative increase of electrolyte into the dye layer of 600 hrs aged sample. In NICISS, employing He^+ as a projectile could not result in separate Ru and I peak in aged photoanodes and by substituting Ne^+ as a projectile the issue was resolved. Thus, by comparing the peak area of individual elemental peaks in NICIS spectra, the molecular coverage can be determined.

5.5. Acknowledgements

The authors acknowledge the facilities, and the scientific and technical assistance of Microscopy Australia and the Australian National Fabrication Facility (ANFF) under the National Collaborative Research Infrastructure Strategy, at the South Australian Regional Facility, Flinders Microscopy and Microanalysis, Flinders University.

5.6. Appendix

The appendix section includes the elemental ratios of the N-species with the peak position and relative intensity ratios for the blank TiO_2 before and after ethanol rinsing. It further includes the table enlisted with the PV parameter of the cell aged under light throughout the ageing period. Further, the change in the elemental composition of the dye- TiO_2 -electrolyte interface for 0 hrs and 600 hrs samples aged under light is detailed in a table with the respective peak positions. Finally, the UP spectra for the dye adsorbed onto TiO_2 and the electrolyte adsorbed onto TiO_2 sample are included.

5.7. References

1. O'regan, B.; Grätzel, M., A Low-Cost, High-Efficiency Solar Cell Based on Dye-Sensitized Colloidal Tio₂ Films. *nature* **1991**, *353*, 737-740.
2. Grätzel, M.; Kalyanasundaram, K., Artificial Photosynthesis: Efficient Dye-Sensitized Photoelectrochemical Cells for Direct Conversion of Visible Light to Electricity. *Current Science* **1994**, 706-714.
3. Ren, Y.; Zhang, D.; Suo, J.; Cao, Y.; Eickemeyer, F. T.; Vlachopoulos, N.; Zakeeruddin, S. M.; Hagfeldt, A.; Grätzel, M., Hydroxamic Acid Pre-Adsorption Raises the Efficiency of Cosensitized Solar Cells. *Nature* **2023**, *613*, 60-65.
4. Grünwald, R.; Tributsch, H., Mechanisms of Instability in Ru-Based Dye Sensitization Solar Cells. *The Journal of Physical Chemistry B* **1997**, *101*, 2564-2575.
5. Xue, G.; Guo, Y.; Yu, T.; Guan, J.; Yu, X.; Zhang, J.; Liu, J.; Zou, Z., Degradation Mechanisms Investigation for Long-Term Thermal Stability of Dye-Sensitized Solar Cells. *Int. J. Electrochem. Sci* **2012**, *7*, 1496-1511.
6. Kohle, O.; Grätzel, M.; Meyer, A. F.; Meyer, T. B., The Photovoltaic Stability of, Bis (Isothiocyanato) Rlutheniurn (Ii)-Bis-2, 2' Bipyridine-4, 4'-Dicarboxylic Acid and Related Sensitizers. *Advanced Materials* **1997**, *9*, 904-906.
7. Nakade, S.; Kanzaki, T.; Kambe, S.; Wada, Y.; Yanagida, S., Investigation of Cation-Induced Degradation of Dye-Sensitized Solar Cells for a New Strategy to Long-Term Stability. *Langmuir* **2005**, *21*, 11414-11417.
8. Kato, N.; Takeda, Y.; Higuchi, K.; Takeichi, A.; Sudo, E.; Tanaka, H.; Motohiro, T.; Sano, T.; Toyoda, T., Degradation Analysis of Dye-Sensitized Solar Cell Module after Long-Term Stability Test under Outdoor Working Condition. *Solar Energy Materials and Solar Cells* **2009**, *93*, 893-897.
9. Krašovec, U. O.; Bokalič, M.; Topič, M., Ageing of Dssc Studied by Electroluminescence and Transmission Imaging. *Solar Energy Materials and Solar Cells* **2013**, *117*, 67-72.
10. Ciani, L.; Catelani, M.; Carnevale, E. A.; Donati, L.; Bruzzi, M., Evaluation of the Aging Process of Dye-Sensitized Solar Cells under Different Stress Conditions. *IEEE Transactions on Instrumentation and Measurement* **2014**, *64*, 1179-1187.
11. Mohanty, S. P.; More, V.; Bhargava, P., Effect of Aging Conditions on the Performance of Dip Coated Platinum Counter Electrode Based Dye Sensitized Solar Cells. *RSC advances* **2015**, *5*, 18647-18654.
12. Xue, G.; Guo, Y.; Yu, T.; Guan, J.; Yu, X.; Zhang, J.; Liu, J.; Zou, Z., Degradation Mechanisms Investigation for Long-Term Thermal Stability of Dye-Sensitized Solar Cells. *Int. J. Electrochem. Sci* **2012**, *7*, 1496-1511.
13. Yum, J.-H.; Humphry-Baker, R.; Zakeeruddin, S. M.; Nazeeruddin, M. K.; Grätzel, M., Effect of Heat and Light on the Performance of Dye-Sensitized Solar Cells Based on Organic Sensitizers and Nanostructured Tio₂. *Nano Today* **2010**, *5*, 91-98.
14. Sedghi, A.; Miankushki, H. N., Influence of Ticl₄ Treatment on Structure and Performance of Dye-Sensitized Solar Cells. *Japanese Journal of applied physics* **2013**, *52*, 075002.
15. Adhikari, S. G.; Shamsaldeen, A.; Andersson, G. G., The Effect of Ticl₄ Treatment on the Performance of Dye-Sensitized Solar Cells. *The Journal of Chemical Physics* **2019**, *151*, 164704.
16. Acres, R. G.; Ellis, A. V.; Alvino, J.; Lenahan, C. E.; Khodakov, D. A.; Metha, G. F.; Andersson, G. G., Molecular Structure of 3-Aminopropyltriethoxysilane Layers Formed on Silanol-Terminated Silicon Surfaces. *The Journal of Physical Chemistry C* **2012**, *116*, 6289-6297.

17. Andersson, G.; Morgner, H., Thermodynamics and Structure of Liquid Surfaces Investigated Directly with Surface Analytical Tools. *Annalen der Physik* **2017**, 529, 1600230.
18. Andersson, G.; Morgner, H., Impact Collision Ion Scattering Spectroscopy (Iciss) and Neutral Impact Collision Ion Scattering Spectroscopy (Niciss) at Surfaces of Organic Liquids. *Surface science* **1998**, 405, 138-151.
19. Liu, G.; Klein, A.; Thissen, A.; Jaegermann, W., Electronic Properties and Interface Characterization of Phthalocyanine and Ru-Polypyridine Dyes on Tio₂ Surface. *Surface science* **2003**, 539, 37-48.
20. Trilaksana, H. Analysis of the Dye/Titania Interface as Photo-Anode in Dye Sensitized Solar Cells. Flinders University, College of Science and Engineering., 2018.
21. Sherwood, P. M., X-Ray Photoelectron Spectroscopic Studies of Some Iodine Compounds. *Journal of the Chemical Society, Faraday Transactions 2: Molecular and Chemical Physics* **1976**, 72, 1805-1820.
22. Stec, W. J.; Morgan, W. E.; Van Wazer, J. R.; Proctor, W. G., Inner-Orbital Photoelectron Spectroscopy of Several Pairs of Similar Phosphorus Compounds. *Journal of Inorganic and Nuclear Chemistry* **1972**, 34, 1100-1104.
23. Ahlam Alharbi, P. L. G., Gunther Andersson, In Preparation. **2023**.
24. Zhang, H.; Zhang, H.-W.; Qiao, L.; Zhang, X.-X.; He, R.; Wang, P., Erosion and Deuterium Retention Behavior of Tungsten Exposed to Impurity-Seeded Deuterium Plasma. *Tungsten* **2021**, 3, 448-458.

CHAPTER 6 UNVEILING THE AGEING EFFECT OF N719 DYE-SENSITISED SOLAR CELLS

Abstract

The energy-generating charge transportation in DSSCs occurs at the photoanode interface, and degradation at the interface can severely impact cell performance. The study aims to investigate the degradation of DSSCs and their effect on the photoanode interface to explore the main factor contributing to the decrease in cell performance over time. The cell maintained its stability in the dark but upon light exposure, the cell degraded. Surface-sensitive techniques like XPS, UPS and NISS are employed to investigate the change in the elemental and chemical composition at the electrode interface. Further, FTIR is applied to investigate the change in the functional group throughout the dye-TiO₂ interface. The XPS and NISS results confirmed the penetration of I_x⁻ (x=1 or 3) species into the dye layer as the main reason for cell degradation. Further, UPS results conclude that the electrolyte concentration at the cell surface promotes the cell performance but electrolyte penetration into the dye layer leads to degradation. FTIR and UV Vis Diffuse Reflectance Spectroscopy (UV Vis DRS) further supported the interaction of electrolytes with the dye molecule resulting in changes in the dye structure under light resulting in cell degradation. The main reason for the cell degradation observed is the penetration of I_x⁻ into the dye layer which further instigates changes in the dye molecule affecting the light absorption ability of the dye and thus, decreasing the generation of photoelectrons resulting in poor performance of the cell over time. The results show that ligand exchange of SCN⁻ with I⁻ is a probable cause for the degradation but that also a further change must be occurring of a yet unknown nature.

6.1. Introduction

Since their discovery in 1991, DSSCs have gained significant scientific and technological interest as a low-cost, adaptable, stable, and environmentally friendly alternative to conventional silicon cells¹. The highest efficiency discovered after extensive research spanning more than two decades is 15.2%². DSSCs include three main components: a sensitising dye, a redox electrolyte, and a porous wide-gap semiconductor photoanode. Even with materials of medium to low purity, reasonable efficiency can still be attained³, which is an advantageous feature of DSSCs. The energy region in DSSCs can be easily controlled utilizing a variety of chromophore designs with molecular-level control, in contrast to other

solar technologies⁴. DSSCs have been commercialised a few years after discovery and since then these cells have made excellent candidates for wearables like hats, bags, bag packs, military tents, and other IoT devices due to their ability to function indoors and in low light.

Within DSSC, several interfaces exist and interfacial charge exchange is necessary for the smooth operation of the device. Charges generated in the cell have to be transported across the interfaces. Interfacial degradation can severely impact the overall performance of the cell. A systematic procedure to investigate the change at the interfaces in DSSCs is needed to understand the mechanisms leading to their degradation. Previous ageing investigations have found various mechanisms responsible for the degradation of DSSCs over time, which are described as loss of electrolyte, dye desorption, platinum catalyst dissolution from the counter electrode and degradation of the TiO₂ substrate itself. Under stress factors, I⁻ in the electrolyte system results in the formation of iodates ions, IO₃⁻, when combined with water present in the electrolyte⁵. The I⁻ has been found to react with the glass frit sealant used for sealing the electrodes⁶. Further, the volatile nature of I⁻ has also caused loss of I⁻ or electrolyte in the device due to leakage primarily in the form of I₂, resulting in faster cell degradation and hence demands proper sealing⁷, electrolyte bleaching⁸, and electrolyte degradation that depends on the solvent and electrolyte recipe used⁹⁻¹¹ are some of the degradation phenomena proposed. The ability of NCS ligands of the dye complex to exchange with AN or TBP or water residue or I⁻ species in electrolyte¹²⁻¹⁷ is one of the reasons for the degradation of dye in DSSCs. Platinum dissolution into electrolyte may potentially affect the electrolyte concentration retarding dye regeneration as well as iodide regeneration¹⁸. The shifting of the CB of the TiO₂ substrate with ageing due to proton intercalation and/or moisture has been proposed^{13, 19}. Further, cracks introduced in TiO₂ under stress increase cell resistance and promote degradation²⁰. However, these investigations do not effectively correlate the decrease in cell performance with the interfacial degradations.

The present study investigates the effect of ageing at the dye-TiO₂ interface using a combination of techniques, including JV characterisation, EIS, XPS, MIES, NCISS, FTIR and UV-Vis DRS. The techniques will collectively help in tracking the effect of ageing at the device level via JV and EIS, surface level via XPS, MIES/UPS and NCISS and bulk via FTIR and UV Vis-DRS of the aged photoanodes, to correlate the decrease in cell performance with the interfacial degradation.

6.2. Experimental

6.2.1. Materials

The FTO ($15 \Omega \text{ cm}^{-2}$ and $7 \Omega \text{ cm}^{-2}$) was purchased from Dyesol, while TiO_2 pastes 18NR-AO blend of active anatase with average particle size 20 nm and anatase scatter particle size 450 nm were purchased from Greatcell, Titanium tetrachloride (purity 99.99%) was purchased from Sigma-Aldrich, N719 dye (Greatcell), Chloroplatinic acid hydrate (99.99%) Surlyn frame (60 μm thick; inner 9 mm x 9 mm, outer 11 mm x 11 mm) was bought from Solaronix and Megapoxy 34 for double sealing of the cell.

6.2.2. Sample Preparation

6.2.2.1 Preparation of cell:

DSSCs were fabricated using standard protocols ²¹ and ²². The FTO (TEC 15) was rinsed and cleaned with detergent followed by ethanol using ultrasonication for 30 mins each. A pre-treatment of FTO was performed using 40 mM of TiCl_4 solution in DI water and heating it at 70°C for 30 min followed by sintering it at 300°C for 3 hr in a covered position in an oven. Each photoanodes with an active area of $0.6 \times 0.6 \text{ cm}^2$ were prepared by screen-printing the TiO_2 paste and further heating in a furnace at 120°C for 5 min, 325°C for 10 min 375°C for 10 min and 500°C for 30 min, respectively. Thus, prepared TiO_2 was further post-treated with 40 mM of TiCl_4 solution. The prepared TiO_2 substrate was then soaked into the dye concentration of 0.5mM N719 in ethanol solution for 24 hr. A pre-drilled FTO (TEC 7) coated with Pt that acts as the CE is placed over the dyed TiO_2 substrate and sealed together using a surlyn frame, a sealant. The space between the electrodes is filled with electrolytes by applying a partial vacuum technique. The electrolyte composition used is I_2 (0.03 M), BMII (0.6 M), TBP (0.5 M), and LiI (0.1 M) in an 85:15 ratio of AN to VN. The hole is further sealed with a surlyn frame and a glass cover slip. A double sealing was done using a megapoxy. The sample cells prepared were stored in the dark for 24 hrs to allow the megapoxy to dry before the ageing investigation.

6.2.3. Analysis Measures

6.2.3.1 JV characterisation

The power conversion efficiency of the cell was measured through JV curves. An Oriel solar simulator equipped with a Xenon lamp with an output of 100 mW/cm^2 at AM 1.5 which is equivalent to one sun is used to illuminate each cell. The lamp height was calibrated using a Si reference cell. The efficiency was measured using LabVIEW and a Keithley 2400 source metre.

6.2.3.2 EIS

In this investigation, a potentiostat equipped with an impedance module, a FRA2 Autolab potentiostat/galvanostat, was used to conduct EIS. To rule out the effects of the electron concentration in TiO_2 on the interfacial charge-transfer kinetics, EIS measurements were carried out in the dark at a bias voltage (-0.9 V) for all examined systems. The reference terminal was attached to the CE during the measurement in this case because the cell only has two electrodes. The applied frequency range was 10^5 Hz to 0.1 Hz. A data gathering program called Metrohm Autolab NOVA 2 was used to measure the EI spectra. Additionally, Z-View2 software was used to fit the collected spectra using the proper equivalent circuits as illustrated in Figure 6.1. Circuit A is a standard equivalent model for DSSCs, based on three semi-circles in the Nyquist plot. As with ageing in DSSCs the Nyquist plot changes, hence circuit B model is applied. The least-square value for the fitted data is $(\chi^2) < 0.003$. Each circuit elements indicate the crucial processes occurring at the cell interface such as R1: the series resistance of the cell, R2: the charge transfer at the CE/electrolyte interface, and R3: the charge transfer resistance at the dye/ TiO_2 interface. The constant phase element capacitors; C1: double layer capacitance at CE/electrolyte interface, C2: chemical capacitance at TiO_2 /electrolyte interface and Warburg impedance element W1: Nernst diffusion of I_3^- in electrolyte.

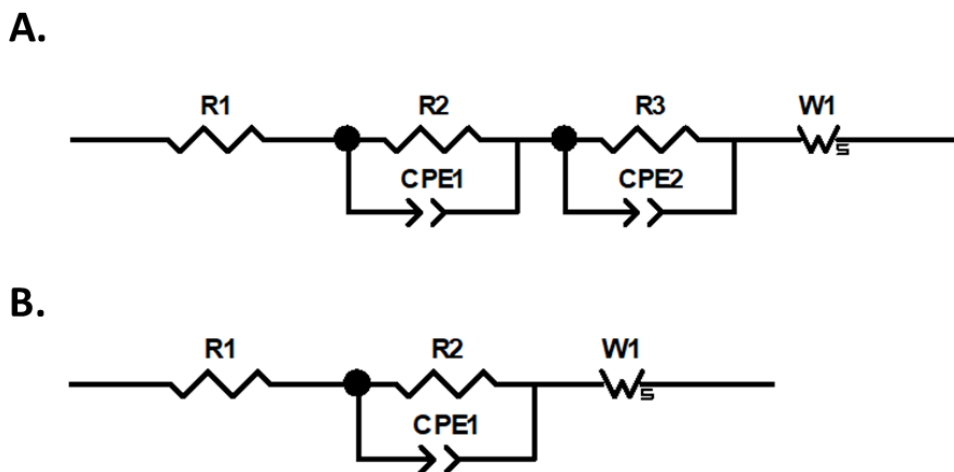


Figure 6.1: The simplified equivalent circuits models for DSSCs: commonly used model (A.) and model (B.) used for 792 hr and 1008 hr light aged DSSCs.

6.2.3.3 XPS

XPS is used to determine the changes in the elemental and chemical composition of the dye- TiO_2 interface within a depth range of 10 nm, over time. XPS analysis was performed using an X-ray source with Mg anode with 1253.6 eV of photon energy (XR-50, SPECS). The detailed description of the spectroscopic apparatus is given in ref ²³. Survey spectra were

conducted with a pass energy 40 eV using SPECS PHOIBOS-HAS 3500 hemispherical analysers equipped with channeltron. High-resolution scans for C, O, N, S, Ti, Ru and I were measured with a pass energy of 10 eV. The C1s spectral line and BE 285.0 eV are used to calibrate the energy scale for each sample. A Shirley background was used to fit the spectra with the background signal from electron scattering.

6.2.3.4 UPS

UPS is applied to investigate the valence electron states of the sample surface and to observe the change in the sample orientation at the dye-TiO₂-electrolyte interface over time. UP spectra were recorded under the same experimental setup as applied for XPS. The sample bias applied is -10eV. The sample surface was irradiated with photons from the He-I (21.2 eV) line using a two-stage He discharge.

6.2.3.5 NICISS

NICISS is used to obtain the elemental concentration depth profiles of the samples up to a depth of 30 nm with a depth resolution of a few angstroms close to the surface. The experimental details can be found in the references²⁴⁻²⁵. In this study, Ne is used as the projectile and the Ne⁺ projectiles are directed at a sample, and the energy of the backscattered projectiles is determined from their TOF. The backscattered projectile loses energy due to two variables. The first energy loss is due to the backscattering of the sample's atoms. Equation 6.1 represents the equation where the target element's mass from which the projectile is backscattered determines the quantity of energy lost.

$$E_{final} = E_0 \frac{(\cos\theta + (A^2 - \sin^2\theta)^{\frac{1}{2}})^2}{(1 + A)^2} - Q_{in} \quad \text{Equation 6.1}$$

where E is the energy of the projectile, θ is the detector angle ($\sim 165^\circ$), Q_{in} is the inelastic energy loss due to backscattering, A is the ratio of the mass of the target element to the mass of the projectile.

The second energy loss is a constant energy loss that occurs along the path of the projectiles because of electronic excitation and small-angle scattering. In this study, the KE of 3 keV of Ne⁺ is used to determine the concentration of Ru and I in aged photoanodes. The measurements are carried out at a 10⁻⁷ mbar high vacuum. Using He⁺ as a projectile aid in estimating the concentration depth profiles of Ru and I, however, the Ru and I peaks are overlapping as their atomic masses are close enough to result in an overlapping of the peak. Using Equation 6.1 the energy separation between Ru and I is calculated to be 82.9 eV. This issue is resolved by using Ne⁺ as a projectile, and result is energy separation of 243.1 eV. Ne⁺

as the projectile restricts the use of NICISS to measure elemental concentration, and does not correlate intensity and depth ²⁶ which is enough to achieve the aim of the measurement in the study.

6.2.3.6 ATR-FTIR

The ATR-FTIR spectra shown in this paper were obtained by employing a Bruker FTIR spectrometer (Vertex 80v) equipped with a diamond ATR crystal and a wide-bandwidth mid-IR source between 4000 cm^{-1} and 400 cm^{-1} . The spectra show a median of 100 scans with a 2 cm^{-1} resolution. There are no penetration depth, incidence angle, or refractive index modifications made to the spectra.

6.2.3.7 UV-Vis DRS

A spectrophotometer (Cary 5000 UV-Vis-NIR) equipped with a Praying Mantis Diffuse Reflection attachment (Harrick, DRP-SAP) was used to quantify UV-Vis DRS. For the backdrop scan, a PTFE disc was employed. Photoanode reflectance measurements on FTO ranged from 200 to 800 nm.

6.2.3.8 Accelerated Ageing Set-up

The accelerated ageing under light is performed by continuous exposure of the sample to a light emitted by the LED solar simulator Sunbrick from G2V Optics Inc. The simulator provided a 1 sun spectrum, equivalent to a solar radiance of 1000 W/m^2 and a spectral distribution of AM 1.5G. The simulator incorporated the ASTM (American Society for Testing and Materials) standards (ASTM E927, ASTM G173-03 and ASTM E490) as well as other international standards (IEC 60904-0 and JIC C8912) ²⁷. The samples are exposed and taken out for characterisation at certain intervals. For dark-aged samples, the samples are stored in a dark cabinet at room temperature. The temperature rise after light exposure is recorded as 54 ± 1 °C.

6.2.4. Theoretical Simulation

The N719 and I substituted analogue dye molecules were studied using density functional theory calculations (DFT). All calculations were carried out using the program package Gaussian 16 (rev. C.01) ²⁹. The molecular dye structures were geometrically optimised. Single-point energy and geometry optimisation calculations were performed using the cam-B3LYP hybrid functional ³⁰. 6-311G basis sets were used for all light elements (H, C, N and O) augmented with further diffuse and polarisation functions for S. The basis sets of the heavier elements included relativistic small-core, effective-core potentials (ECPs) of Stuttgart-Cologne type (MDF28 for Ru and I) amended with large valence basis sets ³¹⁻³². The

results include solvent effects employing the dielectric properties of acetonitrile in the polarisable continuum model (PCM)³³. Excited state energies for singlet-singlet and singlet-triplet transitions were estimated by time-dependent DFT (TD-DFT) computations involving the 12 lowest-energy triplet and 24 lowest-energy singlet states using the same functional as for the preceding computations.

6.3. Results and Discussion

6.3.1. Device Level Analysis

6.3.1.1. JV characterisation

Figure 6.2 represents the change in the PV parameter averaged for 10 samples, for respective ageing times, under dark and light conditions. In the dark, the fundamental PV parameters maintained stability but upon light exposure, the fundamental parameter decreased over ageing time. The decrease in the overall cell performance upon light ageing indicates degradation at the cell interface. The starting value for the short-circuit current (J_{sc}) recorded for light-aged sample is (13.4 ± 0.7) mA/cm² which decreased by $(74 \pm 3)\%$ after 1008 hr of ageing. A decrease of $(13.81 \pm 0.02)\%$ and an increase of $(22.5 \pm 0.3)\%$ was observed for open-circuit voltage (V_{oc}) and FF respectively over time with an overall decrease in efficiency by $(73.1 \pm 0.7)\%$. The decrease in efficiency and J_{sc} by 73% concludes the direct influence of J_{sc} decrease on the depletion of cell efficiency.

In Figure 8.14 the JV characteristic curve for the best-performing sample cells for dark and light ageing is shown. Only slight variation in J_{sc} with no change in the characteristic feature of the JV curve and stable V_{oc} was observed for samples aged in the dark. In contrast, under light exposure, both the J_{sc} and V_{oc} of the sample decreased over time. Upon long-term light exposure, the characteristic feature of the JV curve changed with a sharp decrease in current at lower voltage. The change in the quality of the JV characteristic curve for longer-aged samples (after 500 hr) indicates processes occurring in the cell resulting in degradation in the cell performance. Under light ageing, a kink is observed in the JV curve of the long-term aged sample and the reason for the presence of the kink will be discussed in the section “B. Effect of ageing on the electrolyte”.

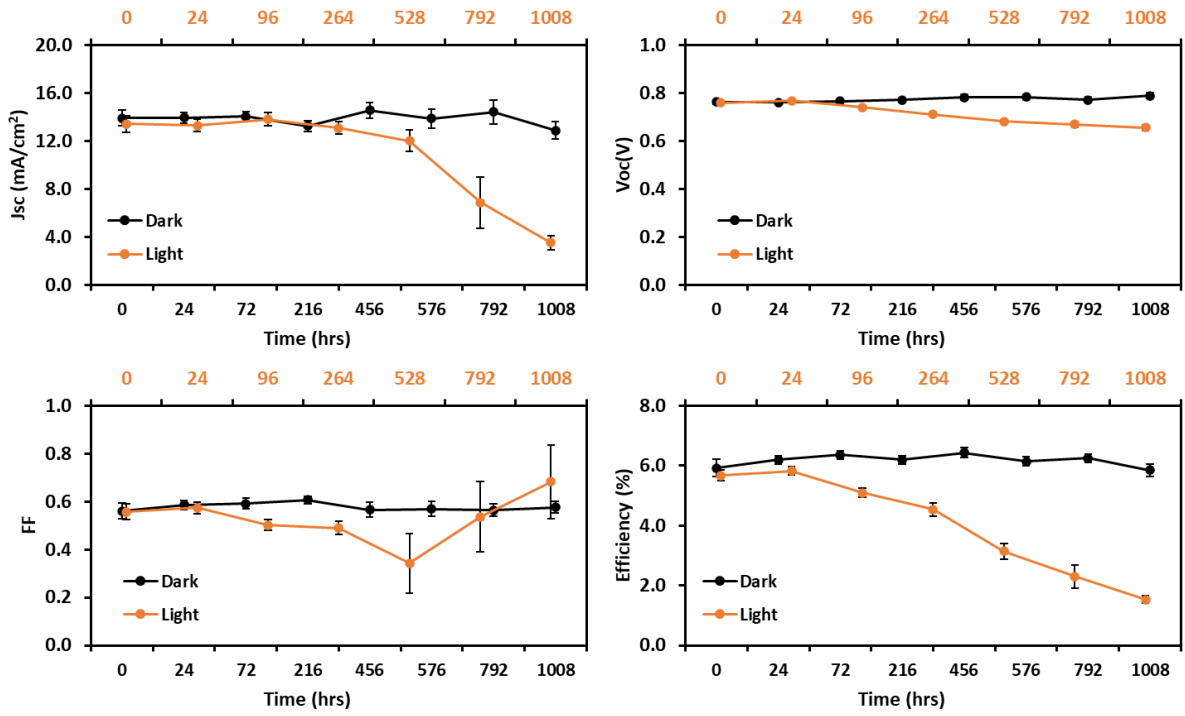


Figure 6.2: The variation in the fundamental PV parameter, J_{sc} , V_{oc} , FF and efficiency, averaged for 10 samples with the error bars, for dark and light-aged samples. The yellow and black line represents the light and dark-aged samples respectively. The primary horizontal axis (black) and secondary horizontal axis (yellow) represents the ageing time for dark and light samples respectively.

A steady decrease J_{sc} , V_{oc} and efficiency was observed over time. For FF, a steady decrease up to 528 hr was noticed which later increased. The increase in FF for the 792 hr and 1008 hr aged sample is due to a change in the characteristic of the JV curve (see Figure 8.14) and seemingly due to the definition of the FF not incorporating effects of deviating shapes in the JV curves. For instance, if we consider the concept of determining the FF from Equation 6.2 a typical JV curve has the maximum power point current (J_{MPP}) $< J_{sc}$ but for the long term degraded cell $J_{MPP} > J_{sc}$ and,

$$FF = \frac{P_{MPP}}{P_{Theo}} = \frac{J_{MPP} V_{MPP}}{J_{sc} V_{oc}} \quad \text{Equation 6.2}$$

where, J_{MPP} is the maximum power point current, V_{MPP} is the maximum power point voltage, and P_{MPP} is the maximum power.

In conclusion, the stability in the PV parameter in the dark concludes the stability of the DSSCs' shelf life, under atmospheric conditions in the dark. The decrease in the PV performance under light conditions show a clear degradation in the devices.

6.3.1.2. EIS

The samples after JV analysis were subjected to EIS measurement to investigate the changes in the interfacial resistances of the electrochemical system. Figure 8.15 shows the Nyquist plot for a representative sample of each ageing period, for both light and dark conditions. A typical DSSCs' Nyquist plot consists of three semi-circles, the semi-circle at the high-frequency region represents the charge transfer process at the CE/electrolyte interface (R_1). Likewise, the middle of the central semi-circle represents the diffusion recombination process in the photoanodes (R_2) and the third semi-circle at the low-frequency region represents the Nernst diffusion of I^-/I_3^- in the electrolyte (R_3). In the dark, the Nyquist plot for the aged sample cell comprises of three semicircles. Upon long-term light ageing the features of the Nyquist plot changed and consist of a semicircle and straight line. This could be due to the second semi-circle overlapping the third semi-circle or vice versa. The second circle overlapping the third circle suggests the internal resistance at the photoanode is extremely large and restricts the flow of electrons. The third semi-circle engulfing the second semi-circle represents high resistance in I_3^- diffusion, conversion of I^- to I_3^- . Here, we do not have any further evidence, to conclude which semi-circle overlaps the other. In either or both cases, the electrolyte and dye regeneration cycle get affected which is the main cause for degradation in the cell performance.

Figure 6.3 represents the simulated values of R_1 , R_2 and R_3 obtained from the intercept of respective impedance curves with the real axis in the Nyquist plot. For dark ageing, the value of resistance did not increase but upon light ageing the value of R_1 and R_2 increased over time. The increase in the resistance of recombination losses at TiO_2 (R_1) is beneficial for the cell performance however, the increase in electrolyte transport resistance (R_2) adversely affect the cell performance. For R_3 no value was obtained for the long-term light sample due to changes in the characteristic of the Nyquist plot.

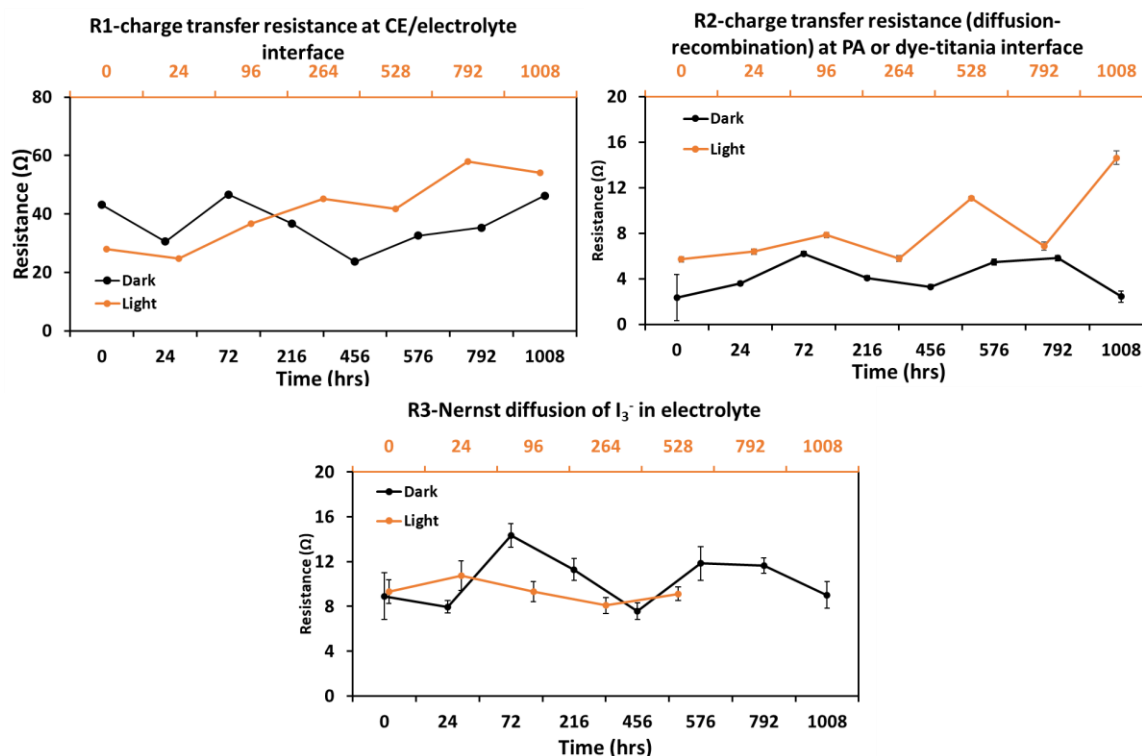


Figure 6.3: The variation of the interfacial resistances as a function of ageing time for DSSCs, R1-charge transfer resistance at the CE, electrolyte interface R2-charge transfer resistance at the photoanode interface and R3-Nernst diffusion in the electrolyte, under dark (black) and light (yellow) ageing with the error bars.

6.3.2. Surface Analysis

6.3.2.1. XPS

A. Effect of ageing on dye-adsorbed layer

Figure 6.4 shows the high-resolution scan of the respective elements obtained after XPS analysis of the photoanode of the sample cell that was kept in the dark for 24 hr. The C1s/Ru3d region was fitted with five peaks, three of which were associated with C1s and two of which were related to Ru3d. The main C-peak has the largest contribution at 285.0 eV, followed by the C-O/C-N and COOH at 286.4 ± 0.2 eV and 288.7 ± 0.2 eV, respectively. All C peaks can be assigned to the various functional groups of the dye the solvent residue or the adventitious carbon. Ru3d5/2 at 281.0 ± 0.2 eV is the metal component of the dye molecule³⁴⁻³⁵. The high-resolution scan of O 1s at (529.9 ± 0.2) eV represents oxygen from TiO₂³⁴. The peak at (531.1 ± 0.2) eV represents O²⁻ and Ti-OH from the TiO₂ substrate, and C=O from dye molecule³⁴. The peak at (532.4 ± 0.2) eV represents COOH³⁵. The high-resolution scan of TiO₂ shows the Ti 2p3/2 peak at (458.8 ± 0.2) eV which can be identified as Ti⁴⁺¹⁰. The high-resolution scan of S 2p region comprises four doublets, (162.4 ± 0.2) eV (2p3/2) from SCN⁻ denoted by S-1³⁶ and (168.6 ± 0.2) eV (2p3/2) for oxidised sulphur probably as sulphate

denoted by S-2³⁷ and S3 (2p3/2) at (164.8 ± 0.2) representing TiOS³⁸. This is compatible with SCN⁻ decomposing to form TiOS and a compound with S being in a state similar to SO₄²⁻. The high-resolution scan of N 1s consists of three peaks. The main N peak at (400.6 ± 0.2) eV with the highest contribution, represents the organometallic functional group of N719. The peaks at (397.7 ± 0.2) eV, and (401.8 ± 0.2) eV are attributed to the contribution from SCN⁻ and TBA⁺ respectively³⁹⁻⁴⁰. For the I 3d region, the high-resolution scan enveloped three peaks. The I 3d5/2 peaks are found at (618.8 ± 0.2) eV (I1) and is attributed to I⁻, at (621.2 ± 0.2) eV (I2) and is attributed to I₃⁻⁴¹, and at (623.0 ± 0.2) eV (I3) attributed to an oxidised state of I representing iodates or periodates^{42 43}.

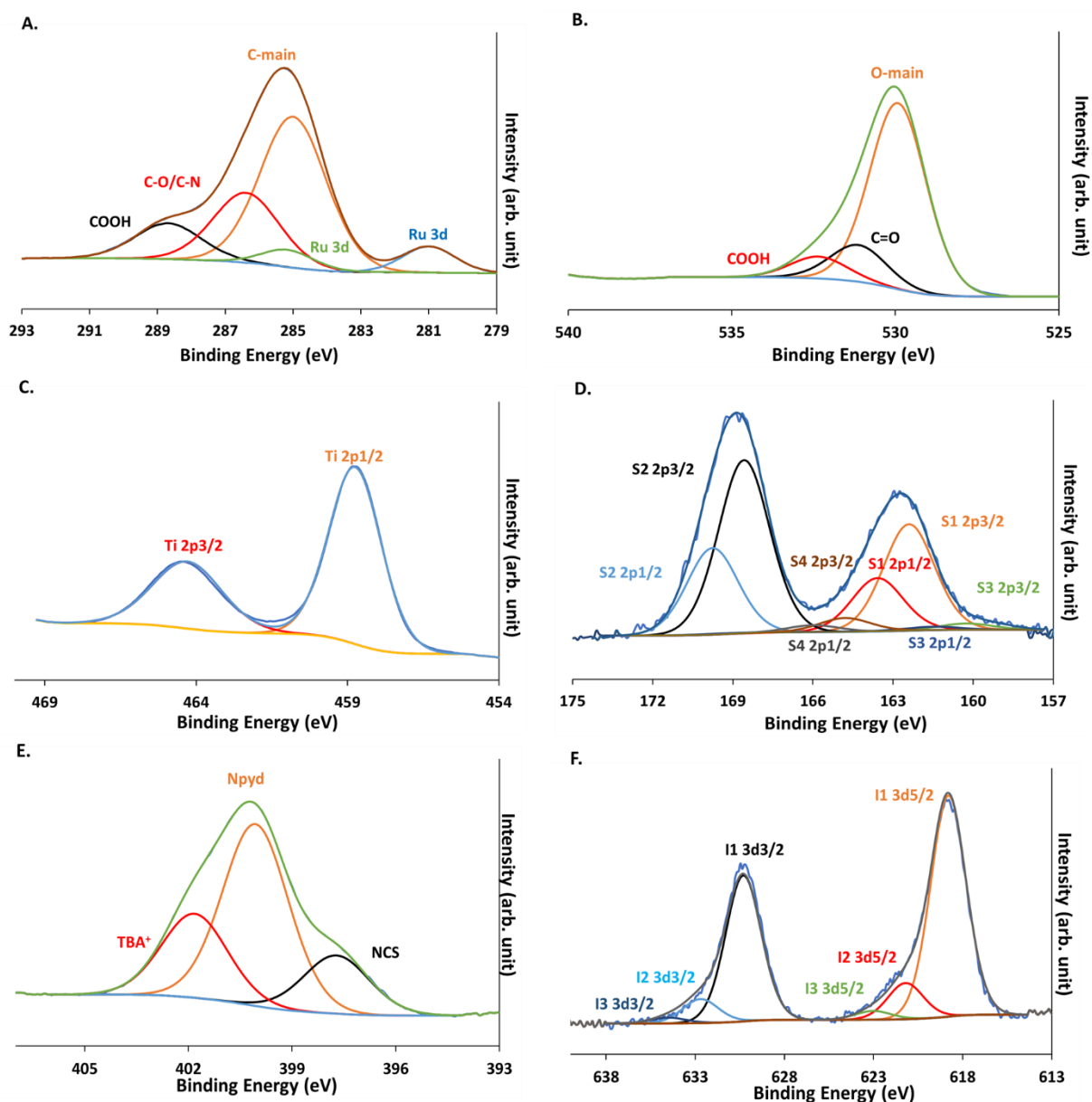


Figure 6.4: The high-resolution XP spectra of the core dye elements in 0 hrs photoanode, fitted with Shirley background, representing the relative intensity of (A.) C1s-Ru3d, (B.) O1s, (C.) Ti2p, (D.) S2p, and (E.) N1s and (F.) I3d. Here, 0 hrs aged sample refers to the cell with electrolyte injected and stored in the dark for 24 hrs.

The changes in the elemental ratios of different chemical species under dark and light for the ageing period are tabulated in the appendix section in Table 8.12 and

Table 8.13. The intensity represents the average relative intensity of three samples analysed for every ageing step. The intensity of adsorbent TiO_2 is decreasing with time owing to an increase in adsorbate which could be from the electrolyte species or any by-product of ageing Figure 6.5. A possible reason could be the formation of a solid electrolyte interface (SEI) like

that observed in Li^+ batteries attenuating the signals from Ti and O. However, it needs to be noted that the decrease in performance is observed only for the light-exposed samples.

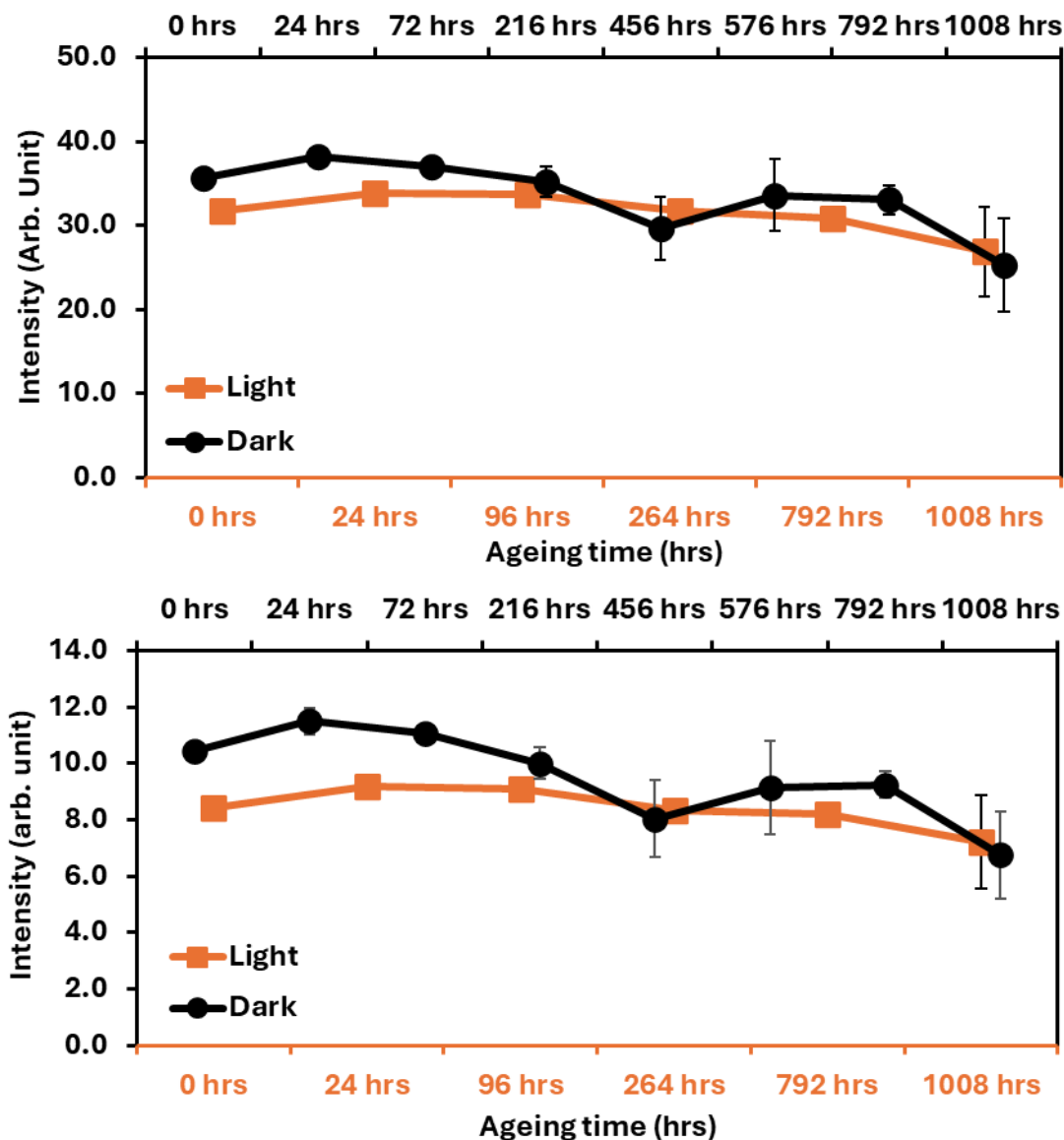


Figure 6.5: The variation in the XPS relative intensity of O1s (top) and Ti (bottom) as a function of ageing time for DSSCs under dark and light conditions.

Furthermore, considering the relative intensity and the error bars, the core metal of the dye element, Ru remains stable throughout the ageing period in light but slightly decreases for dark-aged samples, supporting the stability of the core dye element under light Figure 6.6. Despite this, the decrease in Ru in the dark with the stable performance of the cell throughout the ageing period, suggests the observation is not to be a causative factor for degradation. The decrease in Ru in the dark indicates the desorption of Ru, may be from the top of multilayers as it did not impact the cell performance, or it could be an initial stage of degradation in the dark.

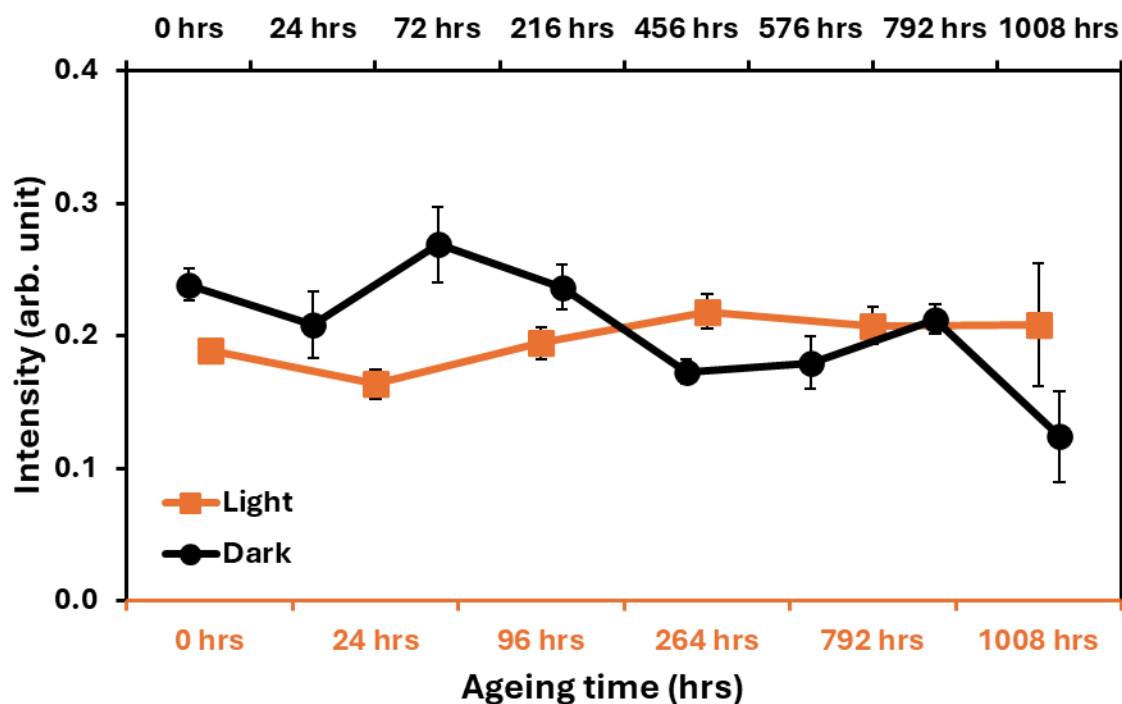


Figure 6.6: The variation in XPS relative intensity of Ru, in the photoanodes of the cells, as a function of ageing time for DSSCs under dark and light.

The intensity of Npyd was almost constant for both cases. For SCN^- no specific trend was observed for either dark or light-aged samples, however, the intensity of TBA^+ decreased in both cases suggesting the instability of counterion and the possibility of ionic replacement (see Figure 6.7).

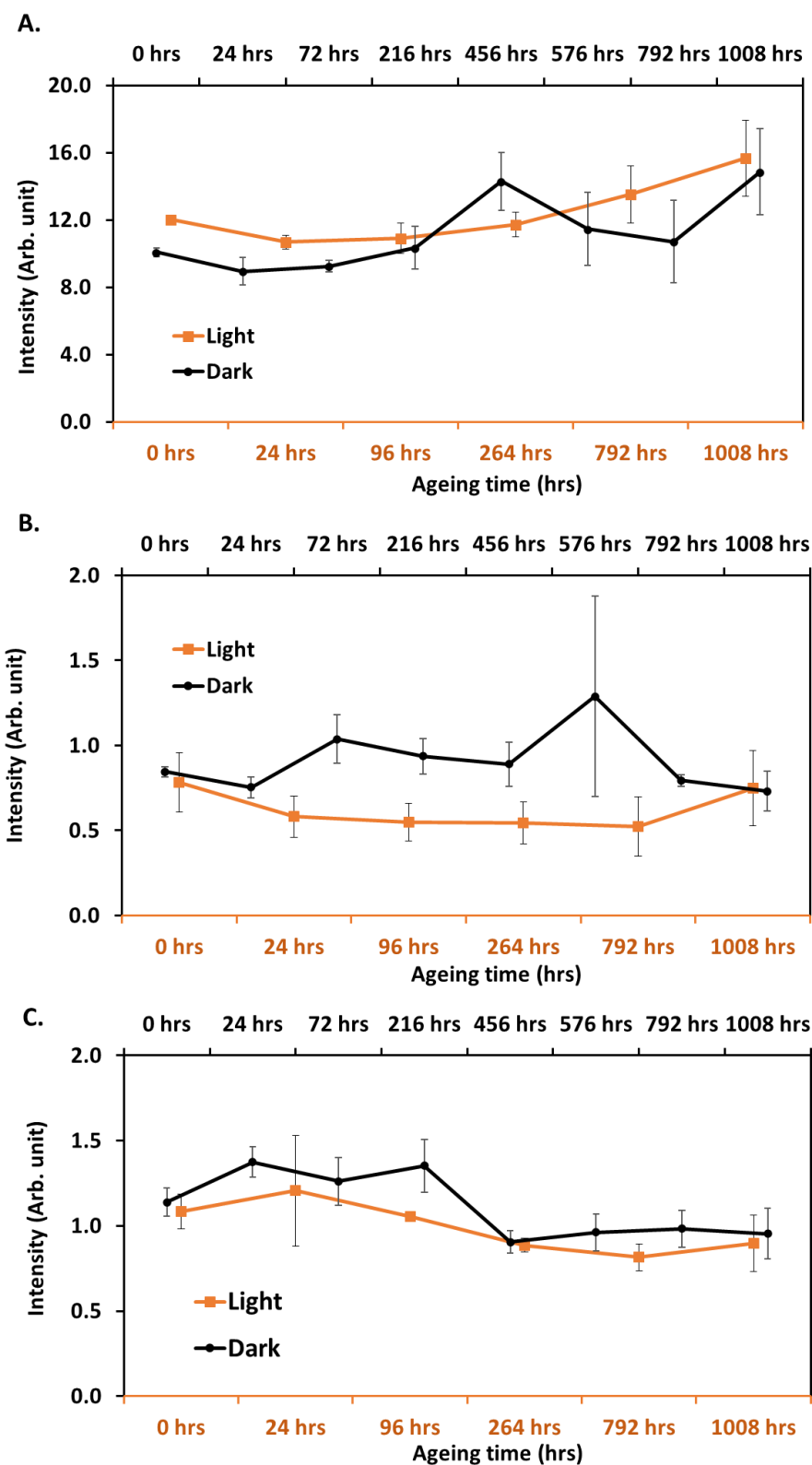


Figure 6.7: The variation in XPS relative intensity of (A.) Npyd, (B.) SCN⁻ and (C.) TBA⁺ in the photoanodes of the cells, as a function of ageing time for DSSCs under dark and light.

Figure 6.8 shows the variation in the relative intensity of S. In the dark-aged samples, the intensity of S1 increased and later decreased over time. For light-aged samples, a reverse pattern was observed. The explanation and relevance are still open. Conversely, the intensity

of S2 representing the oxidised S decreased in both dark and light. For, S3 it decreased upon light exposure and slightly increased in dark-aged samples. Furthermore, the relative intensity of total S decreased for light and dark-aged samples, but the intensity decrease for light-aged samples was somewhat larger.

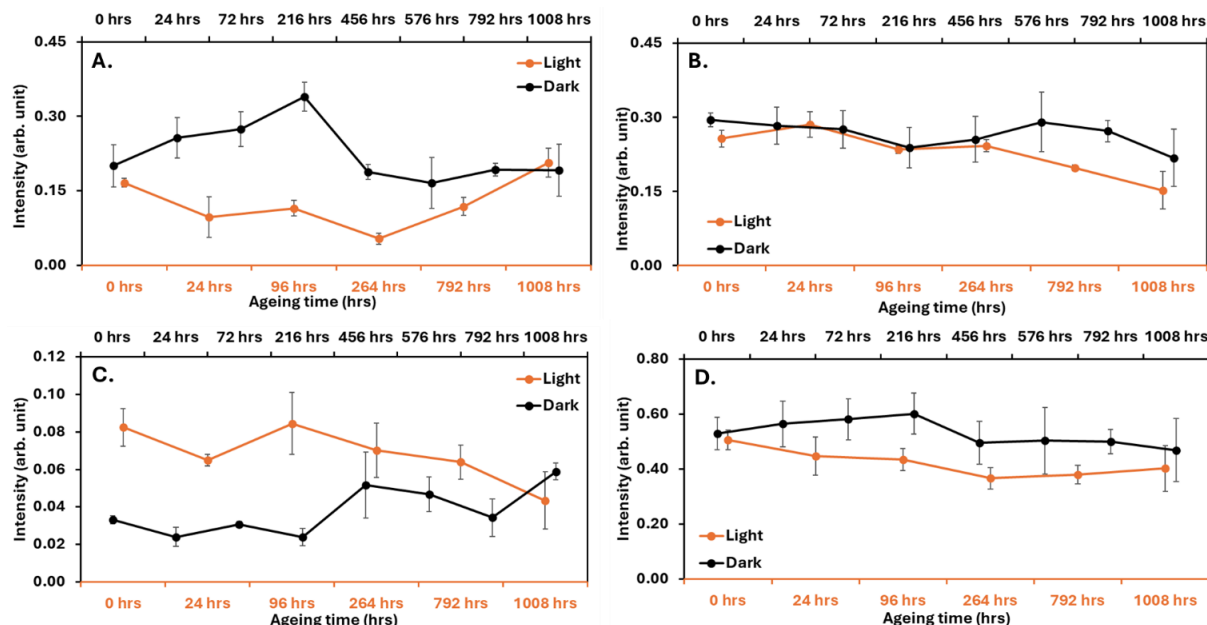


Figure 6.8: The variation in XPS relative intensity of Sulphur species, (A.) S1-from SCN^- , (B.) S2-oxidised S and (C.) S3-TiOS and (D.) sum of S, in the photoanodes of the cells, as a function of ageing time for DSSCs under dark and light.

Based on the XPS analysis, the relative intensity of Ru and TBA^+ decreased in the dark-aged sample while a decrease in total S and TBA^+ intensity was observed for the light-aged samples. The stable cell performance in the dark suggests the observed changes in the dye layer are not influencing the cell performance and hence do not contribute to cell degradation. Similarly, with the degree of changes in the dye layer observed for light-aged samples as compared to the change observed in the cell performance, the change in the dye layer cannot be the only reason for the cell degradation and instability.

B. Effect of ageing on the electrolyte

To understand the effect of ageing on the electrolyte at the dye- TiO_2 interface, the intensity of electrolyte components, I^- and I_3^- is investigated. In Figure 6.9, under light the intensity of I^- increased; the intensity of I_3^- initially increased but decreased at the later stage of ageing. However, under dark no significant increase in intensity of either species was observed. The total intensity of I increased with time for light-aged sample cells, on the contrary, no significant increase in the intensity of total I species was observed for dark-aged samples. Thus, the penetration of I into the dye layer upon ageing is the main reason for degradation in

the cell performance over time under light. Having penetrated into the dye layer the I^- could have replaced the SCN^- ligand of N719, with the replaced SCN^- still present in the proximity in the dye layer. This is compatible with the I^-/SCN^- exchange reported in ¹³ and also with the SCN^- signal not significantly decreasing in intensity in XPS as per Figure 6.8A but an increasing presence of I^- as per Figure 6.9A.

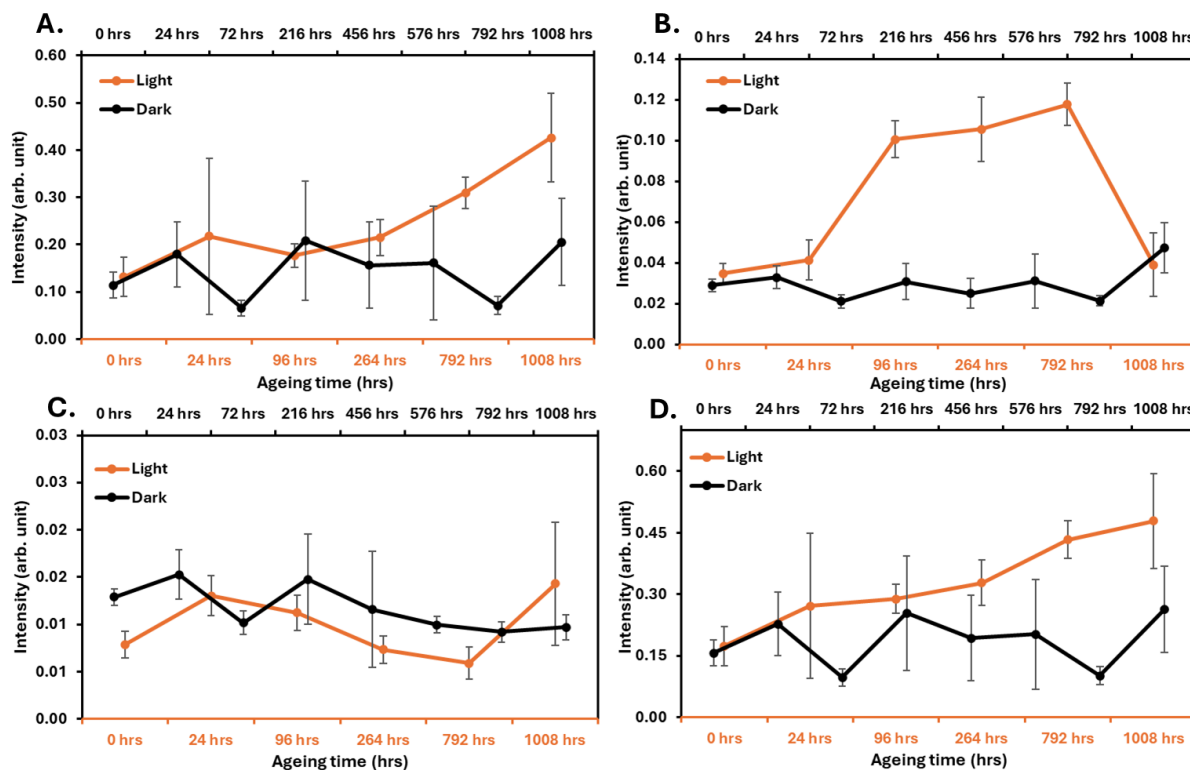


Figure 6.9: The variation in XPS relative intensity of I species, (A.) I1-I, (B.) I2-I, (C.) higher oxidised I-species, and (D.) sum of I in the photoanodes of the cells, as a function of ageing time for DSSCs under dark and light.

In conclusion, the XPS result shows changes in the dye layer under dark and light ageing. In the dark the intensity of Ru and TBA^+ slightly decreased over time, however, the stability in the cell performance in the dark supports the changes are not causative for cell degradation. In light ageing, the intensity of TBA^+ , S-2 and total S slightly decreased over time with a decrease in cell performance. This support changes in the dye layer could contribute to cell degradation but with the degree of change in the dye layer observed for light-aged samples compared to the change in the cell performance, the dye layer change cannot be the only cause for decrease in the cell performance. Further, an increase in I_x^- (with $x = 1$ or 3) penetration into the dye- TiO_2 interface under light ageing was observed with stability in relative intensity. In contrast, in the dark no relative increase in I and no change in the cell performance was observed. Thus, I_x^- penetration into the photoanode is the main reason for the cell degradation

as with the increase in I_x^- penetration the PV performance of the electrochemical system decreased overtime and no I_x^- penetration in dark-aged samples led to stability in cell performance.

A similar kink was observed in the JV curve for 792 hr and 1008 hr (see Figure 8.14) was found in a study and interpreted as a trapping/de-trapping mechanism linked to migratory defects caused by I interstitials and related to a change in the characteristic of the JV curve resulting in the kink in perovskites ⁴⁴. The increase in I in the photoanode as observed from XPS thus confirms the observation of the origin of the kink in the JV characteristic curve.

6.3.2.2. NICISS

A. Effect of ageing on dye-adsorbed layer

Figure 6.10 illustrates the NICIS spectra of Ru, for both dark and light-aged samples. The highlighted region represents the region of the Ru element which extends from 1200 to 1400 eV. For dark ageing, the peak area for the 1008 hr sample decreased compared to the 0 hr aged sample suggesting a decrease in the molecular coverage of Ru over time. Upon light exposure, the molecular coverage of Ru did not decrease. A complete NICIS spectra for Ru under light and dark ageing is given in the appendix section Figure 8.16. Thus, the relative decrease in the peak area for the Ru in the dark suggests a minor dye desorption in dark ageing but the stability of dye molecule in light.

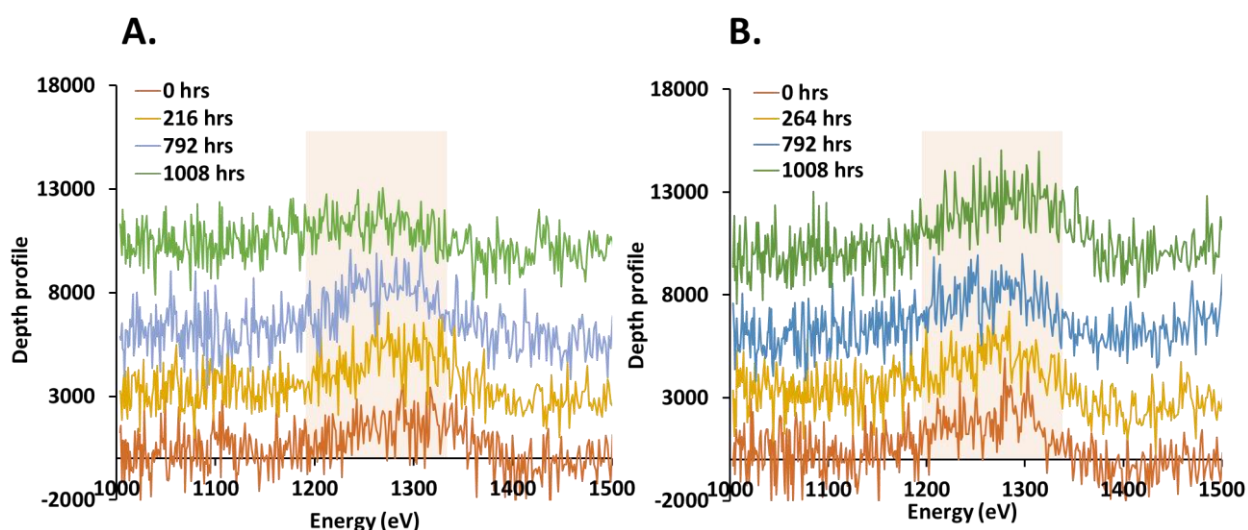


Figure 6.10: The Ru peak in NICIS spectra for the dark (A.) and light (B.) aged DSSCs.

B. Effect of ageing on electrolyte

Figure 6.11 illustrates the NICIS spectra of I, for both dark and light-aged samples. The highlighted region represents the coverage of the I element which extends from 1500 to 1650

eV. For dark ageing, no change in the peak area for aged samples compared to the 0 hr sample was observed. This supports no change in the molecular coverage of I over time in the dark. Upon light exposure, the relative increase in peak area with time supports the increase in molecular coverage of I over time. Thus, NICISS confirms the I concentration in the dye layer to increase upon light exposure. A complete NICIS spectra for I element under light and dark ageing is given in the appendix section Figure 8.17.

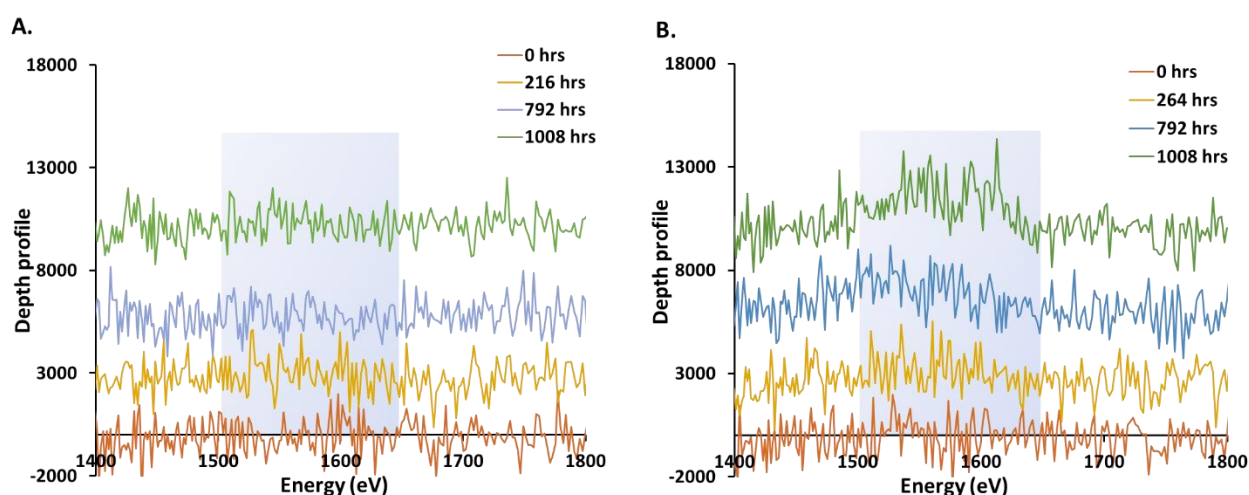


Figure 6.11: The I peak in NICIS spectra for the dark (A.) and light (B.) aged DSSCs.

In conclusion, the NICISS result concludes the decrease in relative molecular coverage of Ru in dark and stability under light ageing. For I, in dark ageing, the relative molecular coverage was stable but under light, it increased over time. Therefore, results from XPS and NICISS both support the I_x^- penetration into the dye/ TiO_2 interface as the main reason for cell degradation.

6.3.2.3 UPS for aged photoanodes

Figure 6.12 and Figure 6.13 show the UP spectra and the difference of the 1008 hr aged samples with the 0 hr sample for dark and light-aged sample sets, respectively. The difference spectrum (dashed line) is the difference between the average of three UP spectra of the ageing period.

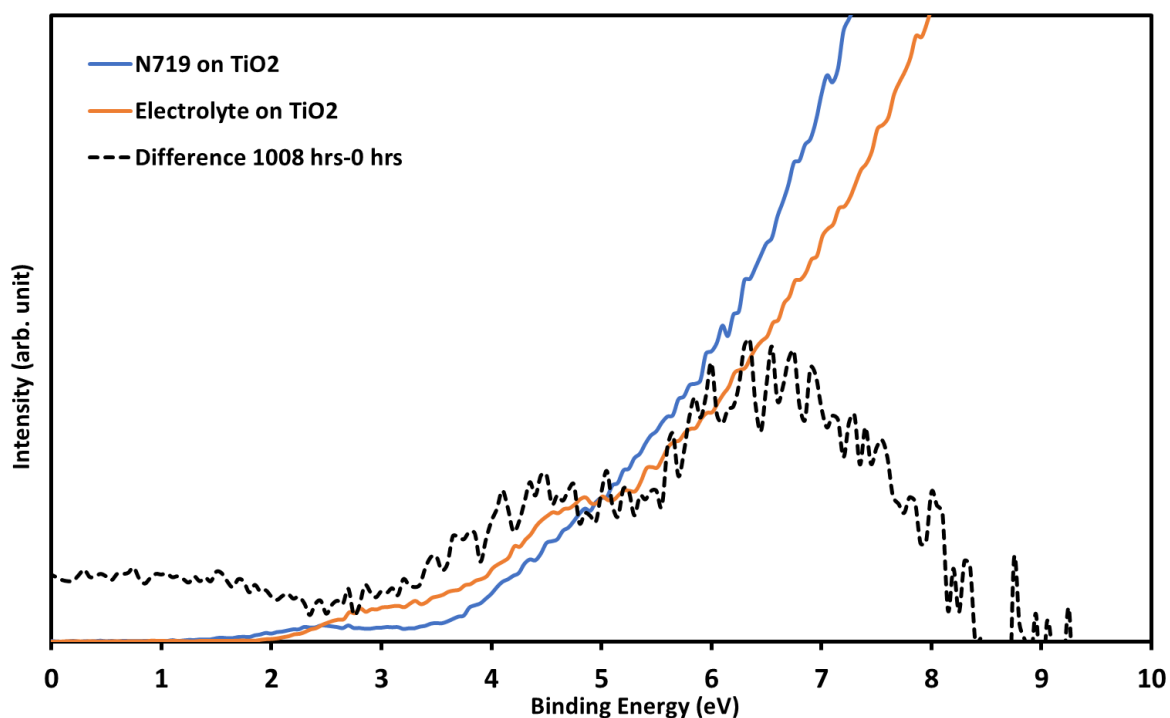


Figure 6.12: The UP spectra obtained after taking the spectral difference of the average of three samples in each 0 hr and 1008 hr ageing period for the dark-aged cells with the reference spectra of dye and electrolyte adsorbed on TiO₂.

In Figure 6.12 the feature for the dark ageing sample that corresponds to Ru of the dye layer (BE = 2-3eV) is seen to decrease in the resultant spectrum but the feature corresponding to the I in the electrolyte (BE = 3-5eV) is increased. This confirms a decrease in dye intensity with an increase in I intensity at the sample surface upon ageing. Further, comparing with the XPS and NCISS observation that no increase in I penetration into the dye- TiO₂ interface occurred in the dark, the UPS observation concludes that although the I is present on the dark-aged photoanodes, the I is concentrated at sample surface and does not penetrate the dye layer overtime. This conclusion is based on the fact, that the probing depth of XPS is deeper than that of UPS⁴⁵. In Figure 6.13, the feature corresponding to the Ru of the dye layer (BE = 2-3eV) suggests no dye desorption but no feature representing electrolyte (BE = 3-5eV) suggests no I at the surface. Further, comparing the XPS and NCISS results that support the stability of Ru but increase in intensity of I_x⁻ over time, the UPS concludes that for light-aged samples, the I penetrate deeper into the dye layer and is not concentrated at the surface.

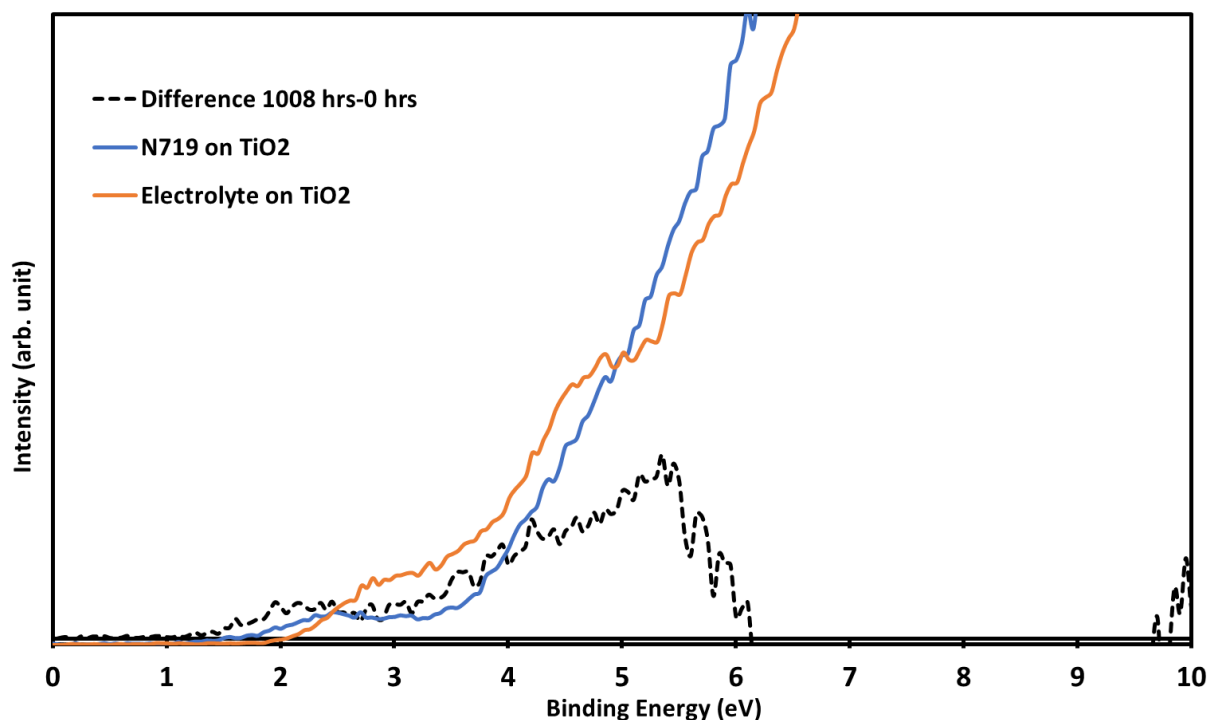


Figure 6.13: The UP spectra obtained after taking the spectral difference of the average of three samples in each 0 hr and 1008 hr ageing period for the light-aged cells with the reference spectra of dye and electrolyte adsorbed on TiO₂.

Overall, UPS concludes that the electrolyte concentration at the sample surface is required to continue the device operation and hence, with electrolytes mostly concentrated at the surface the performance of the sample aged in the dark was stable. But upon light ageing, the electrolyte penetrates the dye/TiO₂ interface and hence, adversely affects the cell operation cycle and leads to cell degradation or the formation of a new dye species after an SCN-/I- ligand exchange forming a less efficient dye, which has been reported before ⁴⁶.

In Figure 6.13 a peak is observed at ~2eV represents the dye molecule in the dye adsorbed sample. In the difference spectrum, the peak at ~2eV representing the dye molecule is shifted towards lower BE. Likewise, in Figure 6.12 as relative intensity of Ru was observed to decrease in XPS, a dip at ~2eV is observed in the difference spectrum. But, on comparing the peak at ~4eV for electrolyte adsorbed sample with the difference spectrum, the shift is evident. A shift in the UP spectra indicates a change in dipole on the material. The UP spectra are caused only by the dye layer and not by TiO₂. This concludes that the electrolyte, in either case, cause a dipole change. A similar dipole change in dye layers due to electrolyte penetration was observed by Trilaksana for N719 and Z907 ⁴⁷.

6.3.3. FT-IR analysis

To further investigate the change in the dye layer upon ageing, the samples were analysed with ATR-FTIR. Table 6.1 refers to the functional group and the peak assignments of dye adsorbed on TiO₂. The IR spectrum of dye adsorbed on TiO₂ is presented in appendix Figure 8.18.

Table 6.1: The IR modes of N719 adsorbed on TiO₂ substrate with the peak assignment.

IR modes	Dye adsorbed on TiO ₂ (cm ⁻¹)
C-O	1231
Sym (COO ⁻)	1378
Bpy	1405
TBA (CH ₂)	1466
C=C	1542
Asym (COO ⁻)	1607
C=O	1725
SCN ⁻	2096
TBA (CH)	2854

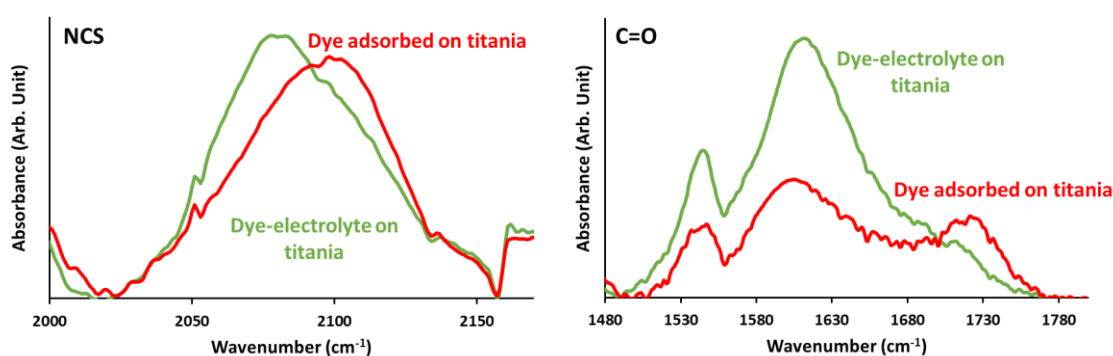
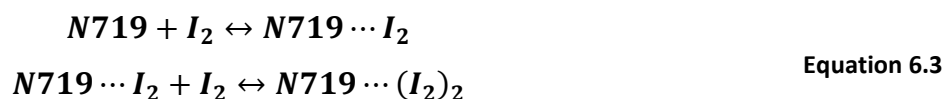


Figure 6.14: The IR spectra for the NCS and C=O on dye adsorbed sample and dye adsorbed sample after electrolyte injection.

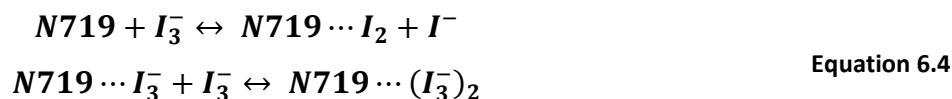
Figure 6.14 compares the IR spectra between the dye-adsorbed sample, and electrolyte injected samples cells. Electrolyte injection causes the NCS peak to shift towards lower wavenumbers and decreases the relative intensity of the C=O peak at 1725 cm⁻¹. This suggests changes in the chemical environment of the NCS and carbonyl dye components. The other functional groups show only minor changes upon electrolyte interaction which is shown in appendix Figure 8.19. Additionally, to investigate whether the shift in the SCN⁻ peak is induced by the presence of polar solvents, namely acetonitrile (AN) and valeronitrile (VN) used in the electrolyte system, the N719 dye adsorbed onto TiO₂ was further adsorbed into AN and AN:VN respectively and analysed using FTIR. In Figure 8.20, the IR spectra of the

dye adsorbed onto a TiO₂ reference sample, dye adsorbed onto TiO₂ further exposed to AN, and AN:VN concluded no shift in the SCN⁻ peak due to the solvent interaction. Thus, the shift in the SCN⁻ functional group is explicitly due to the interaction of the electrolyte with the dye molecule. However, the decrease in the IR intensity of C-N confirms the change introduced by the solvent AN:VN.

The shift of the NCS peak towards lower wavenumber suggests a weakening of the SCN⁻ functional group bonding which could affect any of the C-N, C-S or symmetric or anti-symmetric vibrations bond upon electrolyte injection. The potential cause of the weakening of the bonding in the SCN⁻ group is due to the interaction of I⁻ with the SCN⁻. This interaction causes shifting in the electron density away from the SCN⁻ group, thus causing a redshift of the NCS vibration. Further evidence of this interaction is observed in the visible reflectance spectra presented in the appendix Figure 8.21. The electrolyte interaction with adsorbed dye molecule may result in the formation of complexes via interaction of SCN⁻ which is discussed in previous works ^{46, 48}. The interactions are proposed to proceed via Equation 6.3 and Equation 6.4.



or,



Through the above reaction, the electrolyte participates in the process of dye regeneration and also regenerating the electrolyte during cell operations. Interestingly, a decrease in the relative intensity of carbonyl group was observed upon electrolyte injection. In our previous study on dye anchoring modes ⁴⁹, the shift in the carbonyl peak confirmed the presence of ester bonding upon dye adsorption. The decrease in C=O peak intensity suggests the possibility of the reduction of ester binding modes with the introduction of electrolyte.

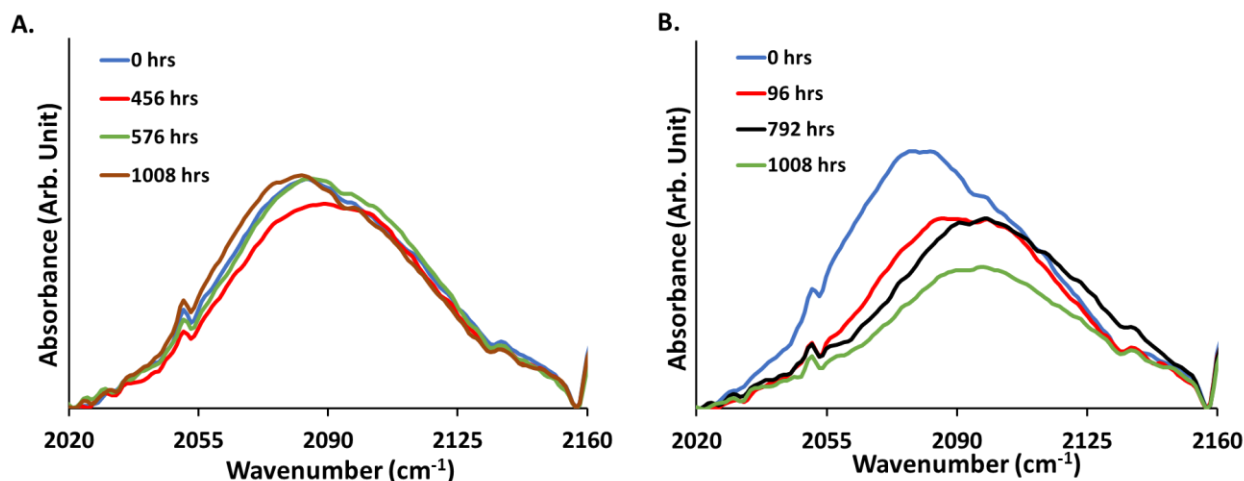


Figure 6.15: The IR spectra for the variation in the SCN^- group for dark (A.) and light-aged (B.) DSSCs.

For ageing investigations, the IR spectra for dark and light-aged samples as a function of time are shown in Figure 8.22. The peak positions for different dye functional groups did not change significantly, except for the SCN^- antisymmetric stretching group in light-aged samples. Figure 6.15 shows the changes in the SCN^- peak spectrum for dark and light-aged samples. For samples not exposed to light, the peak positions for SCN^- did not alter over time, however, a shift was observed in light-aged samples. The stability of the SCN^- peak in dark-aged samples confirms the $\text{N719}\cdots\text{I}$ complex at the dye-electrolyte interface is not changing over time. Since the $\text{N719}\cdots\text{I}$ complex participates in the dye regeneration cycle during cell operation, the continued presence of the complex in dark-aged samples is consistent with the observed stability in the cell performance (see above Figure 6.2). On the contrary, samples aged under light exposure exhibited a peak shift of the SCN^- towards higher wavenumber, approaching the peak position of electrolyte-free dye adsorbed onto TiO_2 (see Figure 6.16). Under solar irradiation it appears that the $\text{N719}\cdots\text{I}$ complex is decomposing back to the N719 dye plus an I species. XPS results showed that the relative intensity of I_x^- increased in the photoanode of the light-aged samples over time, and hence, it is possible that the decomposed I_x^- gets trapped in the photoanode. When the cell is under operation, it is very likely that the SCN^- in the dye molecule gets replaced by I^- and vice versa. But with an increase in I_x^- penetration into the dye/ TiO_2 interface the I^- binds more strongly by completely replacing the SCN^- of the dye molecule. This might affect the light absorption ability of the dye molecule, hence a steep drop in the J_{sc} with the increase in I_x^- is observed.

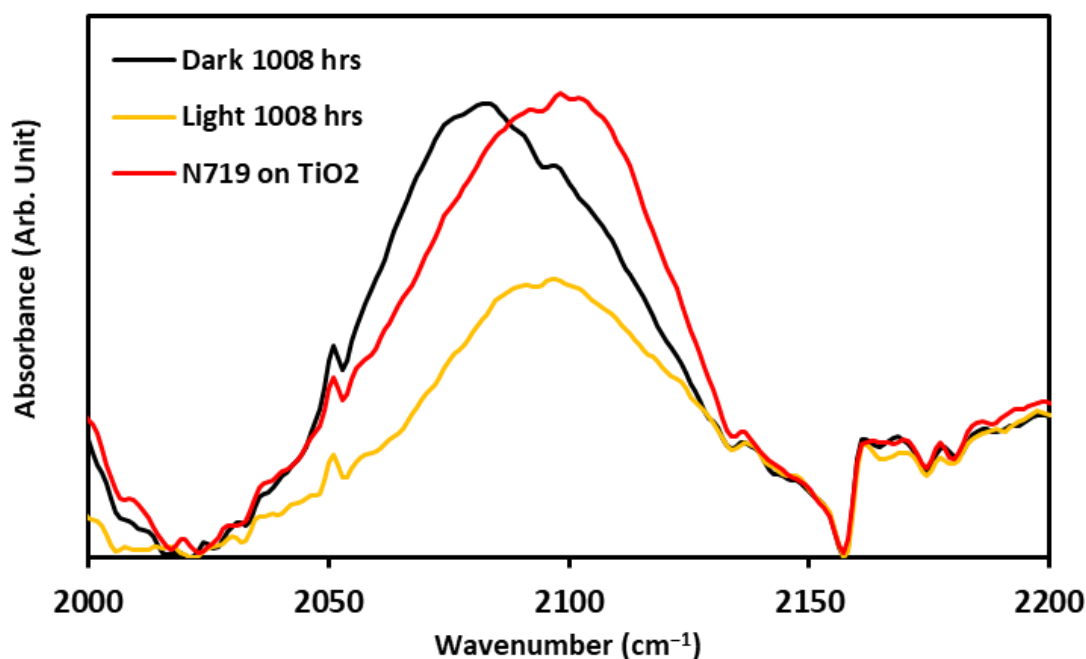


Figure 6.16: The IR spectra for NCS functional group for electrolyte-free dye adsorbed onto TiO_2 , and 1008 hrs light and dark-aged sample.

In conclusion, upon introducing of electrolyte into the cell, a $\text{N719} \cdots \text{I}$ complex is formed due to the interaction between SCN^- of the dye molecule and I^- and vice-versa. This complex is needed for the cell to perform as it participates in the dye regeneration cycle. Under dark conditions, the complex formation/decomposition process continues hence the sample performance is maintained over time. However, under solar irradiation conditions, due to an increase in penetration of I_x^- in dye/ TiO_2 interface ligand exchange occurs and N719 ($\text{NCS} \rightarrow \text{I}$) complex is formed with strong bonding resulting in an unwanted irreversible change which hinders the light absorption ability of the dye molecule.

6.3.4. UV-Vis DRS

To further investigate the changes in the dye with ageing, the samples were analysed with UV-Vis DRS. Figure 6.17 (A) shows the reflectance spectrum after 0 and 1008 hours of solar irradiation. For the purposes of comparing spectra, the wavelength at the inflection point in the reflectance spectra was determined by smoothing and taking the derivative of the reflectance spectrum as shown in Figure 6.17 (B). The derivative spectra were fit with the sum of two Gaussian functions to determine the inflection point in the reflectance spectra.

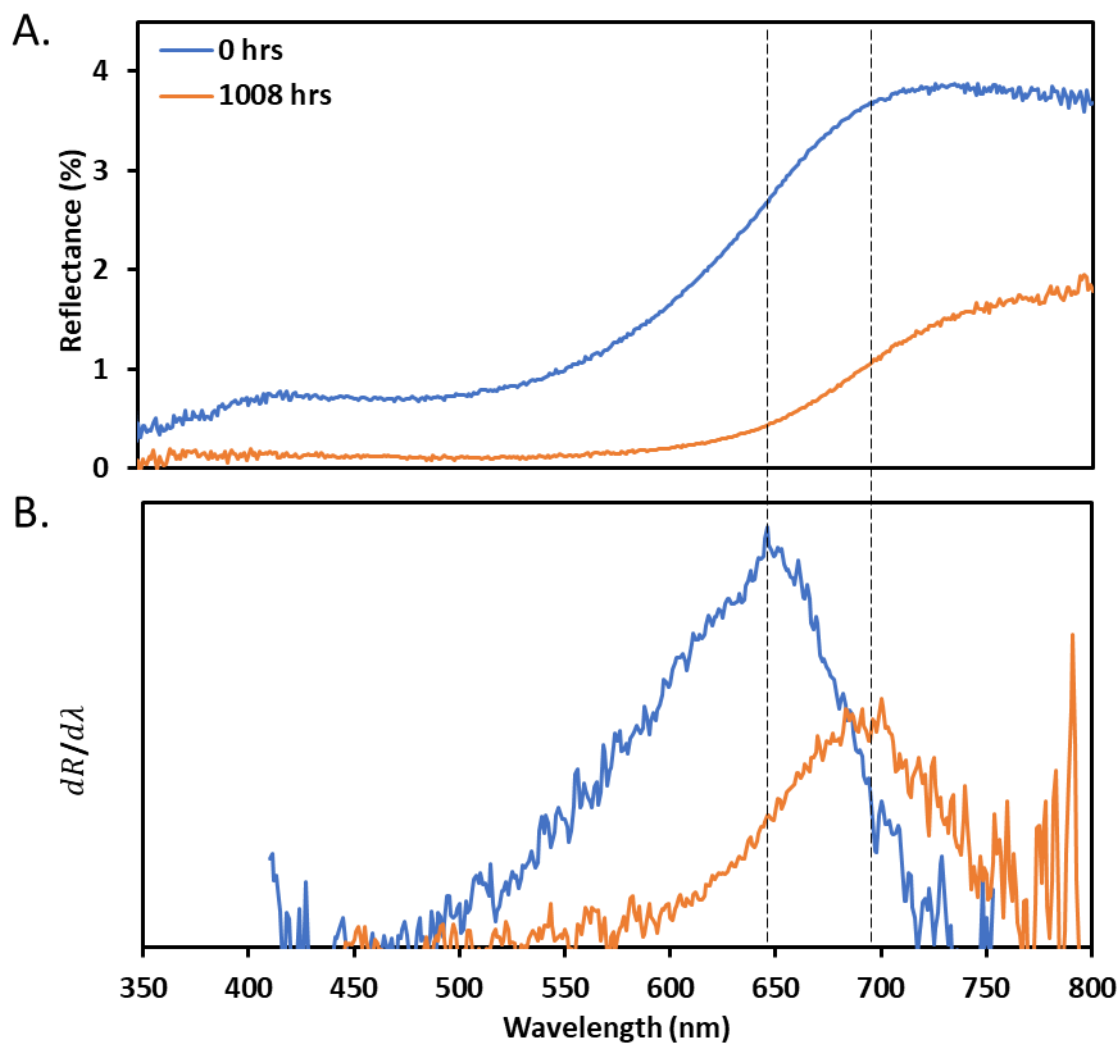


Figure 6.17: The UV-Vis DRS reflectance spectra of the 0 hrs aged sample and 1008 hrs aged sample under light irradiation (A.) and the wavelength at the inflection point in reflectance spectra obtained by smoothing and taking derivative of reflectance spectra (B.).

Upon electrolyte injection into the cell, the reflectance spectrum of the dye changes shifting the inflection point to higher wavelength (see **Error! Reference source not found.**). The reflectance increases at longer wavelengths since the dye absorption decreases in this region. The shift in the onset of reflectance is related to a change in the absorption spectrum of the dye due to the changes in the electronic state of dye molecule upon introducing electrolyte. The observations from FTIR (see Figure 6.14) established that the electrolyte interacts with the SCN^- group of dye molecule to form a dye-I complex resulting in a red shift in the SCN^- peak. This weakening of the C-N bond, observed in FTIR, is due to a shift in the electron density of the dye which is also directly observed as an inflection point shift in the DRS due to a blue shift of the dye's absorption spectrum.

Figure 6.18 illustrates how the maximum point of inflection of wavelength in the reflectance spectra of the dark and light-aged sample changes with time. Upon ageing the point of inflection for the dark-aged samples remained constant through the ageing period as no significant change in the reflectance spectra was observed. However, for light-aged samples the maximum point of inflection continuously shifted towards higher wavelength until it reached the position corresponding to the electrolyte-free dye sample. This is further evidence, first observed via FTIR, that the N719...I complex is stable under dark conditions but is degraded when exposed to light.

To understand if the changes in the UV-Vis DRS of the aged photoanode are explicitly due to the ligand exchange in the dye molecule, the DFT calculation for the N719 dye molecule and an I-substituted i.e., N719 (NCS→I) in AN was studied. The optimised structure of the N719 molecule and the N719 (NCS→I) in AN solvent is given in appendix Figure 8.23 and the simulated UV-Vis is provided in the appendix Figure 8.24. The DFT analysis confirms only a marginal shift in the UV-Vis spectrum upon ligand exchange which is further supported by the reference ⁵⁰. This confirms the presence of additional, currently unknown degradation phenomena, as evidenced by the shift IR and later in visible spectra of the aged samples, which cannot be elucidated here.

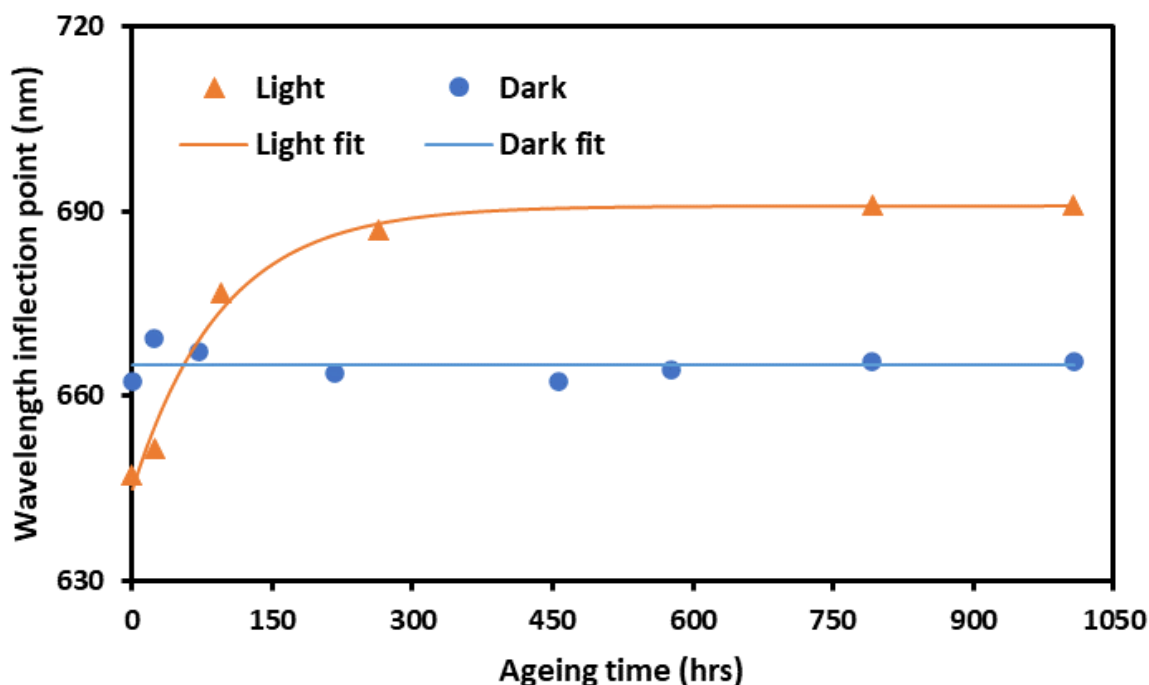


Figure 6.18: The variation in the inflection point in the wavelength of reflectance spectra of different sample aged in dark and light, with their respective fitting line.

When comparing the kinetics of the band shift for both the SCN^- peak position in FTIR and the inflection point in DRS, it was found that both followed the same behaviour as can be seen through comparison in Figure 6.19A. The fit to an exponential function to both data sets results in a decay rate of $(0.011 \pm 0.001) \text{ hr}^{-1}$ for the DRS data and $(0.0076 \pm 0.0026) \text{ hr}^{-1}$ for the SCN^- peak shift in the IR, where the uncertainty is the 1σ standard deviation from the non-linear least squares fit. Thus, within experimental error the DRS and the SCN^- absorption are concomitant indicating the two are linked as previously proposed. In Figure 6.19, the changes observed in IR and UV-Vis spectra show a probable correlation, suggesting a potential connection between the two. However, due to a lack of absolute evidence, it cannot be confirmed that these changes represent the same degradation mechanism. Interestingly, the degradation mechanisms represented by IR and UV-Vis appear to occur in relation to the degradation time, indicating a time-dependent relationship. Thus, light exposure to the DSSCs introduces different ageing phenomena including ligand exchange.

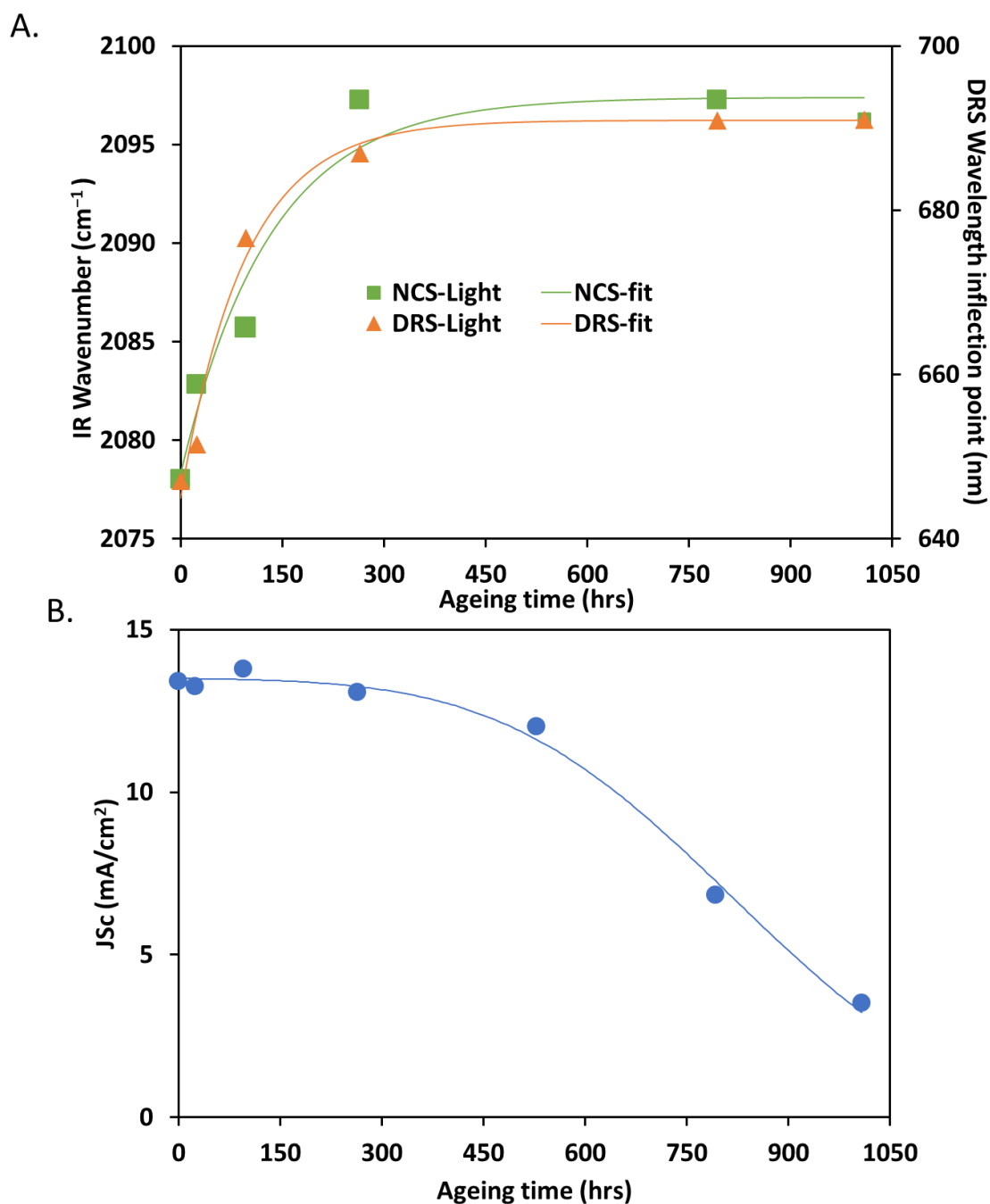


Figure 6.19: The variation in the NCS peak position in IR spectrum and wavelength inflection point in UV-Vis DRS for light-aged sample cells with their respective fitting line (A.) and the variation in the J_{sc} for light-aged sample cells with their respective fitting line.

6.4. Conclusion

In the study, the device performance analysis and surface analysis combinedly supported in the investigation of the potential cause of the cell degradation. Although slight dye desorption was observed in both dark and light ageing, the stable performance of the sample cell under dark shows that the dye desorption is not the main reason for cell degradation. The main reason for the cell degradation has been identified as the I_x^- penetration into the dye layer. The

electrolyte component is responsible for maintaining the redox cycle to regenerate itself and the dye molecule. The ageing of the cell under light causes the I_x^- to penetrate and get trapped in the dye layer ceasing the electrochemical reaction needed to continue the cell performance. With the increase in I^- into the dye/ TiO_2 interface, I^- forms a strong bond with the dye molecule by replacing the SCN^- . This decreases the ability of the dye molecule to absorb light and generate current. The role of I is very crucial in the cell performance as it participates in the redox cycle for regenerating the dye and itself under cell operation. Upon penetration of electrolyte into the dye layer, the I_x^- gets trapped and participates in different unknown degradation phenomena. A known degradation phenomenon is the ligand exchange, however, there are shifts which cannot be explained with ligand exchange and conclude the presence of additional unknown phenomena resulting in cell degradation.

6.5. Acknowledgements

The authors acknowledge the facilities, and the scientific and technical assistance of Microscopy Australia and the Australian National Fabrication Facility (ANFF) under the National Collaborative Research Infrastructure Strategy, at the South Australian Regional Facility, Flinders Microscopy and Microanalysis, Flinders University. The authors thank Prof. Greg Metha's research group at the University of Adelaide for the opportunity to conduct UV Vis-DRS measurements and valuable discussions.

6.6. Appendix

In the appendix section, the JV characterisation curve and Nyquist plot for high-performing cells aged in dark and light. It further includes tables comparing the changes in relative intensity of different elemental species in aged photoanodes in dark and light, respectively. Further, a table with the elemental species of the electrolyte adsorbed onto the TiO_2 substrate is displayed. NICIS analysis for the Ru and I peak in the dark-aged and light-aged samples is included. It further includes UP spectra for the dye and dye-electrolyte adsorbed onto TiO_2 substrate. The FTIR analysis of different dye functional groups and the variation upon electrolyte introduction are shown. It further includes the FTIR analysis of variation in dye functional groups with ageing.

6.7. References

1. Grätzel, M., Dye-Sensitized Solar Cells. *Journal of photochemistry and photobiology C: Photochemistry Reviews* **2003**, 4, 145-153.
2. Ren, Y.; Zhang, D.; Suo, J.; Cao, Y.; Eickemeyer, F. T.; Vlachopoulos, N.; Zakeeruddin, S. M.; Hagfeldt, A.; Grätzel, M., Hydroxamic Acid Pre-Adsorption Raises the Efficiency of Cosensitized Solar Cells. *Nature* **2023**, 613, 60-65.
3. Jyoti, D.; Mohan, D.; Singh, A.; Ahlawat, D. S. In *A Critical Review on Mesoporous Photoanodes for Dye-Sensitized Solar Cells*, Materials Science Forum, Trans Tech Publ: 2014; pp 53-69.
4. Roy, J. K.; Kar, S.; Leszczynski, J., *Development of Solar Cells*; Springer, 2021.
5. Flasque, M.; Van Nhien, A. N.; Swiatowska, J.; Seyeux, A.; Davoisne, C.; Sauvage, F., Interface Stability of a $\text{TiO}_2/\text{3-Methoxypropionitrile}$ -Based Electrolyte: First Evidence for Solid Electrolyte Interphase Formation and Implications. *ChemPhysChem* **2014**, 15, 1126-1137.
6. Jensen, K. F.; Rahman, M. M.; Veurman, W.; Brandt, H.; Im, C.; Wilde, J.; Hinsch, A.; Lee, J.-J., Glass Frit Dissolution Influenced by Material Composition and the Water Content in Iodide/Triiodide Electrolyte of Dye-Sensitized Solar Cells. *International Journal of Photoenergy* **2013**, 2013.
7. Matsui, H.; Okada, K.; Kitamura, T.; Tanabe, N., Thermal Stability of Dye-Sensitized Solar Cells with Current Collecting Grid. *Solar Energy Materials and Solar Cells* **2009**, 93, 1110-1115.
8. Ciani, L.; Catelani, M.; Carnevale, E. A.; Donati, L.; Bruzzi, M., Evaluation of the Aging Process of Dye-Sensitized Solar Cells under Different Stress Conditions. *IEEE Transactions on Instrumentation and Measurement* **2014**, 64, 1179-1187.
9. Nakajima, S.; Katoh, R., Mechanism of Degradation of Electrolyte Solutions for Dye-Sensitized Solar Cells under Ultraviolet Light Irradiation. *Chemical Physics Letters* **2015**, 619, 36-38.
10. Kato, N.; Higuchi, K.; Tanaka, H.; Nakajima, J.; Sano, T.; Toyoda, T., Improvement in Long-Term Stability of Dye-Sensitized Solar Cell for Outdoor Use. *Solar Energy Materials and Solar Cells* **2011**, 95, 301-305.
11. Sommeling, P. M.; Späth, M.; Smit, H.; Bakker, N.; Kroon, J., Long-Term Stability Testing of Dye-Sensitized Solar Cells. *Journal of Photochemistry and Photobiology A: Chemistry* **2004**, 164, 137-144.
12. Grünwald, R.; Tributsch, H., Mechanisms of Instability in Ru-Based Dye Sensitization Solar Cells. *The Journal of Physical Chemistry B* **1997**, 101, 2564-2575.
13. Greijer, H.; Lindgren, J.; Hagfeldt, A., Resonance Raman Scattering of a Dye-Sensitized Solar Cell: Mechanism of Thiocyanato Ligand Exchange. *The Journal of Physical Chemistry B* **2001**, 105, 6314-6320.
14. Hansen, P. E.; Nguyen, P. T.; Krake, J.; Spanget-Larsen, J.; Lund, T., Dye-Sensitized Solar Cells and Complexes between Pyridines and Iodines. A Nmr, Ir and Dft Study. *Spectrochimica Acta Part A: Molecular and Biomolecular Spectroscopy* **2012**, 98, 247-251.
15. Hoang, N.; Thoa, N.; Lund, T., Thermal Degradation Kinetics of Solar Cell Dye N719 Bound to Nanocrystalline TiO_2 Particles. *Adv. Nat. Sci.(Hanoi, Viet Nam)* **2009**, 10, 51-58.
16. Nguyen, P. T.; Degn, R.; Nguyen, H. T.; Lund, T., Thiocyanate Ligand Substitution Kinetics of the Solar Cell Dye Z-907 by 3-Methoxypropionitrile and 4-Tert-Butylpyridine at Elevated Temperatures. *Solar Energy Materials and Solar Cells* **2009**, 93, 1939-1945.
17. Nour-Mohammadi, F.; Nguyen, H. T.; Boschloo, G.; Lund, T., An Investigation of the Photosubstitution Reaction between N719-Dyed Nanocrystalline TiO_2 Particles and 4-

- Tert-Butylpyridine. *Journal of Photochemistry and Photobiology A: Chemistry* **2007**, *187*, 348-355.
18. Mohanty, S. P.; More, V.; Bhargava, P., Effect of Aging Conditions on the Performance of Dip Coated Platinum Counter Electrode Based Dye Sensitized Solar Cells. *RSC advances* **2015**, *5*, 18647-18654.
19. Likodimos, V.; Stergiopoulos, T.; Falaras, P.; Harikisun, R.; Desilvestro, J.; Tulloch, G., Prolonged Light and Thermal Stress Effects on Industrial Dye-Sensitized Solar Cells: A Micro-Raman Investigation on the Long-Term Stability of Aged Cells. *The Journal of Physical Chemistry C* **2009**, *113*, 9412-9422.
20. Xue, G.; Guo, Y.; Yu, T.; Guan, J.; Yu, X.; Zhang, J.; Liu, J.; Zou, Z., Degradation Mechanisms Investigation for Long-Term Thermal Stability of Dye-Sensitized Solar Cells. *Int. J. Electrochem. Sci* **2012**, *7*, 1496-1511.
21. Sedghi, A.; Miankushki, H. N., Influence of TiCl₄ Treatment on Structure and Performance of Dye-Sensitized Solar Cells. *Japanese Journal of applied physics* **2013**, *52*, 075002.
22. Adhikari, S. G.; Shamsaldeen, A.; Andersson, G. G., The Effect of TiCl₄ Treatment on the Performance of Dye-Sensitized Solar Cells. *The Journal of Chemical Physics* **2019**, *151*, 164704.
23. O'regan, B.; Grätzel, M., A Low-Cost, High-Efficiency Solar Cell Based on Dye-Sensitized Colloidal TiO₂ Films. *nature* **1991**, *353*, 737-740.
24. Andersson, G.; Morgner, H., Thermodynamics and Structure of Liquid Surfaces Investigated Directly with Surface Analytical Tools. *Annalen der Physik* **2017**, *529*, 1600230.
25. Andersson, G.; Morgner, H., Impact Collision Ion Scattering Spectroscopy (Iciss) and Neutral Impact Collision Ion Scattering Spectroscopy (Niciss) at Surfaces of Organic Liquids. *Surface science* **1998**, *405*, 138-151.
26. Ahlam Alharbi, P. L. G., Gunther Andersson, In Preparation. **2023**.
27. G2V Solar Simulation Technology. https://g2voptics.com/solar-simulation/?utm_source=sharpspring-chatbot&utm_medium=referral&utm_campaign=G2V+SS+Chatbot+Link (accessed 25-07).
28. M. J. Frisch; G. W. Trucks; H. B. Schlegel; G. E. Scuseria; M. A. Robb; J. R. Cheeseman; G. Scalmani; V. Barone; G. A. Petersson; H. Nakatsuji, et al., Gaussian16 (Rev. C.01). In *Gaussian, Inc.*, , Wallingford CT, , 2016.
29. Yanai, T.; Tew, D. P.; Handy, N. C., A New Hybrid Exchange–Correlation Functional Using the Coulomb-Attenuating Method (Cam-B3lyp). *Chemical physics letters* **2004**, *393*, 51-57.
30. Peterson, K. A.; Figgen, D.; Dolg, M.; Stoll, H., Energy-Consistent Relativistic Pseudopotentials and Correlation Consistent Basis Sets for the 4d Elements Y–Pd. *The Journal of chemical physics* **2007**, *126*.
31. Peterson, K. A.; Shepler, B. C.; Figgen, D.; Stoll, H., On the Spectroscopic and Thermochemical Properties of ClO, BrO, IO, and Their Anions. *The Journal of Physical Chemistry A* **2006**, *110*, 13877-13883.
32. Tomasi, J.; Mennucci, B.; Cammi, R., Quantum Mechanical Continuum Solvation Models. *Chemical reviews* **2005**, *105*, 2999-3094.
33. Singh, J.; Gusain, A.; Saxena, V.; Chauhan, A.; Veerender, P.; Koiry, S.; Jha, P.; Jain, A.; Aswal, D.; Gupta, S., Xps, Uv–Vis, Ftir, and Exafs Studies to Investigate the Binding Mechanism of N719 Dye onto Oxalic Acid Treated TiO₂ and Its Implication on Photovoltaic Properties. *The Journal of Physical Chemistry C* **2013**, *117*, 21096-21104.
34. Zen, S.; Inoue, Y.; Ono, R., Low Temperature (150° C) Fabrication of High-Performance TiO₂ Films for Dye-Sensitized Solar Cells Using Ultraviolet Light and

- Plasma Treatments of TiO₂ Paste Containing Organic Binder. *Journal of Applied Physics* **2015**, *117*, 103302.
35. Bharti, B.; Kumar, S.; Lee, H.-N.; Kumar, R., Formation of Oxygen Vacancies and Ti³⁺ State in TiO₂ Thin Film and Enhanced Optical Properties by Air Plasma Treatment. *Scientific reports* **2016**, *6*, 1-12.
36. Siow, K. S.; Britcher, L.; Kumar, S.; Griesser, H. J., Xps Study of Sulfur and Phosphorus Compounds with Different Oxidation States. *Sains Malaysiana* **2018**, *47*, 1913-1922.
37. Database, N. X.-r. P. S. X., Nist Standard Reference Database 20, Version 4.1. 2000 ed.; The U.S. Secretary of Commerce on behalf of the United States of America: 2012.
38. Oscarsson, J.; Fredin, K.; Ahmadi, S.; Eriksson, A. I.; Johansson, E. M.; Rensmo, H., Molecular Degradation of D35 and K77 Sensitizers When Exposed to Temperatures Exceeding 100° C Investigated by Photoelectron Spectroscopy. *Physical Chemistry Chemical Physics* **2016**, *18*, 8598-8607.
39. Hahlin, M.; Johansson, E. M.; Scholin, R.; Siegbahn, H.; Rensmo, H., Influence of Water on the Electronic and Molecular Surface Structures of Ru-Dyes at Nanostructured TiO₂. *The Journal of Physical Chemistry C* **2011**, *115*, 11996-12004.
40. Stec, W. J.; Morgan, W. E.; Van Wazer, J. R.; Proctor, W. G., Inner-Orbital Photoelectron Spectroscopy of Several Pairs of Similar Phosphorus Compounds. *Journal of Inorganic and Nuclear Chemistry* **1972**, *34*, 1100-1104.
41. Sherwood, P. M., X-Ray Photoelectron Spectroscopic Studies of Some Iodine Compounds. *Journal of the Chemical Society, Faraday Transactions 2: Molecular and Chemical Physics* **1976**, *72*, 1805-1820.
42. Technology, N. I. o. S. a., Nist X-Ray Photoelectron Spectroscopy Database. NIST: 2023.
43. Li, C.; Tscheuschner, S.; Paulus, F.; Hopkinson, P. E.; Kießling, J.; Köhler, A.; Vaynzof, Y.; Huettner, S., Iodine Migration and Its Effect on Hysteresis in Perovskite Solar Cells. *Advanced Materials* **2016**, *28*, 2446-2454.
44. Krishna, D. N. G.; Philip, J., Review on Surface-Characterization Applications of X-Ray Photoelectron Spectroscopy (Xps): Recent Developments and Challenges. *Applied Surface Science Advances* **2022**, *12*, 100332.
45. Kusama, H.; Sayama, K., A Comparative Computational Study on the Interactions of N719 and N749 Dyes with Iodine in Dye-Sensitized Solar Cells. *Physical Chemistry Chemical Physics* **2015**, *17*, 4379-4387.
46. Trilaksana, H. Analysis of the Dye/Titania Interface as Photo-Anode in Dye Sensitized Solar Cells. Flinders University, College of Science and Engineering., 2018.
47. Li, X.; Reynal, A.; Barnes, P.; Humphry-Baker, R.; Zakeeruddin, S. M.; De Angelis, F.; O'Regan, B. C., Measured Binding Coefficients for Iodine and Ruthenium Dyes; Implications for Recombination in Dye Sensitised Solar Cells. *Physical Chemistry Chemical Physics* **2012**, *14*, 15421-15428.
48. Adhikari, S. G.; Gascooke, J. R.; Alotabi, A. S.; Andersson, G. G., Anchoring Modes of Ru-Based N719 Dye onto Titania Substrates. *The Journal of Physical Chemistry C* **2024**, *12*.
49. Adhikari, S. G.; Gascooke, J. R.; Alotabi, A. S.; Andersson, G. G., Anchoring Modes of Ru-Based N719 Dye onto Titania Substrates. *The Journal of Physical Chemistry C* **2024**.
50. Nazeeruddin, M. K.; Kay, A.; Rodicio, I.; Humphry-Baker, R.; Müller, E.; Liska, P.; Vlachopoulos, N.; Grätzel, M., Conversion of Light to Electricity by Cis-X2bis (2, 2'-Bipyridyl-4, 4'-Dicarboxylate) Ruthenium (II) Charge-Transfer Sensitizers (X= Cl-, Br-, I-, Cn-, and SCN-) on Nanocrystalline Titanium Dioxide Electrodes. *Journal of the American Chemical Society* **1993**, *115*, 6382-6390.

CHAPTER 7 CONCLUSION AND OUTLOOK

7.1. Summary

This thesis presents the results of various studies performed on the investigation of the electrochemical properties of cell interfaces and their influence on overall cell performance. The main research question is to understand the changes introduced in the electrochemical properties at the cell interface with time when aged in dark and light.

To begin with, in Chapter 4, the dye anchoring has direct influence on the performance and cell stability. Hence, investigating the anchoring modes of the N719 dye will further help in correlating the change in the anchoring modes with the degradation in cell performance. The anchoring mode of the N719-TiO₂ configuration of interest was investigated using FTIR and ARXPS. The anchoring mode investigation is not a novel topic but with the variations in anchoring modes owing to dye anchoring mechanisms and dye-TiO₂ configuration, the anchoring modes for dye-TiO₂ configuration of our interest were studied.

The research strategy comprised evaluating the anchoring modes of individual functional groups to investigate the possible anchoring modes of dye. Formic acid, PITC, and TBA-Br salt were studied for this purpose. A re-sensitizing test was also performed where there were disagreements about the involvement of TBA⁺. FTIR analysis revealed that the anchoring mode of N719 dye is a combination of several ways of attachment, such as bidentate bridging via COO⁻; ester bonding, and a weak contact of NCS to the TiO₂ substrate. The ARXPS assisted in obtaining the dye-TiO₂ concentration depth profile. According to the concentration depth profile, the dye is more concentrated near the surface than at depth and the COO⁻ group penetrates deeper into the substrate and hence is the main anchoring group.

Moving towards ageing investigation, the aim of Chapter 5 is to develop an effective approach for investigating ageing and the application of numerous techniques to analyse various elements of cell degradation. The research method incorporates a large number of samples, around 70 cells, which were then exposed to light using a suntest device to accelerate ageing. To track the change in device performance over time, the fundamental PV parameters were traced using the JV characterisation technique. Furthermore, to analyse the changes in the photoanode over time, several surface analytical methods such as XPS, MIES, UPS, and NICISS were employed. These procedures function under UHV conditions, and to use them, the aged cell must be opened and cleaned. Rinsing the aged sample substrate is critical for examining changes in the

photoanode since otherwise the electrolyte layer on the sample surface would be probed. As a result, the rinsing method must have no/minimal influence on the dye-adsorbed layer. Hence, it is important to quantify the change in the dye layer with the rinsing process. The investigation includes the use of an electrolyte extraction approach by ethanol rinsing studies. The result concludes that the procedure of electrolyte extraction provides little or minimum risk of introducing alterations into the dye layer. Thus, an efficient approach to excess the cell interface after cell operation was established.

After rinsing, different techniques were used to monitor the possible changes in the aged sample and to understand the application of the techniques in degradation analysis. For the purpose, the samples aged for 0 hrs and 600 hrs were analysed. Surface sensitive techniques: XPS was applied to compare the changes in chemical and elemental states of the dye and electrolyte components, and UPS to observe the change in the DOS of the aged photoanode. The study also includes the use of NISS, and the substitution of He^+ by Ne^+ to investigate the changes in I and Ru in the aged sample. Surface analytical techniques such as XPS, UPS, and NISS have proven to be capable of detecting changes in the elemental composition of the dye and the electrolyte. Thus, these techniques can contribute to a better understanding of ageing and its effects at the dye/ TiO_2 /electrolyte interface with variety of dye configurations from high-performing dyes like ADEKA, LEG4, SL9 and newly developed dyes like porphyrins. A variety of cell configurations not limited to DSSCs can be investigated via this technique.

Expanding to Chapter 6, which is the application of procedure set-up in Chapter 5 to ageing investigation in Chapter 6. The goal of this chapter is to analyse the changes brought in different cell components and to discover the reason of ageing over time by employing various methodologies to track changes at the device and cell-interface levels. The study investigated the reasons of ageing in DSSCs, following the replication of the cell structure of interest. The DSSCs were prepared and aged under various stress conditions such as dark and light. In the dark, the sample was held at ambient temperature. This study employs device-level analytic approaches such as JV characterisation and EIS analysis to follow changes in the PV performance of the cell as well as the contribution of internal resistance to cell performance. Furthermore, surface analytical approaches such as XPS, MIES, UPS, and NISS aid in establishing the underlying cause of cell deterioration.

The device level analysis and surface analysis of the sample cells were conducted in the study, to investigate the cause of cell instability. The dark ageing is associated with steady cell functioning and stable interfacial resistance. This confirms no deterioration occurring at the cell

interface overtime. XPS and NCISS demonstrated the penetration of I into the dye-layer over time for light aged samples. Furthermore, UPS concluded the penetration of electrolyte into the dye layer is responsible for cell deterioration, and the presence of electrolyte at the surface is required for the cell to continue operating. FTIR confirmed that when electrolyte is injected into the dye layer, a dye-I complex is formed, which is required to continue the dye regeneration cycle. The continuous formation of the dye-I complex is maintained in the dark aged samples, but the complex decomposes in the light aged samples over time. Thus, the main reason for the cell degradation, as observed for the investigation, is depletion in the dye and electrolyte regeneration cycle because of I penetration into dye layer. The novelty in the observed result explains the reason for decrease in cell performance over time and correlates it with the changes at the cell interface.

7.2. Outlook

Expanding Chapter 4, the anchoring modes of different dye system to dye-electrolyte system can be investigated, to understand the charge transfer mechanism at the cell interface, and hence to develop more stable cells. With recent record-breaking efficiency achieved for DSSCs after treating the titania substrate with hydroxamic acid ¹, it is of interest to investigate the function of pH on the anchoring modes of dye. In addition, a time resolved *in situ*-FTIR analysis can help in understanding the variation in the anchoring modes overtime. This can further help in understanding the changes in the energy kinetics and thus, reveal information about the best soaking time for optimum favorable absorption and the functional group that are more stable.

Further extending to ageing investigation, an interesting future work could be application of an *in situ* FTIR technique. An *in situ* FTIR is a powerful technique to acquire real-time information about the changes in the chemical nature of dye and electrolyte. Hence, it can be applied to investigate changes in the chemical nature of dye and electrolyte overtime under different stress conditions. The external quantum efficiency (EQE) spectrum represents the percentage of photons participating in current generation in the cells. An EQE analysis of aged sample cells can help in understanding the level of degradation introduced in every interface layer over time. This can be further applied in developing more stable cells. An advanced technique like PEEM can be applied to understand the change in the energy band structure of the photoanode and the dye titania interface with ageing which will assist in understanding the change in the band alignment.

In addition, as the main cause of cell degradation is I penetration introducing different passivation layers and investigating the effect on cell stability would be an interesting aspect to

explore. To add, the effect of other electrolytes like $[\text{Co}(\text{phen})_3]^{2+/3+}$, $[\text{Co}(\text{bpy})_3]^{2+/3+}$, $[\text{Cu}(\text{tmby})_2]^{2+/1+}$ and other efficient electrolyte system in DSSCs would be an interesting aspect to investigate. This will help in unravelling the effect of different electrolyte systems at the cell interface over time. Further helping in identifying an electrolyte configuration that offers cell stability with efficient cell performance. Further, application of a real-life scenario like partial exposure to light and dark while cell ageing, may help in understanding the potential healing effect in DSSCs. Also, introducing moisture (rain) and variation of humidity when measured indoors and or ageing at different locations (real) to understand impact of various weather-related degradation will lead to more realistic approach to ageing analysis.

Furthermore, with increase in number of people relying on technology for entertainment, informatics, communication, health, security, and several other reasons, DSSCs may be the best option for providing a portable, wirelessly convenient, and sustainable energy source to meet the demands of charging devices' batteries due to their ability to work indoors and in low light circumstances. Additionally, DSSCs holds the ability to revolutionize the textiles industry. The potential of textile DSSCs lies in their easy weaving into fabrics, which allows them to absorb sunlight at 360° angles and maximize the absorption of both direct and dispersed light ². Nevertheless, DSSCs have also been studied in the field of Agrovoltatics as panels for greenhouse applications, with encouraging results ³. Meanwhile, the application of DSSCs in hydrogen production, photodynamic therapy, and wastewater treatment is also gaining research attention. In regard to water splitting, since the introduction of DSSCs for the purpose in 2009, a lot of research focus has concentrated on re-designing of the photoanode; to improve the quantum yield, to decrease the back electron transfer reaction and to improve the water oxidation process ⁴⁻⁶. A typical DSSCs structure requires an additional small to generate H_2 from water splitting and a tandem DSSCs system could contribute to water splitting without any applied bias voltage. To date DSSCs have demonstrated encouraging outcomes in photocatalysis for successful water splitting. The configuration of DSSCs with $\text{TiO}_2/\text{Nb}_2\text{O}_5$ as the semiconductor, $\text{RuP}2$ as sensitizer and $\text{IrO}_2 \cdot n\text{H}_2\text{O}$ as oxygen evolution reaction (OER) catalyst achieved 109% of the Faradaic efficiency of O_2 generation ⁷. Furthermore, in DSSCs, photo-absorbance can be increased to enhance charge transfer, which in turn can boost H_2 production, by using the right chromophore. The alteration of dye and cell architecture to enhance H_2 production has garnered interest for future research work.

The DSSCs meet the two fundamental characteristics of the multijunction solar cell by being able to employ high energy photons and operate in low light circumstances. In contrast to other solar technologies, the energy region in DSSCs can be easily modified utilising different

chromophore designs and molecular-level control ⁸. Furthermore, the DSSCs components can be modified to achieve desirable absorption width, active layer thickness variation, and chromophore adsorption to calibrate the output photocurrents for low heat loss. This technology can be integrated with any other technology that employs lower energy photons to create a high-performing multijunction system ⁸. In addition, the DSSCs have demonstrated encouraging results on repeated electric erasure and re-sensitization of cell components with 90.98% efficiency even after being recycled six times. Therefore, the state-of-art can help in reducing costs and waste generation, and promoting reuse and reduce ⁹. Hence, DSSC hold potential to lead towards more sustainable energy source for future use.

DSSCs have many potential avenues for future investigation and improvement. DSSCs have achieved a recording breaking efficiency of 15% ¹ while the highest efficiency recorded for solar cell is 39.5% ¹⁰. Although DSSCs has its advantages, it is still withheld due to comparable poor performance, hence focus on material development, device architecture, stability and durability, large-scale manufacturing, cost-reduction and integrating with other technologies like developing hybrid systems could be of future interest.

7.2. References

1. Ren, Y.; Zhang, D.; Suo, J.; Cao, Y.; Eickemeyer, F. T.; Vlachopoulos, N.; Zakeeruddin, S. M.; Hagfeldt, A.; Grätzel, M., Hydroxamic Acid Pre-Adsorption Raises the Efficiency of Cosensitized Solar Cells. *Nature* **2023**, *613*, 60-65.
2. Chae, Y.; Park, J. T.; Koh, J. K.; Kim, J. H.; Kim, E., All-Solid, Flexible Solar Textiles Based on Dye-Sensitized Solar Cells with ZnO Nanorod Arrays on Stainless Steel Wires. *Materials Science and Engineering: B* **2013**, *178*, 1117-1123.
3. Barichello, J.; Vesce, L.; Mariani, P.; Leonardi, E.; Braglia, R.; Di Carlo, A.; Canini, A.; Reale, A., Stable Semi-Transparent Dye-Sensitized Solar Modules and Panels for Greenhouse Application. *Energies* **2021**, *14*, 6393.
4. Watanabe, M., Dye-Sensitized Photocatalyst for Effective Water Splitting Catalyst. *Science and Technology of advanced MaTerialS* **2017**, *18*, 705-723.
5. Yu, Z.; Li, F.; Sun, L., Recent Advances in Dye-Sensitized Photoelectrochemical Cells for Solar Hydrogen Production Based on Molecular Components. *Energy & Environmental Science* **2015**, *8*, 760-775.
6. Sherman, B. D.; McMillan, N. K.; Willinger, D.; Leem, G., Sustainable Hydrogen Production from Water Using Tandem Dye-Sensitized Photoelectrochemical Cells. *Nano Convergence* **2021**, *8*, 1-15.
7. Lee, S.-H. A.; Zhao, Y.; Hernandez-Pagan, E. A.; Blasdel, L.; Youngblood, W. J.; Mallouk, T. E., Electron Transfer Kinetics in Water Splitting Dye-Sensitized Solar Cells Based on Core-Shell Oxide Electrodes. *Faraday discussions* **2012**, *155*, 165-176.
8. Roy, J. K.; Kar, S.; Leszczynski, J., *Development of Solar Cells: Theory and Experiment*; Springer, 2021.
9. Liu, W.; Liu, Y.; Liu, F.; Yang, Y., Regeneration Performance Tolerance of Dye-Sensitized Solar Cells Based on Continuous Repeated Electric Erasure/Re-Sensitization. *Electrochimica Acta* **2019**, *307*, 488-494.
10. Ozdemir, D., Scientist Just Broke the Recored for the Highest Efficiency Solar Cells. *Interesting Engineering* 2022.

CHAPTER 8 APPENDICES

8.1 Chapter 1: Dye Sensitised Solar Cells-An Overview

Table 8.1: The record-keeping cell configuration with the components. The section for photoanode is non-included because TiO₂ is the substrate used for dye-adsorption in the listed configuration.

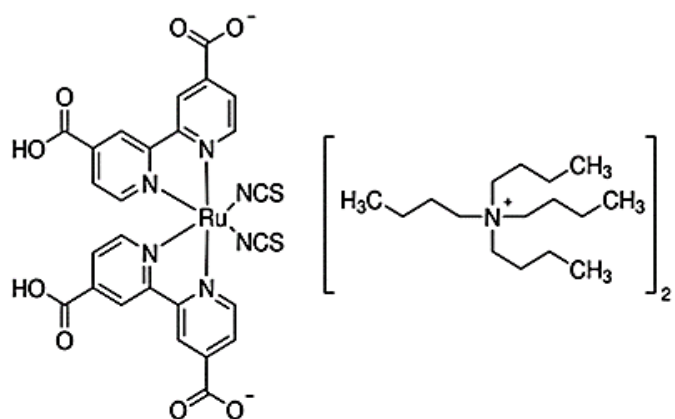
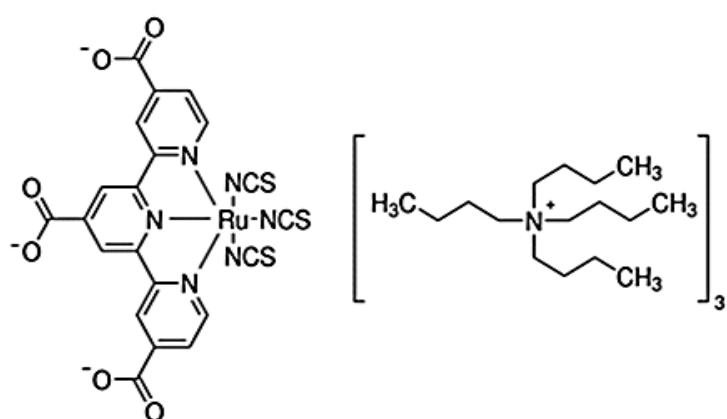
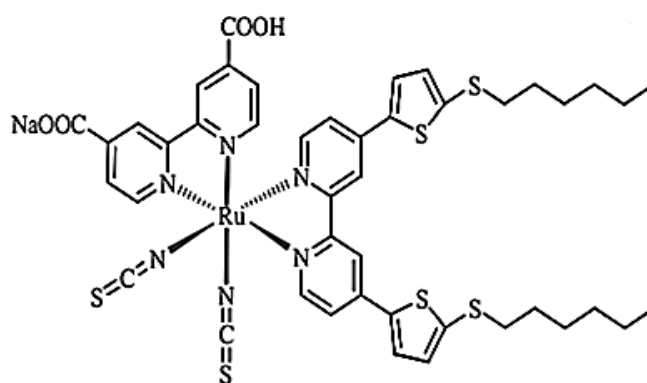
Sensitiser	Electrolyte Composition	Counter Electrode	J _{sc} [mA/cm ²]	V _{oc} [mV]	FF	η [%]	Ref
N719	BMII, I ₂ , LiI, TBP in AN	Pt	18.9	686	0.86	11.2	(1)
N749 with HNO ₃ treatment	DMPII, I ₂ , TBP, LiI in MAN	-	20.53	720	0.70	10.4	(2)
C106 + CDCA	DMII, I ₂ , TBP, GuNCS, LiI in MPN	Pt	17.6	753	0.75	9.8	(3)
N621 in MPN	BMII, I ₂ , GuNCS, TBP in AN:VN	Pt	16.81	777	0.73	9.6	(4)
C101 + CDCA	DMII, I ₂ , LiI, TBP, GuNCS in AN:VN	Pt	17.94	777	0.79	11	(5)
LD4	PMII, I ₂ , LiI, TBP in AN:VN	Pt	19.63	711	0.72	10.1	(6)
LD13	LiI, I ₂ , PMII, TBP in AN:VN	Pt	18.44	697	0.73	9.3	(6)

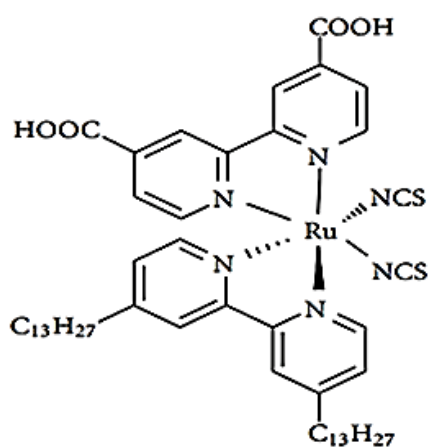
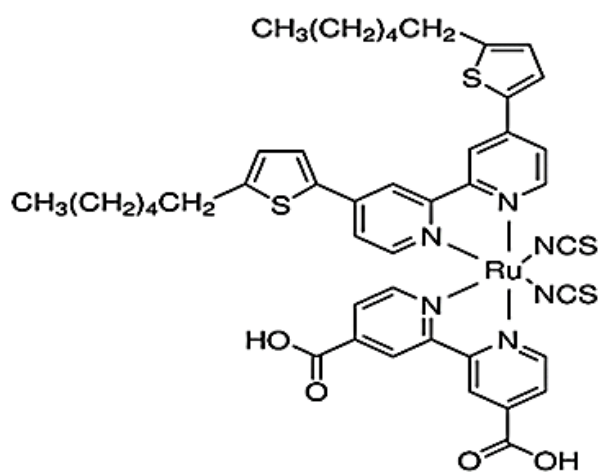
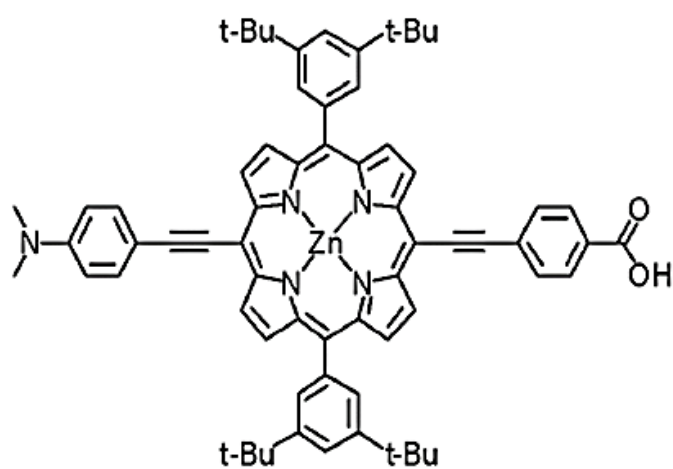
LD14	LiI, I ₂ , PMII, TBP in AN:VN	Pt	19.17	736	0.71	10.2	(6)
LD31 + AN-4	LiI, I ₂ , PMII, TBP, in AN:VN	Pt	20.27	704	0.72	10.3	(7)
ZnPBAT + CDCA	DMII, I ₂ , LiI, GuNCS, TBP in AN:VN	Pt	19.33	719	0.72	10.1	(8)
XW4 + C1	LiI, I ₂ , PMII, TBP, in AN:VN	Pt	20.15	736	0.71	10.5	(9)
LW4	PMII, LiI, I ₂ , TBP in AN:VN	Pt	17.65	750	0.72	9.5	(10)
LWP1	PMII, LiI, I ₂ , TBP in AN:VN	Pt	17.77	730	0.75	9.7	(11)
LWP3	PMII, LiI, I ₂ , TBP in AN:VN	Pt	17.76	720	0.74	9.5	(11)
C217 + dihydroxycholic acid	DMII, LiI, TBP, I ₂ GuNCS in AN:VN	Pt	16.1	803	0.76	9.8	(12)
SM315 + CDCA	Co(bpy) ₃ (TFSI) ₂ Co(bpy) ₃ (TFSI) ₃ , LiTFSI, TBP in AN	Graphene Nanoplates	18.1	910	0.78	13	(13)
SM371 + CDCA	Co(bpy) ₃ (TFSI) ₂	Graphene	15.9	910	0.79	12	(13)

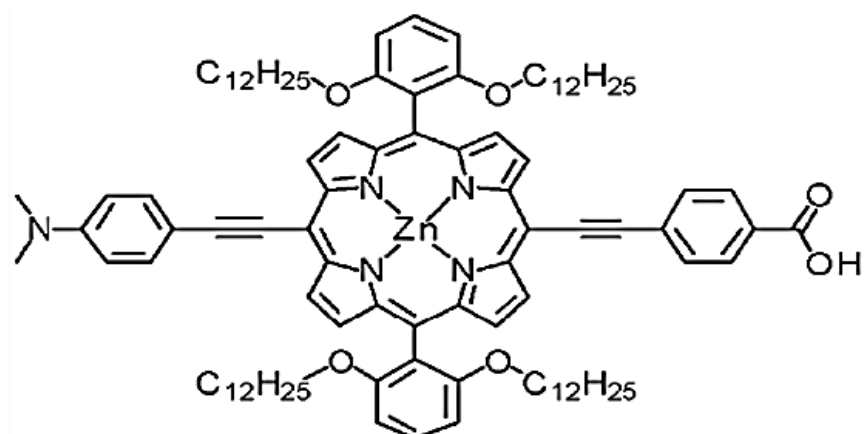
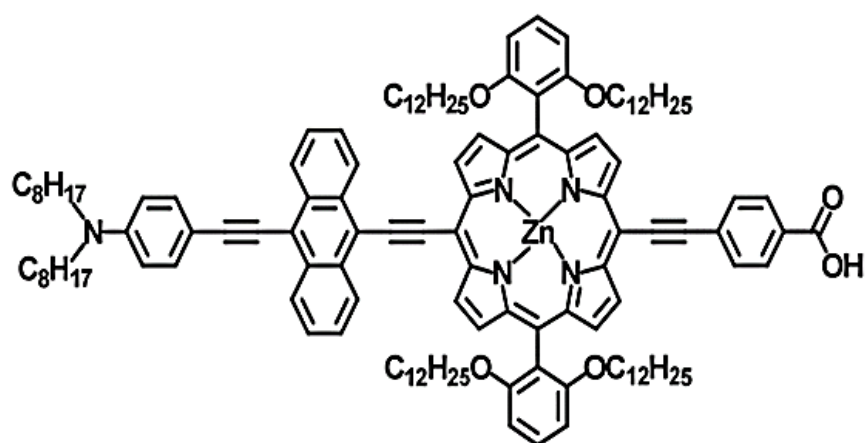
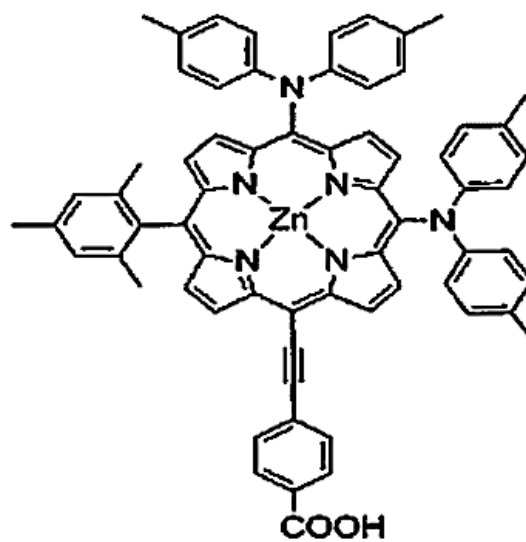
	Co(bpy) ₃ (TFSI) ₃ , LiTFSI, TBP in AN	Nanopl ates					
C275	Co(phen) ₃ (TFSI) ₂ Co(phen) ₃ (TFSI) ₃ , LiTFSI, TBP in AN	Au/Cr	17.03	956	0.77	12.5	(14)
C272	Co(phen) ₃ (TFSI) ₂ Co(phen) ₃ (TFSI) ₃ , LiTFSI, TBP in AN	Au/Cr	15.81	897	0.74	10.6	(14)
ADEKA + LEG4	Co(phen) ₃ (PF ₆) ₂ , Co(phen) ₃ (PF ₆) ₃ , LiClO ₄ , NaClO ₄ , TBAPF, TBPPF, HMIImPF, TBP, TMSP, MP, CPrBP, CPeBP, COcBP in MeCN	Au/GN P	18.27	1014	0.77	14.3	(15)
JK306 + HC-A	Co(bpy) ₃ [B(CN) ₄] ₂ Co(bpy) ₃ [B(CN) ₄] ₃ TBP, LiClO ₄ in AN	I-GNP	14.81	977	0.71	10.3	(16)

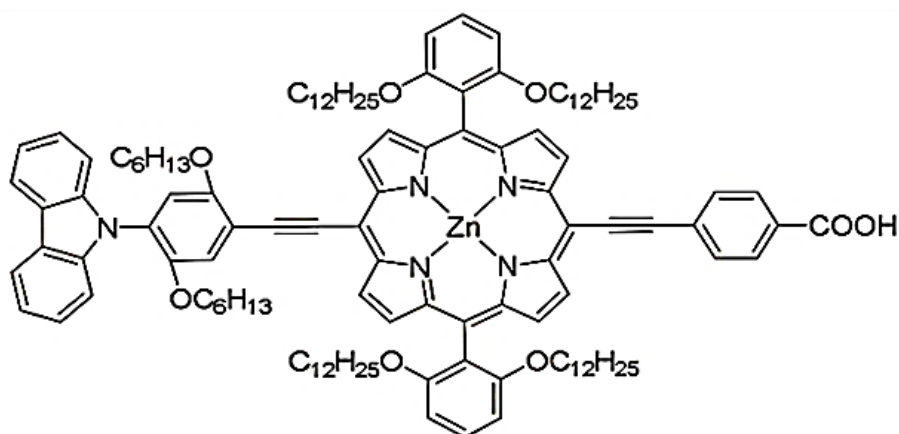
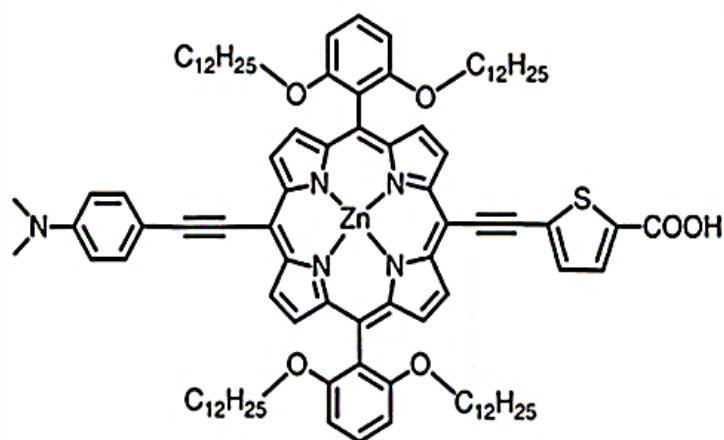
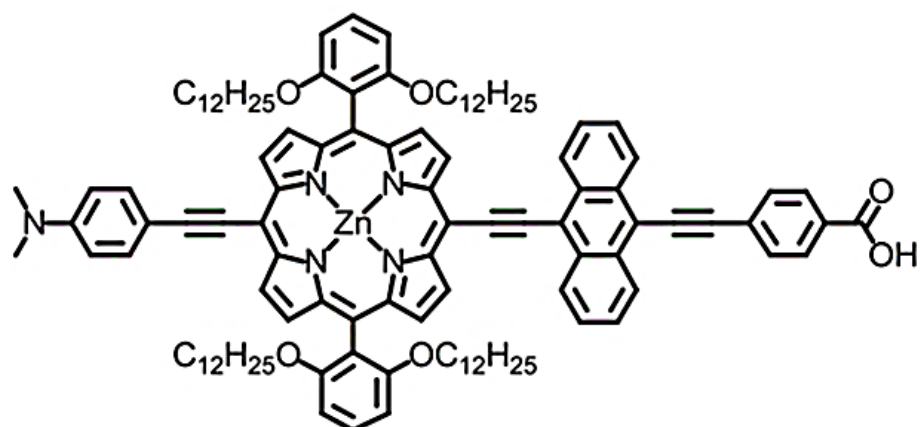
YA422 + CDCA	Co(bpy) ₃ [B(CN) ₄] ₂ Co(bpy) ₃ [B(CN) ₄] ₃ TBP, LiClO ₄ in AN	GNP+ Au	16.25	890	0.74	10.7	(17)
ADEKA + SFD-5	Co [(Cl-phen) ₃] ₂ , Co [(Cl-phen) ₃] ₃ , LiClO ₄ , NaClO ₄ , TBAPF, TBPPF, HMIImPF, TBP, TMSP, MP in AN	Pt	16.07	1035	0.77	12.9	(18)
YD2-o-C8 + Y123	Co(bpy) ₃ [B(CN) ₄] ₂ Co(bpy) ₃ [B(CN) ₄] ₃ TBP, LiClO ₄ in AN	Pt	17.05	927	0.78	12.3	(19)
Y123	Co(bpy) ₃ [B(CN) ₄] ₂ Co(bpy) ₃ [B(CN) ₄] ₃ TBP, LiClO ₄ in AN	PEDOT	15.9	910	0.71	10.3	(20)
YD2 + CDCA	DMII, I ₂ , LiI, GuNCS, TBP in AN:VN	Pt	17.05	742	0.72	9.1	(8)

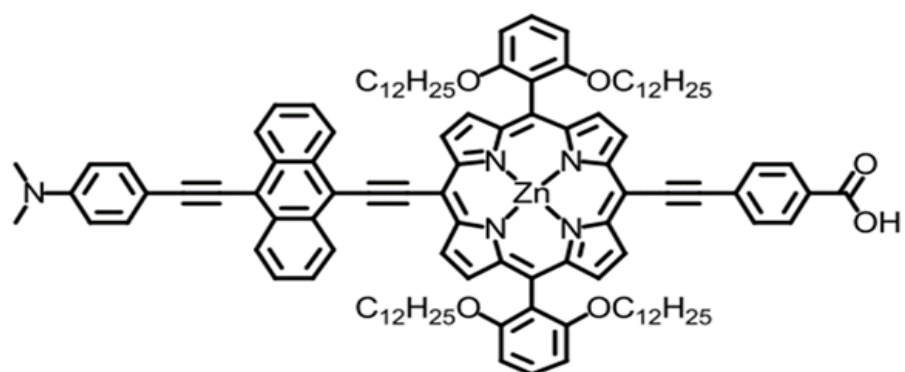
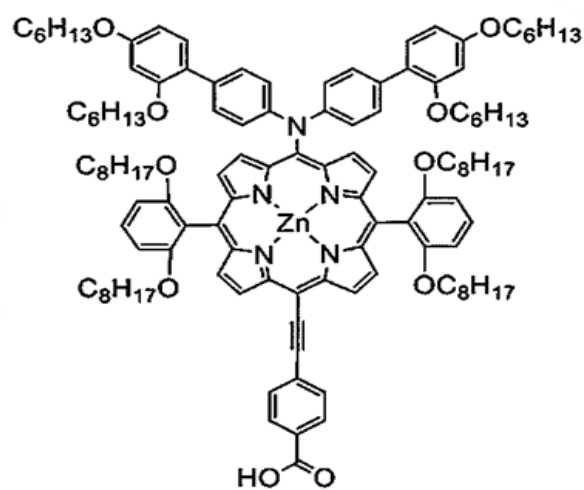
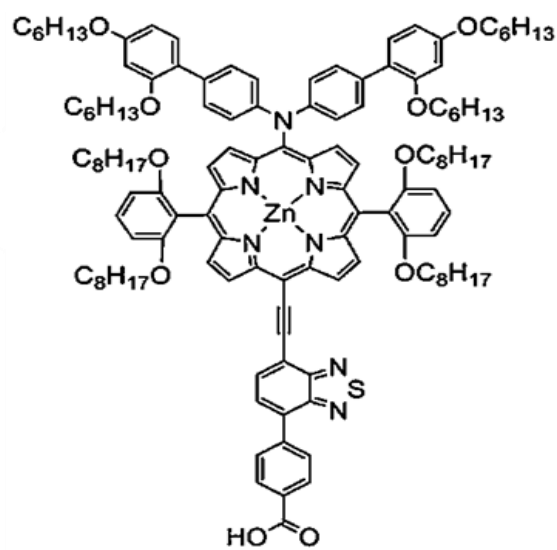
CYC-B11	BMII, LiI, I ₂ , TBP, GuNCS, in AN	PEDOT -F	18.5	723	0.67	9	(21)
D149 + CDCA	LiI, BMII, I ₂ , TBP in AN:VN	Pt	19.96	653	0.69	9	(22)
C106TBA + DMSO + DINHOP	DMII, GuNCS, I ₂ , NBB in MPN	PDDA @ ERGO	18.77	692	0.74	9.5	(23)
YD2-o-C8	Co(bpy) ₃ [B(CN) ₄] ₂ , Co(bpy) ₃ [B(CN) ₄] ₃ , TBP, LiClO ₄ in AN	Pt	17.3	965	0.71	11.9	(19)
WW-5	Co(bpy) ₃ (TFSI) ₂ Co(bpy) ₃ (TFSI) ₃ , LiTFSI, TBP in AN	Pt	18.43	766	0.73	10.3	(24)
SL9+SL10+BP HA	Cu ^(I) (tmby) ₂ (T FSI), Cu ^(II) (tmby) ₂ (T FSI) ₂ , NaTFSI and CEMI in 3-MPN	PEDOT	17.8	1040	0.82	15.2	(25)

N719**N749****C106**

N621**C101****LD13**

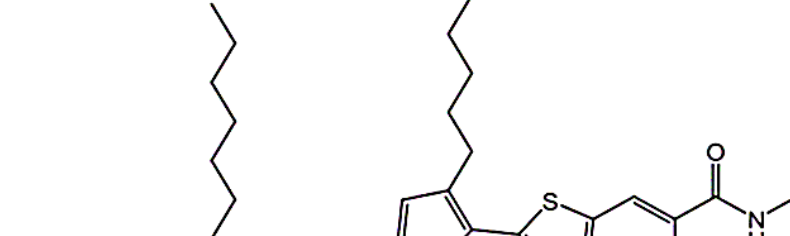
LD14**LD31****ZnPBAT**

XW4**LW4****LWP1**

LWP3**SM371****SM315**

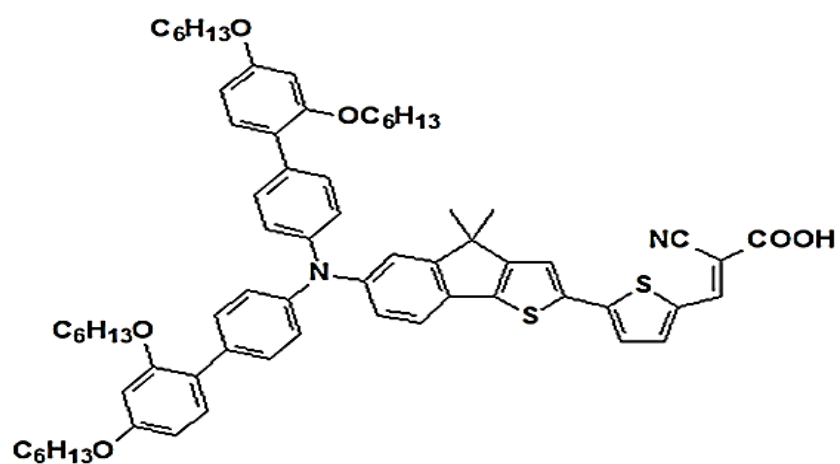
[illegible]CCCCCCCCC(C)COc1ccc(cc1)-c2ccc3c4ccc5c6ccc7c8ccc9c2c3c4c5c6c7c8c9N(CCCCCC)CCCCCCCC

A-1

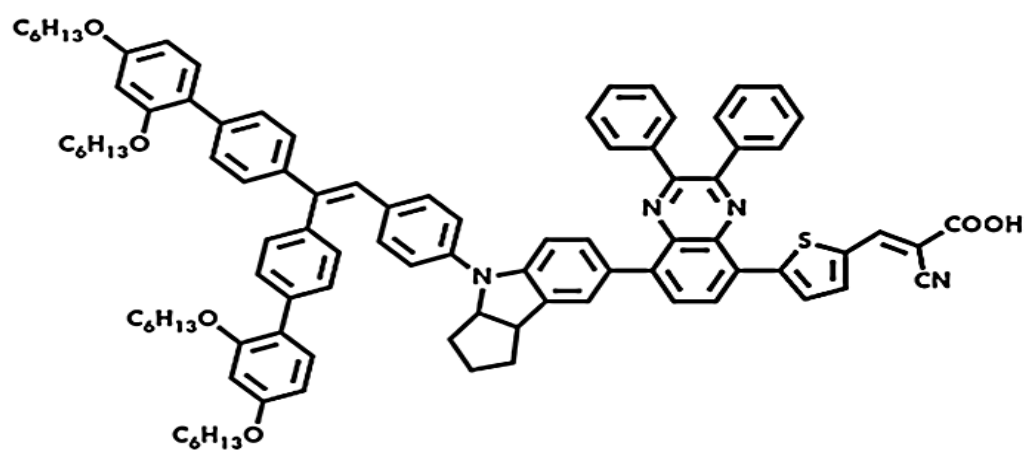


The chemical structure of compound A-1 is a complex organic molecule. It features a central chain of five thiophene rings connected by single bonds. The first thiophene ring on the left is substituted with a 1-ethyl-2,3-bis(phenyl)indole group. The second thiophene ring is substituted with a heptyl group. The third thiophene ring is substituted with a heptyl group. The fourth thiophene ring is substituted with a heptyl group. The fifth thiophene ring is substituted with a 2-cyano-3-(4-(trimethylsilyl)phenyl)acrylamide group. The trimethylsilyl group is represented as a silicon atom bonded to three methoxy (OMe) groups and a phenyl ring.

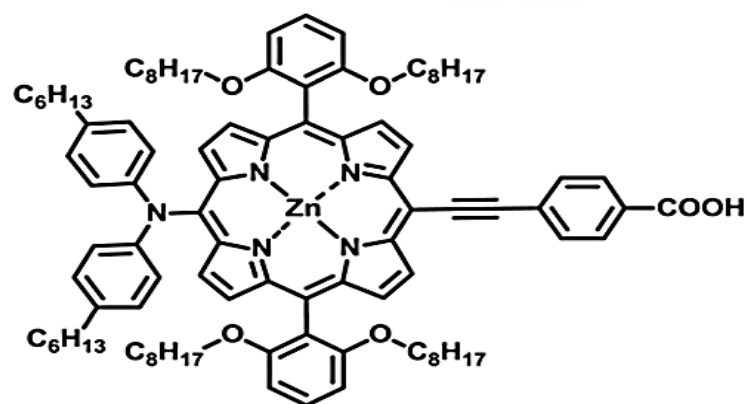
JK306

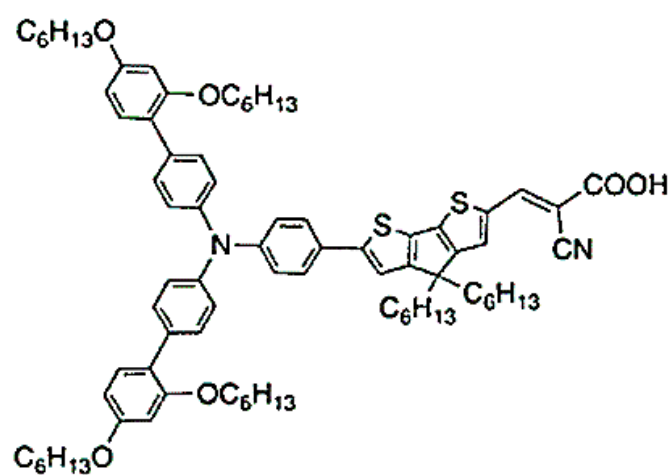
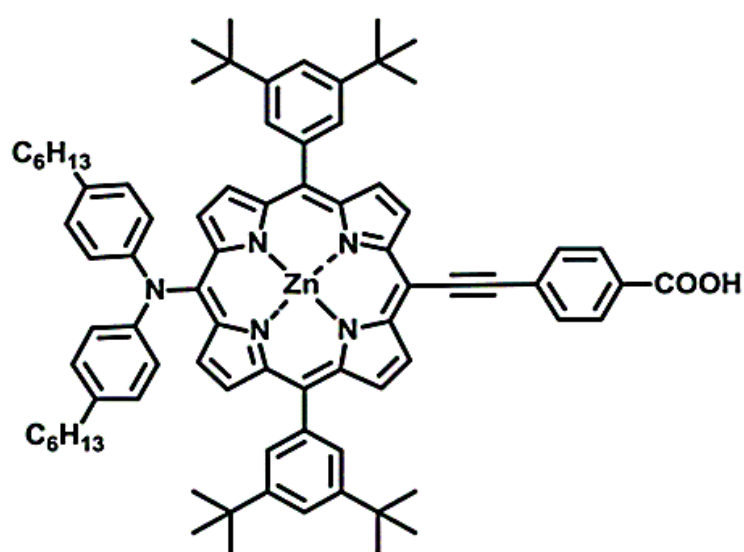
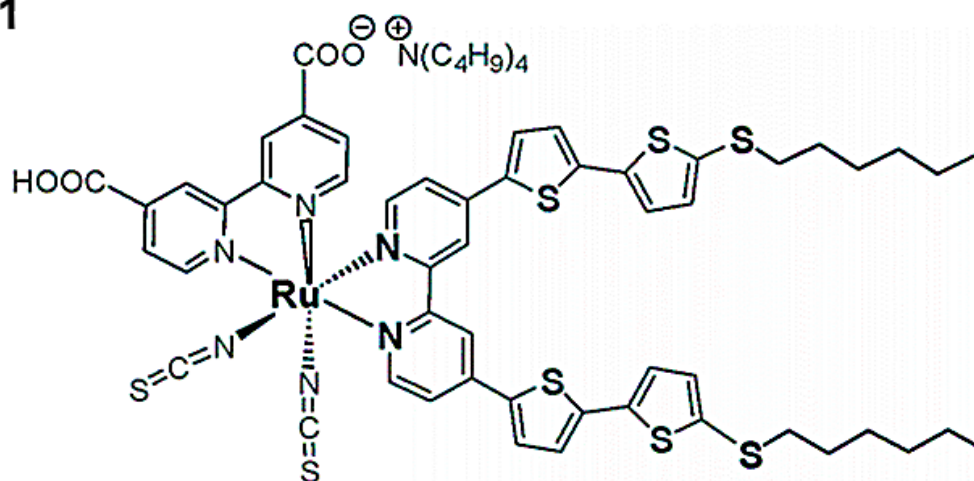


YA422



YD2-o-C8



Y123**YD2****CYC-B11**

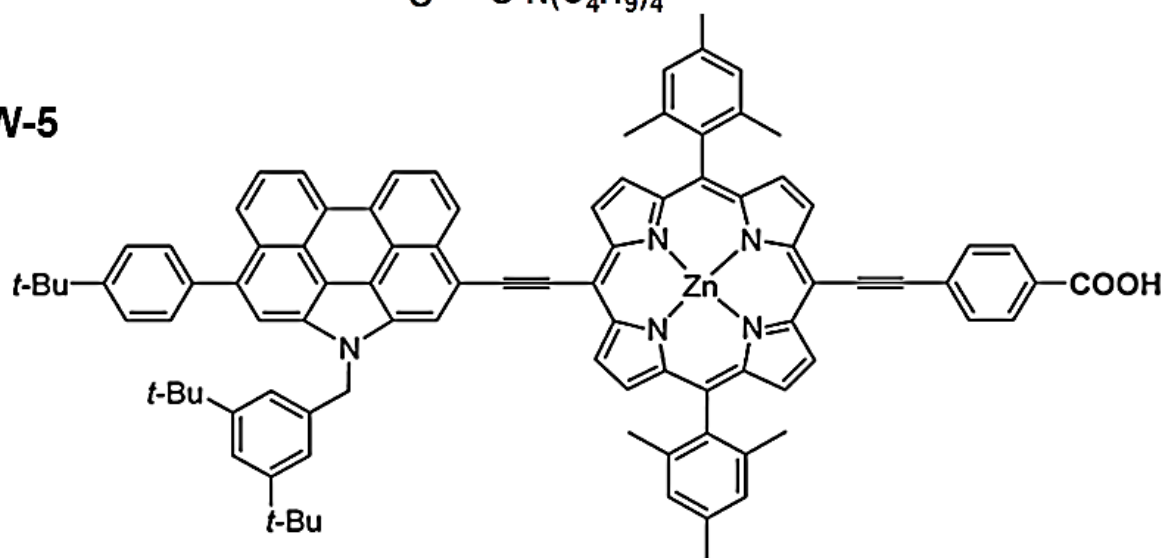
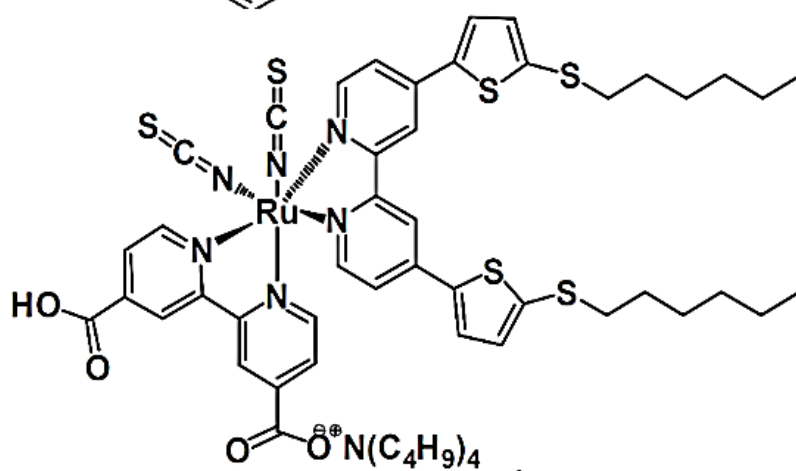
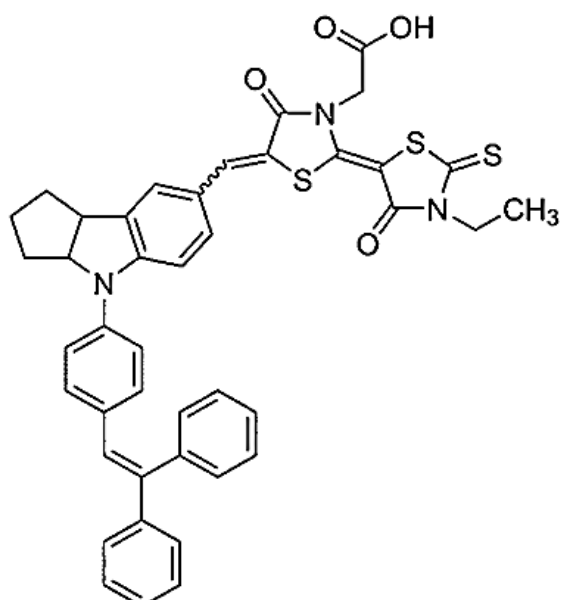


Figure 8.1 The molecular structure of high performing dyes

8.1.1. References

1. Sun KC, Sahito IA, Noh JW, Yeo SY, Im JN, Yi SC, et al. Highly efficient and durable dye-sensitized solar cells based on a wet-laid PET membrane electrolyte. *Journal of Materials Chemistry A*. 2016;4(2):458-65.
2. Nazeeruddin MK, Pechy P, Renouard T, Zakeeruddin SM, Humphry-Baker R, Comte P, et al. Engineering of efficient panchromatic sensitizers for nanocrystalline TiO₂-based solar cells. *Journal of the American Chemical Society*. 2001;123(8):1613-24.
3. Yu Q, Zhou D, Shi Y, Si X, Wang Y, Wang P. Stable and efficient dye-sensitized solar cells: photophysical and electrical characterizations. *Energy & Environmental Science*. 2010;3(11):1722-5.
4. Nazeeruddin MK, De Angelis F, Fantacci S, Selloni A, Viscardi G, Liska P, et al. Combined experimental and DFT-TDDFT computational study of photoelectrochemical cell ruthenium sensitizers. *Journal of the American Chemical Society*. 2005;127(48):16835-47.
5. Gao F, Wang Y, Shi D, Zhang J, Wang M, Jing X, et al. Enhance the optical absorptivity of nanocrystalline TiO₂ film with high molar extinction coefficient ruthenium sensitizers for high performance dye-sensitized solar cells. *Journal of the American Chemical Society*. 2008;130(32):10720-8.
6. Wang C-L, Chang Y-C, Lan C-M, Lo C-F, Diao EW-G, Lin C-Y. Enhanced light harvesting with π -conjugated cyclic aromatic hydrocarbons for porphyrin-sensitized solar cells. *Energy & Environmental Science*. 2011;4(5):1788-95.
7. Wang C-L, Hu J-Y, Wu C-H, Kuo H-H, Chang Y-C, Lan Z-J, et al. Highly efficient porphyrin-sensitized solar cells with enhanced light harvesting ability beyond 800 nm and efficiency exceeding 10%. *Energy & Environmental Science*. 2014;7(4):1392-6.
8. Kurotobi K, Toude Y, Kawamoto K, Fujimori Y, Ito S, Chabera P, et al. Highly Asymmetrical Porphyrins with Enhanced Push–Pull Character for Dye-Sensitized Solar Cells. *Chemistry—A European Journal*. 2013;19(50):17075-81.
9. Wang Y, Chen B, Wu W, Li X, Zhu W, Tian H, et al. Efficient solar cells sensitized by porphyrins with an extended conjugation framework and a carbazole donor: from molecular design to cosensitization. *Angewandte Chemie*. 2014;126(40):10955-9.
10. Lu J, Xu X, Cao K, Cui J, Zhang Y, Shen Y, et al. D– π –A structured porphyrins for efficient dye-sensitized solar cells. *Journal of Materials Chemistry A*. 2013;1(34):10008-15.
11. Wu C-H, Chen M-C, Su P-C, Kuo H-H, Wang C-L, Lu C-Y, et al. Porphyrins for efficient dye-sensitized solar cells covering the near-IR region. *Journal of Materials Chemistry A*. 2014;2(4):991-9.
12. Zhang G, Bala H, Cheng Y, Shi D, Lv X, Yu Q, et al. High efficiency and stable dye-sensitized solar cells with an organic chromophore featuring a binary π -conjugated spacer. *Chemical Communications*. 2009(16):2198-200.
13. Mathew S, Yella A, Gao P, Humphry-Baker R, Curchod BF, Ashari-Astani N, et al. Dye-sensitized solar cells with 13% efficiency achieved through the molecular engineering of porphyrin sensitizers. *Nature chemistry*. 2014;6(3):242-7.
14. Yao Z, Zhang M, Wu H, Yang L, Li R, Wang P. Donor/acceptor indenoperylene dye for highly efficient organic dye-sensitized solar cells. *Journal of the American Chemical Society*. 2015;137(11):3799-802.
15. Kakiage K, Aoyama Y, Yano T, Oya K, Fujisawa J-i, Hanaya M. Highly-efficient dye-sensitized solar cells with collaborative sensitization by silyl-anchor and carboxy-anchor dyes. *Chemical Communications*. 2015;51(88):15894-7.
16. Jeon I-Y, Kim HM, Choi IT, Lim K, Ko J, Kim JC, et al. High-performance dye-sensitized solar cells using edge-halogenated graphene nanoplatelets as counter electrodes. *Nano Energy*. 2015;13:336-45.

17. Yang J, Ganesan P, Teuscher J, Moehl T, Kim YJ, Yi C, et al. Influence of the donor size in D- π -A organic dyes for dye-sensitized solar cells. *Journal of the American Chemical Society*. 2014;136(15):5722-30.
18. Kakiage K, Aoyama Y, Yano T, Oya K, Kyomen T, Hanaya M. Fabrication of a high-performance dye-sensitized solar cell with 12.8% conversion efficiency using organic silyl-anchor dyes. *Chemical Communications*. 2015;51(29):6315-7.
19. Yella A, Lee H-W, Tsao HN, Yi C, Chandiran AK, Nazeeruddin MK, et al. Porphyrin-sensitized solar cells with cobalt (II/III)-based redox electrolyte exceed 12 percent efficiency. *science*. 2011;334(6056):629-34.
20. Tsao HN, Burschka J, Yi C, Kessler F, Nazeeruddin MK, Grätzel M. Influence of the interfacial charge-transfer resistance at the counter electrode in dye-sensitized solar cells employing cobalt redox shuttles. *Energy & Environmental Science*. 2011;4(12):4921-4.
21. Chiang C-H, Chen S-C, Wu C-G. Preparation of highly concentrated and stable conducting polymer solutions and their application in high-efficiency dye-sensitized solar cell. *Organic Electronics*. 2013;14(9):2369-78.
22. Ito S, Zakeeruddin SM, Humphry-Baker R, Liska P, Charvet R, Comte P, et al. High-efficiency organic-dye-sensitized solar cells controlled by nanocrystalline-TiO₂ electrode thickness. *Advanced Materials*. 2006;18(9):1202-5.
23. Xu X, Huang D, Cao K, Wang M, Zakeeruddin SM, Grätzel M. Electrochemically reduced graphene oxide multilayer films as efficient counter electrode for dye-sensitized solar cells. *Scientific reports*. 2013;3(1):1-7.
24. Luo J, Xu M, Li R, Huang K-W, Jiang C, Qi Q, et al. N-annulated perylene as an efficient electron donor for porphyrin-based dyes: enhanced light-harvesting ability and high-efficiency Co (II/III)-based dye-sensitized solar cells. *Journal of the American Chemical Society*. 2014;136(1):265-72.
25. Ren Y, Zhang D, Suo J, Cao Y, Eickemeyer FT, Vlachopoulos N, et al. Hydroxamic acid pre-adsorption raises the efficiency of cosensitized solar cells. *Nature*. 2023;613(7942):60-5.

8.2 Chapter 4: Anchoring Modes of Ru-based N719 dye onto Titania

Substrate

SEM analysis for the thickness of mesoporous TiO_2 :

Scanning electron microscopy (SEM) was used to determine the thickness of TiO_2 deposited onto FTO. Secondary electron cross-sectional images of the samples were captured using an FEI F50 SEM at a working distance of 10.6 mm. No coatings to prevent charging were applied to the samples, thus a low electron beam energy of 2 keV was used.

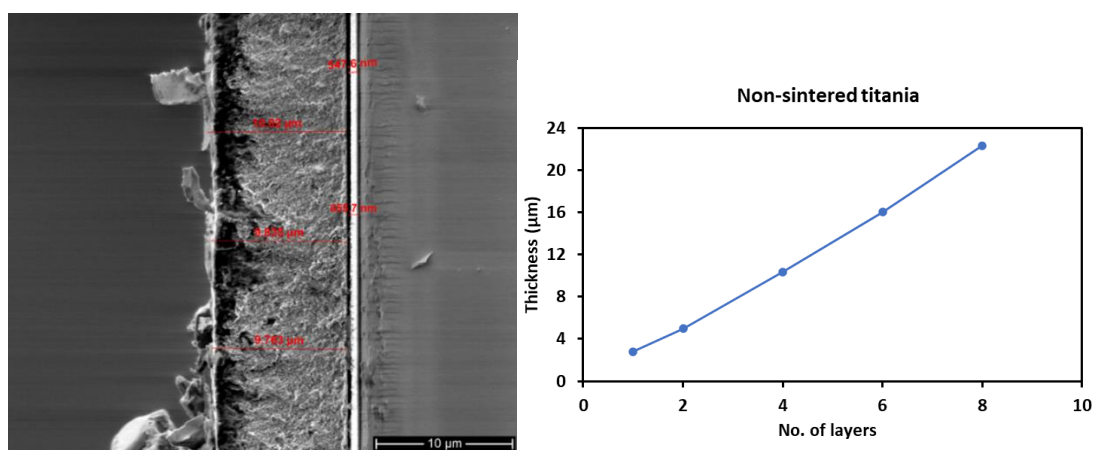


Figure 8.2: SEM image of the cross-section of 4 layered TiO_2 deposited on FTO (left) and the thickness of TiO_2 in μm as y-axis and number of layers deposited as x-axis (right).

In this study, the screen-printing method is the standard procedure selected for the deposition of TiO_2 . Hence, it is very important to have a good estimation of the thickness of TiO_2 as the function of the number of layers deposited. Hence, different layers of TiO_2 were deposited on the FTO, and the cross-section was analysed by SEM. From Figure 8.2 the number of layers needed to deposit on the FTO can be determined based on the desired thickness throughout the project.

XPS defect analysis:

To investigate the defect introduced by the X-ray source, the dye adsorbed sample was measured successively for 2 hrs. Figure 8.3 represents the variation in the relative ratio of different elements. The plots concludes that the relative intensity of different elements remained constant and hence prove XPS to be non-destructive technique.

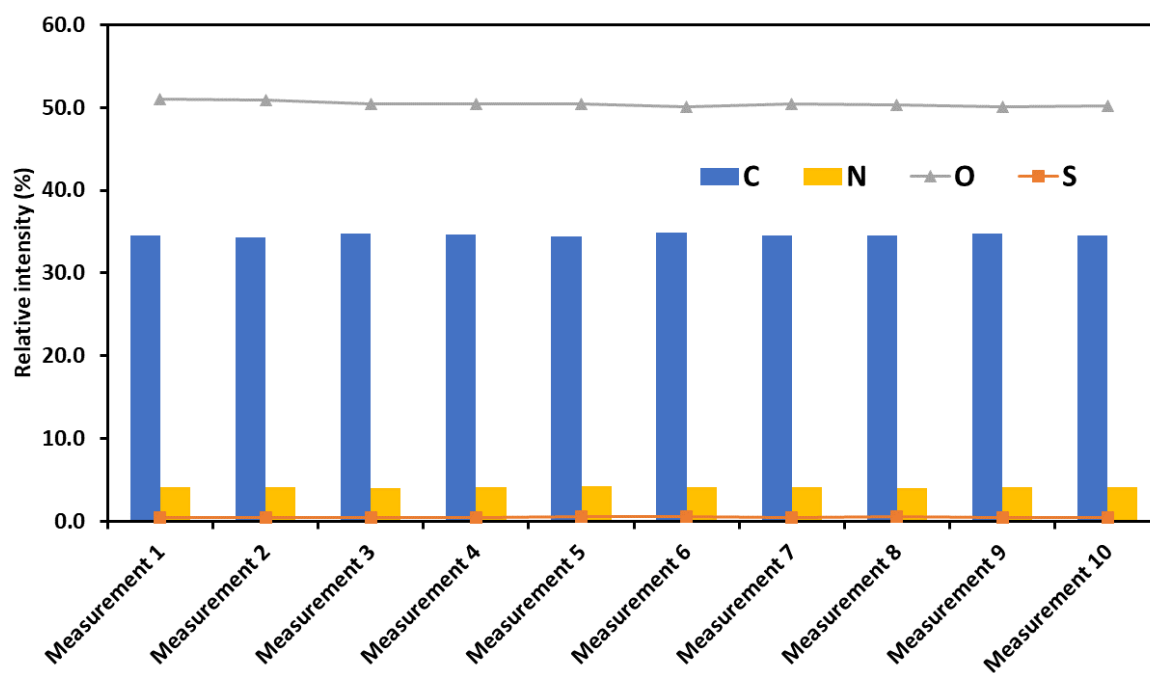


Figure 8.3: The XPS relative intensity of different elements on the dye adsorbed TiO_2 sample. The sample was successively measured with continuously X-ray exposure for 2 hrs.

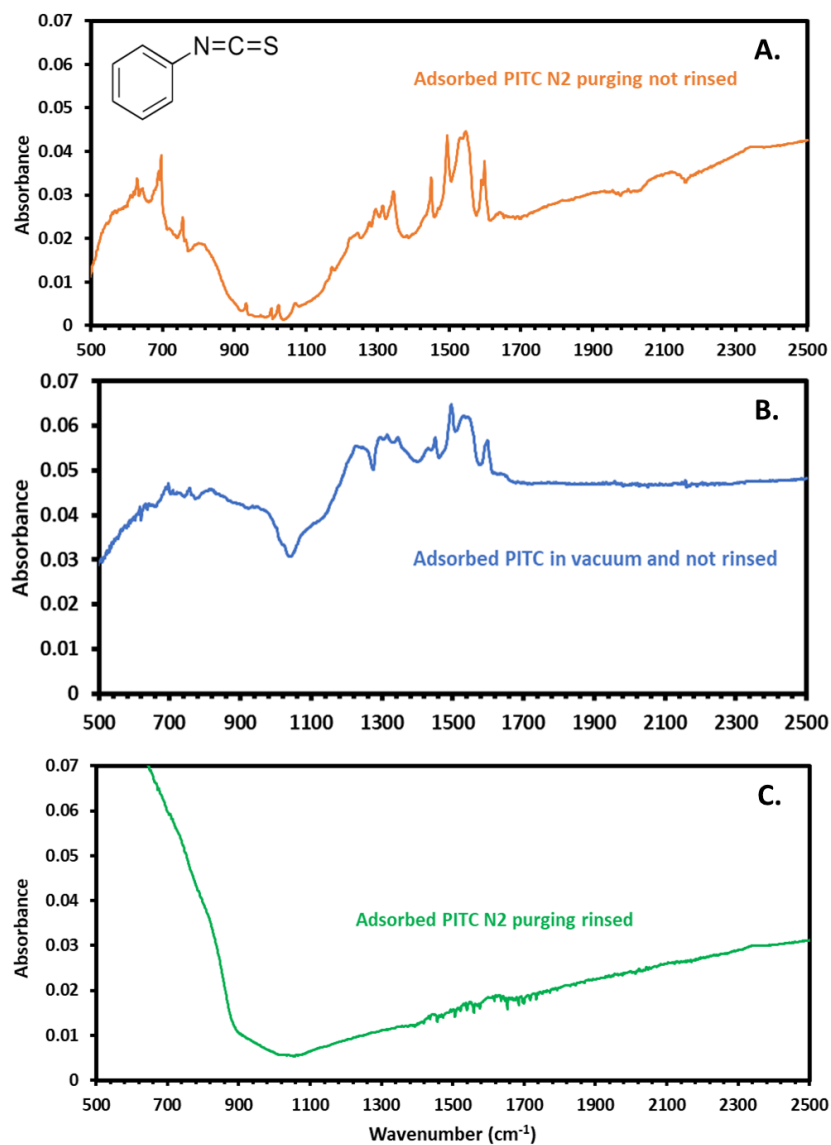
FTIR Phenyl isothiocyanate:

Figure 8.4: FTIR spectra of phenyl isothiocyanate adsorbed on TiO_2 (A.) without rinsing measured in N_2 purged environment (B.) in a vacuum without rinsing, and (C.) in N_2 purged environment with rinsing. The spectra have had the spectrum of blank TiO_2 subtracted.

Table 8.2: The IR spectrum assignments for liquid phenyl isothiocyanate and the adsorbed phenyl isothiocyanate on a TiO₂ substrate.

Liquid Wavenumber (cm⁻¹)	Adsorbed Wavenumber (cm⁻¹)	Assignments
1069	1074	C–H in-plane bending and C–C stretching
1157	1157	C–H in-plane bending and C–C stretching
1168	1173	C–N stretching or C–H in-plane bending
-	1202	C–N amine
-	1225	C–N amine
1283	1295	-
-	1316	C–N amine
-	1345	C–N amine
1395	-	-
-	1430	-
1473	-	-
1489	1496	C=C stretching vibration
-	1530	N–H amine bending
-	1545	N–H amine bending
1584	1590	C=C stretching
1590	1599	C=C stretching N–H bending
2030	-	C=N
2170	-	C=N
3024	3038	C–H stretching
3037	3046	C–H stretching
3062	3062	C–H stretching
3086	-	-
3094	-	C–H stretching
3175	Obscured	-
	3205	N–H stretching

TBA-adsorption

The spectrum for the adsorbed sample was obtained after subtracting the blank TiO_2 spectrum and presented in Figure 8.5. Interestingly, a small broad peak at region 1487 cm^{-1} upon adsorption was observed which could be related to the reduction in intensity of the 1454 cm^{-1} peak due to the CH_2 backbone interaction with the surface upon physisorption.

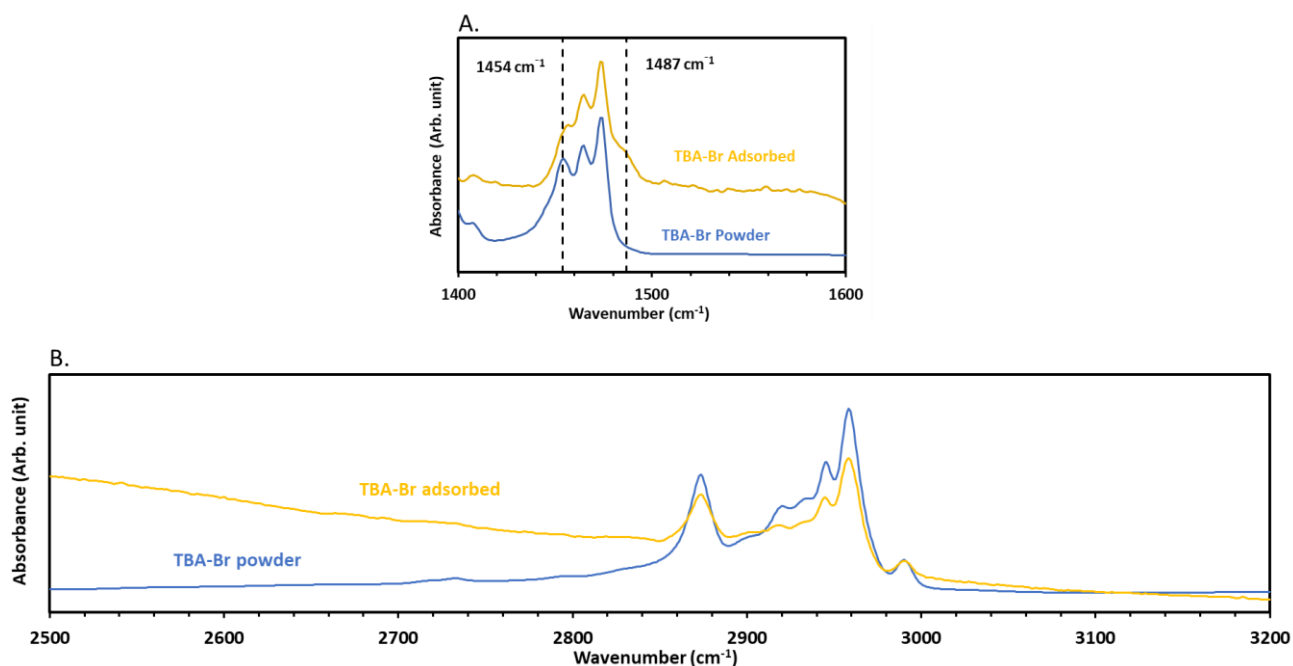


Figure 8.5:The IR spectrum of TBA-Br powder (blue) and 1 M TBA-Br adsorbed onto TiO_2 substrate measured under vacuum (A.) in region $1400\text{-}1550\text{ cm}^{-1}$ and (B.) in region $2500\text{-}3200\text{ cm}^{-1}$.

RF-sputtered TiO₂ and Mesoporous TiO₂ from XRD:

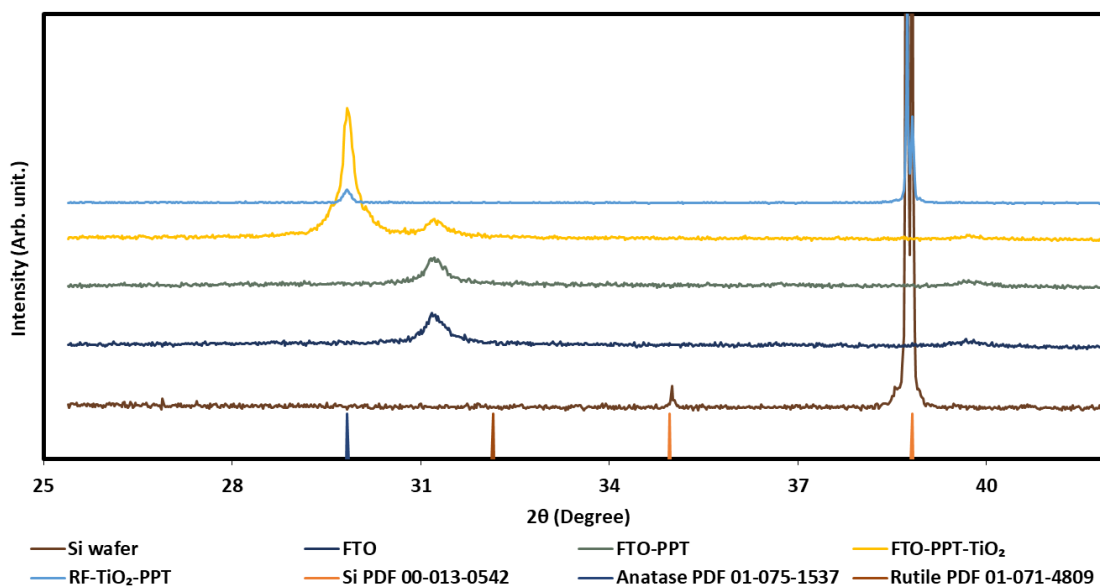


Figure 8.6: The XRD spectra of the mesoporous TiO₂ and RF-sputtered TiO₂ compared with the reference of Si wafer.

XRD was used to examine the crystal and phase structure of heated and TiCl₄-treated RF-sputtered TiO₂, blank FTO, TiCl₄-treated FTO, and Si. The XRD patterns were recorded using Bruker D8 Advance equipment with a Co-K ($\lambda = 1.789 \text{ \AA}$) irradiation source operating at 35 kV and 28 mA.

The RF-sputtered TiO₂ was heated in an oven at the temperature of 1000°C for 6 hrs. This procedure of heating RF-sputtered TiO₂ is expected to form an anatase phase on the RF-sputtered TiO₂ (1). In addition, the RF-sputtered TiO₂ was treated with 40 mM TiCl₄ solution to have a comparable substrate to the mesoporous TiO₂ used in the experiment. To confirm the crystallinity of mesoporous TiO₂ and RF-sputtered TiO₂ are the same, the sample was analysed using a Bruker D8 Advance XRD apparatus with Co-K α ($\lambda = 1.789 \text{ \AA}$) irradiation source under 35 kV and 28 mA operating condition. The spectra were recorded over the range of $2\theta = 20^\circ$ to 70° .

Figure 8.6 shows the XRD spectra of mesoporous TiO₂ and RF-sputtered TiO₂ with the Si and FTO substrates. It is obvious that both the samples have a peak at $\sim 29^\circ$ that represents the anatase phase of TiO₂. Note that the intensity of the anatase diffraction peak of RF-sputtered TiO₂ is low due to the low total amount of TiO₂ in the RF-sputtered TiO₂ film compared to mesoporous TiO₂. This is because the thickness of TiO₂ deposited on the RF-sputtered TiO₂ is $\sim 400 \text{ nm}$ (2) and the thickness of the 5-layered mesoporous TiO₂ is $\sim 13 \mu\text{m}$, Figure 8.2 refer to

the SEM analysis. The peaks positioned at $\sim 31^\circ$ and $\sim 38^\circ$ represent the FTO and Si, which are the substrates for the mesoporous TiO_2 and RF-sputtered TiO_2 respectively. The XRD result concludes that both substrates have the same crystallinity and hence, the samples are comparable.

ARXPS

The relative peak intensities for the elements of dye- TiO_2 are shown in Figure 8.7. The intensity of C is increasing with increasing angle of observation. The intensity of TiO_2 and oxygen are decreasing with increasing angle of observation. The amount of Ru and N is low on the sample itself and hence it does not show any meaningful change with the increasing emission angle. On the other hand, the amount of sulphur was observed to decrease with the emission angle.

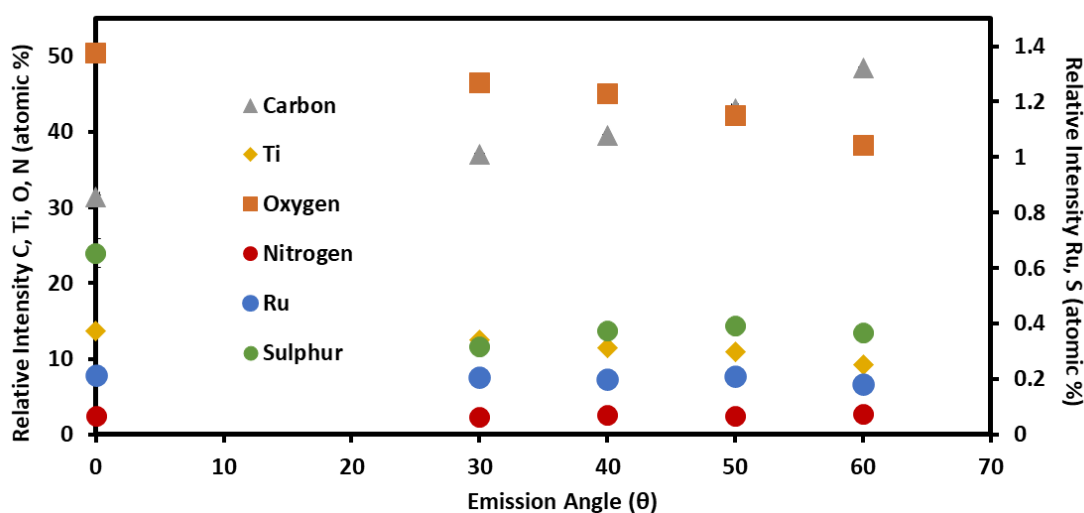


Figure 8.7: Illustration of the variation in the intensities of the elements on N719 adsorbed RF-sputtered TiO_2 substrate to the emission angles in ARXPS. The secondary axis represents the relative atomic intensity of Ru and S.

To investigate the TBA adsorption onto the TiO_2 , the relative intensities of the three different nitrogen species present in the dye as shown in Figure 8.8 are analysed. The intensities of the pyridine group (Npyd) and the NCS group are plotted on the primary y-axis and the TBA^+ intensity is plotted on the secondary y-axis. With increasing emission angle, the intensity of TBA^+ decreases and no TBA^+ is observed at 40° , 50° , and 60° . This observation suggests that TBA^+ is located deeper in the sample than NCS and the pyridine group. However, the low intensity of TBA^+ is the limitation of the ARXPS fitting procedure.

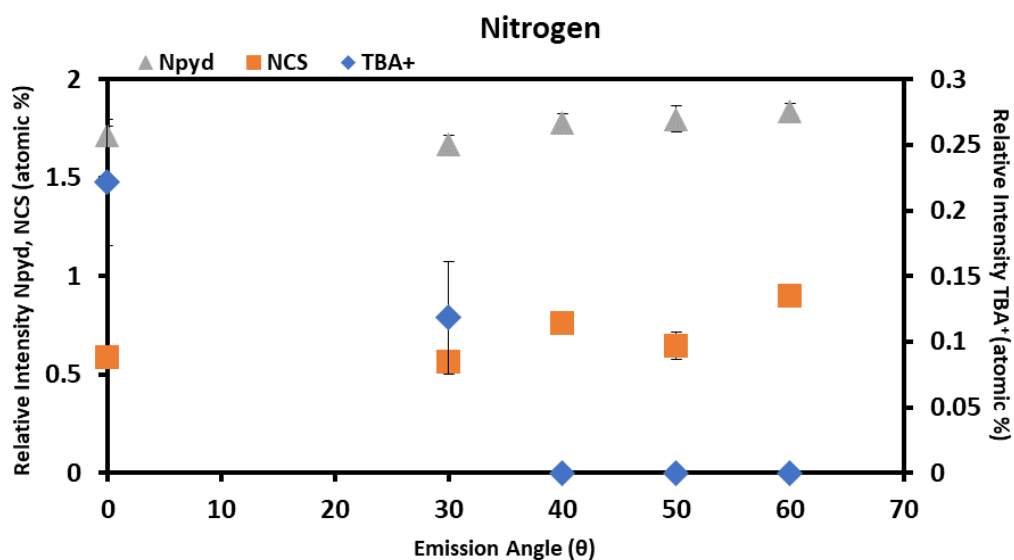


Figure 8.8: The relative intensity of three Nitrogen components, Npyd, NCS, and TBA⁺, for the emission angle in ARXPS. The intensity of TBA⁺ is extremely low, hence, for better data visualization TBA⁺ is plotted against the secondary axis.

XPS analysis for the re-sensitizing test for analysing the TBA⁺ adsorption**Table 8.3: The elemental ratios of the elements of the 1st, 5th, 10th, 15th, and 20th samples respectively re-sensitised in order.**

Elements	1 st	5 th	10 th	15 th	20 th
C-main	18.6± 0.1	19.4± 0.1	21.5± 0.2	17.6± 0.1	17.5± 0.2
C-O/C-N	8.7± 0.1	9.0± 0.1	8.4± 0.2	9.2± 0.1	9.0± 0.2
COO⁻ /COOH-C	2.4± 0.1	2.4± 0.1	2.3± 0.2	2.4± 0.1	2.4± 0.2
Ti	14.6± 0.1	14.3± 0.1	13.92± 0.03	14.80± 0.02	14.87± 0.04
O-main	39.9± 0.3	39.4± 0.1	37.8± 0.1	40.9± 0.1	41.0± 0.1
C=O/O⁻/Ti- OH	6.5± 1.7	6.3± 0.1	7.5± 0.1	6.7± 0.1	7.1± 0.1
COO⁻ /COOH-O	3.2± 3.4	2.3± 0.1	3.1± 0.1	2.4± 0.1	2.0± 0.1
Ru	0.39± 0.02	0.42± 0.03	0.36± 0.01	0.42± 0.01	0.378± 0.005
N_{pyd}	3.19± 0.02	3.19± 0.03	2.76± 0.05	3.1± 0.1	2.8± 0.1
NCS	0.7± 0.1	1.05± 0.03	0.67± 0.05	0.8± 0.1	0.8± 0.1
TBA⁺	0.3± 0.1	0.51± 0.03	0.39± 0.05	0.4± 0.1	0.4± 0.1
S-C-S/C=S	0.32± 0.01	0.54± 0.01	0.18± 0.01	0.30± 0.01	0.26± 0.01
S-S⁶⁺	0.22± 0.01	0.14± 0.01	0.26± 0.01	0.23± 0.01	0.22± 0.01
F	0.73± 0.02	1.00± 0.01	0.80± 0.01	0.92± 0.02	1.20± 0.02

Here, the presence of sulphur peaks at (168.82±0.020) eV suggests the S from NCS (thiocyanate ligand) undergoing partial oxidation and formation of SO₂ or SO₃ (3).

Table 8.4: The elemental peak positions of the 1st, 5th, 10th, 15th, and 20th samples respectively re-sensitised in order.

Elements	1st	5th	10th	15th	20th
C-main	285.0	285.0	285.0	285.0	285.0
C-O/C-N	286.2	286.1	286.2	286.2	286.2
COO⁻ /COOH-C	288.5	288.5	288.6	288.6	288.4
Ti	458.8	458.8	458.9	458.8	458.8
O-main	530.0	530.0	530.1	530.0	530.0
C=O/O⁻ /Ti-OH	531.2	531.2	531.3	531.3	531.3
COO⁻ /COOH-O	532.2	532.2	532.3	532.3	531.4
Ru	281.0	281.0	281.1	281.0	281.0
N_{pyd}	400.1	400.1	400.2	400.2	400.2
NCS	397.9	397.9	397.7	397.7	397.7
TBA⁺	402.3	402.3	402.4	402.3	402.3
S-C- S/C=S	162.4	162.3	162.3	162.3	162.4
S-S⁶⁺	168.5	168.5	168.6	168.5	168.6
F	684.0	684.0	684.1	684.1	684.0

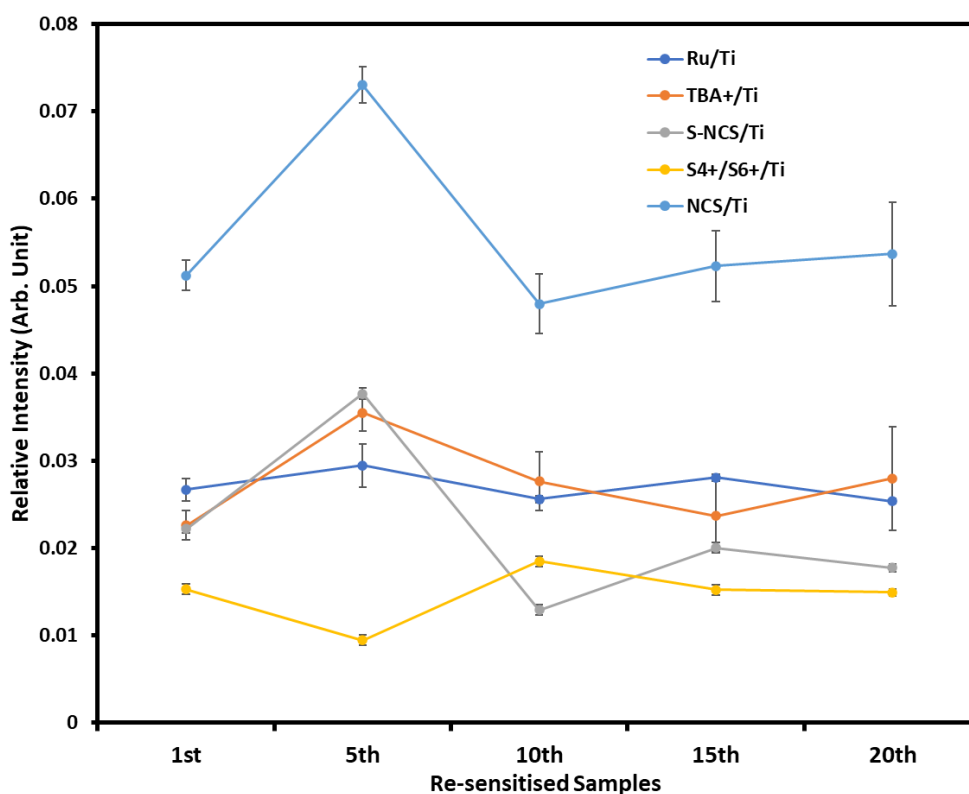


Figure 8.9: The XPS intensity ratio of individual dye elements with the substrate on multiple sensitised samples mentioned in the x-axis, respectively. The sample number on the x-axis indicates the number in the sequence of samples dipping into the dye solution.

Further, on comparing the adsorption of individual dye elements to the substrate ratio as shown in Figure 8.9. The adsorption of dye elements to TiO_2 does not show much deviation, suggesting a similar adsorption tendency of dye elements towards TiO_2 substrate and concludes that dilution has a nominal effect on dye adsorption.

Table 8.5: The elemental ratios of fresh dye and the re-sensitised dye solutions drop-cast on TiO₂ substrate and analysed with XPS.

Elements	Fresh Dye	Re-sensitised Dye
C-C	18.0 ± 0.1	11.8 ± 0.1
C-O/C-N	7.5 ± 0.1	3.2 ± 0.1
COO⁻/COOH-C	1.4 ± 0.1	1.0 ± 0.1
Ti	16.24 ± 0.03	19.80 ± 0.01
O-main	41.0 ± 0.1	46.8 ± 0.2
C=O/O⁻/Ti-OH	6.4 ± 0.1	10.3 ± 0.2
COO⁻/COOH-O	4.0 ± 0.1	3.6 ± 0.2
Ru	0.270 ± 0.004	0.051 ± 0.004
N_{pyd}	2.2 ± 0.1	0.88 ± 0.01
NCS	0.7 ± 0.1	0.23 ± 0.01
TBA⁺	0.5 ± 0.1	0.07 ± 0.01
S-C-S/C=S	0.464 ± 0.002	0.018 ± 0.002
S-S⁶⁺	0.030 ± 0.002	0.040 ± 0.002
F	1.16 ± 0.01	2.24 ± 0.01

The re-sensitised dye solution was drop-cast on blank TiO₂ and a reference sample was prepared by drop-casting the fresh dye solution on blank TiO₂. to understand the residue of dye elements before and after multiple sensitizing Both samples were further investigated with XPS. It can be seen in Table 8.3 that the relative intensity of dye elements Ru, TBA⁺, and S components quantitatively decrease to the same degree through re-sensitizing. The reduction in the number of dye elements in the dye solution due to multiple adsorptions, suggests the active involvement of all these dye components in dye adsorption.

To investigate further if the TBA⁺ adsorbs onto the TiO₂ substrate with the same degree as other dye components, the intensity ratio of Ru/TBA⁺ for the fresh dye (before) and the re-sensitised dye solution (after) was compared and is shown in Figure 8.10.

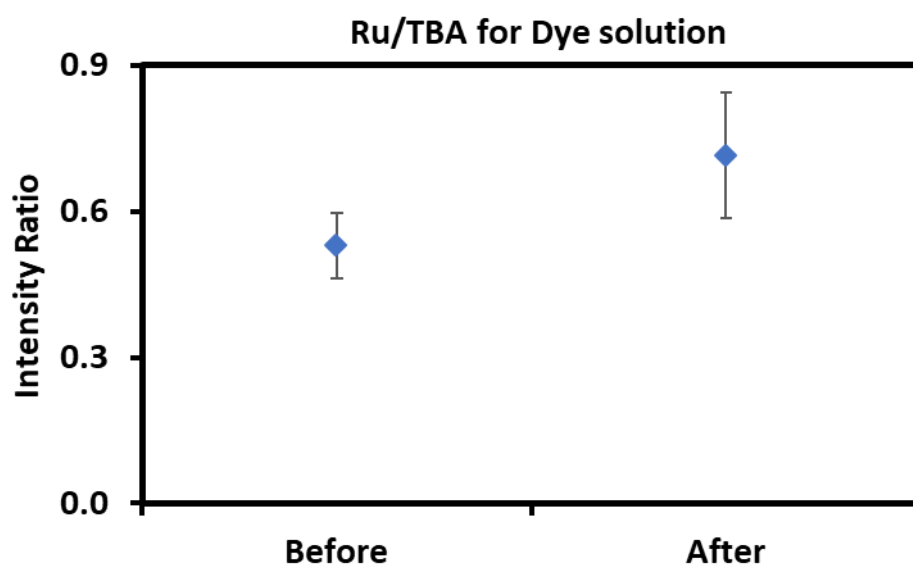


Figure 8.10: The intensity ratio of Ru/TBA^+ of the dye solution drop cast onto the TiO_2 substrate for the fresh dye (before sensitisation) and re-sensitised dye (after multiple sensitisations).

8.2.1. References

1. Alotabi AS, Gibson CT, Metha GF, Andersson GG. Investigation of the Diffusion of Cr₂O₃ into different phases of TiO₂ upon Annealing. *ACS Applied Energy Materials*. 2021;4(1):322-30.
2. Alotabi AS, Yin Y, Redaa A, Tesana S, Metha GF, Andersson GG. Effect of TiO₂ Film Thickness on the Stability of Au₉ Clusters with a CrO_x Layer. *Nanomaterials*. 2022;12(18):3218.
3. Lee KE, Gomez MA, Regier T, Hu Y, Demopoulos GP. Further understanding of the electronic interactions between N719 sensitizer and anatase TiO₂ films: a combined X-ray absorption and X-ray photoelectron spectroscopic study. *The Journal of Physical Chemistry C*. 2011;115(13):5692-707.

8.3 Chapter 5. Exploring Alteration in Electrochemical Interface of Dye Sensitised Solar Cells-An Experimental Set-up for Ageing Investigation

XPS analysis for the blank TiO₂ substrate before and after ethanol rinsing

Table 8.6: The change in the elemental composition of the dye-titania substrate measured before and after ethanol rinsing. The reading displays an average of four photoanodes with the standard error calculated.

	Before	After	Difference
C-C	18.5 ± 0.4	18.9 ± 2.3	0.3
C-COOH	2.8 ± 0.2	2.8 ± 0.5	0.0
C-N	9.6 ± 0.6	10.1 ± 1.0	0.5
Ru	0.6 ± 0.0	0.5 ± 0.0	0.0
O 1s	38.8 ± 0.5	38.2 ± 1.6	-0.6
C=O	6.7 ± 0.2	7.0 ± 0.4	0.4
O-COOH	2.0 ± 0.1	2.5 ± 0.1	0.5
Ti	14.0 ± 0.2	13.5 ± 0.4	-0.5
F	1.1 ± 0.1	1.3 ± 0.1	0.2
S1	0.9 ± 0.0	0.6 ± 0.1	-0.3
S2	0.1 ± 0.0	0.2 ± 0.1	0.2
Npyd	3.2 ± 0.1	3.2 ± 0.2	0.0
NCS	1.3 ± 0.1	1.0 ± 0.1	-0.4
TBA ⁺	0.5 ± 0.0	0.3 ± 0.0	-0.2

Table 8.7: The change in the elemental composition of the TiO₂ substrate measured before and after ethanol rinsing. The reading displays an average of three photoanodes with the standard error calculated.

	Peak position	Before	After	Difference
C-C	285.0 \pm 0.2	26.1 \pm 5.9	29 \pm 16.0	2.9
C-N	286.2 \pm 0.2	12.2 \pm 9.6	11.1 \pm 16.0	-1.1
C-COOH	288.6 \pm 0.2	2.9 \pm 1.3	1.7 \pm 1.0	-1.2
O 1s	529.6 \pm 0.2	31.1 \pm 3.7	33.2 \pm 15.1	2.2
C=O	531.7 \pm 0.2	10.6 \pm 1	9.2 \pm 1	-1.3
O-COOH	533.8 \pm 0.2	6.3 \pm 4.3	4.0 \pm 2.4	-2.3
Ti	458.3 \pm 0.2	8.1 \pm 1.4	8.9 \pm 4.3	0.8
F	683.9 \pm 0.2	0.4 \pm 0.1	0.7 \pm 0.5	0.3
S2	168.2 \pm 0.2	0.2 \pm 0.1	0.2 \pm 0.1	0.2
N-1	400.0 \pm 0.2	0.4 \pm 0.1	0.6 \pm 0.2	0.1
N-2	397.9 \pm 0.2	0.7 \pm 0.5	0.5 \pm 0.2	-0.2

Device level analysis of DSSCs

To investigate the degradation in cell performance, 70 sample cells were prepared. All the cells were exposed to the sun-test equipment. In ageing investigations, it is critical to keep track of the decrease in device performance over time. The cell functioning was traced through JV analysis to track the change in the PV parameter with time under light ageing.

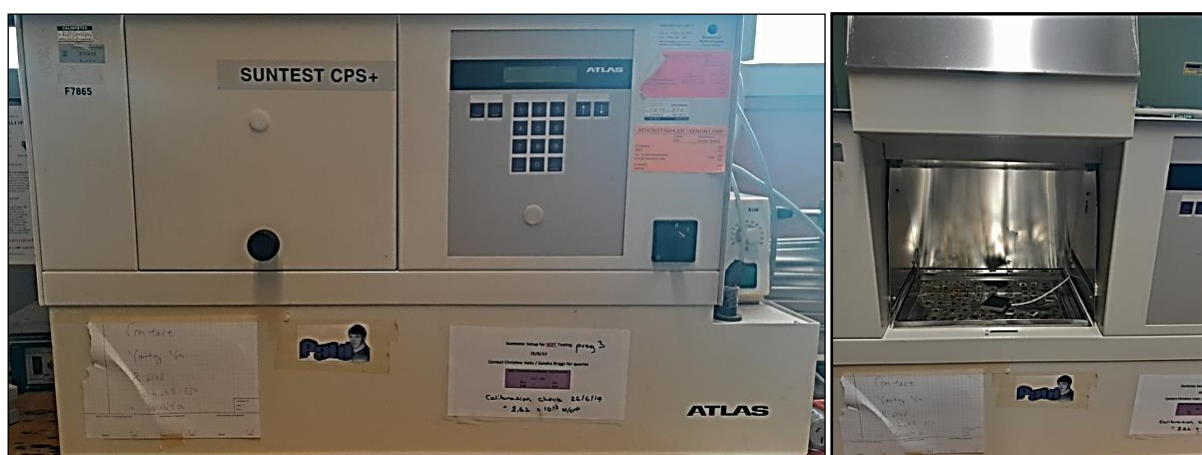


Figure 8.11: The CPS⁺ sun-test equipment used for accelerated ageing in DSSCs (left) and sample loaded on the loading compartment (right).

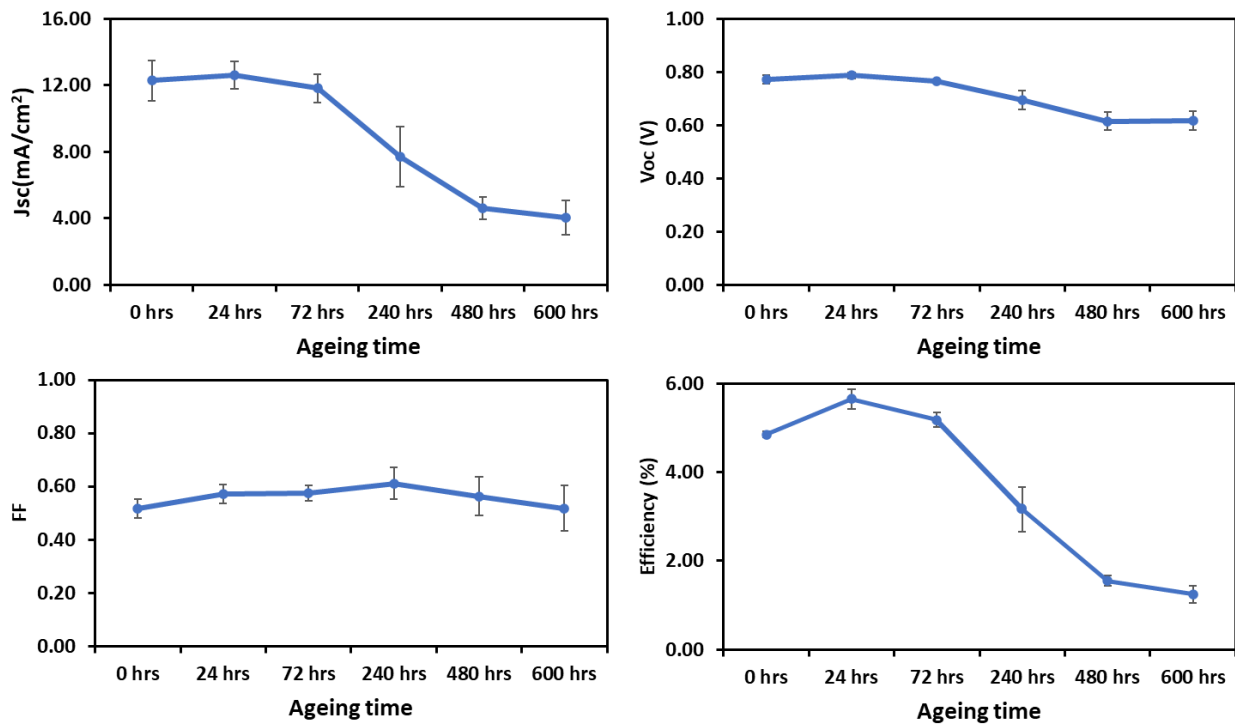


Figure 8.12: The fundamental PV parameters, namely, Jsc, Voc, FF, and efficiency for the sample cells aged in light for the mentioned time in hrs. The parameters are an average of 10 samples.

Table 8.8: The summary of PV performance of the cell aged under light. Average values and standard deviations of 10 cells along with the parameters of the best cells are highlighted in bold.

	Jsc (mA/cm ²)	Voc (V)	FF	η (%)
0 hrs	13.3, 12.3 \pm 1.2	0.8, 0.8 \pm 0.0	0.5, 0.5 \pm 0.0	5.0, 4.9 \pm 0.1
24 hrs	12.7, 12.6 \pm 0.8	0.8, 0.8 \pm 0.0	0.6, 0.6 \pm 0.0	6.1, 5.7 \pm 0.2
72 hrs	12.4, 11.8 \pm 0.9	0.8, 0.8 \pm 0.0	0.6, 0.6 \pm 0.0	5.4, 5.2 \pm 0.2
240 hrs	9.8, 7.7 \pm 1.8	0.7, 0.7 \pm 0.0	0.6, 0.6 \pm 0.1	3.9, 3.2 \pm 0.5
480 hrs	4.7, 4.6 \pm 0.7	0.6, 0.6 \pm 0.0	0.6, 0.6 \pm 0.1	1.7, 1.6 \pm 0.1
600 hrs	4.9, 4.1 \pm 1.0	0.6, 0.6 \pm 0.0	0.5, 0.5 \pm 0.1	1.6, 1.3 \pm 0.2

XPS analysis

Table 8.9: The change in the elemental composition of the dye-TiO₂-electrolyte interface measured for 0 hrs and 600 hrs aged photoanode in light. The reading displays an average of three photoanodes with the standard error calculated.

Elements	0 hrs	600 hrs
C-C	22.4±4.2	27.1±2.8
C-COOH	3.9±0.2	3.7±0.0
C-N	15.4±2.2	9.1±0.8
Ru	0.2±0.0	0.1±0.0
O 1s	26.2±5.4	33.8±2.7
C=O	13.2±6.0	9.0±0.5
O-COOH	3.1±0.8	2.6±0.2
Ti	9.2±0.7	9.1±0.7
F	1.1±0.2	0.7±0.0
S-1	0.4±0.1	0.1±0.0
S-2	0.2±0.0	0.1±0.0
Npyd	2.6±0.0	1.8±0.1
NCS	1.0±0.1	0.6±0.2
TBA⁺	1.1±0.1	1.2±0.3
I⁻	0.1±0.0	0.7±0.1
I₃⁻	0.0±0.0	0.1±0.0
higher oxidised I-species	0.0±0.0	0.0±0.0

Table 8.10: The peak position in eV for different elemental species of the dye-TiO₂-electrolyte interface measured for 0 hrs and 600 hrs aged photoanodes in light. The reading displays an average of three photoanodes with uncertainty of ± 0.2 .

Elements	0 hrs	600 hrs
C-C	285.0 \pm 0.2	285.0 \pm 0.2
C-COOH	288.7 \pm 0.2	288.6 \pm 0.2
C-N	286.2 \pm 0.2	286.3 \pm 0.2
Ru	281.1 \pm 0.2	280.9 \pm 0.2
O 1s	529.7 \pm 0.2	529.8 \pm 0.2
C=O	531.4 \pm 0.2	531.6 \pm 0.2
O-COOH	533.1 \pm 0.2	532.8 \pm 0.2
Ti	458.8 \pm 0.2	458.6 \pm 0.2
F	684.3 \pm 0.2	684.2 \pm 0.2
S-1	162.2 \pm 0.2	162.5 \pm 0.2
S-2	168.2 \pm 0.2	168.5 \pm 0.2
Npyd	399.9 \pm 0.2	399.9 \pm 0.2
NCS	397.8 \pm 0.2	397.6 \pm 0.2
TBA⁺	401.7 \pm 0.2	401.6 \pm 0.2
I⁻	618.6 \pm 0.2	618.7 \pm 0.2
I₃⁻	621.0 \pm 0.2	621.1 \pm 0.2
higher oxidised I-species	623.2 \pm 0.2	622.4 \pm 0.2

Table 8.11: The elemental ratio obtained from XPS analysis of drop-cast substrates after rinsing off the aged cells. The drop-cast samples were prepared by drop-casting the rinsed-off solution onto a blank TiO₂ substrate.

Elements	0 hrs	600 hrs
C-C	16.3±3.4	18.4±2.7
C-COOH	1.8±0.3	2.2±0.2
C-N	5.4±1.5	7.3±0.9
Ru 3d 5/2	0.0±0.0	0.0±0.0
O 1s	44.5±3.2	45.9±0.9
C=O	9.8±2.9	6.5±1.2
O-COOH	3.9±0.2	3.0±0.8
Ti	14.9±1.1	13.7±0.8
F	2.2±0.4	1.8±0.3
S-1	0.0±0.0	0.0±0.0
S-2	0.1±0.0	0.0±0.0
Npyd	0.7±0.1	0.5±0.1
NCS	0.1±0.0	0.1±0.0
TBA⁺	0.4±0.1	0.4±0.1
I⁻	0.2±0.0	0.1±0.0
I₃⁻	0.0±0.0	0.0±0.0

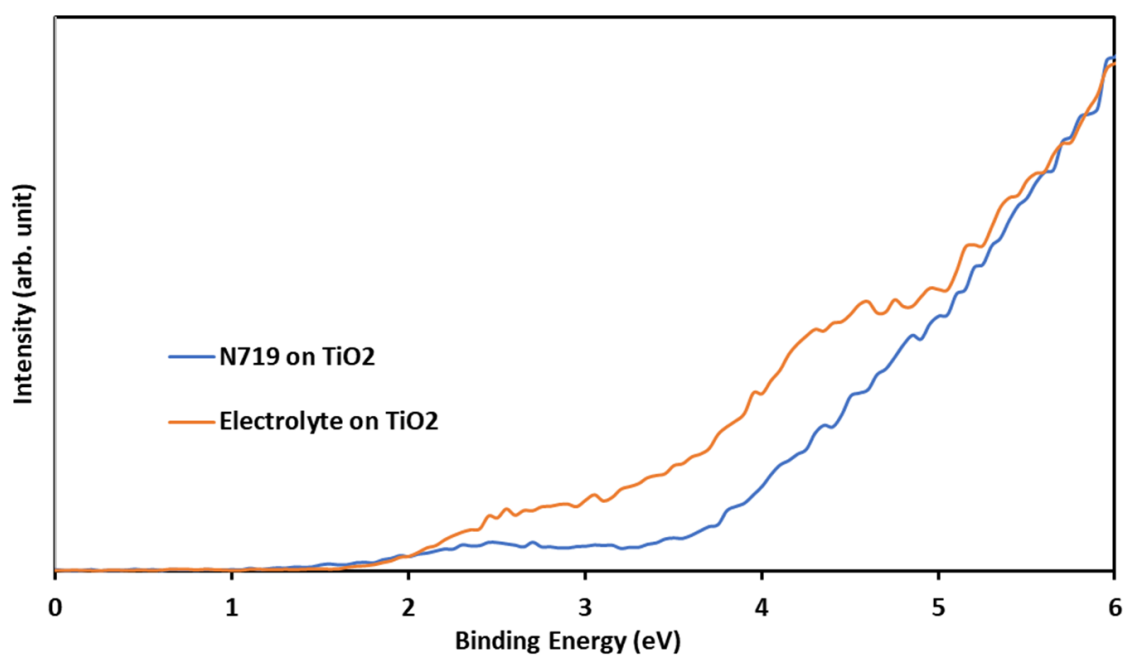
UPS analysis for reference samples

Figure 8.13: The UP spectra for the dye adsorbed onto TiO_2 (blue) and electrolyte adsorbed onto TiO_2 (orange).

8.4 Chapter 6. Unveiling the Ageing Effect at the Interface of N719 Dye Sensitised Solar Cells

JV characterisation curve for high-performing cells in both dark and light-aged samples

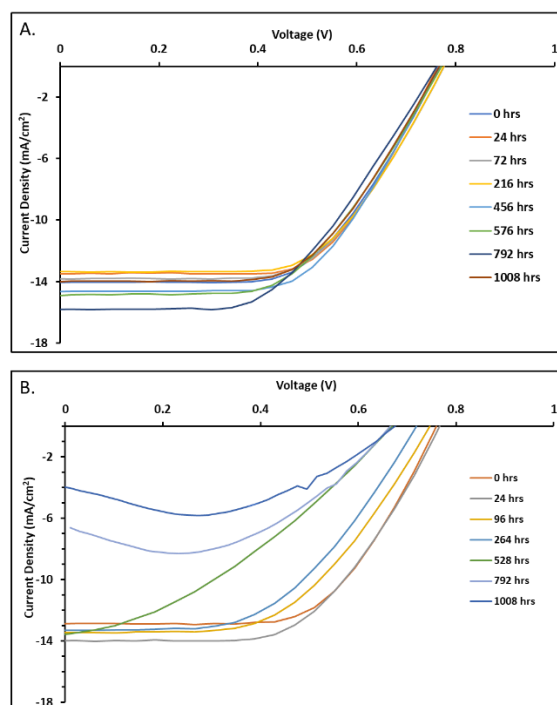


Figure 8.14: The JV characteristics of the best-performing sample cells aged in dark (A.) and under light (B.) conditions.

Nyquist plot for high performing samples cells aged in dark and light

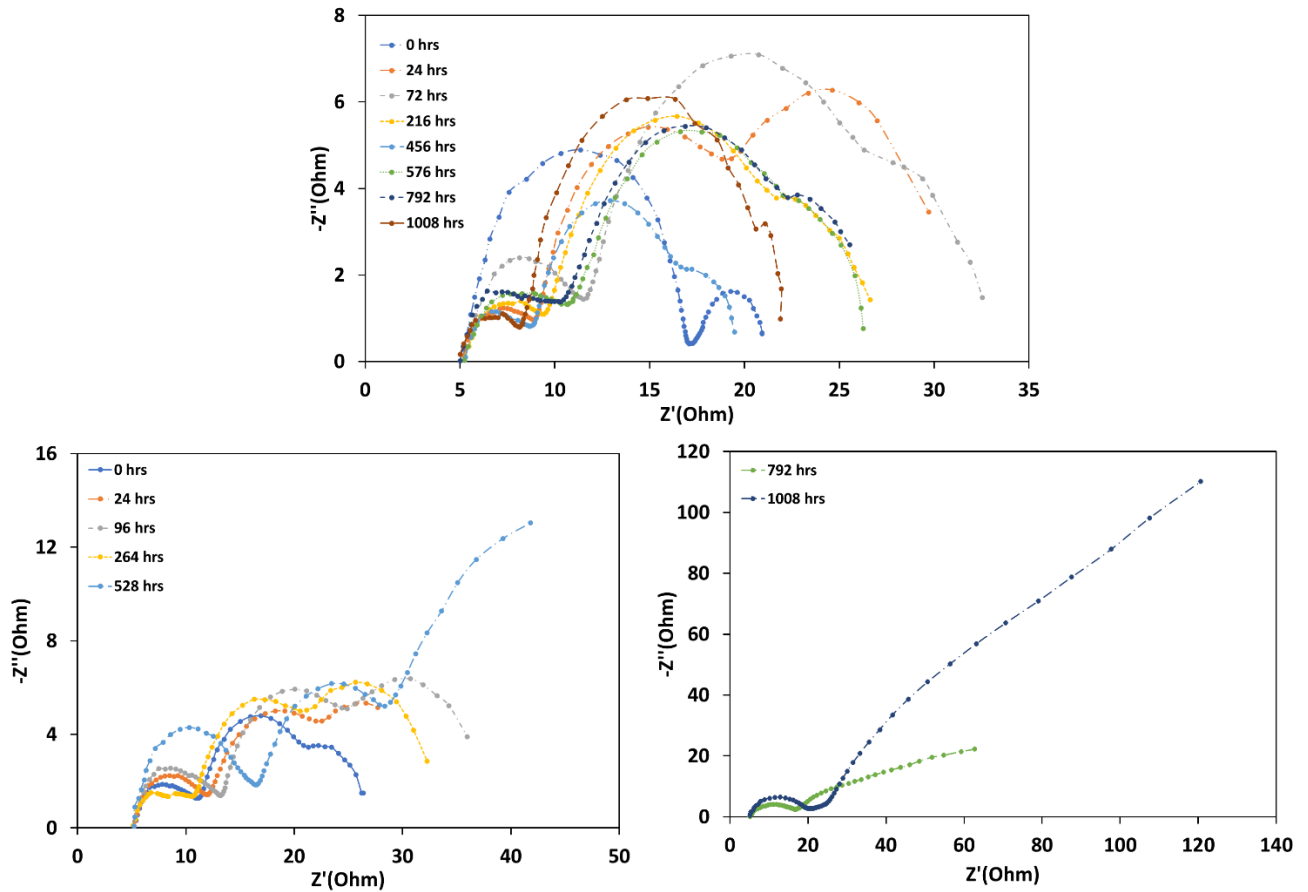


Figure 8.15: The Nyquist plot of the samples aged in dark (top) and light (bottom) with respective aged time. The bottom right represents the Nyquist plot for two samples, 792 hr and 1008 hr, and the rest are included in the bottom right.

The XPS intensity variation in the elemental ratio of the photoanode for the sample cells aged in dark and light

Table 8.12: The change in the elemental composition of the dye-TiO₂-electrolyte interface measured for different aged photoanode samples in the dark. The reading displays an average of three photoanodes with the standard error calculated.

	0 hr	24 hr	72 hr	216 hr	456 hr	576 hr	792 hr	1008 hr
C-C	21.9±0.6	18.7±1.3	19.2±0.9	22.9±1.5	26.6±2.4	24.0±2.9	24.8±2.0	31.2±4.6
C-COOH	5.0±0.4	4.4±0.5	4.8±0.4	4.8±0.2	4.9±0.8	4.1±0.1	6.3±2.4	5.5±1.5
C-N	10.1±0.3	8.9±0.8	9.2±0.4	10.3±1.3	14.3±1.7	11.5±2.2	10.7±2.5	14.9±2.6
Ru	0.24±0.01	0.21±0.03	0.27±0.03	0.24±0.02	0.17±0.01	0.18±0.02	0.21±0.01	0.12±0.03
O 1s	35.6±0.9	38.2±1.0	37.1±0.5	35.2±1.8	29.7±3.7	33.6±4.3	33.1±1.7	25.3±5.6
C=O	7.3±0.3	7.2±0.1	7.2±0.2	6.8±0.5	7.2±0.1	7.5±0.5	6.9±0.7	6.6±0.7
O-COOH	3.0±0.5	4.1±0.4	3.9±0.4	2.8±0.3	2.8±0.8	3.0±0.5	2.8±0.2	3.7±0.5
Ti	10.4±0.1	11.5±0.5	11.1±0.2	10.0±0.5	8.0±1.4	9.1±1.7	9.3±0.5	6.7±1.5
F	1.0±0.2	1.3±0.1	1.2±0.1	1.0±0.0	1.0±0.2	0.9±0.2	0.9±0.1	0.7±0.3
S1-from SCN ⁻	0.20±0.04	0.26±0.04	0.27±0.03	0.34±0.03	0.19±0.01	0.17±0.05	0.19±0.01	0.19±0.05
S2-oxidised S	0.30±0.01	0.28±0.04	0.28±0.04	0.24±0.04	0.26±0.05	0.29±0.06	0.27±0.02	0.22±0.06
S3-TiOS	0.033±0.002	0.024±0.005	0.031±0.001	0.024±0.005	0.052±0.018	0.047±0.009	0.03±0.01	0.059±0.005
Npyd	2.7±0.1	2.4±0.2	2.9±0.3	2.8±0.1	2.8±0.3	3.1±0.5	2.6±0.2	2.8±0.3
SCN ⁻	0.85±0.03	0.8±0.1	1.0±0.1	0.9±0.1	0.9±0.1	1.3±0.6	0.80±0.03	0.7±0.1
TBA ⁺	1.1±0.1	1.4±0.1	1.3±0.1	1.4±0.2	0.9±0.1	1.0±0.1	1.0±0.1	1.0±0.2
I ⁻	0.11±0.03	0.18±0.07	0.07±0.02	0.21±0.13	0.16±0.09	0.16±0.12	0.07±0.02	0.21±0.09
I ₃ ⁻	0.029±0.003	0.033±0.006	0.021±0.003	0.031±0.009	0.025±0.007	0.031±0.013	0.021±0.003	0.047±0.012
Higher oxidised I-species	0.013±0.001	0.015±0.003	0.010±0.001	0.015±0.005	0.012±0.006	0.010±0.001	0.009±0.001	0.010±0.001

Table 8.13: The change in the elemental composition of the dye-TiO₂-electrolyte interface measured for different aged photoanode samples in light. The reading displays an average of three photoanodes with the standard error calculated.

	0 hrs	24 hrs	96 hrs	264 hrs	792 hrs	1008 hrs
C-C	27.6±1.5	26.5±0.9	25.9±0.2	27.9±1.1	27.6±0.5	30.1±4.9
C-COOH	3.2±0.1	3.3±0.1	3.7±0.1	3.7±0.0	3.4±0.1	3.4±0.1
C-N	12.0±0.2	10.7±0.4	10.9±0.9	11.7±0.7	13.5±1.7	15.7±2.3
Ru	0.19±0.01	0.16±0.01	0.19±0.01	0.22±0.01	0.21±0.01	0.21±0.05
O 1s	31.8±1.0	33.9±0.9	33.8±0.7	31.8±0.3	30.8±0.8	26.9±5.4
C=O	8.2±0.3	8.2±0.5	8.2±0.3	8.3±0.3	7.8±0.0	7.3±0.4
O-COOH	2.6±0.1	2.3±0.1	2.4±0.2	2.2±0.1	2.5±0.2	3.0±0.5
Ti	8.4±0.3	9.2±0.3	9.1±0.2	8.3±0.2	8.2±0.2	7.2±1.7
F	0.9±0.2	1.1±0.2	1.1±0.1	1.0±0.0	1.1±0.2	0.8±0.2
S1-from SCN ⁻	0.17±0.01	0.10±0.04	0.12±0.01	0.05±0.01	0.12±0.02	0.21±0.03
S2-oxidised S	0.26±0.02	0.29±0.03	0.23±0.01	0.24±0.01	0.20±0.01	0.2±0.04
S3-TiOS	0.08±0.01	0.07±0.00	0.08±0.02	0.07±0.01	0.06±0.01	0.04±0.02
Npyd	2.5±0.1	2.1±0.1	2.4±0.1	2.7±0.2	2.7±0.1	2.9±0.3
SCN ⁻	0.8±0.2	0.6±0.1	0.5±0.1	0.5±0.1	0.5±0.2	0.8±0.2
TBA ⁺	1.1±0.1	1.2±0.3	1.1±0.0	0.9±0.0	0.8±0.1	0.9±0.2
I ⁻	0.13±0.04	0.22±0.17	0.18±0.02	0.22±0.04	0.31±0.03	0.43±0.09
I ₃ ⁻	0.035±0.005	0.04±0.01	0.101±0.009	0.105±0.016	0.12±0.01	0.039±0.016
Higher oxidised I-species	0.008±0.001	0.013±0.002	0.011±0.002	0.007±0.001	0.006±0.002	0.014±0.007

NICISS characterisation of Ru and I in aged samples

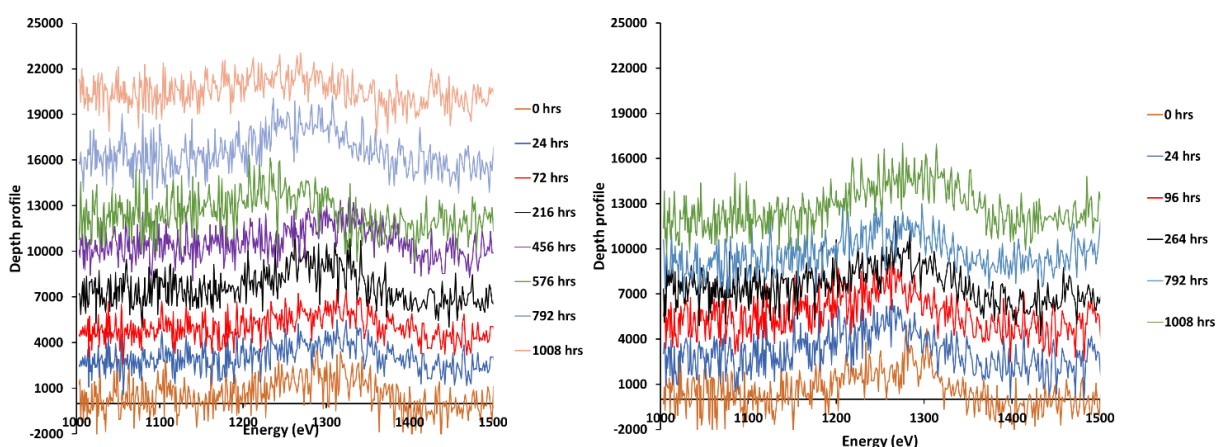


Figure 8.16: NICIS spectra for the presence of Ru on the dark (left), and light (right) aged sample through the ageing period.

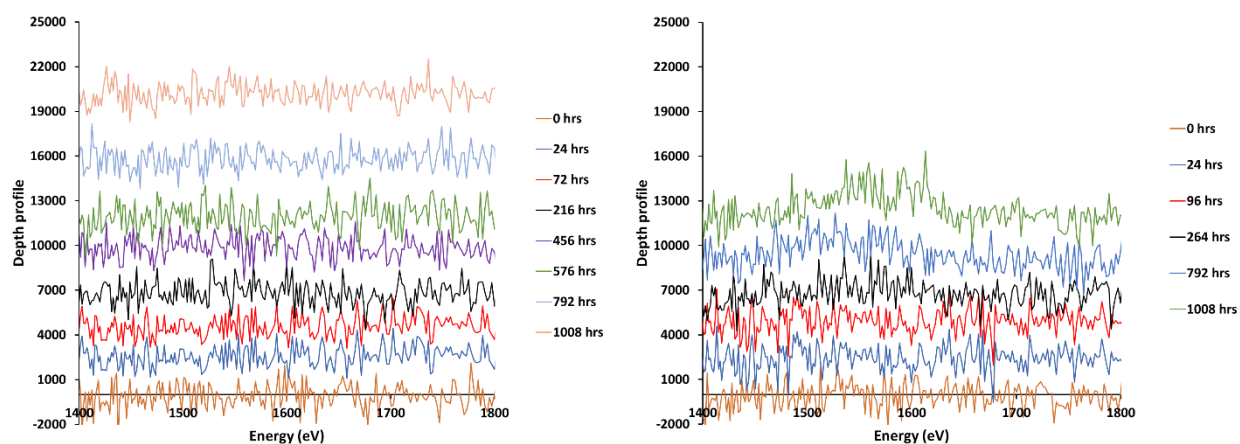


Figure 8.17: NICIS spectra for the presence of I on the dark (left), and light (right) aged sample through the ageing period.

FTIR spectral analysis of N719 dye, electrolyte and electrolyte solvent adsorbed onto TiO₂ substrate

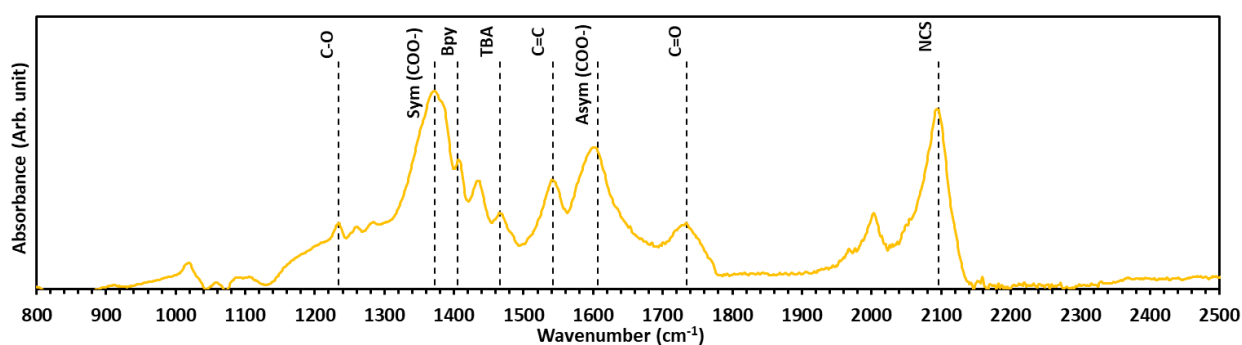


Figure 8.18: FTIR spectra of N719 solution adsorbed on TiO₂ substrate subtracted from blank TiO₂.

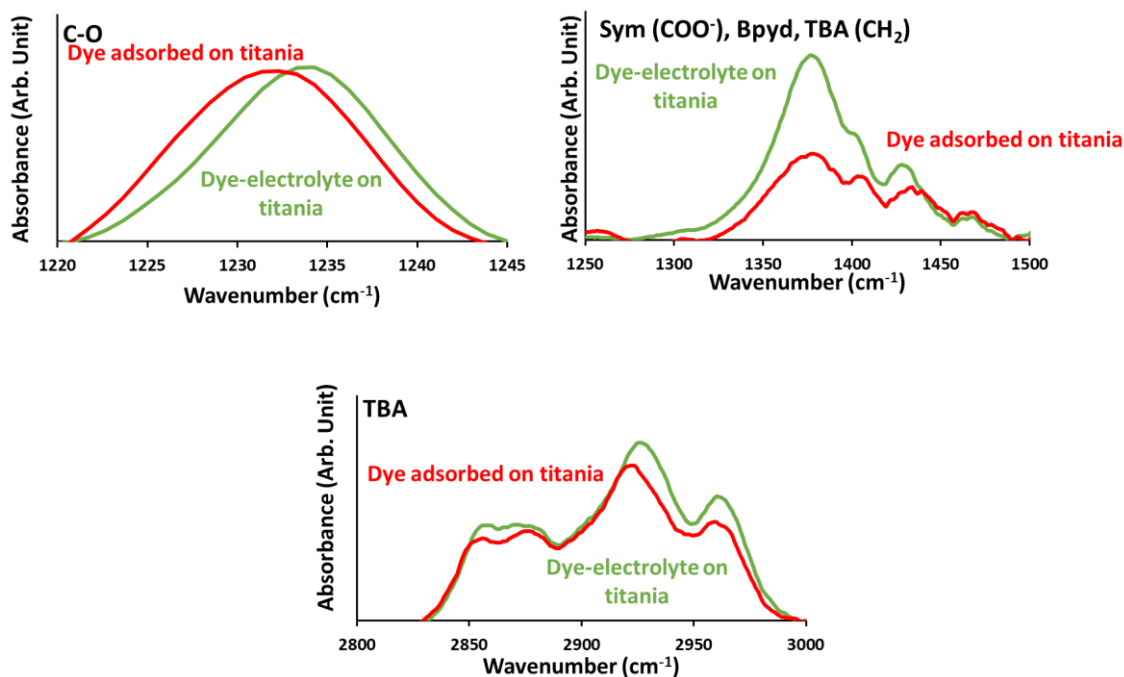


Figure 8.19: IR spectra for different functional groups representing the adsorbed dye molecule onto TiO_2 substrate for dye adsorbed sample and dye-electrolyte sample.

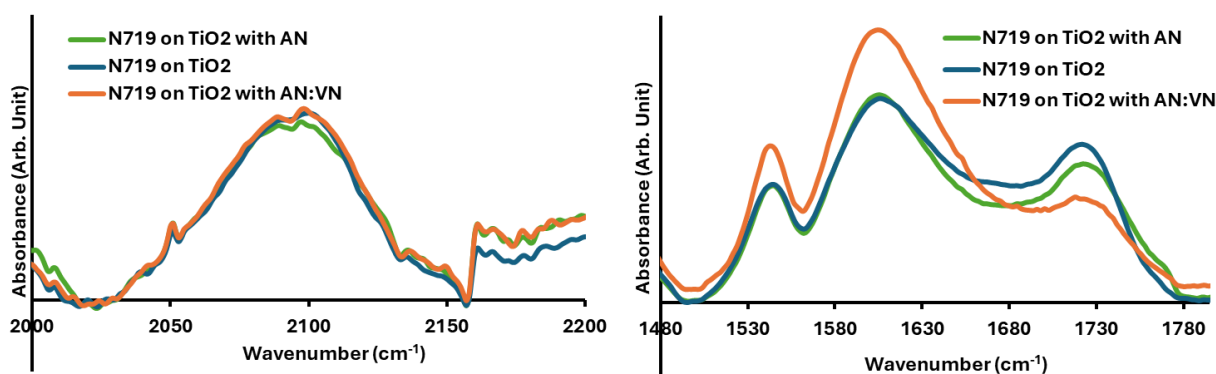


Figure 8.20: IR spectra for reference N719 adsorbed onto TiO_2 and N719 adsorbed onto TiO_2 further adsorbed into AN and AN:VN solvents. The figure on the left represents the IR for the SCN^- group and the right represents the $\text{C}=\text{O}$ at 1725 cm^{-1} .

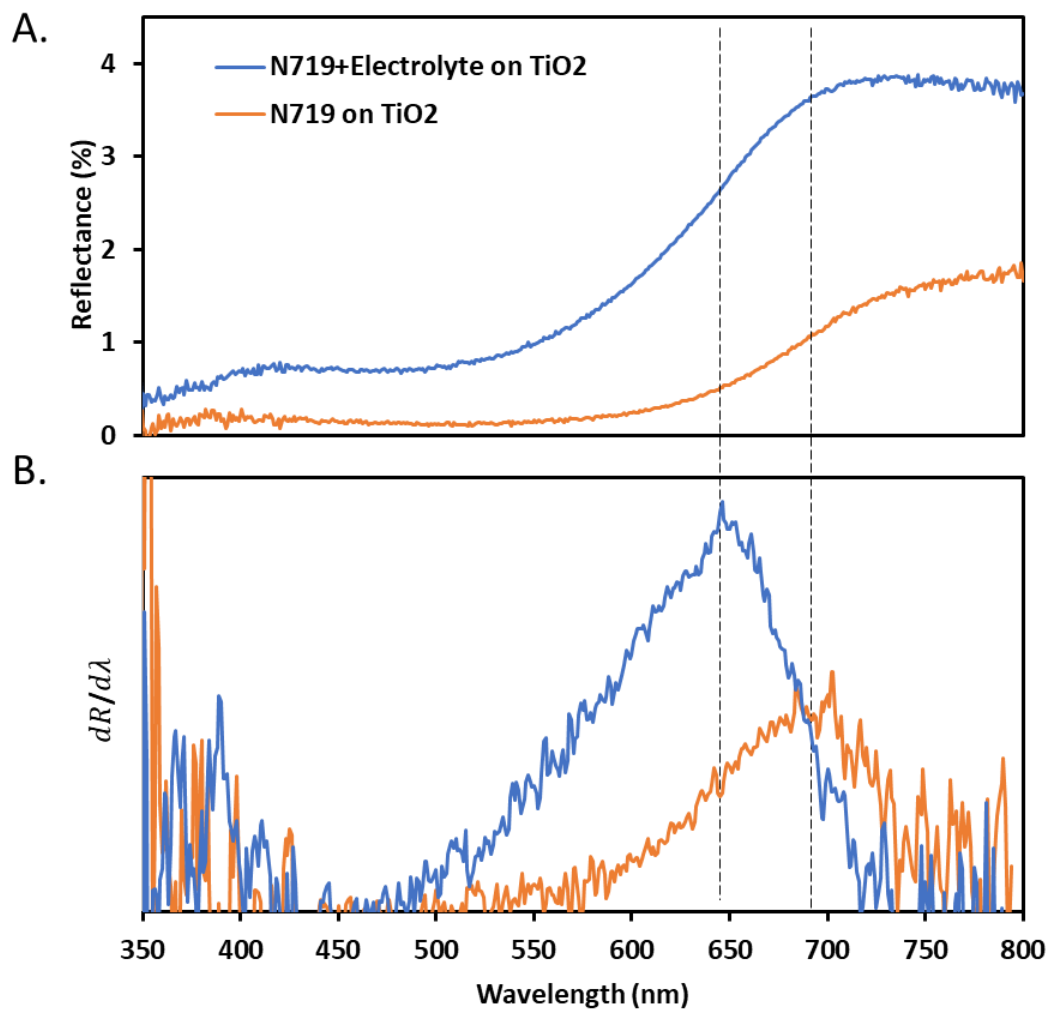
UV-Vis DRS spectral analysis of N719 dye and electrolyte onto TiO₂ substrate

Figure 8.21: The UV-Vis DRS reflectance spectra of the dye adsorbed on TiO₂ with and without electrolyte (A) and of the first derivative to determine the inflection point of the reflectance spectra (B).

FTIR spectral analysis of various functional group in aged samples

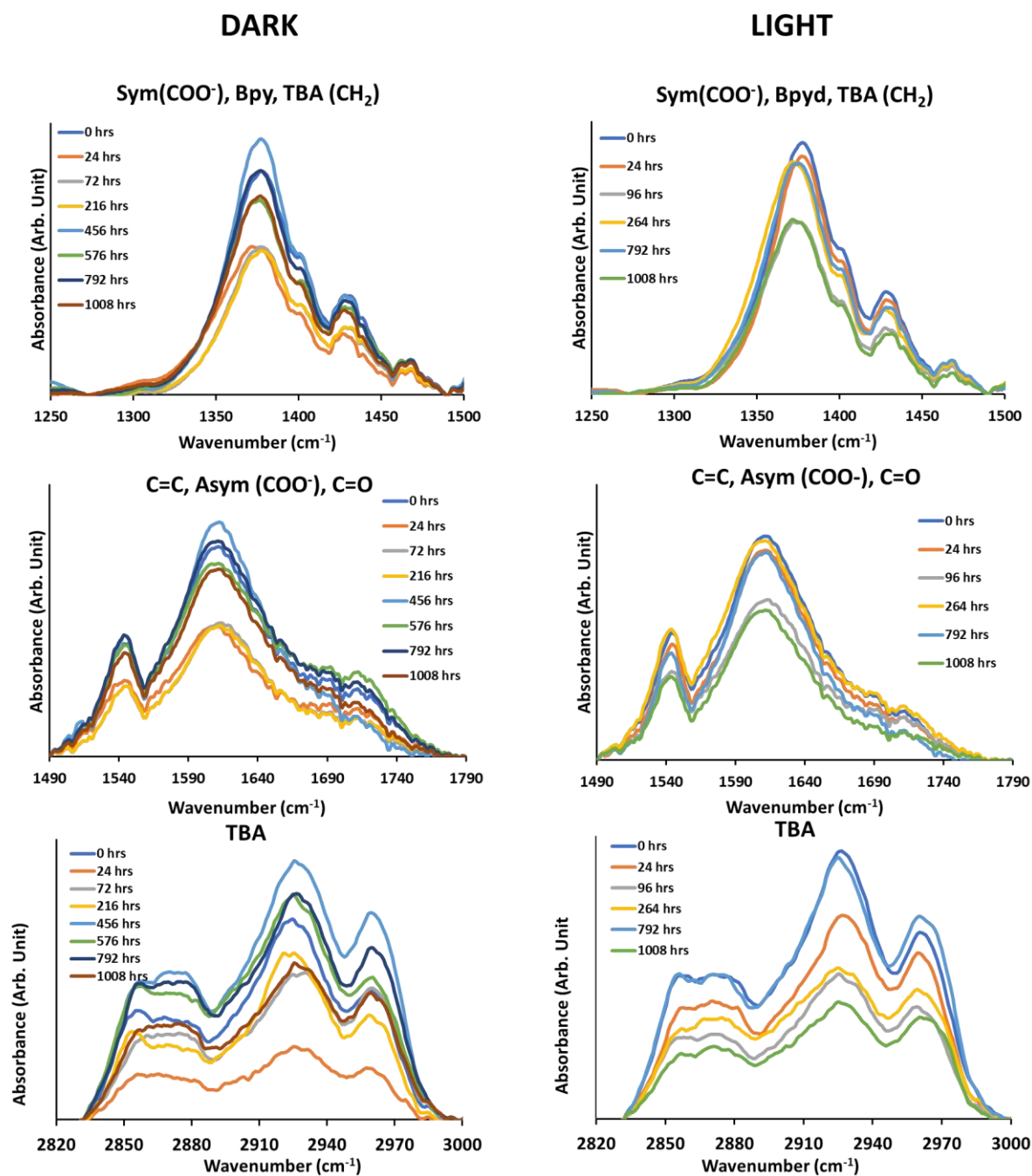


Figure 8.22: IR spectra for respective functional groups for dark (left) and light (right) aged samples.

DFT calculation and modelling

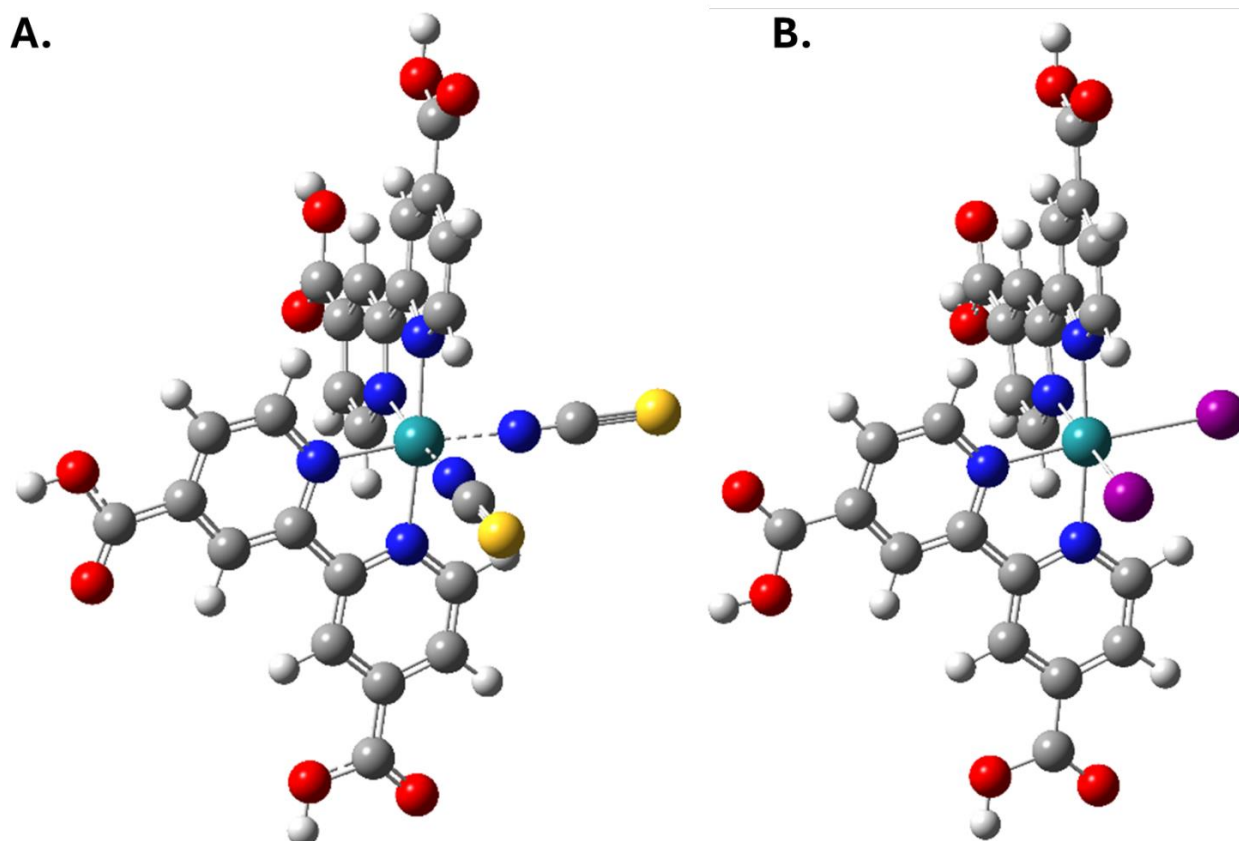


Figure 8.23: Geometrically optimised structure of molecule (A.), referenced as N719, and molecule (B.), denoting N719 with the substitution of the SCN⁻ ligand by I⁻ in AN.

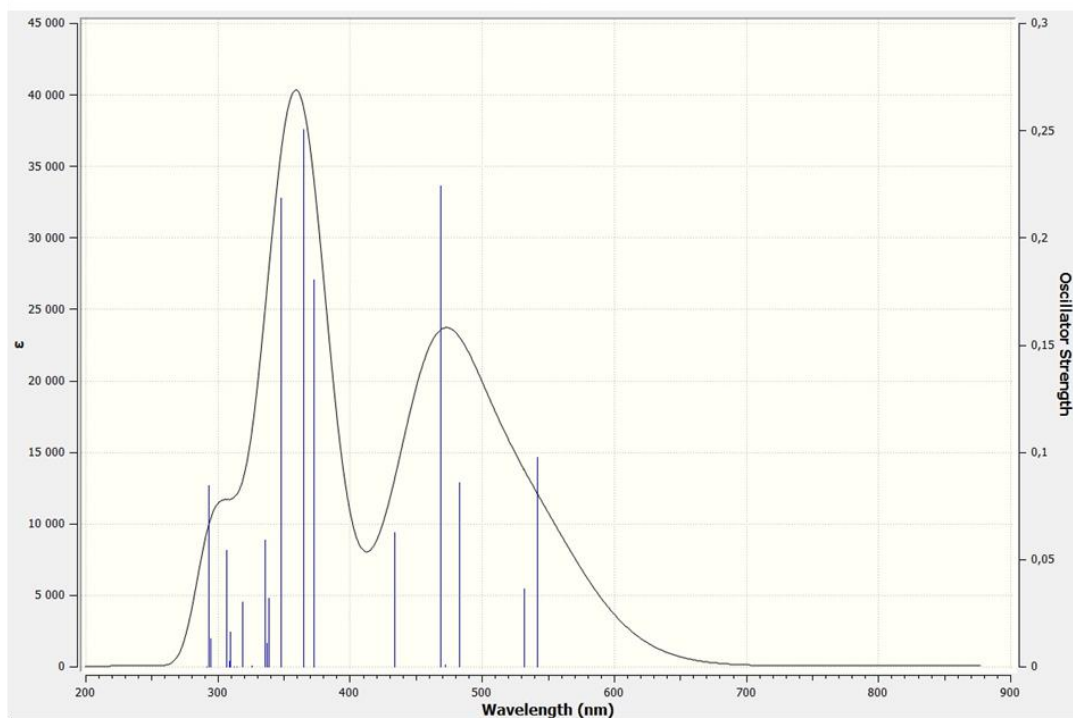
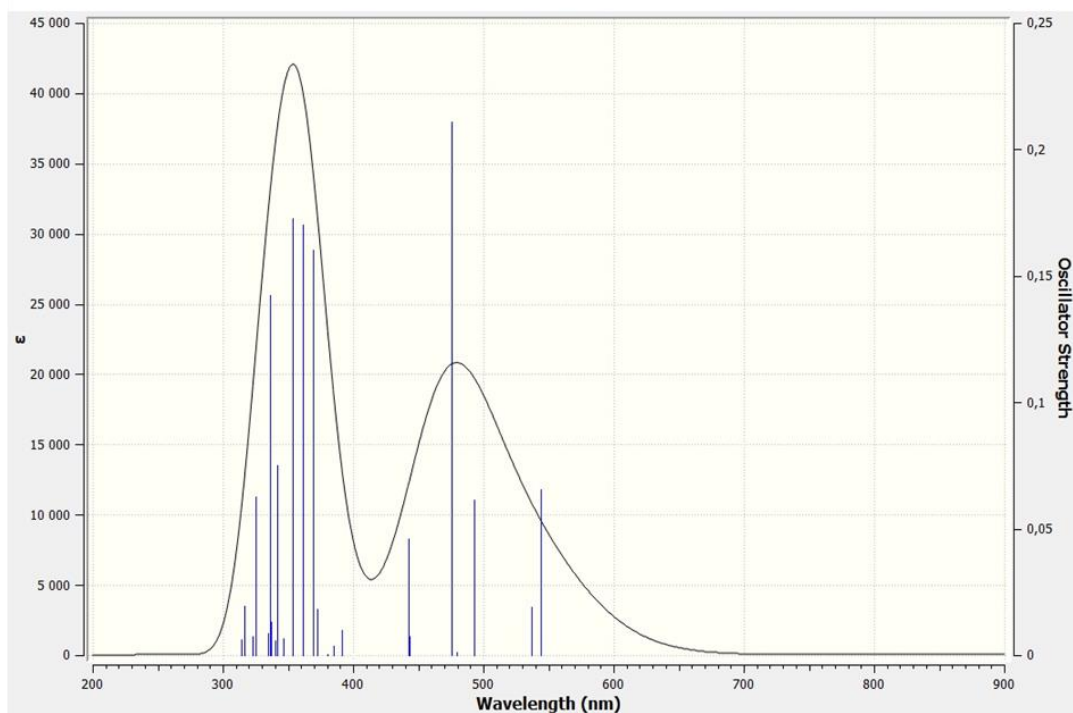
A. N719**B. N719 (NCS \rightarrow I)**

Figure 8.24: The simulated UV-Vis spectrum of molecule (A.) referenced as N719, and molecule (B.), denoting N719 with the substitution of the SCN⁻ ligand by I⁻ in AN solvent.